Technical Report

TR-13-06

EBS TF – THM modelling

BM 1 – Small scale laboratory tests

Lennart Börgesson, Mattias Åkesson,
Martin Birgersson, Harald Hökmark
Clay Technology AB

Jan Hernelind, 5T Engineering AB

December 2016

Svensk Kärnbränslehantering AB
Swedish Nuclear Fuel
and Waste Management Co

Box 250, SE-101 24 Stockholm
Phone +46 8 459 84 00

ISSN 1404-0344
SKB TR-13-06
ID 1385779
December 2016

EBS TF – THM modelling

BM 1 – Small scale laboratory tests

Lennart Börgesson, Mattias Åkesson,
Martin Birgersson, Harald Hökmark
Clay Technology AB

Jan Hernelind, 5T Engineering AB

Abstract

Phase 1 of the EBS Task Force on modelling THM processes in buffer and backfill materials for nuclear waste disposal has been running between the years 2005 and 2010. This phase included a number of THM (thermo-hydro-mechanical) tasks for modelling both well-defined laboratory tests and large scale field tests such as the two Canadian URL tests ITT and BCE and the Swedish ÄHRL test CRT.

This report deals with the modelling results of the small scale laboratory tests (Benchmark 1) from the two teams granted by SKB. The large scale field tests (Benchmark 2) are reported in another report.

The following tasks are included in BM 1:

Task 1 – THM tests

Task 1.1.1 Two tests with constant volume and an applied temperature gradient on MX-80 (CEA).

Task 1.1.2 Two tests with constant volume on FEBEX bentonite – one with thermal gradient and one isothermal (Ciemat).

Task 1.1.3 One test with constant external total pressure test and an applied temperature gradient on FEBEX bentonite (UPC).

Task 2 – Gas migration tests

Task 1.2.1 One test with constant external total pressure (BGS).

Task 1.2.2 One test with constant volume (BGS).

All the three tasks in Task 1 were modelled by both teams, while only one team (SKB 1) modelled the gas migration tests. The report describes the test set up, the tasks, the results of the modelling and analyses made by the two modelling teams.

Sammanfattning

Fas 1 av ”EBS Task Force” avseende modellering av THM-processer i buffert- och återfyllningsmaterial för slutförvaring av radioaktivt avfall har pågått mellan åren 2005 och 2010. Denna fas har inkluderat ett flertal THM (termo-hydro-mekaniska) beräkningsuppgifter som innebar att modellera både väldefinierade småskaliga laboratorieförsök och storskaliga fältförsök såsom de två kanadensiska försöken ITT och BCE och det svenska försöket CRT i Äspö.

Denna rapport beskriver den modellering av de småskaliga laboratorieförsöken (Benchmark 1) som utförts av de två svenska modelleringsgrupperna som finansierats av SKB. Modelleringen av de storskaliga fältförsöken (Benchmark 2) beskrivs i en separat rapport.

Följande beräkningsuppgifter inkluderas i BM 1:

Task 1 – THM försök

Task 1.1.1 Två försök med konstant volym och en termisk gradient gjorda på MX-80 bentonit med olika densitet (CEA).

Task 1.1.2 Två försök med konstant volym gjorda på FEBEX-bentonit – ett med en termisk gradient och ett isotermiskt (Ciemat).

Task 1.1.3 Ett försök med konstant yttre tryck och en termisk gradient gjort på FEBEX-bentonit (UPC).

Task 2 – Gasmigrationsförsök

Task 1.2.1 Ett försök med konstant yttre totaltryck (BGS).

Task 1.2.2 Ett försök med konstant volym (BGS).

Alla tre beräkningsuppgifterna i Task 1 har modellerats av båda modelleringsgrupperna, emedan bara en grupp (SKB 1) modellerat gasmigrationsförsöken. Rapporten beskriver försöksuppställningarna, beräkningsuppgifterna, modelleringsresultaten och analyser av resultaten gjorda av respektive modelleringsgrupp.

Contents

1 Introduction

The Task Force on Engineered Barrier System (EBS) is an international project arranged by SKB with the purpose to verify and evaluate the capability to model THM-processes in unsaturated and saturated buffer materials and to further develop the codes.

Phase 1 of the EBS Task Force on modelling THM processes in buffer and backfill materials for nuclear waste disposal has been running between the years 2005 and 2010. This phase included a number of THM (thermo-hydro-mechanical) tasks for modelling both well-defined laboratory tests and large scale field tests such as the two Canadian URL tests IT and BCE and the Swedish ÄHRL test CRT.

The Task Force is initiated and managed by SKB under supervision by Anders Sjöland, SKB. Antonio Gens, UPC has been chairman and Lennart Börgesson, Clay Technology AB has been secretary.

All defined tasks are given in Table 1-1. Participating organisations besides SKB have for this phase been Andra (France), BMWi (Germany), CRIEPI (Japan), Nagra (Switzerland), Posiva (Finland), NWMO (Canada), ENRESA (Spain) and RAWRA (Czech Republic). All together 9 modelling teams have been participating in the work using 7 different codes.

Table 1-1. Modelled tests in the EBS Task Force, phase 1.

Benchmark 1 – Laboratory tests
Task 1 – THM tests
1.1.1 Two constant volume tests on MX-80 (CEA)
1.1.2 Two constant volume tests on FEBEX bentonite – one with thermal gradient and one isothermal (Ciemat)
1.1.3 Constant external total pressure test with temperature gradient on FEBEX bentonite (UPC)
Task 2 – Gas migration tests
1.2.1 Constant external total pressure (BGS)
1.2.2 Constant volume (BGS)
Benchmark 2 – Large scale field tests
Task 1 – URL tests (AECL)
2.1 Buffer/Container Experiment and Isothermal Test
Task 2 – Äspö HRL test (SKB)
2.2 Canister Retrieval Test

The present report deals with the tasks in Benchmark 1. The tasks in Benchmark 2 are reported separately (Börgesson et al. 2016). The tasks in BM 1 concern well-defined laboratory tests from different laboratories. These tests and the proposed tasks were described in so called task descriptions that were delivered in advance. Those task descriptions are included in the report.

Twice a year there has been a Task Force meeting for a couple of days where the tasks, the modelling results and comparison between results and measurements were presented and discussed.

This report only describes the tasks and the results of the modelling and analyses made by the two modelling teams granted by SKB. The contributions of the other teams are reported separately. A general analysis and comparison of results between different modelling groups will be made in a separate report by A. Gens (Gens 2016).

The two modelling teams (named SKB 1 and SKB 2) are the following for Benchmark 1:

SKB 1: Mattias Åkesson, Martin Birgersson and Harald Hökmark, Clay Technology AB.

SKB 2: Lennart Börgesson, Clay Technology AB and Jan Hernelind 5T Engineering AB.

Tasks 1.1.1, 1.1.2 and 1.1.3 have been modelled and reported by Mattias Åkesson, Martin Birgersson and Harald Hökmark of SKB 1 and by Lennart Börgesson and Jan Hernelind of SKB 2.Tasks 1.2.1 and 1.2.2 have been modelled by Martin Birgersson, Mattias Åkesson, and Harald Hökmark of SKB 1.

The motivation for having two teams is that different codes with different capabilities and advantages have been used by the two teams. SKB 1 has mainly used Code Bright while SKB 2 has used Abaqus. Both these codes have been used in the modelling for SR-Site.

2 BM 1.1.1 – THM mock-up experiments made by CEA

2.1 General

The first year of the project was devoted to Benchmarks 1.1.1, 1.1.2 and 1.1.3. In these benchmarks five laboratory tests were modelled and the results compared to measurements. This chapter describes the tests and the modelling results of BM 1.1.1. The specifications were compiled by Claude Gatabin (CEA).

2.2 Specifications

This section describes the proposal of Benchmark THM 1.1.1, based on the performance of THM mock-up experiments on MX-80 bentonite by CEA. The information provided by Claude Gatabin on this experimental programme is gratefully acknowledged.

2.2.1 Description of the THM mock up tests

Two THM mock up tests have been performed on vertical cylindrical columns of compacted MX-80 bentonite. Two different initial water contents have been used to form the samples.

Each test is composed of two phases. In Phase 1 heat is applied to one end of the column while the temperature at the other end is kept constant and equal to 20 °C. A maximum temperature of 150 °C is applied. Phase 2 starts after thermal equilibrium has been achieved and involves the gradual hydration of the sample. A constant water pressure is applied to the end opposite to the one where the temperature variation was prescribed. Constant volume conditions are ensured in the two phases of the test.

The following parameters are measured during the tests:

- Temperatures.
- Relative humidity.
- Pore pressure.
- Total axial stress.
- Total radial stress.

It is advised to read carefully the CEA report: “Bentonite THM mock up experiments. Sensor data report (DPC/SCCME 05-300-A)” (Gatabin and Billaud 2005) that contains a detailed description of equipment and experiments. Only the most immediately relevant information is given in this document.

Apparatus and monitoring system

The samples have both a diameter and a height of 203 mm. The specimens are tested in an apparatus the diagram of which is shown in Figure 2-1. The samples are tightly enclosed in a PTFE sleeve. To minimize heat losses, the cells were insulated with a heatproof envelope. Experiments are not gas tight. Heat is applied at the bottom plate whereas hydration proceeds from the top of the sample.

The monitoring sensors are installed normal to the vertical axis. Measurements of temperature, relative humidity and pore pressures are performed close to the axis of the column whereas radial stress sensors are placed in contact with the outside surface of the sample. The vertical location of the various sensors is given in Appendix 1. In addition each cell is equipped with a force sensor to measure the axial load. This sensor is located at the top of the sample.

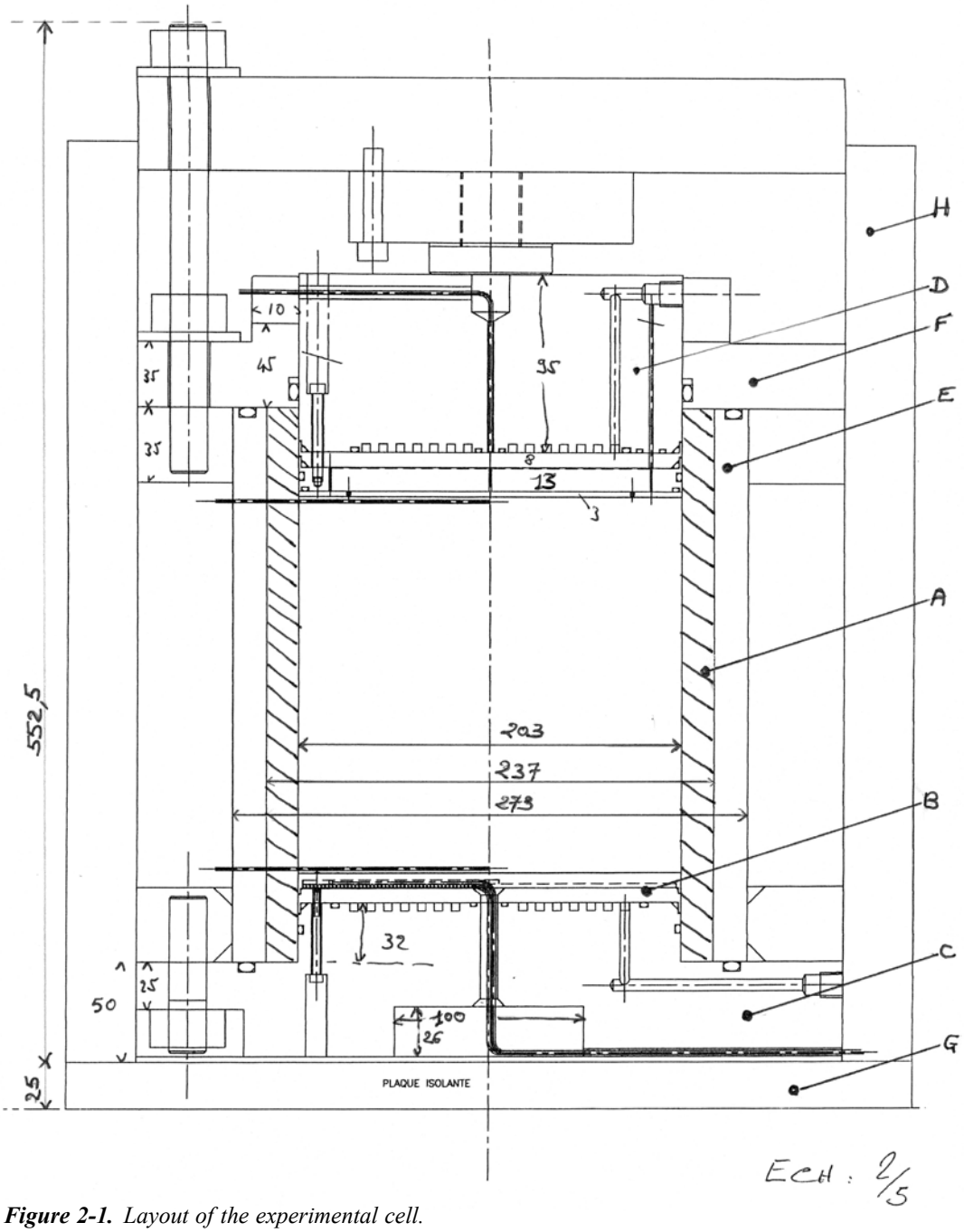

Figure 2-1. *Layout of the experimental cell.*

Material

Compacted MX-80 bentonite has been used to manufacture the specimens tested. For the specimen of Cell 1, the bentonite was stabilised in an atmosphere with a relative humidity of 60 % whereas for the specimen of Cell 2, the bentonite was stabilised in an atmosphere with a relative humidity of 90 %. A target dry density of 1.7 g/cm^3 was adopted for compaction. The characteristics of the material at the time of emplacement in the apparatus are given in Table 2-1.

A review of the reported THM properties of MX-80 bentonite has yielded the information presented in Appendix 2.

Table 2-1. Characteristics of the MX-80 samples after compaction.

	Cell 1: 1858iA	Cell 2: 1857iA
Powder conditioning, HR (%)	60	90
Compaction pressure (MPa)	33	33
Sample mass (g)	13332	13395
Water content (%)	13.66	17.86
Diameter (mm)	202.7	202.7
Height (mm)	203.0	203.0
Bulk density (g/cm^3)	2.035	2.045
Dry density (g/cm^3)	1.791	1.735
Porosity	0.3242	0.3453
Void ratio	0.48	0.527
Degree of saturation	0.755	0.897
Swelling pressure at saturation (MPa)	24.5	18.2

Note: The selected density of MX80 grains used for calculation purposes is equal to 2.65 g/cm^3.

Protocol of the experiments

In Phase 1 of the experiments, the temperature at the bottom end of the specimen was raised in steps until reaching 150 °C. Table 2-2 contains the temperature increase schedule. The temperature at the top end of the specimen was kept constant at 20 °C. The two experiments Phase 1 started at 15:27 on May 26, 2003 and considered finished, after 2706 hours, at 9:00 on September 16, 2003.

Phase 2 involved the application of a 1 MPa water pressure at the top of the sample whereas at the bottom, the temperature was maintained at 150 °C. Some water leaks developed in Cell 1 but no leaks were apparently observed in Cell 2. Phase 2 for Cell1 started at 14:23 on September 16, 2003 and ended on May 25, 2004 and for Cell 2, it started at 14:26 on September 18, 2003 and ended at 9:00 on March 12, 2004.

It should be noted that the transition from Phase 1 to Phase 2 involved some manipulation of the apparatus resulting in a variation of the recorded stresses, notably the value of the axial stresses (Gatabin and Billaud 2005).

Table 2-2. Protocol for temperature increase in Phase 1 of the experiments.

Start-up date	Initial temperature (°C)	Ending date	Final temperature (°C)	Heat velocity (°C/h)	Stable stage (h)	Gradient (°C/cm)
26/05/03 15:27	21.6	02/06/03 11:27	30	0.4	21	0.5
02/06/03 11:27	30	05/06/03 16:05	40	0.4	25	1.0
05/06/03 16:05	40	08/06/03 16:09	50	0.4	25	1.5
08/06/03 16:09	50	12/06/03 09:19	60	0.4	25	2.0
12/06/03 09:19	60	16/06/03 11:46	70	0.4	25	2.5
16/06/03 11:46	70	20/06/03 10:11	80	0.4	25	3.0
20/06/03 10:11	80	24/06/03 16:07	90	0.4	25	3.5
24/06/03 16:07	90	30/06/03 11:08	100	0.4	25	4.0
30/06/03 11:08	100	03/07/03 17:30	105	0.2	25	4.25
03/07/03 17:30	105	10/07/03 14:46	110	0.2	25	4.50
10/07/03 14:46	110	17/07/03 16:19	115	0.2	25	4.75
17/07/03 16:19	115	22/07/03 15:04	120	0.2	25	5.0
22/07/03 15:04	120	28/07/03 10:31	125	0.2	25	5.25
28/07/03 10:31	125	05/08/03 09:38	130	0.2	25	5.50
05/08/03 09:38	130	18/08/03 09:55	135	0.2	25	5.75
18/08/03 09:55	135	05/09/03 18:01	140	0.2	25	6.0
05/09/03 18:01	140	16/09/03 09:00	150	0.2	50	6.50

2.2.2 Test results

A number of selected results can be seen in the report by Gatabin and Billaud (2005). The full data sets are included in the Excel files distributed within the EBS Task Force, as described below.

Phase 1

Temperature: File "THM BM 1.1 Phase 1 Temperature.xls"

- Cell 1: Sheet: *Cell 1*. Relevant columns: "Date/time" and "Cell1T0, Cell1T1, Cell1T2, Cell1T3, Cell1T4, Cell1T5, Cell1T6, Cell1T7, Cell1T8, Cell1T9, Cell1T10, Cell1T11, Cell1T12, Cell1T13, Cell1T14".
- Cell 2: Sheet: *Cell 2*. Relevant columns: "Date/time" and "Cell2T0, Cell2T1, Cell2T2, Cell2T3, Cell2T4, Cell2T5, Cell2T6, Cell2T7, Cell2T8, Cell2T9, Cell2T10, Cell2T11, Cell2T12, Cell2T13, Cell2T14".

Relative humidity: File "THM BM 1.1 Phase 1 RH.xls"

- Cell 1: Sheet: *Cell 1*. Relevant columns: "Date/time" and "Cell1HR1, Cell1HR2, Cell1HR3, Cell1HR4, Cell1HR5, Cell1HR6, Cell1HR7". The columns "Cell1HRT1, Cell1HRT2, Cell1HRT3, Cell1HRT4, Cell1HRT5, Cell1HRT6, Cell1HRT7" contain the associated temperatures data.
- Cell 2: Sheet: *Cell 2*. Relevant columns: "Date/time" and "Cell2HR1, Cell2HR2, Cell2HR3, Cell2HR4, Cell2HR5, Cell2HR6, Cell2HR7". The columns "Cell2HRT1, Cell2HRT2, Cell2HRT3, Cell2HRT4, Cell2HRT5, Cell2HRT6, Cell2HRT7" contain the associated temperatures data.

Pore Pressures: File "THM BM 1.1 Phase 1 Pore P.xls"

- Cell 1: Sheet: *Cell 1*. Relevant columns: "Date/time" and "PI1, PI2, PI3, PI4".
- Cell 2: Sheet: *Cell 2*. Relevant columns: "Date/time" and "PI1, PI2, PI3, PI4".

Radial stress: File "THM BM 1.1 Phase 1 Radial P.xls"

- Cell 1: Sheet: *Cell 1*. Relevant columns: "Date/time" and "1PTK1, 1PTE2, 1PTK3, 1PTE4, 1PTK5, 1PTE6, 1PTK7, 1PTK8".
- Cell 2: Sheet: *Cell 2*. Relevant columns: "Date/time" and "2PTK1, 2PTE2, 2PTK3, 2PTE4, 2PTK5, 2PTE6, 2PTK7, 2PTE8".

Axial stress: File "THM BM 1.1 Phase 1 Axial P.xls".

- Cell 1: Sheet: *Cell 1*. Relevant columns: "Date/time" and "Confining pressure".
- Cell 2: Sheet: *Cell 2*. Relevant columns: "Date/time" and "Confining pressure".

Phase 2

Temperature: File "THM BM 1.1 Phase 2 Temperature.xls".

- Cell 1: Sheet: *Cell 1*. Relevant columns: "Date/time" and "Cell1T0, Cell1T1, Cell1T2, Cell1T3, Cell1T4, Cell1T5, Cell1T6, Cell1T7, Cell1T8, Cell1T9, Cell1T10, Cell1T11, Cell1T12, Cell1T13, Cell1T14".
- Cell 2: Sheet: *Cell 2*. Relevant columns: "Date/time" and "Cell2T0, Cell2T1, Cell2T2, Cell2T3, Cell2T4, Cell2T5, Cell2T6, Cell2T7, Cell2T8, Cell2T9, Cell2T10, Cell2T11, Cell2T12, Cell2T13, Cell2T14".

Relative humidity: File "THM BM 1.1 Phase 2 RH.xls".

- Cell 1: Sheet: *Cell 1*. Relevant columns: "Date/time" and "Cell1HR1, Cell1HR2, Cell1HR3, Cell1HR4, Cell1HR5, Cell1HR6, Cell1HR7". The columns "Cell1HRT1, Cell1HRT2, Cell1HRT3, Cell1HRT4, Cell1HRT5, Cell1HRT6, Cell1HRT7" contain the associated temperatures data.
- Cell 2: Sheet: *Cell 2*. Relevant columns: "Date/time" and "Cell2HR1, Cell2HR2, Cell2HR3, Cell2HR4, Cell2HR5, Cell2HR6, Cell2HR7". The columns "Cell2HRT1, Cell2HRT2, Cell2HRT3, Cell2HRT4, Cell2HRT5, Cell2HRT6, Cell2HRT7" contain the associated temperatures data.

Pore Pressures: File "THM BM 1.1 Phase 2 Pore P.xls".

- Cell 1: Sheet: *Cell 1*. Relevant columns: "Date/time" and "PI1, PI2, PI3, PI4".
- Cell 2: Sheet: *Cell 2*. Relevant columns: "Date/time" and "PI1, PI2, PI3, PI4".

Radial stress: File "THM BM 1.1 Phase 2 Radial P.xls"

- Cell 1: Sheet: *Cellule 1*. Relevant columns: "Date/time" and "1PTK1, 1PTE2, 1PTK3, 1PTE4, 1PTK5, 1PTE6, 1PTK7, 1PTK8".
- Cell 2: Sheet: *Cellule 2*. Relevant columns: "Date/time" and "2PTK1, 2PTE2, 2PTK3, 2PTE4, 2PTK5, 2PTE6, 2PTK7, 2PTE8".

Axial stress: File "THM BM 1.1 Phase 2 Axial P.xls".

- Cell 1: Sheet: *Cellule 1*. Relevant columns: "Date/time" and "Confining pressure".
- Cell 2: Sheet: *Cellule 2*. Relevant columns: "Date/time" and "Confining pressure".

2.2.3 Requested results

The following information is requested:

a) Main features of the analyses performed.

b) Results of the analyses and comparison with experimental results.

Main features of the analyses performed

This basic description should contain summarised information on:

- Geometry adopted for the analysis.
- Type of analysis (e.g. 1-D, 2-D, axisymmetric...).
- Element types used.
- Constitutive laws adopted (thermal, hydraulic, mechanical).
- Constitutive parameters used and procedure used in their determination or estimation.
- Boundary conditions (thermal, hydraulic, mechanical).
- Initial conditions (thermal, hydraulic, mechanical).
- Hypothesis adopted for gas pressure and gas flow.
- Any other features that are deemed important in the analysis.

Results of the analyses and comparison with experimental results

The following analysis results should be provided graphically together with comparison with observed data. The Excel files of the submitted graphs should also be made available. It should be noted that reliability of radial stress measurements is not high.

Phase 1 (for both Cell 1 and Cell 2)

- Temperature vs. time for sensors T0, T1, T2, T3, T4, T5, T6, T7, T8, T9, T10, T11, T12, T13, T14.
- Relative humidity vs. time for sensors HR1, HR2, HR3, HR4, HR5, HR6, HR7.
- Radial stress vs. time for sensors PT1, PT2, PT3, PT4, PT5, PT6, PT7, PT8.
- Axial stress vs. time.
- Temperature vs. distance for days 28/06/03, 31/07/03 and 15/09/03.
- Relative humidity vs. distance days 28/06/03, 31/07/03 and 15/09/03.

Phase 2 (for both Cell 1 and Cell 2)

- Temperature vs. time for sensors T0, T1, T2, T3, T4, T5, T6, T7, T8, T9, T10, T11, T12, T13, T14.
- Relative humidity vs. time for sensors HR1, HR2, HR3, HR4, HR5, HR6, HR7.
- Radial stress vs. time for sensors PT1, PT2, PT3, PT4, PT5, PT6, PT7, PT8.
- Axial stress vs. time.
- Temperature vs. distance for days 15/10/03, 14/01/04 and 4/03/04.
- Relative humidity vs. distance days 15/10/03, 14/01/04 and 4/03/04.

2.2.4 Sensor locations

The location of the sensors are specified in Appendix 1.

2.2.5 Properties of MX-80

The properties of MX-80 as delivered to the participants are shown in Appendix 2.

2.3 Modelling results with Code Bright

2.3.1 Introduction

This section presents the calculations made by Clay Technology Team 1 on benchmark 1.1 – THM mock-up experiments made by CEA, France.

In Section 2.3.2 the experiment is briefly described. In Section 2.3.3 the model is described. In Section 2.3.4 the results are presented and compared with experimental data. A sensitivity analysis of relevant model parameters is also presented. In Section 2.3.5 some discussion is made on difficulties which arose in the modeling work. Finally conclusions of the modeling calculations are made (Section 2.3.6).

2.3.2 Experimental background

This section briefly describes the experiment on which the benchmark calculation is based. It is explained in greater detail in the specifications in Section 2.2.

A cylindrical MX-80 bentonite sample, of height and diameter both 203 mm, was enclosed in a Teflon PTFE sleeve and mounted in a steel cell. The system was heated at the lower and cooled (kept at constant temperature) at the upper edge. The cell was thermally insulated in order to get the heat transport to be dominated by flux parallel to the cylindrical axis.

Furthermore, the setup allowed a water pressure to be applied at the upper edge. Temperature, relative humidity and pore pressure as well as axial and radial stresses were recorded by sensors throughout the sample. Additionally, the amount of water injected from the upper edge was continuously measured.

The experiment was divided into two phases. In the first phase, lasting 113 days, a thermal gradient was established across the sample by increasing the temperature at the lower edge in a stepwise manner while keeping the upper part at a constant temperature. In the next phase, water was injected from the cooler side by applying a water pressure of 1 MPa. In this phase the established final temperature gradient from the first phase was maintained. The system was unloaded (the top being disassembled) between the two phases.

Two versions of the experiment were conducted in two identical cells and with identical schemes for thermal control and water injection. The two bentonite samples had approximately the same dry density but different values of the initial water content.

2.3.3 Model description

The modeling work was performed with the finite element program Code_Bright, version 2.2 (CIMNE 2000). Simultaneous consideration was made concerning thermal, hydrodynamic and mechanical processes. The design of the models on the basis of the experimental setup is discussed below.

Geometry

The two cells were modeled adopting a 2-dimensional axisymmetric geometry shown in Figure 2-2. Only the bentonite was explicitly modeled, the container being taken into account by suitable boundary conditions.

The clay itself, however, is divided into two parts according to whether the material loses or gains water during the moisture redistribution under the establishment of a thermal gradient over the sample. The mechanical behavior of the clay in these two regions are rather different as the bentonite swells in the parts which gains water, while it shrinks in the hotter parts where the material dries. The position of the interface between these domains was based on results from the initial thermo-hydraulic (TH) analysis of Cell 1 (i.e. the relative humidity profile at the end of phase 1, see below). For simplicity, this division was used throughout the thermo-hydro-mechanical (THM) analyses of both analysed cells.

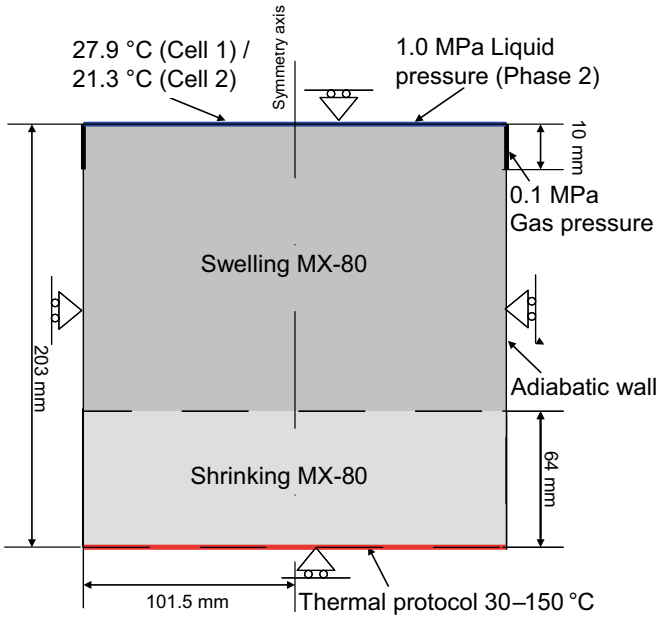

Figure 2-2. *Geometry and boundary conditions for the model of the bentonite samples in the two cells.*

Boundary conditions

The thermal, hydrodynamic and mechanical boundary conditions imposed on the systems are schematically pictured in Figure 2-2.

Thermal boundaries

In phase 1, the lower edge of the cylinders are gradually heated in accordance with the prescribed experimental thermal protocol – from 30 to100 °C in steps of 10 °C and thereafter in steps of 5 °C up to 150 °C, as seen in Figure 2-3.

The second phase starts after 113 days and continues to day 365 for Cell 1 and to day 296 for Cell 2. During this phase the lower edge temperature of 150 °C is maintained. The top parts of the cylinders are kept at a constant temperature throughout the entire simulation.

In the experimental setup the temperature is held at approximately 20 °C at the upper edge of the containing cylinder. However, this temperature is kept on the outer side of a containing upper steel plate, and the edge temperature of the bentonite itself varies slightly both with time and from cell to cell. Since we only model the clay, the edge temperature is chosen as the average of the measured (and interpolated) values for each cell; 27.9 and 21.3 °C for Cell 1 and 2 respectively. With the selected edge temperatures a maximum thermal gradient of 6.1 °C/cm in Cell 1 and of 6.4 °C/cm in Cell 2 is achieved.

Apart from the heating and cooling processes imposed on the edges of the cylinder, the system is assumed completely thermally isolated by an adiabatic boundary on the cylindrical surface of the bentonite samples.

Liquid pressure

During phase 1 (the first 113 days) the two cells are kept strictly isolated concerning liquid flow. In phase 2, the top edges are exposed to a liquid pressure of 1 MPa while the other boundaries still are kept impervious to liquid.

Gas pressure

The experiment is not considered to be gas-tight. In order to handle gas escaping from the cells during the course of the experiment, the models incorporate a 10 mm wide boundary strip where the gas pressure is kept at 0.1 MPa as pictured in Figure 2-2.

Obviously, the choice of location of this strip together with the choice of the transport parameters for the gas phase (see Table 2-4 below) influences the gas pressure distribution in the cell. The current choice of boundary is made mainly because it produces a reasonable gas pressure profile throughout the experiment. The description of gas transport is further discussed in Section 2.3.5.

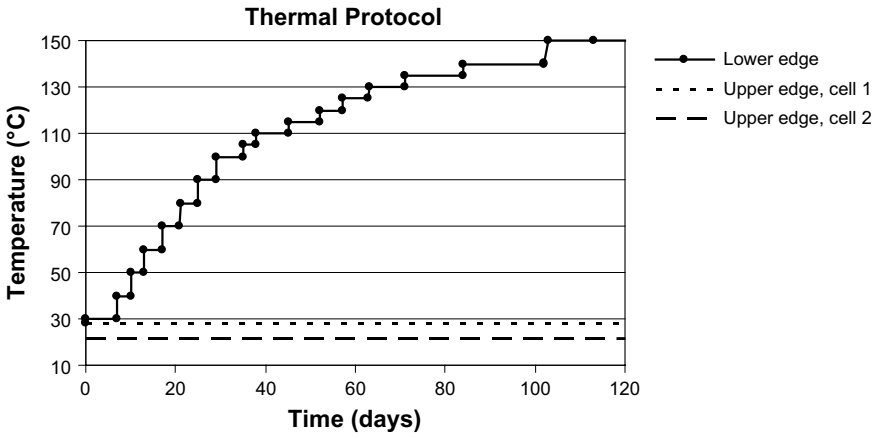

Figure 2-3. *Thermal protocol enforced on the edges of the cells. After phase 1 (day 113), the temperature is kept at 150 °C on the lower edge.*

Mechanical boundaries

The systems are prohibited to move in the normal direction at the confining boundaries, while parallel motion is allowed (roller boundaries).

Initial conditions

The cells are prepared as described in the specification for the present benchmark calculation (CEA 2005) and relevant initial parameter values are found in Table 2-3. Note that the solid phase density here adopted is 2.78 g/cm^3 (based on measurements in water solutions (Karnland et al. 2006)) rather than the value 2.65 g/cm^3 assumed in the specifications. To reproduce the given water ratios values of the initial saturation, the porosity and the void ratio were modified accordingly.

Table 2-3. Initial model parameters for the two cells.

	Cell 1	Cell 2	
Water ratio, w_{ini}	13.66	17.86	%
Dry density, ρ_{dry}	1.791	1.735	g/cm^3
Solid phase density, ρ_s	2.78	2.78	g/cm^3
Porosity, ϕ_{ini}	0.356	0.376	–
Void ratio, e_{ini}	0.552	0.603	–
Saturation level, S_{ini}	69	82	%
Temperature, T_{ini}	27.9	21.3	°C
Gas pressure, $P_{g,ini}$	0.1	0.1	MPa
Liquid pressure $P_{l,ini}$	−70	−43	MPa
Stress ($\sigma_{x,ini}$, $\sigma_{y,ini}$ and $\sigma_{z,ini}$)	0.5	0.5	MPa

Constitutive laws

Thermal and Hydrodynamic laws

The equations involved in describing the thermal and hydrodynamic transport are listed together with relevant transport parameters in Table 2-4. The values adopted for the intrinsic permeability are based on laboratory studies (Börgesson and Hernelind 1999) as is the description of the saturation dependency of the heat conductivity (Börgesson et al. 1995).

Table 2-4. Hydrodynamic and thermal transport equations and associated parameters.

Darcy's law ***(Advective mass flow of gas and liquid)***

$$\vec{q} = \frac{k \cdot k_r}{\mu} \nabla P$$

Intrinsic permeability (isotropic) $k = 1.6\ 10^{-21}\text{m}^2$ (Cell 1), $2.0\ 10^{-21}\text{m}^2$ (Cell 2)

Liquid relative permeability $k_r = \text{S}^3$

Gas phase relative permeability $k_{rg} = 10^8(1\text{-S})^3$

P and μ denote pressure and viscosity respectively. S is the liquid saturation level.

Fourier's law ***(Conductive heat flow)***

$$\vec{i}_c = -\lambda \cdot \nabla T$$

Heat conductivity $\lambda = 0.3 \cdot (1\text{-S}_r) + 1.2 \cdot \text{S}_r$ W/mK

Fick's law ***(Diffusive vapor transport)***

$$\vec{i} = -\phi \cdot \tau \cdot D \cdot (1 - S_r) \cdot \rho_g \cdot \nabla \omega_g^w$$

Diffusion coefficient $D = 5.9 \cdot 10^{-6} \dfrac{(273.15 + T)^{2.3}}{P_g}$ m^2/s

Tortuosity for vapor diffusion, $\tau = 0.15$

ρ_g and ω_g^w denote gas phase density and mass fraction of vapor in gas, respectively. ϕ is the porosity.

It should be noted that a constant intrinsic permeability is used throughout the calculation as further discussed below in the section on mechanical constitutive laws.

The tortuosity factor has been used as a fitting parameter in the present study. This matter is further discussed in Section 2.3.5.

Table 2-5. Retention curve parameters.

	Cell 1	Cell 2	
P_0	89	98	MPa
λ	0.38	0.35	–
P_m	452	417	MPa
λ_m (not fitted)	1	1	–
σ_0 (not fitted)	0.072	0.072	N/m

For the retention curve an extended van Genuchten model is adopted,

$$S_r = \left\{1+\left(\frac{P_g - P_l}{P_0 \dfrac{\sigma}{\sigma_0}}\right)^{\frac{1}{1-\lambda}}\right\}^{-\lambda} \cdot \left\{1-\frac{P_g - P_l}{P_m}\right\}^{\lambda_m},$$

which is fitted to experimental data (Dueck 2004). The fitted parameters are listed in Table 2-5 and Figure 2-4 displays the retention curves for the two cells.

Mechanical laws

Mechanical processes were addressed only after the thermohydraulic problems were satisfactorily solved. The M→H couplings were minimized by neglecting any porosity dependence of the permeability and the retention properties. The processes were further simplified by not considering the unloading of the sample after the first phase of the test.

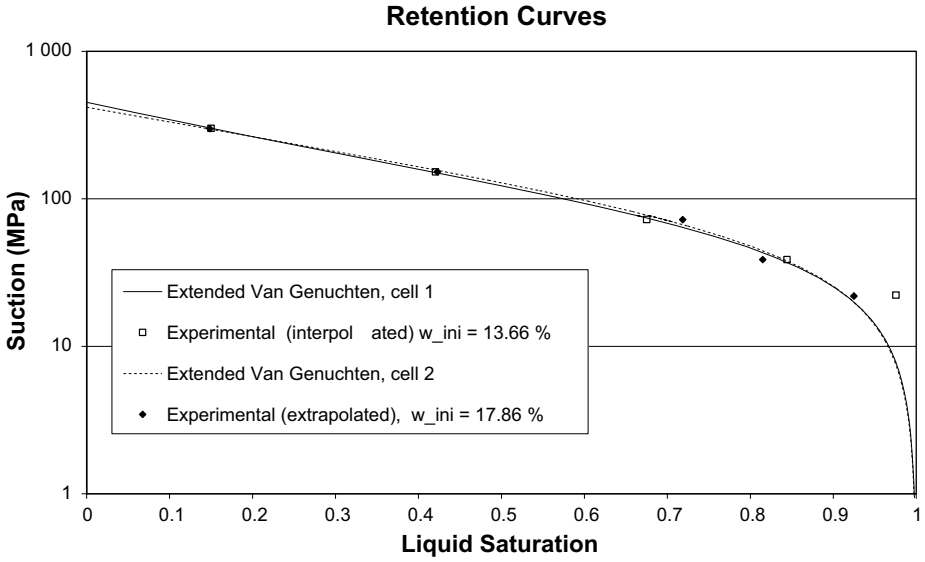

Figure 2-4. *Retention curves used in the modeling of the two cells.*

The mechanical constitutive law used in the model was the Thermo-Elastoplastic (TEP) laws (based on the Barcelona Basic Model, BBM), which are implemented in Code_Bright. The processes were only regarded as elastic. Mechanical parameter values were basically based on lab-test results and previous calibration calculations. The problem of concurrent drying and wetting at different levels in the sample was treated by dividing the model in two domains with different parameter settings, denoted swelling and shrinking, respectively. The reason for this is that the suction-induced strains ($\sim\kappa_s$) are larger during swelling than during shrinkage, and a uniform parameter setting would lead to unrealistic displacements or pressure buildups.

The κ_{i0} and κ_{s0}-values for swelling material were derived from a compression test with a saturated sample and an unloaded swelling test, respectively. The κ_{s0}-value for shrinking material was derived from an unloaded shrinkage test.

Table 2-6. Mechanical equations and associated parameters*.

Thermo-elastoplastic constitutive law (elastic domain)

$$d\varepsilon_v^e = \frac{\kappa_i(s)}{1+e}\frac{dp}{p} + \frac{\kappa_s(p,s)}{1+e}\frac{ds}{s+0.1} + (\alpha_0 + 2\alpha_2\Delta T)\,dT$$

$$\kappa_i(s) = \kappa_{i0}\left[1 + \alpha_i\, s + \alpha_{ils}\ln\left(\frac{s+0.1}{0.1}\right)\right]$$

$$\kappa_s(p,s) = \kappa_{s0}\left[1 + \alpha_{sp}\ln\left(\frac{p}{p_{ref}}\right)\right]e^{\alpha_{ss}\,s}$$

dε = Volumetric strain (–)
p = Net mean stress (MPa)
s = Suction (MPa)
T = Temperature (°C)

Swelling:	Shrinking:
$\kappa_i(s) = 0.25\cdot\left[1 + 0.0009\cdot s - 0.15\cdot\ln\left(\frac{s+0.1}{0.1}\right)\right]$	$\kappa_i(s) = 0.02$
$\kappa_s(p) = 0.28\cdot\left[1 - 0.21\cdot\ln\left(\frac{p}{0.1}\right)\right]$	$\kappa_s(s) = 0.16\cdot e^{-0.04s}$

*All other elastic parameters (i.e. α_{ss} and α_2) were set to zero.

κ_i for the initial unsaturated condition in the swelling material was reduced approximately one order of magnitude in relation to the value for saturated conditions. A suction dependence in between these points was set using both the linear and the logarithmic term in the TEP expression. In the shrinking material a constant value of κ_i was used (cf Figure 2-5, upper).

The stiffness parameter for suction-induced strains (κ_s) for swelling material was assigned a pressure dependence that corresponds to a swelling pressure of 12 MPa, while no suction dependence was assigned. The shrinking material was instead given a suction dependence with a quite extensive suppression of strains at high suction levels, while no pressure dependence was assigned (cf Figure 2-5, lower).

Poisson's ratio for unsaturated blocks is generally found to be in the order of 0.2, while saturated samples exhibit a higher value of around 0.4. Since the upper parts of the test reach saturated conditions, the higher value was assigned to the swelling material, while the lower value was assigned to the shrinking material.

Finally, a linear thermal expansion coefficient (α_0) of 3×10^{-6} (K^{-1}) were assigned to both domains.

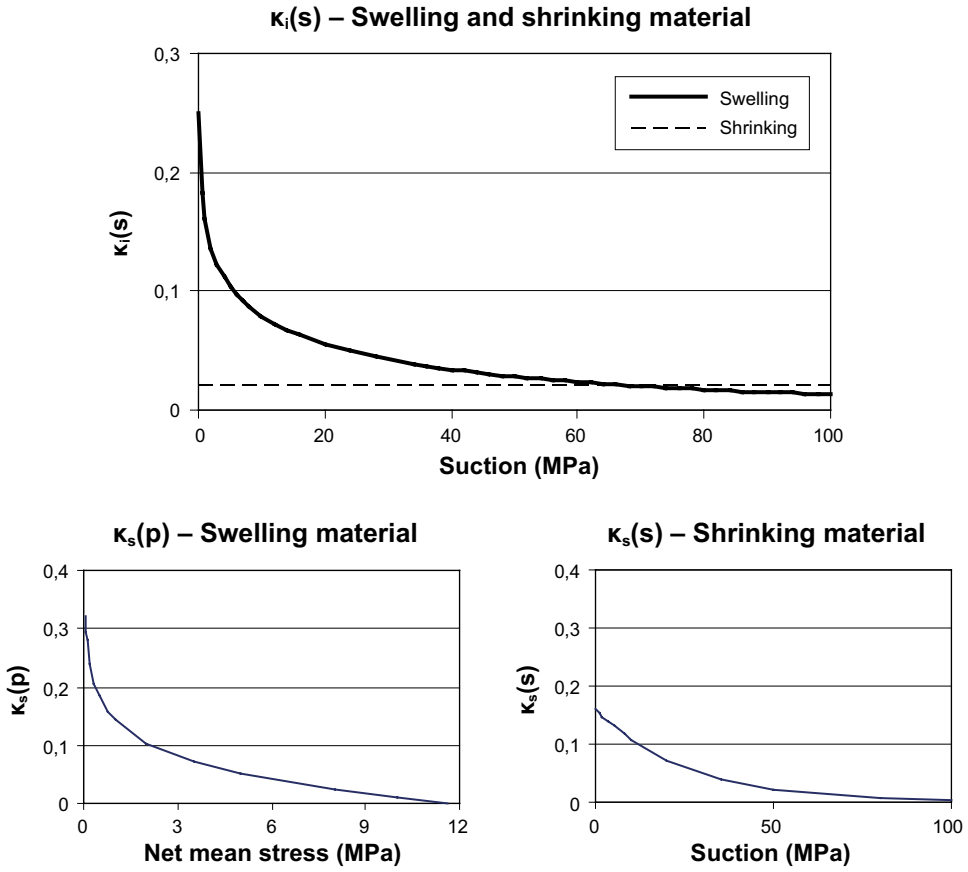

Figure 2-5. *Assigned functions for the stiffness parameters κ_i and κ_s.*

2.3.4 Results

The main results requested are presented below. Except for the case of radial stresses, these plots show modelled results on the symmetry line (Figure 2-2); the time evolution plots furthermore show the evolution in points corresponding to the vertical coordinate of the corresponding sensor. The presented radial stresses regard the periphery of the cylindrical sample.

Temperatures

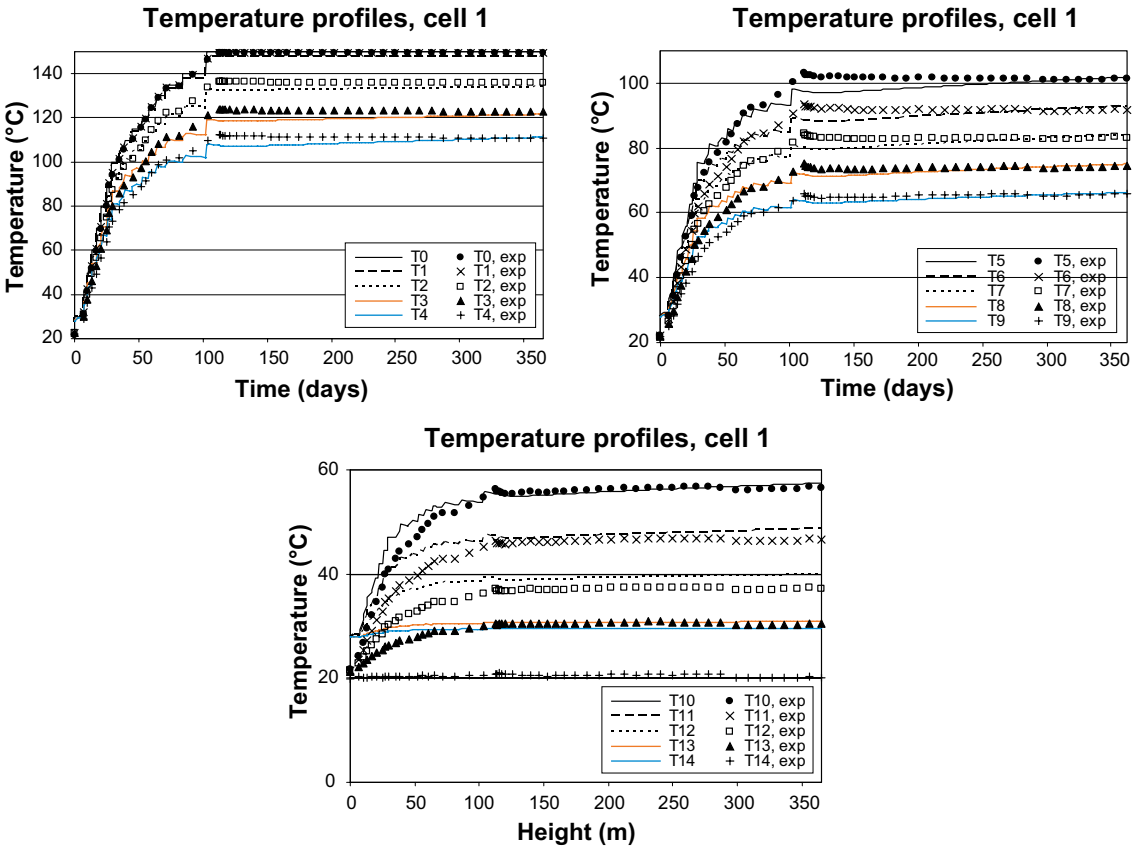

Figure 2-6. *Temperature vs. time in Cell 1 for the sensors T0–T14.*

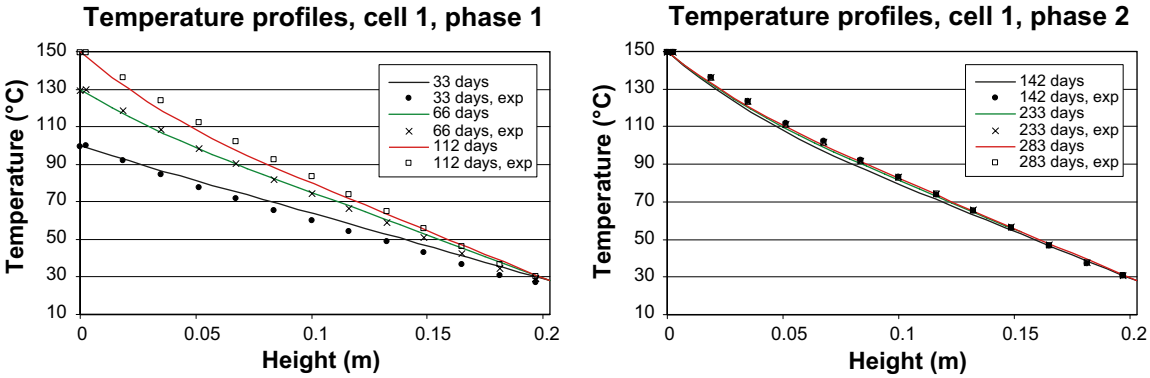

Figure 2-7. *Temperature profiles in Cell 1 at the requested dates for phase 1 and phase 2.*

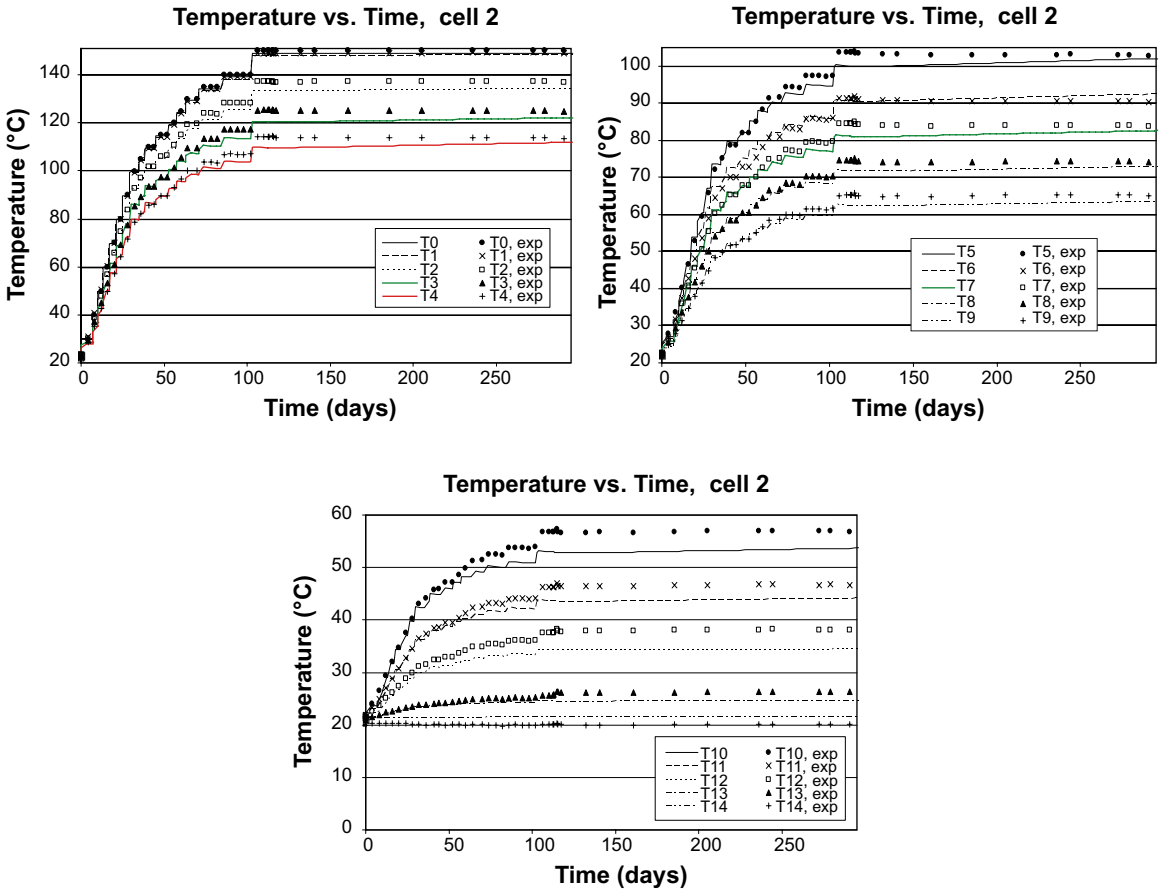

Figure 2-8. *Temperature vs. time in Cell 2 for the sensors T0–T14.*

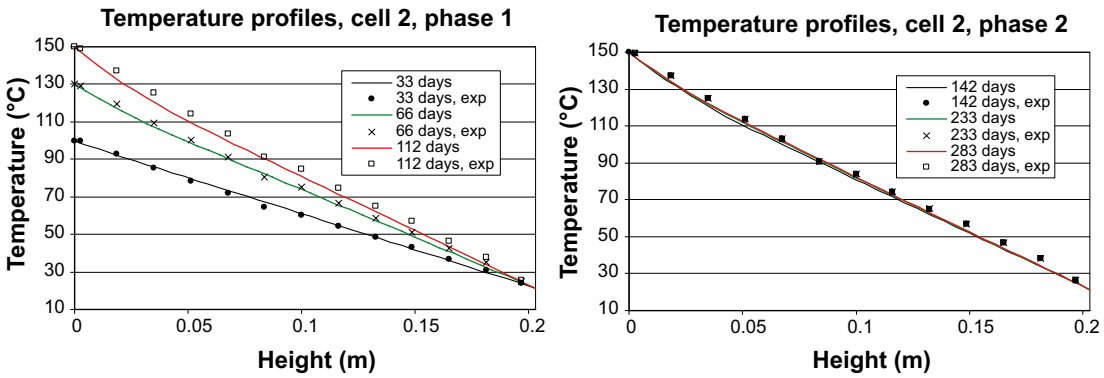

Figure 2-9. *Temperature profiles in Cell 2 at the requested dates for phase 1 and phase 2.*

Relative Humidity

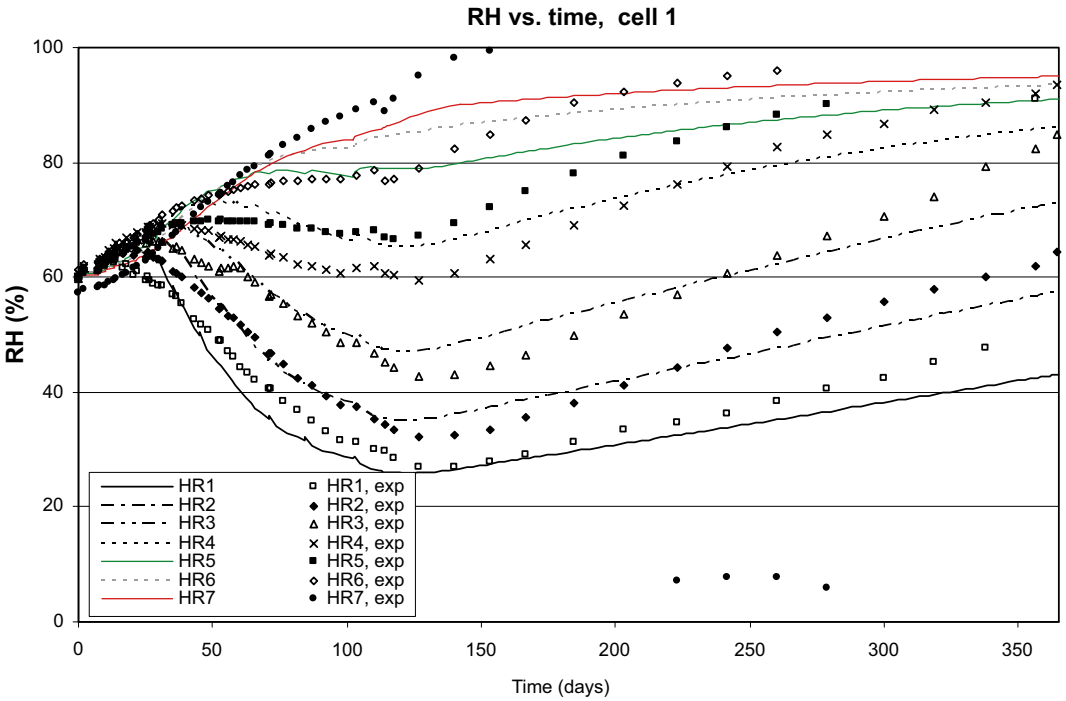

Figure 2-10. *Relative humidity vs. time in Cell 1 for sensors HR1–HR7.*

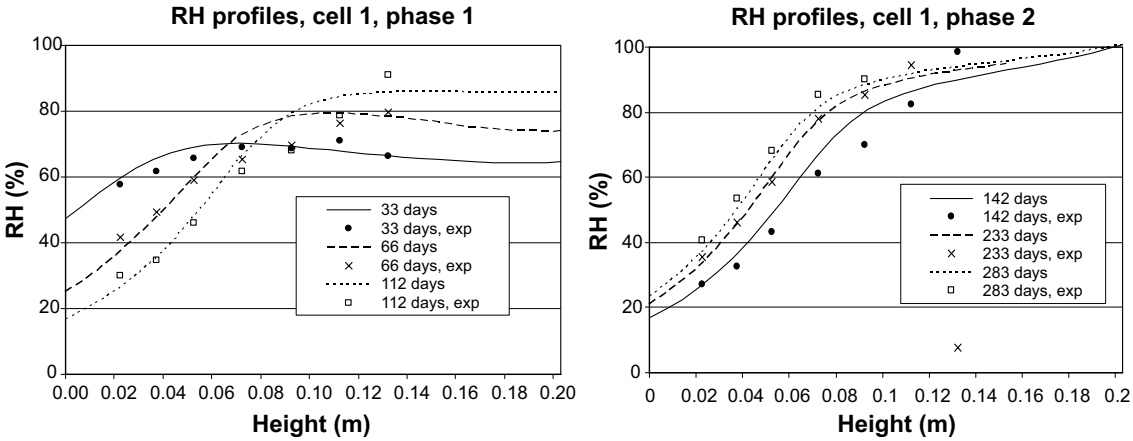

Figure 2-11. *RH profiles in Cell 1 at the requested dates for phase 1 and phase 2.*

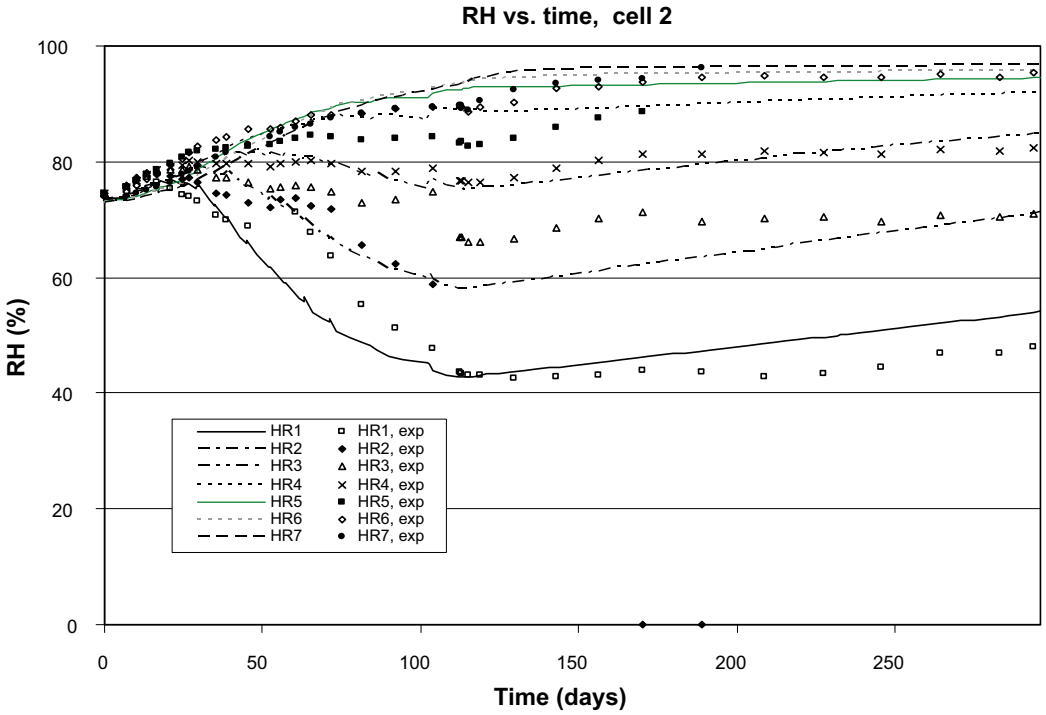

Figure 2-12. *Relative humidity vs. time in Cell 2 for sensors HR1–HR7.*

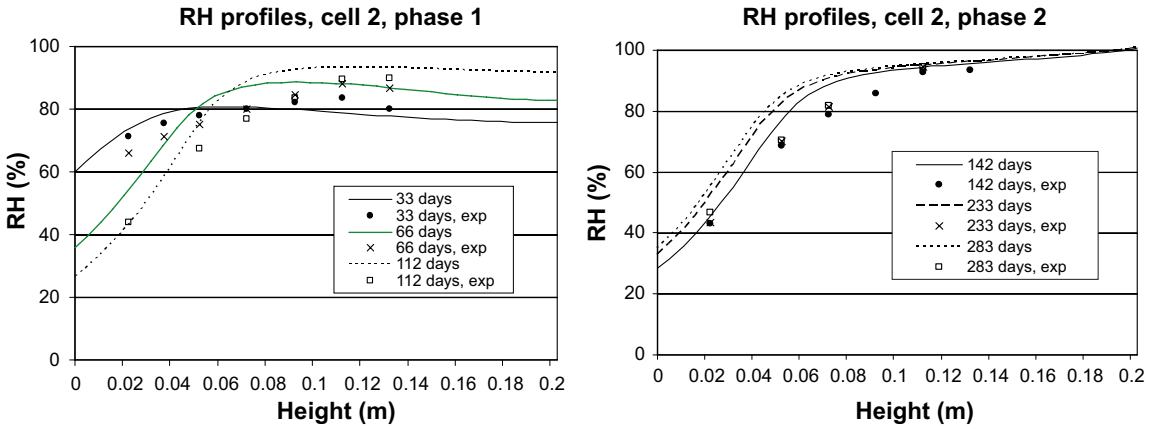

Figure 2-13. *RH profiles in Cell 2 at the requested dates for phase 1 and phase 2.*

Stresses

Axial Stress

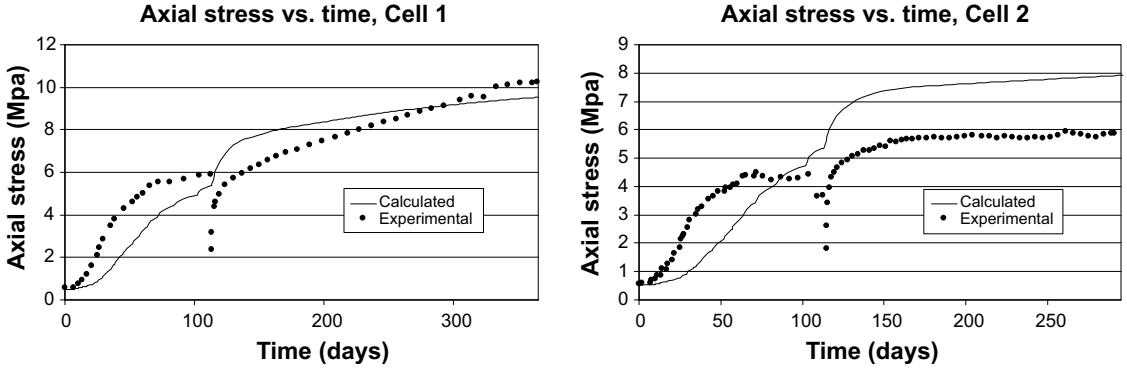

Figure 2-14. *Axial stress vs. time for Cell 1 and Cell 2.*

Radial Stress

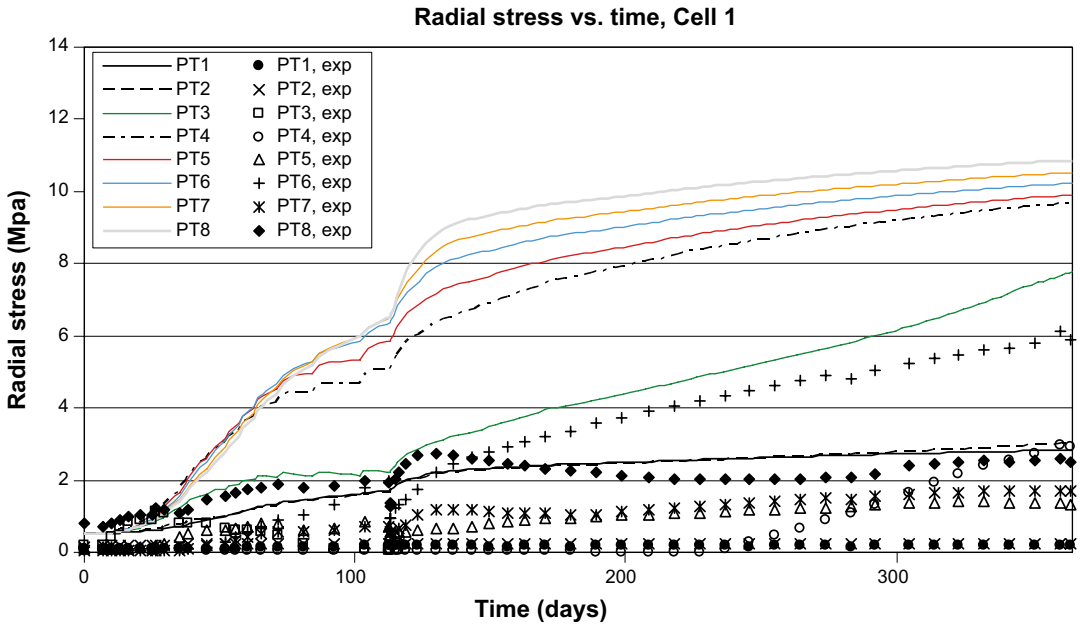

Figure 2-15. *Radial stress vs. time in Cell 1 for sensors PT1–PT8.*

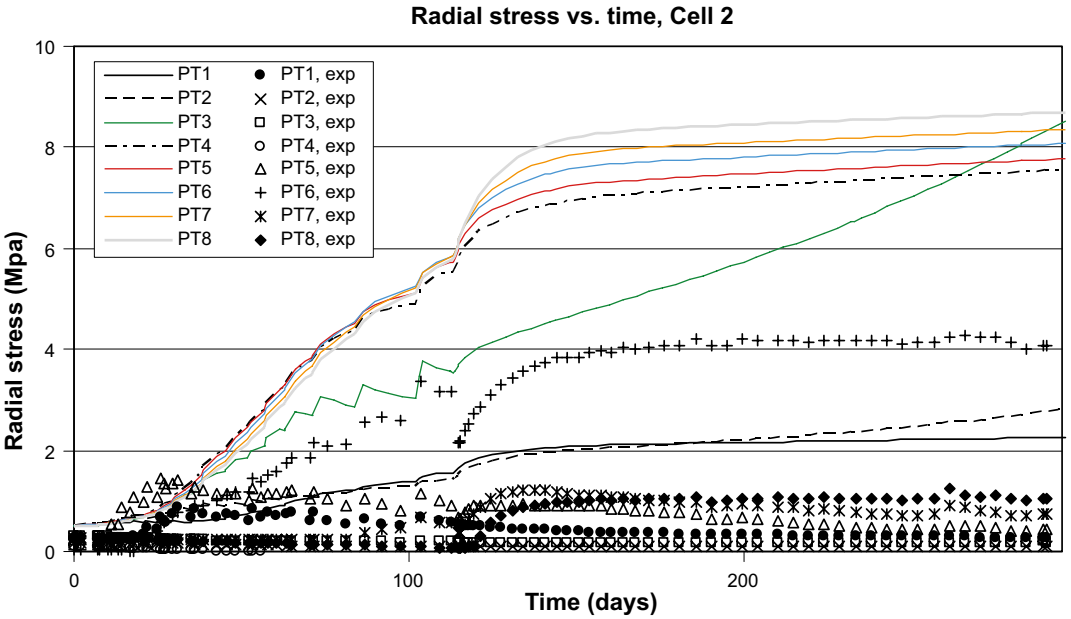

Figure 2-16. *Radial stress vs. time in Cell 2 for sensors PT1–PT8.*

Injected water

By integrating the liquid flow across the top boundary of the models over time, values of the amount of injected water at given times were obtained. This calculated inflow is compared to measurements in Figure 2-17 for both cells. We note a large difference between calculations and measurements.

The total volume available for water injection is readily calculated from the data in Table 2-3 and Figure 2-2,

$$V_{\max} = \pi \cdot 10.15^2 \cdot 20.3 \cdot \phi_{ini} \cdot (1 - S_{ini})\ cm^3 = \begin{cases} 725\ cm^3\ (cell1) \\ 445\ cm^3\ (cell2) \end{cases},$$

suggesting that the experimental values might be questionable – as pointed out in the experimental sensors report (Gatabain and Billaud 2005), leaks of the injection system of Cell 1 were experienced during the tests.

The water content of the bentonite of Cell 2 was determined after the termination of the experiment. In Figure 2-18 this water ratio data is compared to the results of the model. In this diagram it should be pointed out that the rightmost experimental points corresponds to a liquid saturation larger than unity, suggesting a different porosity profile than obtained in the calculation.

Sensitivity Analysis

A sensitivity analysis of relevant parameters in the presented models has been performed. The analysis focuses mainly on Cell 1.

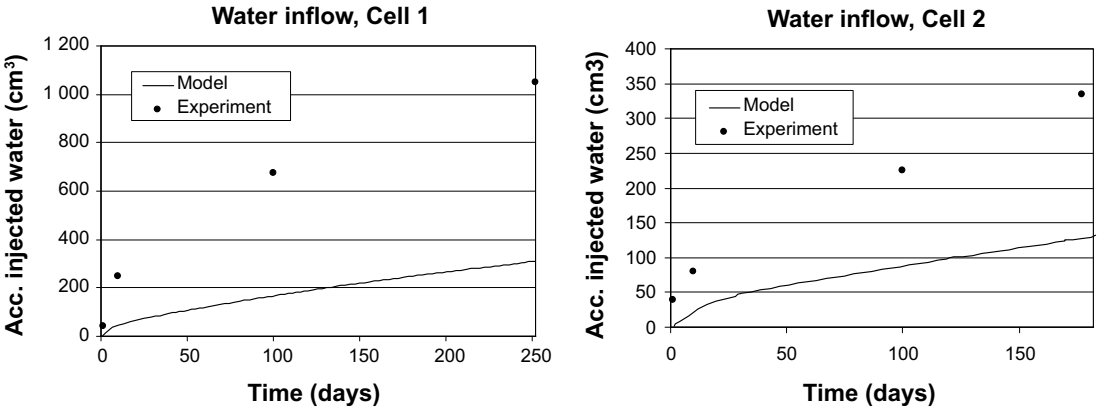

Figure 2-17. *Accumulated water inflow for phase 2 for Cell 1 and Cell 2.*

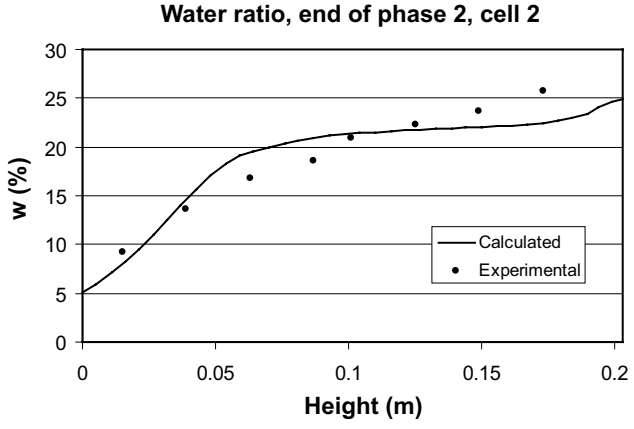

Figure 2-18. *Water ratio after phase 2 for Cell 2.*

Water mass conservation

The total mass of water has been calculated as a function of time during phase 1 in Cell 1. This quantity should in principle be constant as no external water is introduced during this phase. In reality a mass loss of approximately 1 % occurs over the examined time period as seen from the results in Figure 2-19. Several modifications of the base case model have been calculated in order to investigate the cause of this mass loss. Thus, as also shown in Figure 2-19, it has been ruled out that the loss is caused by leaking gas – with a gas tight model there is actually a greater loss at the end of the phase, a discrepancy which must be attributed to numerical accuracy. Furthermore, the gas tight model has been executed with a finer finite element mesh, showing that the model is converged concerning this quantity. A slightly larger mass loss is experienced if the model is executed without solving the mechanical part of the THM(g)-model. A satisfactory explanation for the documented mass loss is missing.

Tortuosity

The impact of tortuosity (i.e. diffusivity) on the redistribution of liquid has been examined by recalculating the model with various values of τ. The results are presented in Figure 2-20. Not surprisingly, a smaller value of τ decreases the liquid redistribution in phase 1 and increases the infiltration in phase 2. Figure 2-20c shows the saturation evolution at the point in the sample where the effect of varying tortuosity is the largest. Figure 2-20d shows the point where the effect is the smallest (which of course is the point where drying and wetting parts meet).

An interesting observation is that the tortuosity dependence on redistribution is larger for smaller tortuosities while it is more insensitive at higher values. This is illustrated in Figure 2-21 where the quantity

$$\int_0^L |S_0 - S(h,t)|dh$$

is used as a measure of redistribution of water in the sample. S_0 is the initial (spatially constant) water saturation, L is the height of the sample and $S(h,t)$ denotes the saturation as a function of height (h) at time t. In this figure a comparison is made to Cell 2 as well. Note the threshold-like behavior for both cells at around $\tau = 0.15$ at the end of phase 1 (day 112).

Intrinsic Permeability

The intrinsic permeability has been varied in the same manner as the previously examined parameters. Figure 2-22 shows the redistribution behavior after phase 1. The impact of changing permeability is seen to be minor which is evidence that it is the vapor diffusion mass transport which is most influential during this phase.

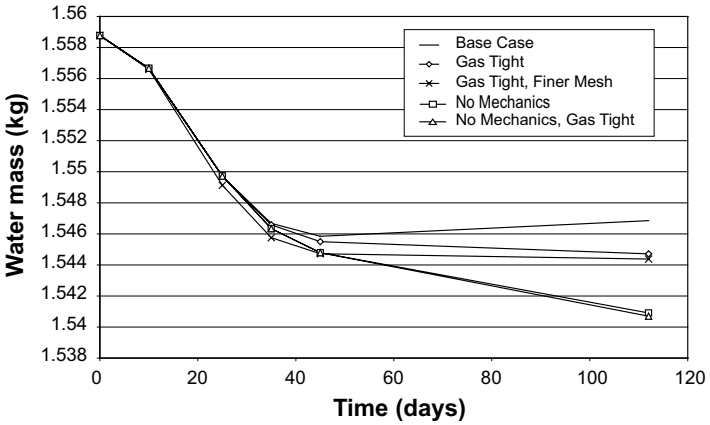

Figure 2-19. *Water mass loss during phase 1 in Cell 1.*

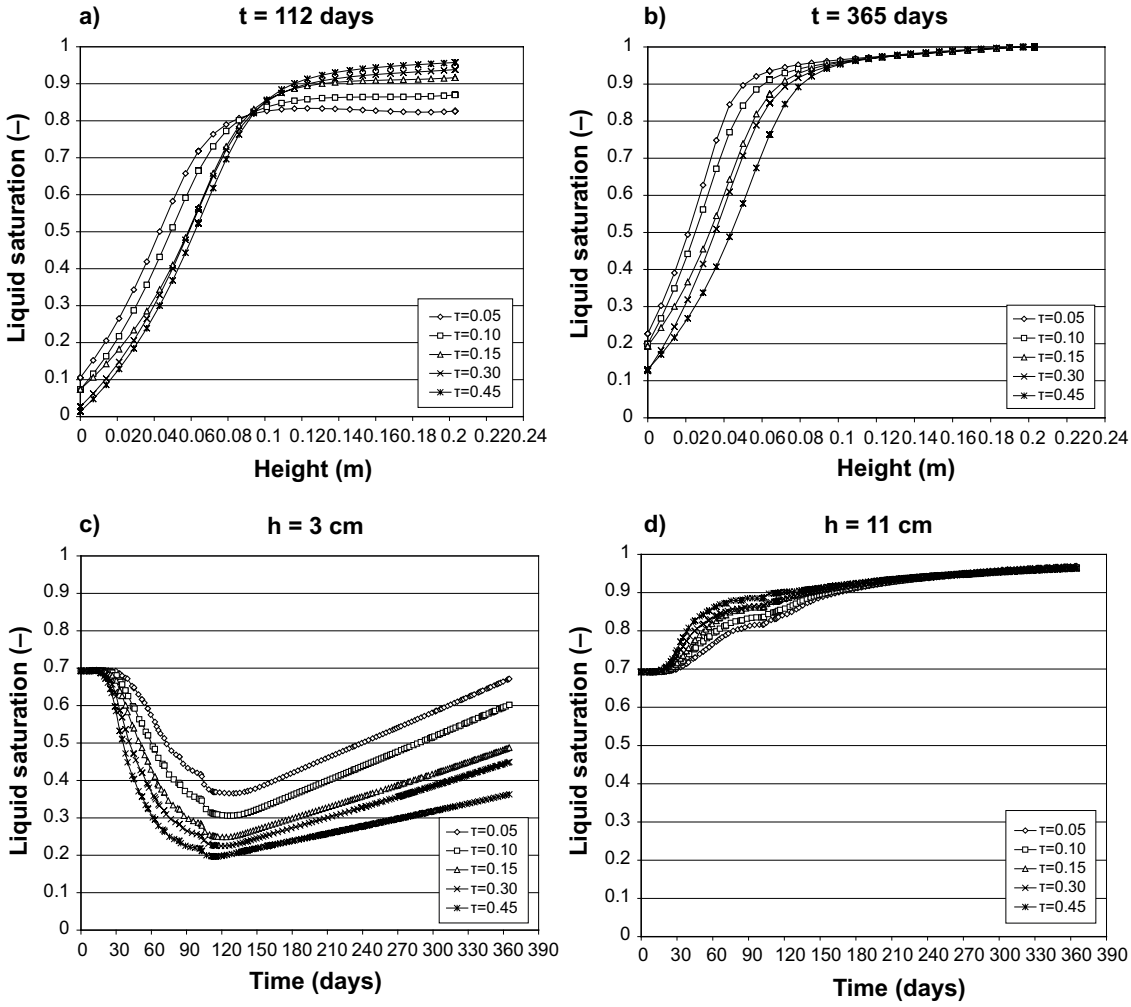

Figure 2-20. *Liquid saturation profiles at the end of phase 1 (a) and phase 2 (b) for various tortuosities in Cell 1. Figure c shows the liquid saturation evolution at the point (3 cm) where the effect of varying tortuosity is the largest and figure d shows the point (11 cm) where the effect is minimized.*

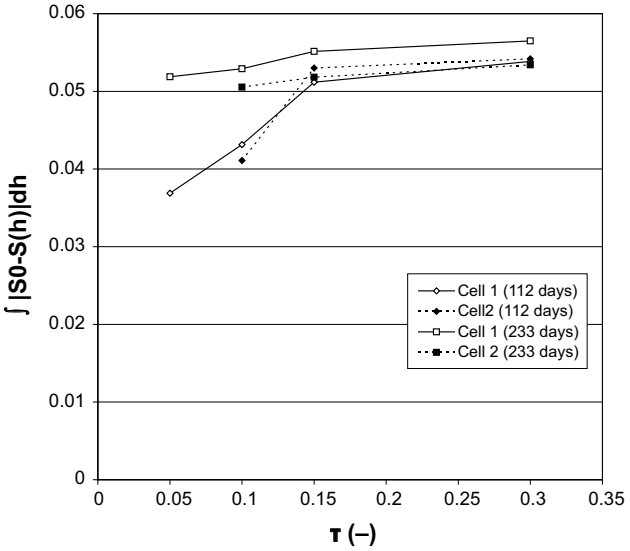

Figure 2-21. *Moisture redistribution vs. tortuosity in both cells.*

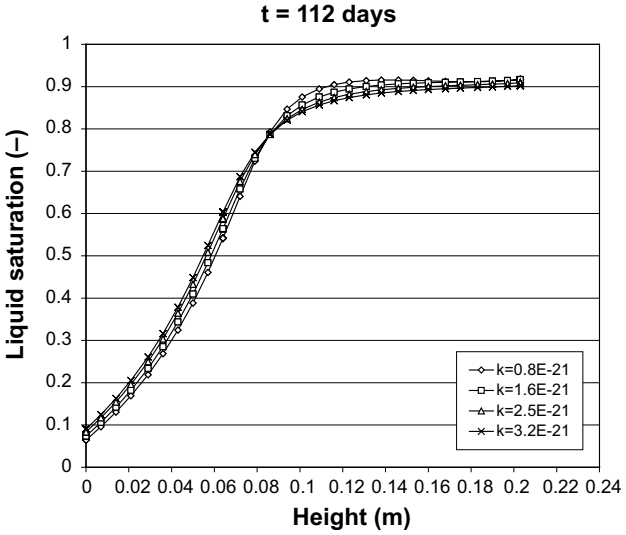

Figure 2-22. *Liquid saturation profiles for various values of intrinsic permeability at the end of phase 1 in Cell 1.*

In phase 2 on the other hand, the permeability dependence on the final saturation profile is much more pronounced, as seen in Figure 2-23. Obviously, advective flow is more dominating here as water is injected.

Retention Curve

The effect of varying the strength of the water retention property is displayed in Figure 2-24 for the case of Cell 1 at the end of phase 1. The retention curve has been modified by changing the parameter P_0 in the van Genuchten expression (see part on thermal and hydrodynamic constitutive laws in Section 2.3.3, and Table 2-5). Not surprisingly, lowering the retention capacity results in a larger redistribution of water and vice versa.

Figure 2-25 show the corresponding retention curves.

Porosity

The variation of intrinsic permeability with porosity in Code_Bright is described by Kozney's model

$$\vec{k} = \vec{k}_0 \frac{\phi^3 (1-\phi_0)^2}{(1-\phi)^2 \phi_0^3}$$

where $\vec{k}_0$ is the intrinsic permeability for the reference porosity ϕ_0. Results of water redistribution due to simultaneous variation of ϕ_0 and initial porosity are seen in Figure 2-26 and Figure 2-27. In phase 1, the dependence is almost negligible because both the diffusive flux and the available pore volume scales linear with porosity.

In phase 2 it is seen that a larger porosity slows down the infiltration process. The porosity dependence of the total flow (advective+diffusive) does not completely cancel the effect from increasing the pore volume.

2.3.5 Discussion

Gas transport

Most parameter values used in the calculations were based on experimental evidence (such as intrinsic permeability, heat conductivity and the vapor diffusion coefficient). However, the description of the gas phase behavior is not very well established. Furthermore, in the present case where (uncontrolled) gas leakage is assumed a complete description is of course impossible.

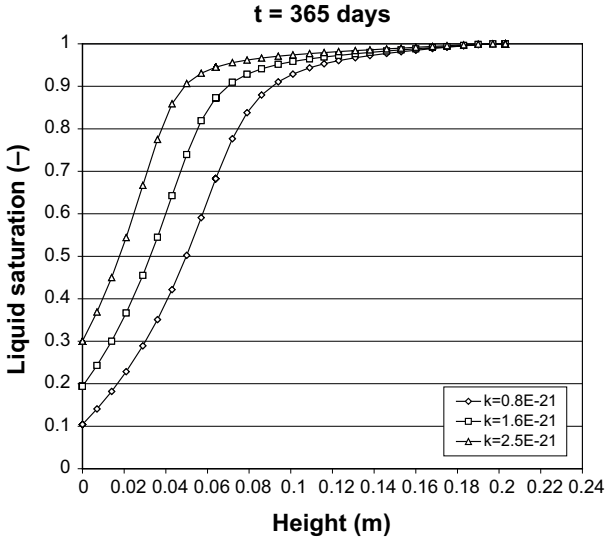

Figure 2-23. *Liquid saturation profiles for various values of intrinsic permeability at the end of phase 2 in Cell 1.*

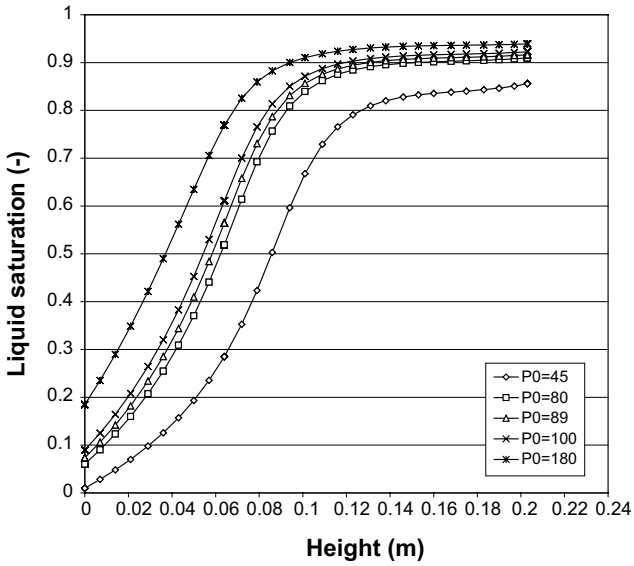

Figure 2-24. *Liquid saturation profiles in Cell 1 at the end of phase 1 for various choices of retention curves.*

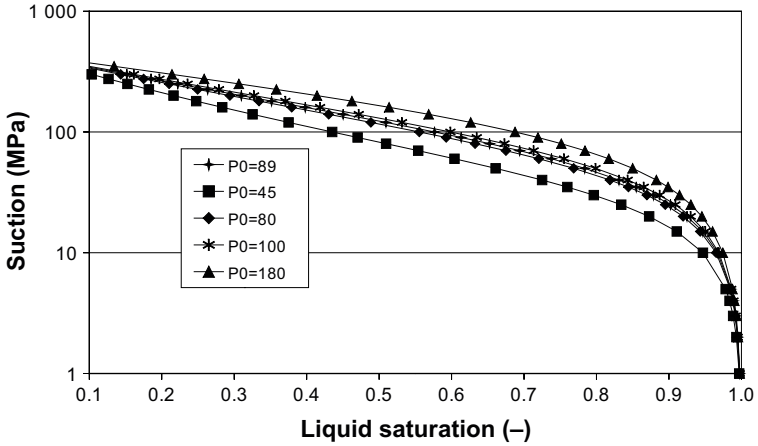

Figure 2-25. *Retention curves used in the sensitivity analysis corresponding to various values of the parameter P_0.*

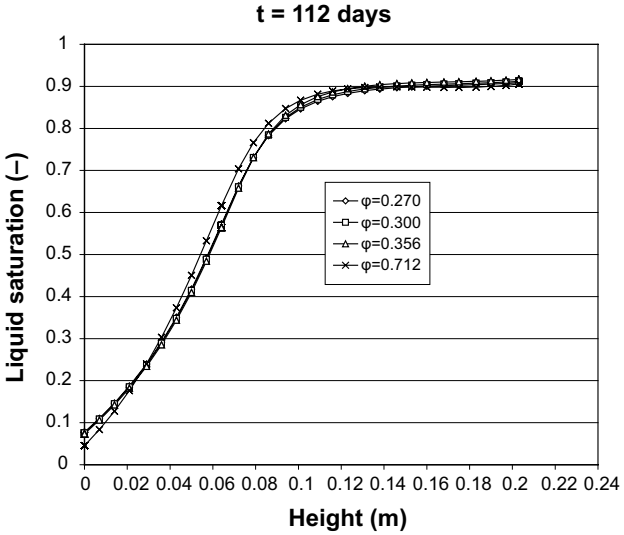

Figure 2-26. *Liquid saturation profiles for various reference porosities in Cell 1.*

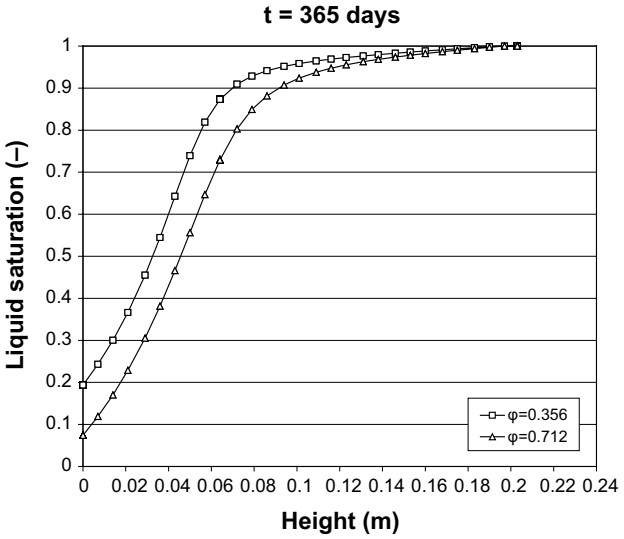

Figure 2-27. *Liquid saturation profiles for different reference/inital porosities at the end of phase 2 in BM 1.1.1.*

The measured RH-values, however, give us a mean to access the vapor pressure profiles of the cells. These values are plotted for Cell 2 in Figure 2-28. In the lower 5 cm part of the cell the vapor pressure is well above 1 atmosphere. Since the total gas pressure (including also the dry air partial pressure) must be even larger than that, it is evident that the gas transport and the gas leaks together are not efficient enough to completely release and level out the gas pressure.

The approach taken in the present calculation is to make a combined choice of gas pressure boundary condition and gas phase transport parameters to achieve a pressure profile in the cell which is compatible with the vapor pressure values. The current description (Figure 2-2 and Table 2-4) produces a (total) gas pressure in the lower parts of Cell 2 of approximately 0.15 MPa at the end of phase 1 (The corresponding value for Cell 1 is 0.12 MPa).

Tortuosity

The diffusive vapor flux is inversely proportional to the gas pressure (Table 2-4). Any uncertainty in the description of the advective transport properties of the gas phase (as discussed above) therefore transforms itself into ~~an~~ uncertainty concerning the diffusive transport.

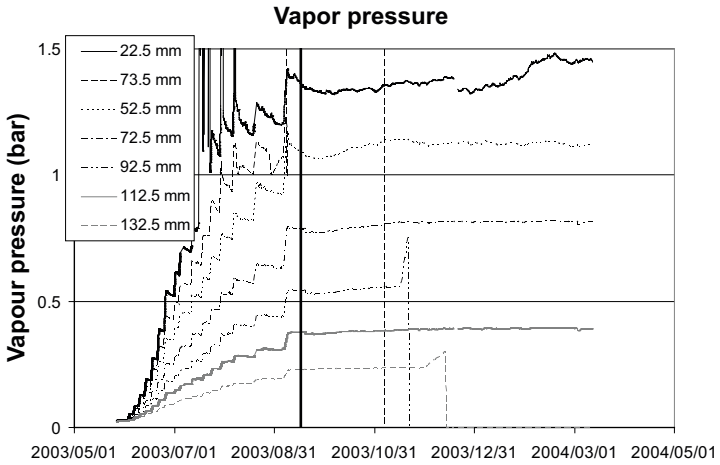

Figure 2-28. *Vapor pressure at different locations in Cell 2.*

According to the vapor transport model used here, the diffusive vapor flux is also directly proportional to the tortuosity, τ, of the porous system. We are not aware of any results from independent measurements of this parameter. Since vapor transport can take place only in still open voids, it is not even clear if it is reasonable to assume that the parameter value should be independent of the saturation. In the present study we have therefore taken the approach of making the tortuosity factor τ a fitting parameter of the model, without any regard to its real, possibly unclear, physical significance.

Mechanical aspects

Calculated axial stresses capture the experimental data fairly well, at least in case of Cell 1. For Cell 2 however, the final axial stresses are somewhat over-predicted. This could probably be refined by modification of the α_{sp}-parameter, which would be justified by the higher porosity value in Cell 2.

Calculated radial stresses exceed the experimental data quite significantly. In the hot end of the experiment, it is reasonable to expect a certain degree of shrinkage, which would imply that the model should produce tensile stresses. This is not the case, although the levels of compressive stresses are fairly low.

Calculated radial stresses corresponding to measured data in sensors PT3 in both cells exhibit a rapid buildup during the second phase. This is probably an effect of the division of the model in two domains. While this boundary between drying and wetting conditions is fairly constant during the first phase, it moves downwards during the second phase.

In the top cold end, the model results in radial stresses that exceed the level of axial stresses, which is not the case in the experimental data. Here the vertical cell/clay interface was modeled without friction and cohesion. Whether this is a relevant approximation or not is hard to tell, *i.e.* it is not clear if the axial force balance is disturbed by shear reactions from the walls. If it is not, the radial stresses should be higher than the axial ones in the upper swelling parts and lower in the hot drying parts. If there is a mechanical disturbance from the walls, this may contribute to explain the difference between model and experiment.

As mentioned earlier, the influence of the mechanical processes on the hydrodynamics were minimized by neglecting any porosity dependence of the permeability and the retention curve. This was justified by the fact that the total volume was constant and that the strains thereby were fairly small.

This assumption has been checked in the case of Cell 1 in which the initial porosity was ~36 %, while the calculated final values ranged within 34–39 %, with the higher value at the cold end. Even if such a range would influence the intrinsic conductivity with a factor of 0.8–1.4, according to the optional relation implemented in the code, the effect on the final suction distribution would be marginal with a general decrease with a maximum deviation of only 3 %.

A similar control of the influence of a porosity dependence of the retention curve would require the use of the conventional van Genuchten expression, rather than the extended version used in this study. The reason for this is that the porosity dependence implemented in the code cannot be used at the same time as the extended version. Therefore, this influence has not been checked.

The apparent agreement between experimental and calculated axial stresses should not be taken as a confirmation of the treatment of the mechanical processes and the inherent strains. For calculations of stress paths at strict constant volume conditions, the direction in the s-p plane is only determined by the κ_s/κ_i-ratio. This is especially apparent in the original BBM formulation with constant stiffness parameters. It is therefore probably possible to produce similar stress results with other sets of parameters, but with significantly different internal strains. This uncertainty illustrates that evaluations of possible M→H couplings should be made with caution.

2.3.6 Conclusions

The presented models produce temperatures, RH-levels and (axial) stresses in fairly good agreement with experimental findings. When evaluating this resemblance however, we must take into account the physical relevance of the underlying model assumptions.

Looking at the calculated temperature profiles, for instance, we find a good agreement with measurement. As we have no reason to doubt the soundness of using Fourier's law in describing the heat transport process and can assume other heat transport mechanisms to be negligible in this case, we can directly relate the small deviations found to approximations made in geometries, boundary conditions, thermal conductivity *etc*. Thus the deviations should be ascribed to possible heat losses over the lateral surface of the cylinder (*i.e*. too approximate boundary conditions in the model) and/or uncertainties regarding the functional form of the dependence of the heat conductivity on liquid saturation.

Looking at the RH results on the other hand, it is harder to make such direct statements about specific parameters as the assumptions underlying the hydraulic model are more involved and might also be more questionable. For instance, the model assumes all water transport induced by the suction gradient to be in liquid form. This means for instance that a steady state in this perspective consists of a cycle where liquid water flowing in one direction is compensated by a vapor diffusion flux of the same magnitude in the opposite direction. This is however a consequence of the assumption that the gas and the liquid phases are continuous media which always are arranged in parallel, rather than in series.

Furthermore, highly compacted bentonite represent an extreme case for which Darcy's law could be assumed to hold (Bear 1972). Darcy's law was originally derived for saturated materials with hydraulic conductivities much larger than those found in the present material.

With objections like these in mind it becomes more difficult to *e.g.* interpret the fitted value of the tortuosity in the present study in terms of a material parameter; as the model assumes two different opposing mass transfer mechanisms the resulting RH profiles depend more strongly on the ratio τ/k (Table 2-4) rather than on the individual parameters. An interesting test would be an infiltration experiment with a (radioactive) tracer. The distribution of the tracer at the end of the experiment may help understand whether vapor or liquid water (or both!) is involved in the suction driven transport.

The performed modeling task highlights two limitations of the used mechanical constitutive laws. The first thing is that there is no implicit void-ratio dependence of the swelling pressure for saturated conditions. This was a minor concern in the performed task with constant volume. But in a full-scale case, in which highly compacted bentonite may be combined with slots, pellets or sand, the ability to predict final swelling pressures would be more important. Although it can be shown that the elastic strain relation is able to handle this to some extent, the precision in such calculations is limited.

The other limitation is the absence of an implicit treatment of hysteretic effects, with different behavior for different directions in suction change. In the performed task, this was handled manually by defining two domains with different parameter settings. Here, this approach appears to be adequate, at least in the first phase without a hydraulic boundary. In a full-scale test however, especially with significant desaturation, there may very well be a moving interface between two such domains. The development of constitutive laws, with the aim to handle these effects, appears therefore to be an important topic.

2.4 Modelling results with Abaqus

2.4.1 Finite element code Abaqus

General

The finite element code Abaqus was used for the calculations. Abaqus contains a capability of modelling a large range of processes in many different materials as well as complicated three-dimensional geometry.

The code includes special material models for rock and soil and ability to model geological formations with infinite boundaries and in situ stresses by e.g. the own weight of the medium. It also includes capability to make substructures with completely different finite element meshes and mesh density without connecting all nodes. Detailed information of the available models, application of the code and the theoretical background is given in the Abaqus Manuals.

Hydro-mechanical analyses in Abaqus

The hydro-mechanical model consists of porous medium and wetting fluid and is based on equilibrium, constitutive equations, energy balance and mass conservation using the effective stress theory.

Equilibrium

Equilibrium is expressed by writing the principle of virtual work for the volume under consideration in its current configuration at time t:

$$\int_V \sigma : \delta\varepsilon \, dV = \int_S \mathbf{t} \cdot \delta\mathbf{v} \, dS + \int_V \hat{\mathbf{f}} \cdot \delta\mathbf{v} \, dV, \tag{2-1}$$

where $\delta\mathbf{v}$ is a virtual velocity field, $\delta\varepsilon^{def} = sym(\partial\delta\mathrm{v}/\partial\mathrm{x})$ is the virtual rate of deformation, s is the true (Cauchy) stress, $\mathbf{t}$ are the surface tractions per unit area, and $\hat{\mathbf{f}}$ are body forces per unit volume. For our system, $\hat{\mathbf{f}}$ will often include the weight of the wetting liquid,

$$\mathbf{f}_w = S_r n \rho_w \mathbf{g}, \tag{2-2}$$

where S_r is the degree of saturation, n the porosity, ρ_w the density of the wetting liquid and $\mathbf{g}$ is the gravitational acceleration, which we assume to be constant and in a constant direction (so that, for example, the formulation cannot be applied directly to a centrifuge experiment unless the model in the machine is small enough that g can be treated as constant). For simplicity we consider this loading explicitly so that any other gravitational term in $\hat{\mathbf{f}}$ is only associated with the weight of the dry porous medium. Thus, we write the virtual work equation as

$$\int_V \sigma : \delta\varepsilon dV = \int_s \mathbf{t} \cdot \delta\mathbf{v} dS + \int_V \mathbf{f} \cdot \delta\mathbf{v} dV + \int_V S_r n \rho_w \mathbf{g} \cdot \delta\mathbf{v} dV, \tag{2-3}$$

where $\mathbf{f}$ are all body forces except the weight of the wetting liquid.

The simplified equation used in Abaqus for the effective stress is:

$$\overline{\sigma}^* = \sigma + \chi \, u_w \mathbf{I}. \tag{2-4}$$

where σ is the total stress, u_w is the pore water pressure, χ is a function of the degree of saturation (usual assumption $\chi = S_r$), and $\mathbf{I}$ the unitary matrix.

Energy balance

The conservation of energy implied by the first law of thermodynamics states that the time rate of change of kinetic energy and internal energy for a fixed body of material is equal to the sum of the rate of work done by the surface and body forces. This can be expressed as (not considering the thermal part, which is solved as uncoupled heat transfer; cf Equation 2-15):

$$\frac{\mathrm{d}}{\mathrm{dt}} \int_V \left(\tfrac{1}{2} \rho \mathbf{v} \cdot \mathbf{v} + \rho \mathrm{U} \right) \mathrm{dV} = \int_s \mathbf{v} \cdot \mathbf{t} \mathrm{dS} + \int_V \mathbf{f} \cdot \mathbf{v} \mathrm{dV} \tag{2-5}$$

where

ρ is the current density,

v is the velocity field vector,

U is the internal energy per unit mass,

t is the surface traction vector,

f is the body force vector, and

Constitutive equations

The constitutive equation for the solid is expressed as:

$$d\tau^{c} = \mathbf{H} : d\varepsilon + \mathbf{g}, \tag{2-6}$$

where $d\tau^{c}$ is the stress increment, **H** the material stiffness, $d\varepsilon$ the strain increment and **g** is any strain independent contribution (e.g. thermal expansion). **H** and **g** are defined in terms of the current state, direction for straining, etc., and of the kinematic assumptions used to form the generalised strains.

The constitutive equation for the liquid (static) in the porous medium is expressed as:

$$\frac{\rho_{w}}{\rho_{w}^{0}} \approx 1 + \frac{u_{w}}{K_{w}} - \varepsilon_{w}^{th}, \tag{2-7}$$

where ρ_w is the density of the liquid, ρ_w^0 is its density in the reference configuration, $K_w(T)$ is the liquid's bulk modulus, and

$$\varepsilon_{w}^{th} = 3\alpha_{w}(T - T_{w}^{0}) - 3\alpha_{w|T^{I}}(T^{I} - T_{w}^{0}) \tag{2-8}$$

is the volumetric expansion of the liquid caused by temperature change. Here $\alpha_w(T)$ is the liquid's thermal expansion coefficient, T is the current temperature, T^I is the initial temperature at this point in the medium, and T_w^0 is the reference temperature for the thermal expansion. Both u_w/K_w and ε_w^{th} are assumed to be small.

Mass conservation

The mass continuity equation for the fluid combined with the divergence theorem implies the pointwise equation:

$$\frac{1}{J}\frac{d}{dt}\left(J\rho_{w}S_{r}n\right) + \frac{\partial}{\partial \mathbf{x}} \cdot \left(\rho_{w}S_{r}n\mathbf{v}_{w}\right) = 0. \tag{2-9}$$

where J is the determinant of the Jacobian matrix of the skeleton motion and **x** is position. The constitutive behaviour for pore fluid is governed by Darcy's law, which is generally applicable to low fluid velocities. Darcy's law states that, under uniform conditions, the volumetric flow rate of the wetting liquid through a unit area of the medium, $S_r n\mathbf{v}_w$, is proportional to the negative of the gradient of the piezometric head:

$$S_{r}n\mathbf{v}_{w} = -\hat{\mathbf{k}}\frac{\partial \phi}{\partial \mathbf{x},} \tag{2-10}$$

where $\hat{\mathbf{k}}$ is the permeability of the medium and ϕ is the piezometric head, defined as:

$$\phi \overset{def}{=} z + \frac{u_{w}}{g\rho_{w}} \tag{2-11}$$

where z is the elevation above some datum and g is the magnitude of the gravitational acceleration, which acts in the direction opposite to z. $\hat{\mathbf{k}}$ can be anisotropic and is a function of the saturation and void ratio of the material. $\hat{\mathbf{k}}$ has units of velocity (length/time). [Some authors refer to $\hat{\mathbf{k}}$ as the hydraulic conductivity and define the permeability as

$$\hat{\mathbf{K}} = \frac{v}{g}\hat{\mathbf{k}} \tag{2-12}$$

where v is the kinematic viscosity of the fluid.]

We assume that g is constant in magnitude and direction, so

$$\frac{\partial \phi}{\partial \mathbf{x}} = \frac{1}{\mathrm{g}\rho_{\mathrm{w}}}\left(\frac{\partial \mathrm{u}_{\mathrm{w}}}{\partial \mathbf{x}} - \rho_w \mathbf{g}\right) \tag{2-13}$$

Vapour flow

Vapour flow is modelled as a diffusion process driven by a temperature gradient (coded as UEL user supplied routine with stiffness and flow).

$$\mathbf{q}_v = -D_{Tv}\frac{\partial T}{\partial \mathbf{x}} \tag{2-14}$$

where $\mathbf{q}_v$ is the vapour flux and D_{Tv} the thermal vapour diffusivity.

Uncoupled heat transfer analysis

Energy balance

The basic energy balance is (neglecting mechanical contribution; cf Equation 2-5)

$$\int_{\mathrm{v}} \rho \dot{\mathrm{U}} \mathrm{dV} = \int_{\mathrm{s}} \mathrm{qdS} + \int_{\mathrm{v}} \mathrm{rdV} \tag{2-15}$$

where V is a volume of solid material, with surface area S; ρ is the density of the material; $\dot{\mathrm{U}}$ is the material time rate of the internal energy; q is the heat flux per unit area of the body, flowing into the body; and r is the heat supplied externally into the body per unit volume.

It is assumed that the thermal and mechanical problems are uncoupled in the sense that $U = U(T)$ only, where T is the temperature of the material, and q and r do not depend on the strains or displacements of the body. For simplicity a Lagrangian description is assumed, so ”volume” and ”surface” mean the volume and surface in the reference configuration.

Constitutive definition

The relationship is usually written in terms of a specific heat, neglecting coupling between mechanical and thermal problems:

$$c(T) = \frac{dU}{dT}, \tag{2-16}$$

Heat conduction is assumed to be governed by Fourier’s law.

$$\mathbf{f}_q = -\mathbf{k}\frac{\partial T}{\partial \mathbf{x}} \tag{2-17}$$

where $\mathbf{f}_q$ is the heat flux and $\mathbf{k}$ is the heat conductivity matrix, $\mathbf{k} = \mathbf{k}(T)$. The conductivity can be fully anisotropic, orthotropic, or isotropic.

Coupling of thermal and hydro-mechanical solutions

In Abaqus the coupled problem is solved through a ”staggered solution technique” as sketched in Figure 2-29 and below.

1. First a thermal analysis is performed where heat conductivity and specific heat are defined as functions of saturation and water content. In the first analysis these parameters are assumed to be constant and in the subsequent analyses they are read from an external file.
2. The hydromechanical model calculates stresses, pore pressures, void ratios, degree of saturation etc. as function of time. Saturation and void ratio histories are written onto an external file.
3. The material parameters update module reads the file with saturation and void ratio data and creates a new file containing histories for saturation and water content.
4. The saturation and water content histories are used by the thermal model in the following analysis.
5. Steps 1–3 are repeated if parameter values are found to be different compared to those of the previous solution.

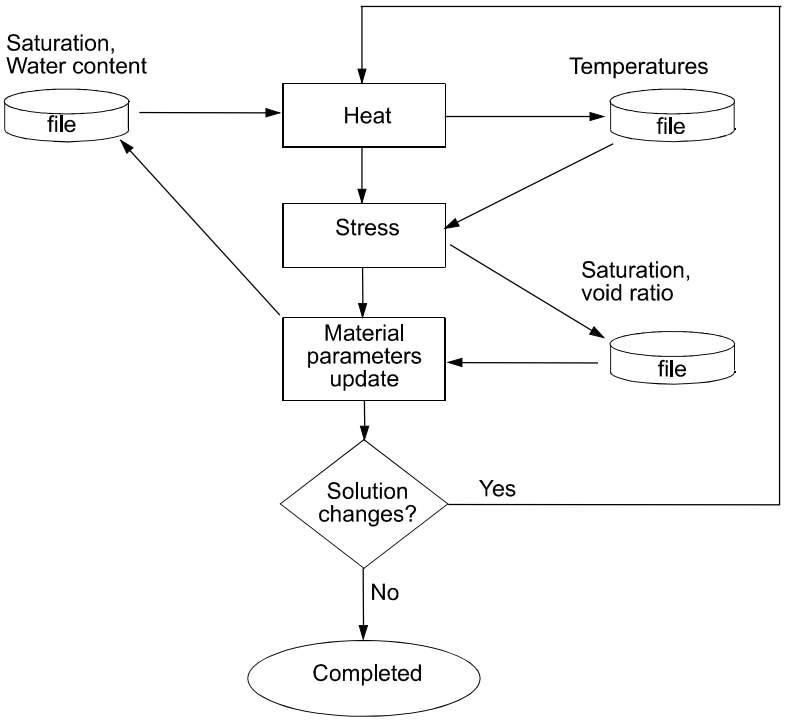

Figure 2-29. *In Abaqus, heat transfer calculations and hydro-mechanical calculations are decoupled. By using the iteration procedure schematically shown above, the effects of a fully coupled THM model are achieved.*

2.4.2 Material model and description

General

This chapter contains a description of the material models for the buffer material and the parameters included in the models

The following processes are modelled:

Thermal:

- Thermal flux from conduction.

Hydraulic:

- Water liquid flux.
- Water vapour flux.
- Hydraulic coupling between the pore water and the pore gas.

Mechanical:

- Mechanical behaviour of the structure.
- Thermal expansion.
- Mechanical behaviour of the separate phases.
- Mechanical coupling between the structure and the pore water.

The model includes complete coupling between all processes. The processes may be a function of the following variables:

- Temperature.
- Degree of water saturation.
- Void ratio.

Material models

The models and data used for the buffer are essentially the same as used for modelling the wetting of KBS-3V (Börgesson and Hernelind 1999) and are mainly valid for the void ratios 0.7–0.9. In the CEA test for BM 1.1.1 the void ratio is 0.55–0.6, which requires recalibration of some of the data.

Thermal flux from conduction

The only thermal flux that is included in the model is thermal conduction with the following parameters:

λ = thermal conductivity

c = specific heat

No thermal modelling was done for BM 1.1.1 since the thermal properties of the insulation and the thermal power applied are not known.

Water liquid flux

The water flux in the liquid phase is modelled to be governed by Darcy's law with the water pressure difference as driving force in the same way as for water saturated clay.

The magnitude of the hydraulic conductivity K_p of partly saturated clay is a function of the void ratio, the degree of saturation and the temperature. K_p is assumed to be a function of the hydraulic conductivity K of saturated clay and the degree of saturation S_r according to Equation 2-18.

$$K_p = (S_r)^{\delta} K \tag{2-18}$$

where

K_p = hydraulic conductivity of partly saturated soil (m/s)

K = hydraulic conductivity of completely saturated soil (m/s)

δ = parameter (usually between 3 and 10)

For the MX-80 the standard value

$\delta = 3$

has been found to be satisfactory according to the calibration calculations (see further down).

Water transport driven by gravity and density gradients is included in the model as well.

The *hydraulic conductivity* of water saturated bentonite has been measured at different temperatures and void ratios (Börgesson et al. 1995). Table 2-7 shows the values for the model.

Water vapour flux

The water vapour flux is modelled as a diffusion processes driven by the temperature gradient and the water vapour pressure gradient (at isothermal conditions) according to Equation 2-19.

$$q_v = -D_{Tv}\nabla T - D_{pv}\nabla p_v \tag{2-19}$$

where

q_v = vapour flow

D_{Tv} = thermal vapour flow diffusivity

T = temperature

D_{pv} = isothermal vapour flow diffusivity

p_v = vapour pressure

Table 2-7. Hydraulic conductivity K as a function of void ratio e and temperature T.

T °C	e	K m/s
20	0.4	0.035×10^{-13}
20	0.6	0.2×10^{-13}
20	0.8	0.65×10^{-13}
20	1.0	1.75×10^{-13}
40	0.4	0.05×10^{-13}
40	0.6	0.31×10^{-13}
40	0.8	1.0×10^{-13}
40	1.0	2.75×10^{-13}
60	0.4	0.07×10^{-13}
60	0.6	0.44×10^{-13}
60	0.8	1.45×10^{-13}
60	1.0	3.85×10^{-13}
80	0.4	0.1×10^{-13}
80	0.6	0.55×10^{-13}
80	0.8	1.8×10^{-13}
80	1.0	4.9×10^{-13}

The isothermal vapour flow is neglected and thus D_{pv} =0.

The thermal water vapour diffusivity D_{Tv} can be evaluated from moisture redistribution tests by calibration calculations. The following relations were found to yield acceptable results:

$$D_{Tv} = D_{Tvb} \qquad 0.3 \le S_r \le 0.7 \qquad (2\text{-}20)$$

$$D_{Tv} = D_{Tvb} \cdot \cos^{a}\left(\frac{S_r - 0.7}{0.3} \cdot \frac{\pi}{2}\right) \qquad S_r \ge 0.7 \qquad (2\text{-}21)$$

$$D_{Tv} = D_{Tvb} \cdot \sin^{b}\left(\frac{S_r}{0.3} \cdot \frac{\pi}{2}\right) \qquad S_r \le 0.3 \qquad (2\text{-}22)$$

a and *b* are factors that regulates the decreased vapour flux at high and low degree of saturation.

The diffusivity is thus constant with a basic value D_{Tvb} between 30 % and 70 % degree of saturation. It decreases strongly to D_{Tv}=0 at 0 % and 100 % saturation. The influence of temperature and void ratio on the diffusivity is not known and not considered in the model.

The *thermal vapour flow diffusivity* D_{Tvb} and the parameters *a* and *b* according to Equations 2-20 to 2-22 have been evaluated for the void ratio 0.8 with calibration calculations of moisture redistribution tests (see further down). No such tests have been performed at the void ratio 0.55–0.6 used in the BM-tests so the following values evaluated for the higher void ratio have been used:

$\boldsymbol{D}_{Tvb} = 0.7 \times 10^{-11}$ m^2/s, K

$a = 6$

$b = 6$

Hydraulic coupling between the pore water and the pore gas

The pore pressure u_w of the unsaturated buffer material, which is always negative, is modelled as being a function of the degree of saturation S_r independent of the void ratio (*water retention curve*).

$$u_w = f(S_r) \qquad (2\text{-}23)$$

Abaqus also allows for hysteresis effects, which means that two curves may be given (drying and wetting curves).

The pore air pressure is not modelled.

The water retention curves have been evaluated according to a method developed by Dueck (2004). The evaluation is described in Appendix 3. Since the void ratio differs in the cells different curves are required. The influence of the temperature has also been considered. Figure 2-30 shows the evaluated retention curves. Since 80 °C is the average temperature in the sample these retention curves have been used for the modelling. However, the influence of temperature on the retention curve is not unambiguous and the basis for doing the strong correction shown in Figure 2-30 is weak. Late tests indicate that the influence is much smaller for MX-80, which thus suggests that the curves at room temperature should have been used.

Since the water transport in Abaqus is governed by the pore water pressure (u_w) but the measurements and requested results are in relative humidity (R_h) a conversion from calculated negative pore water pressure to relative humidity has to be done. The conversion according to Equation 2-24, which is derived from thermodynamic considerations (see e.g. Dueck 2004), has been used.

$$R_h = exp(u_w/462T) \quad (2\text{-}24)$$

where T = absolute temperature (t+273)

Mechanical behaviour of the structure

The mechanical behaviour has been modelled with a non-linear Porous Elastic Model and Drucker-Prager Plasticity model. The effective stress theory is applied and adapted to unsaturated conditions according to Equation 2-4 by Bishop. The shortcomings of the effective stress theory are compensated for by a correction called moisture swelling (see below).

The *Porous Elastic Model* implies a logarithmic relation between the void ratio e and the average effective stress p according to Equation 2-25.

$$\Delta e = \kappa \Delta \ln p \quad (2\text{-}25)$$

where κ = porous bulk modulus

Poisson's ratio v is also required.

Drucker Prager Plasticity model contains the following parameters:

β = friction angle in the p-q plane

d = cohesion in the p-q plane

ψ = dilation angle

q = $f(\varepsilon^d_{pl})$ = yield function

The yield function is the relation between Mises' stress q and the plastic deviatoric strain ε^d_p at a specified stress path. The dilation angle determines the volume change during shear.

The following data has been used for the *Porous Elastic* model:

κ = 0.20

v = 0.4

The value of κ has been derived from oedometer and swelling pressure tests (Börgesson et al. 1995).

The following data was used for the *Drucker Prager Plasticity* model

β = 0.001°

d = 4 500 kPa for e=0.55

d = 3 500 kPa for e=0.6

ψ = 2°

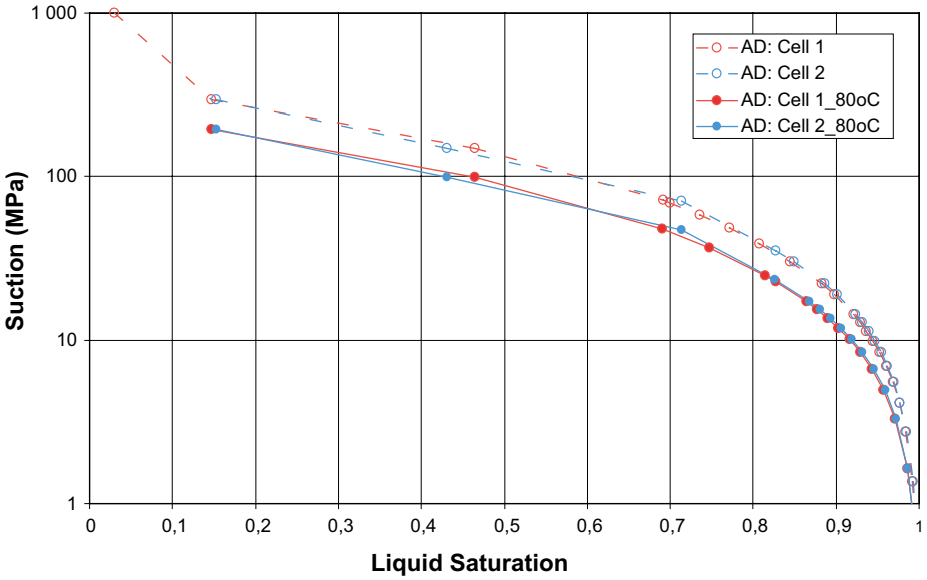

Figure 2-30. *Retention curve of MX-80 at the void ratio 0.55 (Cell 1) and 0.6 (Cell 2) at room temperature and at 80 °C.*

Table 2-8. Yield function.

q (kPa)	ε_{pl}
1	0
50	0.005
100	0.02
150	0.04
200	0.1

The low friction angle and high cohesion are motivated by that the strength depends almost entirely of the void ratio independently of the degree of saturation and not by the effective stress (Dueck 2010).

Thermal expansion

The volume change caused by the thermal expansion of water and particles can be modelled with the parameters

α_s = coefficient of thermal expansion of solids

α_w = coefficient of thermal expansion of water

Only the expansion of the separate phases is taken into account. The possible change in volume of the structure by thermal expansion (not caused by expansion of the separate phases) is not modelled. However, a thermal expansion in water volume will change the degree of saturation which in turn will change the volume of the structure. The following values have been used:

$\alpha_w = 3.0 \times 10^{-4}$

$\alpha_s = 0$

Mechanical behaviour of the separate phases

The water and the particles are mechanically modelled as separate phases with linear elastic behaviour. The pore air is not mechanically modelled. The following standard values have been used for the *properties of the water and solid phases*:

$B_w = 2.1 \times 10^6$ kPa (bulk modulus of water)

$B_s = 2.1 \times 10^8$ kPa (bulk modulus of solids)

$\rho_w = 1\,000$ kg/m^3 (density of water)

$\rho_s = 2\,780$ kg/m^3 (density of solids)

Mechanical coupling between the structure and the pore water

The mechanical behaviour is modelled to be governed by the effective stress theory and a procedure called moisture swelling.

Effective stress theory

The effective stress concept according to Bishop is used for modelling the mechanical behaviour of the water-unsaturated buffer material:

$$s_e = (s - u_a) + \chi(u_a - u_w) \qquad (2\text{-}26)$$

Equation 2-26 is simplified in the following way:

$u_a = 0$ (no account is taken to the pressure of enclosed air)

$\chi = S_r$

Moisture swelling

The shortcomings of the effective stress theory can be compensated in Abaqus by a correction called ”*moisture swelling*”. This procedure changes the volumetric strain ε_v by adding a strain that can be made a function of the degree of saturation S_r.

The effective stress theory decomposes the total stress into pore pressure and effective stress (which only depends on deviatoric strains). However, the effective strain can be made dependent on saturation by using the concept of *moisture swelling* which modify the effective strain by this user defined saturation dependent volumetric strain (*moisture swelling*). In this application the moisture swelling contribution is calibrated by using the measured swelling pressure and assuming that the effective strain (after adding the moisture swelling) should be zero. Neglecting moisture swelling will imply an effective strain defined by the elastic material (porous elastic) and thus the moisture swelling strain can be calculated from Equations 2-27 and 2-28.

$$\Delta\varepsilon_v = f(S_r) = \ln(p_0/p)\cdot\kappa/(1+e_0) \qquad (2\text{-}27)$$

$$p = p_{tot} - u_w \cdot S_r \qquad (2\text{-}28)$$

where

ε_v = volumetric strain

p_0 = initial effective stress taken from the initial conditions

p = actual effective stress

κ = porous bulk modulus (from Equation 2-25)

e_0 = initial void ratio

p_{tot} = actual total stress

u_w = pore water pressure

S_r = degree of water saturation

The moisture swelling relation (*M.S.*) that is needed as input is the logarithmic volumetric strain according to Equation 2-29 where $\Delta\varepsilon_v$ is taken from Equation 2-27.

$$M.S. = \ln(1+\Delta\varepsilon_v) \quad (2\text{-}29)$$

The data for the *moisture swelling procedure* is derived from the assumption that the relation between total stress and degree of saturation of a confined sample (constant volume) is linear when the degree of saturation is increased from its initial value to 100 % (Dueck 2004). During an increase in degree of saturation from the initial value 69 % to 100 % the total pressure increases from 0 to 40 MPa for Cell 1 with e=0.55, while an increase in degree of saturation from the initial value 82.6 % to 100 % yields an increase in total pressure from 0 to 25 MPa for Cell 2 with e=0.60.

M.S. as a function of degree of saturation for the two cases is shown in Figure 2-31.

Required parameters

The required input parameters for the described THM model (Abaqus) are the following:

Thermal

- Tables of thermal conductivity λ and specific heat $\boldsymbol{c}$ as function of void ratio e, degree of saturation S_r, and temperature (not used)

Hydraulic

- Table of the hydraulic conductivity of water saturated material K as function of void ratio $\boldsymbol{e}$ and temperature T.
- Influence of degree of saturation S_r on the hydraulic conductivity K_p expressed as the factor δ in Equation 2-18.
- The basic water vapour flow diffusivity D_{vTb} and the parameters a and b in Equations 2-20 to 2-22.
- Table of the matric suction u_w as a function of the degree of saturation S_r.

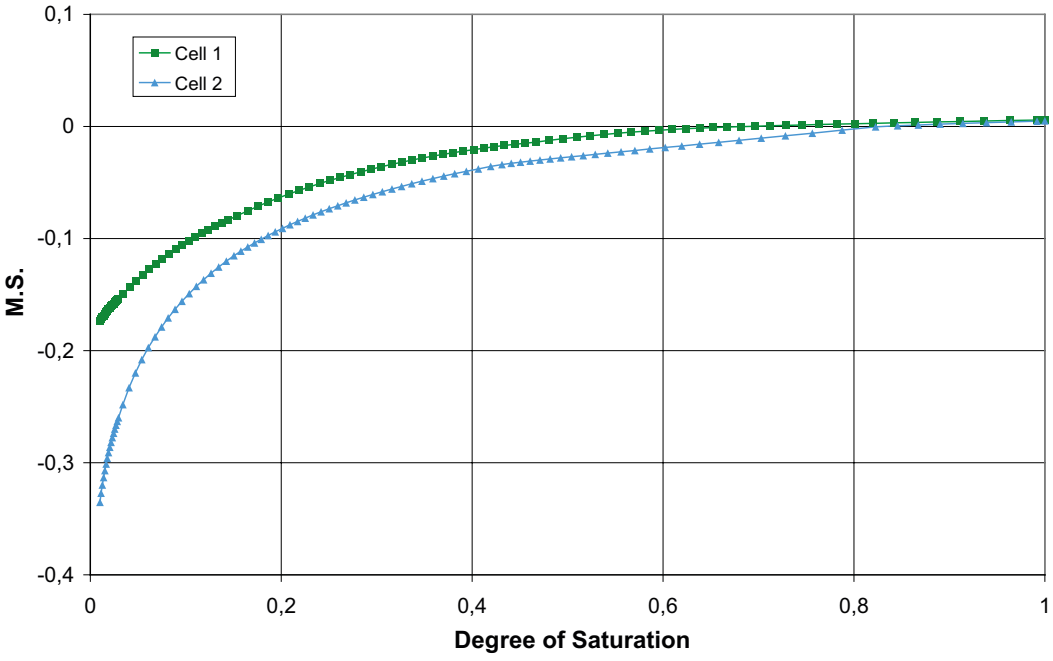

Figure 2-31. *Moisture swelling functions.*

Mechanical

- Porous bulk modulus $\boldsymbol{\kappa}$ according to Equation 2-25 and Poisson's ratio ν.
- Drucker Prager plasticity parameters β, d, ψ, and the yield function.
- Bulk modulus and coefficient of thermal expansion of water (B_w, α_w)and bulk modulus solids (B_s).
- Bishops parameter χ in Equation 2-26 (usual assumption $\chi = S_r$).
- The volume change correction ε_v as a function of the degree of saturation S_r (the "moisture swelling" procedure).

Initial conditions

The following initial conditions of the elements in the structure need to be specified:

- void ratio e
- degree of saturation S_r
- pore pressure u (kPa)
- average effective stress p (kPa)
- the temperature t (°C)

Calibration tests

Most of the required parameters were determined with direct measurements in the laboratory as shown earlier. However, the following parameters cannot be directly measured:

D_{vTb}, a, b *and* δ.

These parameters have been calibrated with some indirect tests.

Water uptake tests

The factor δ in Equation 2-18 can be determined with a number of water uptake tests. These tests are made by confining samples with a known degree of saturation in stiff cylinders and apply a filter stone with zero water pressure at one end. The negative water pressure of the unsaturated sample will suck water into the sample. After a certain time, which must be different for all samples, the test is brought to an end. The sample is then sliced into a number of pieces and the water ratio (and if possible also the density) of each piece is determined.

With these tests the degree of saturation (and void ratio) can be plotted as a function of the distance from the water inlet. By simulating the same test with the code, the factor δ in Equation 2-18 can be checked.

Water uptake tests have been made at different densities and initial water ratios (Börgesson and Hernelind 1999). In these tests water was applied at one end of a 50 mm high sample confined in a stiff oedometer and the axial water ratio distribution measured at different times after start.

The calculations were made with the initial conditions e=0.75 and S_r=0.4. The samples were supplied with water by applying the water pressure 0 kPa at the bottom boundary.

The calculated degree of saturation (using the water retention curve for e=0.75 and δ=3) as a function of the distance from the water inlet at three times is shown in Figure 2-32 together with the measured values at corresponding times The agreement is rather good and confirms that δ=3 is valid for the buffer although the wetting rate seems to be overestimated at high degree of saturation.

Temperature gradient tests

The thermal vapour flow diffusivity can be determined with a number of temperature gradient tests. These tests can be performed in a stiff oedometer with water tight boundaries by applying a constant temperature gradient along the sample. The tests are finished after different times and the sample sliced in the same way as in the previous tests.

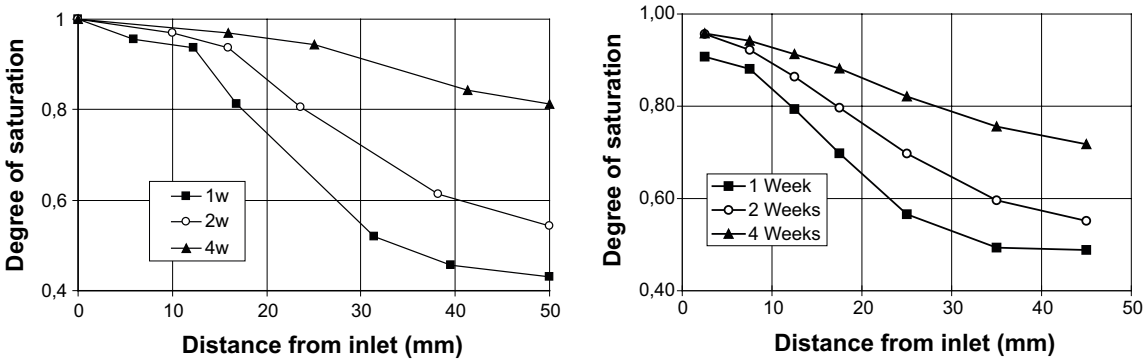

Figure 2-32. *Calculated (left) and measured degree of saturation at different times at a water uptake test.*

With these tests the degree of saturation (and void ratio) can be plotted as a function of the distance to the hot end. By simulating the test with the code D_{vTb}, a, and b in Equations 2-20 to 2-22 can be calibrated.

Several temperature gradient tests at different water ratios and temperatures have been performed (Börgesson and Hernelind 1999, Börgesson 1995). Unfortunately these tests were made at void ratio 1.0 which differs from the reference case. The calibration must thus be considered to be preliminary. The tests were done with a temperature gradient applied along a 5 cm long sample, which was both mechanically and hydraulically confined. The water ratio distribution was measured at different times.

The calculation was done with a 2D element mesh with 20 equally large elements simulating the 5 cm high sample. The model has hydraulically and mechanically confined boundaries. The modelling was made with the void ratio e= 1.0 and the derived parameters used for the void ratio e=0.77. Several calculations of this test were done with different values of the water vapour diffusivity until the agreement between measured and calculated degree of saturation were acceptable (Börgesson et al. 1995).

Figure 2-33 shows the measured and calculated degree of saturation as a function of the distance from the cold end at different times. The agreement is fair although the start value differs slightly.

2.4.3 Finite element model

Element mesh

Only the bentonite sample and the boundaries to the cell were modelled. The element mesh consists of about 3 200 axial symmetric elements. The mesh is shown in Figure 2-34 together with some of the measuring points.

Boundary conditions

Thermal

No thermal calculations were done. The measured temperature distribution was used in the model.

Hydraulic

The hydraulic history is divided into two phases:

- In phase 1 all boundaries are isolated.
- In phase 2 constant water pressure 1 MPa is kept in the top, while the other boundaries are isolated.

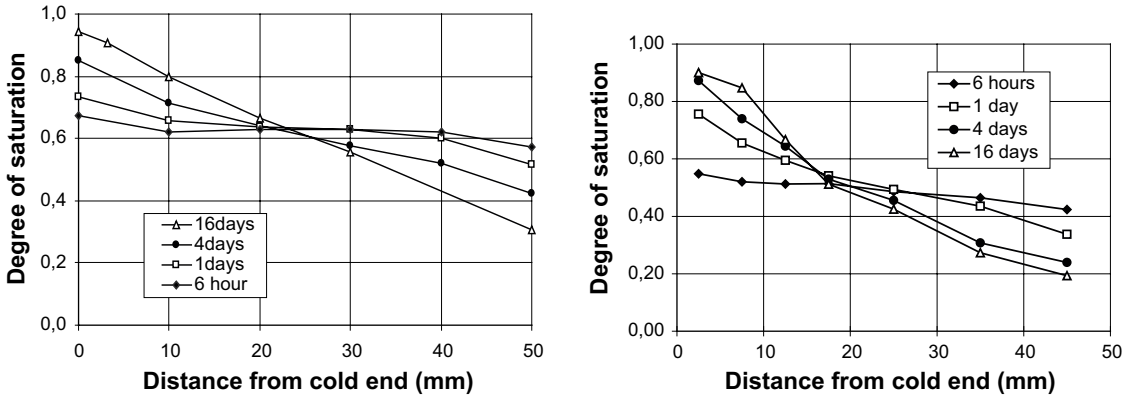

Figure 2-33. *Calculated (left) and measured degree of saturation at different times at a temperature gradient test.*

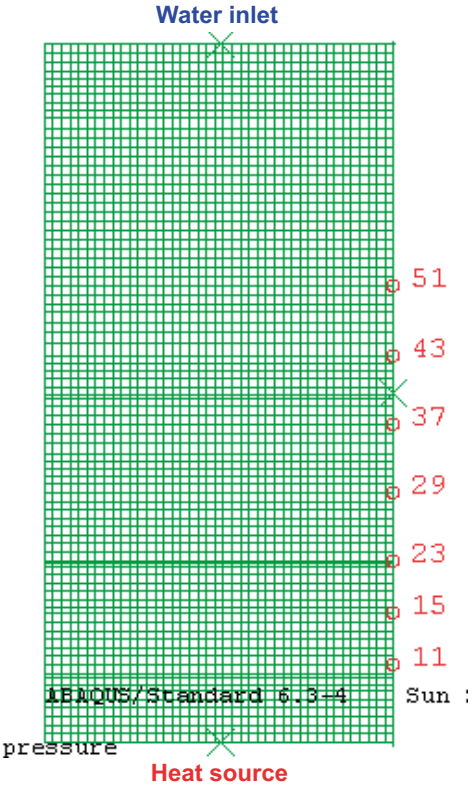

Figure 2-34. *Element mesh of BM 1.1. Axial symmetry around the left boundary. The location of measuring points of RH is shown.*

Mechanical

The mechanical boundary conditions are:

- Axial symmetry at the left boundary.
- Combined contact and friction elements at the other boundaries.

The contact elements allow the sample to release the contact with the boundary in case of tensile total stress that may occur during local shrinkage. The contact surface can slip during compression and has friction and cohesion.

$\phi = 5°$

$c = 50$ kPa

Initial conditions

The density and water ratio differed between the samples in the two cells:

Cell 1:

$\rho = 2\,035$ kg/m^3

$w = 13.66$ %

which yield the following input data:

$e_0 = 0.55$

$S_{r0} = 0.69$

$u_0 = -47\,800$ kPa

$p_0 = 32\,982$ kPa

$T_0 = 20$ °C

Cell 2:

$\rho = 2\,045$ kg/m^3

$w = 17.86$ %

which yield the following input data:

$e_0 = 0.6$

$S_{r0} = 0.826$

$u_0 = -23\,500$ kPa

$p_0 = 19\,411$ kPa

$T_0 = 20$ °C

2.4.4 Calculation sequence

The modeling simulated the actual time history, with two phases. No thermal calculation was thus done. The motivation for this is that the thermal properties of the insulation and the power applied to the bottom are not known.

Phase 1: The temperature was increased in the bottom in steps from the initial value 20 °C to 150 °C in 113 days. Linear temperature distribution through the sample was applied as input data.

Phase 2: The water pressure 1 MPa was applied in the top boundary and kept for 251 days for Cell 1 and 175 days for Cell 2, corresponding to the time the tests were interrupted.

2.4.5 Results

Cell 1

The results of the calculations for Cell 1 and comparison with measurements are shown in Figure 2-35 to Figure 2-39.

Temperature

Since no temperature calculation was done all results will not be shown. Figure 2-35 shows as an example the measured and the applied temperature distribution along the sample. The main difference is caused by the small deviation from the linear relation.

Relative humidity

Relative humidity is plotted as history plots in Figure 2-36 and as path plots at three times in Figure 2-37. The agreement is fair.

Stress

The stress is plotted as history plots. The axial stress measured by the force transducer is shown in Figure 2-38 and the radial stress measured in by small pistons in the cell wall is shown in Figure 2-39. The modeled axial stress is in fair agreement with the measured one, although the stress is underestimated, but the measured radial stress is much lower than the modeled and also much lower than the measured axial stress.

Cell 2

The same results of the calculations and comparison with measurements as for Cell 1 are shown for Cell 2 in Figure 2-40 to Figure 2-44.

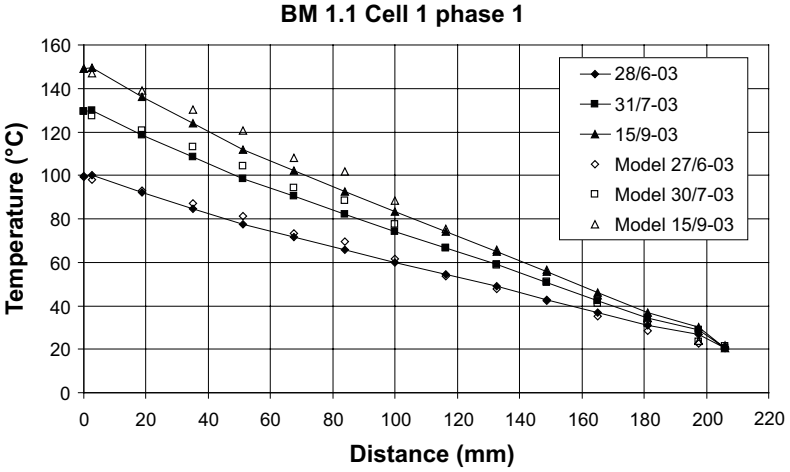

Figure 2-35. *Applied and measured temperature distribution in Cell 1 at three different times. Filled symbols denote measured values.*

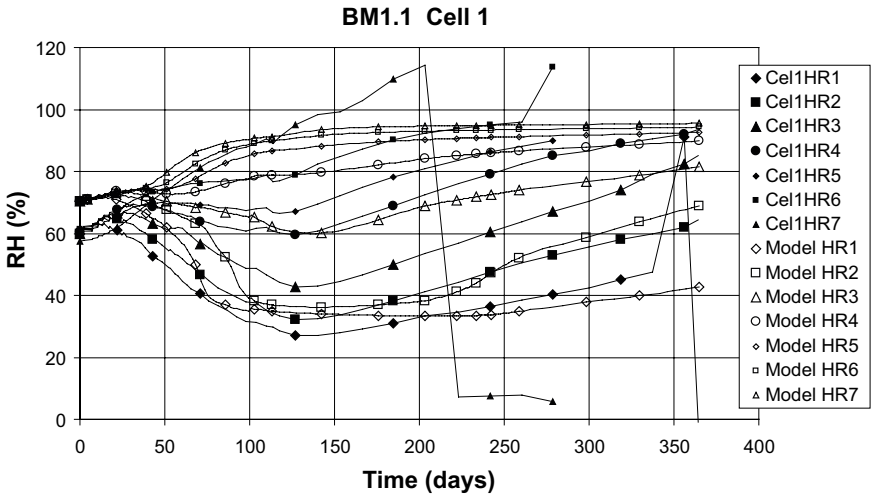

Figure 2-36. *Modelled and measured relative humidity in Cell 1. Filled symbols denote measured values.*

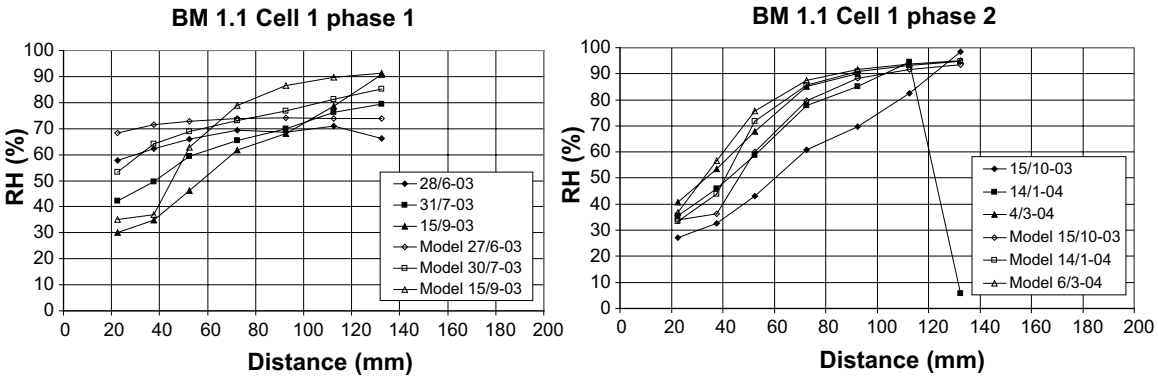

Figure 2-37. *Modelled and measured relative humidity in Cell 1. Filled symbols denote measured values.*

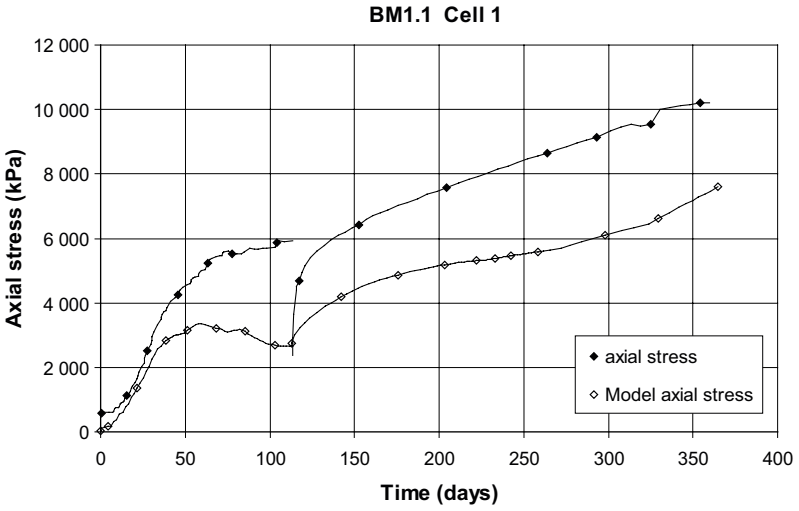

Figure 2-38. *Modelled and measured axial stress in Cell 1. Filled symbols denote measured values.*

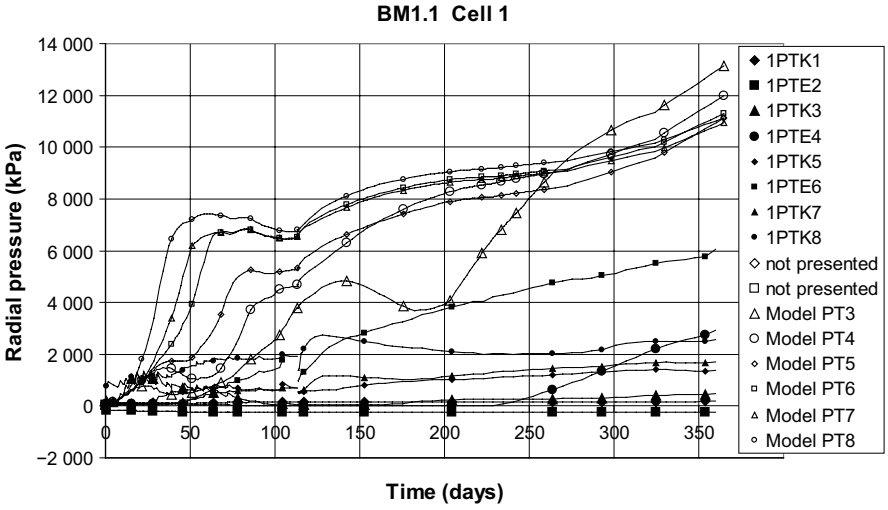

Figure 2-39. *Modelled and measured radial stress in Cell 1. Filled symbols denote measured values.*

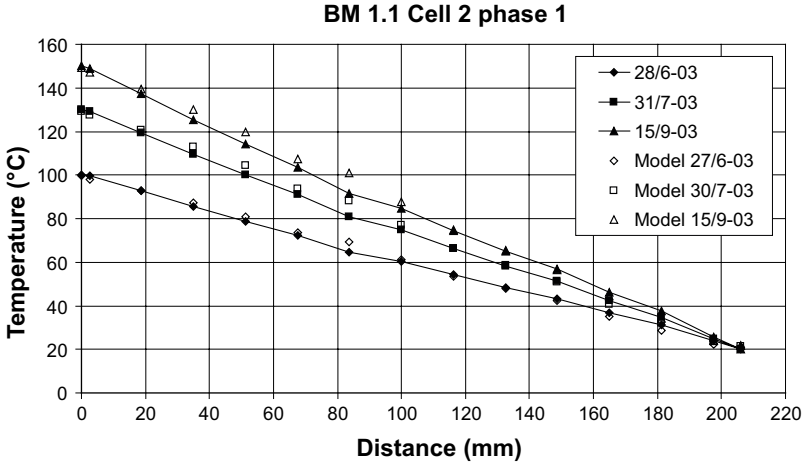

Figure 2-40. *Applied and measured temperature distribution in Cell 2 at three different times. Filled symbols denote measured values.*

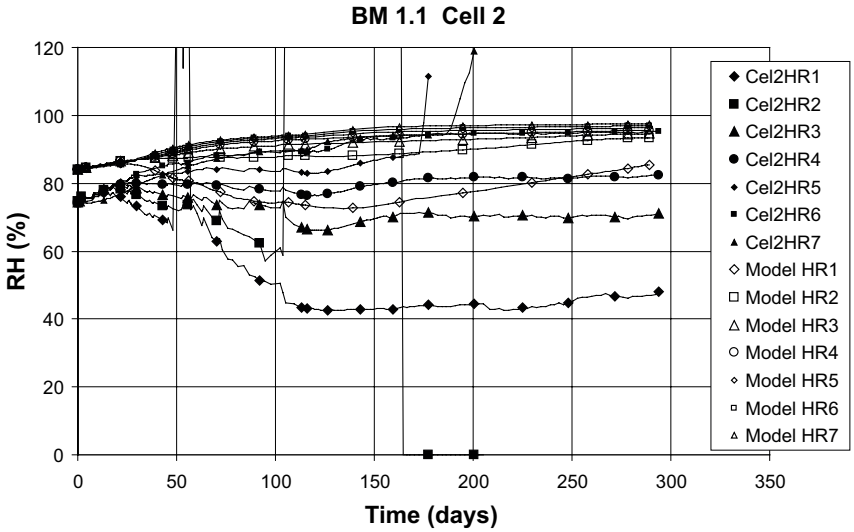

Figure 2-41. *Modelled and measured relative humidity in Cell 2. Filled symbols denote measured values.*

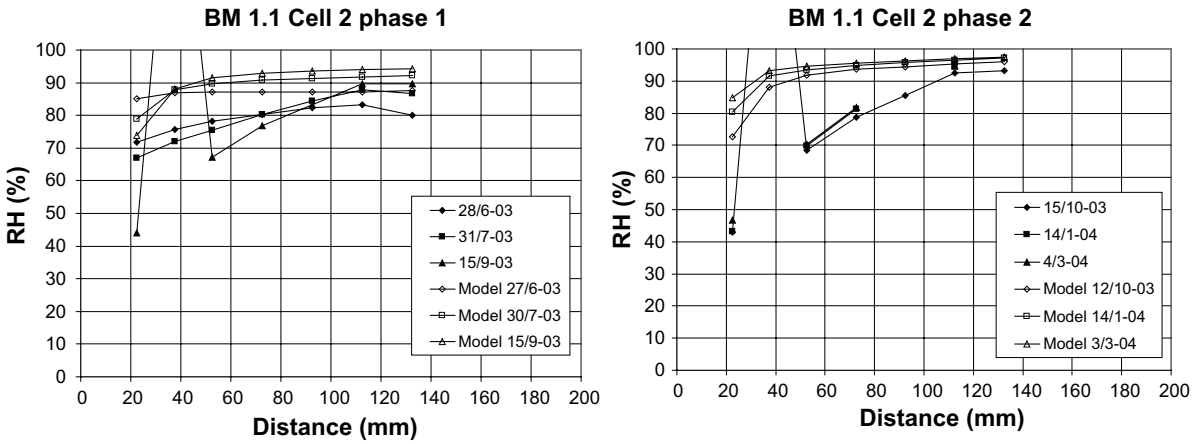

Figure 2-42. *Modelled and measured relative humidity in Cell 2. Filled symbols denote measured values.*

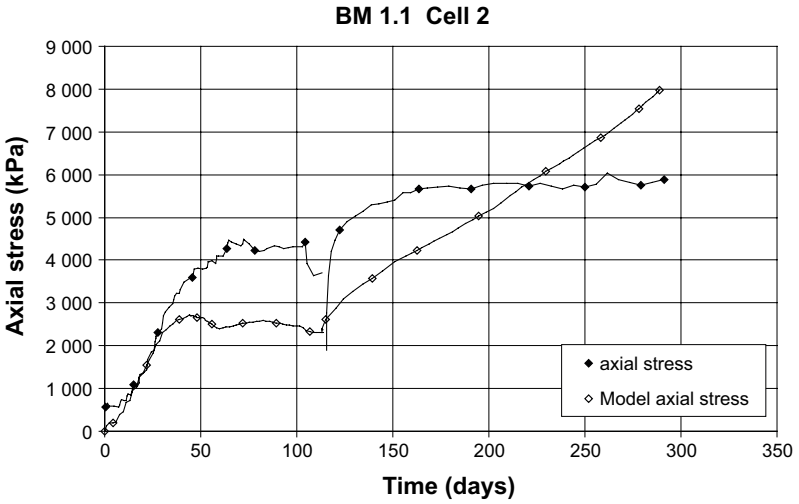

Figure 2-43. *Modelled and measured axial stress in Cell 2. Filled symbols denote measured values.*

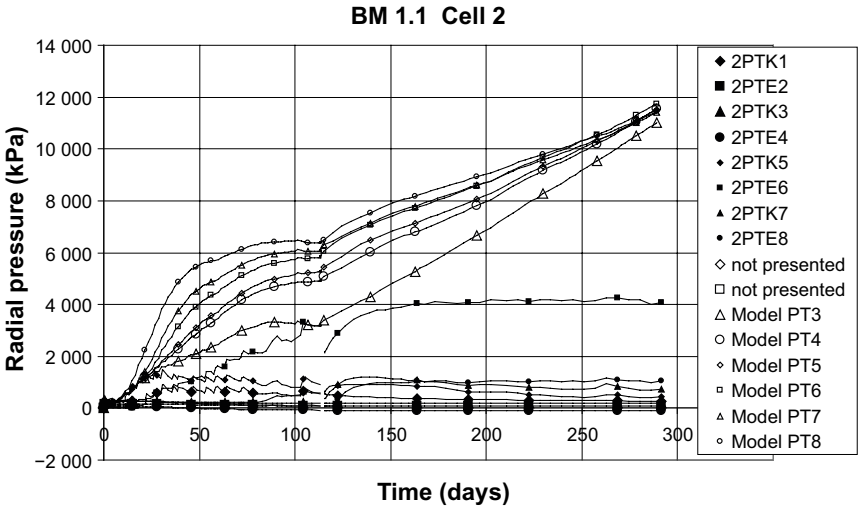

Figure 2-44. *Modelled and measured radial stress in Cell 2. Filled symbols denote measured values.*

Temperature

Figure 2-40 shows as an example the measured and the applied temperature distribution along the sample. The main difference is caused by the small deviation from the linear relation.

Relative humidity

Relative humidity is plotted as history plots in Figure 2-41 and as path plots at three different times in Figure 2-42. The agreement is not good since the measured RH is generally much lower than the calculated and the almost steady state reached according to the measurements is not modelled.

Stress

The stress is plotted as history plots. The axial stress measured by the force transducer is shown in Figure 2-43 and the radial stress measured in by small pistons in the cell wall is shown in Figure 2-44. The modeled axial stress is underestimated in the beginning and the measured constant stress in the late 150 days is not modeled. The measured radial stress is much lower than the modeled radial stress and also much lower than the measured axial stress.

Additional results and analyses

Water inflow

Figure 2-45 shows the calculated distribution of the water ratio in the two cells and comparison with the initial water ratio and the measured water ratio for Cell 2. Unfortunately no measured results were achieved for Cell 1.

Table 2-9 shows a comparison between calculated and measured water inflow as well as the water balance in terms of the volume available to saturate the samples and the volume of water inflow calculated according to the water ratios measured in one sample after interruption.

Table 2-9 Calculated and measured water inflow.

	Calculated ΔV (cm^3)	Measured ΔV (cm^3)	Required ΔV until saturation (cm^3)	ΔV according to measured w (cm^3)
Cell 1	280	1 050	722	–
Cell 2	180	330	429	106

These results clearly show that the measured water inflow is incorrect for both cells.

Influence of temperature

The modeling was done with the retention curve adapted to take into account the influence of temperature as shown in Figure 2-30. However, as mentioned this may be incorrect and a calculation of Cell 2 with the basic retention curve was also done. Figure 2-46 shows the RH history for both cases. The original retention curve for 20 °C yields better agreement with the measured results but not the kind of steady state observed by the measurements.

Bentonite displacements

The mechanical modeling also yields the deformations of the bentonite sample. Figure 2-47 shows the modeled development of the void ratio for the central row of elements in Cell 1. Figure 2-48 shows the modeled radial displacements and the deformed sample at the end of the test. These results show strong density redistribution with swelling at the water inlet side and shrinkage at the hot side. Figure 2-48 shows that a radial gap has been opened between the sample and the cylinder wall. The gap is about 15 mm long and has a maximum opening of about 1.5 mm. No measurements of these effects were reported.

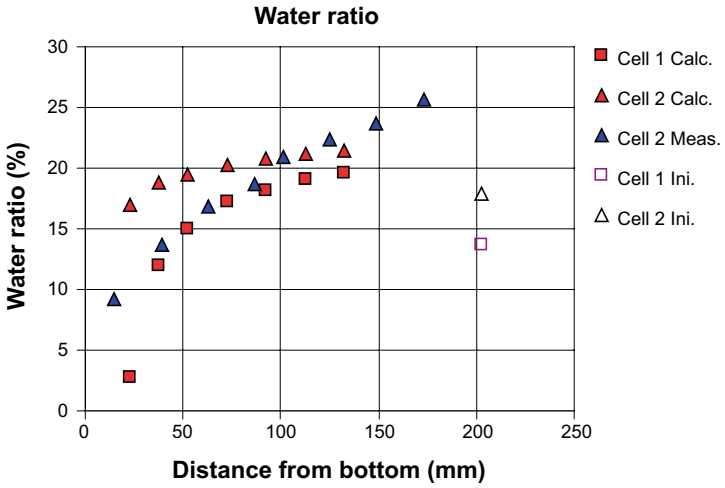

Figure 2-45. *Calculated and measured water ratio. The initial values are also indicated.*

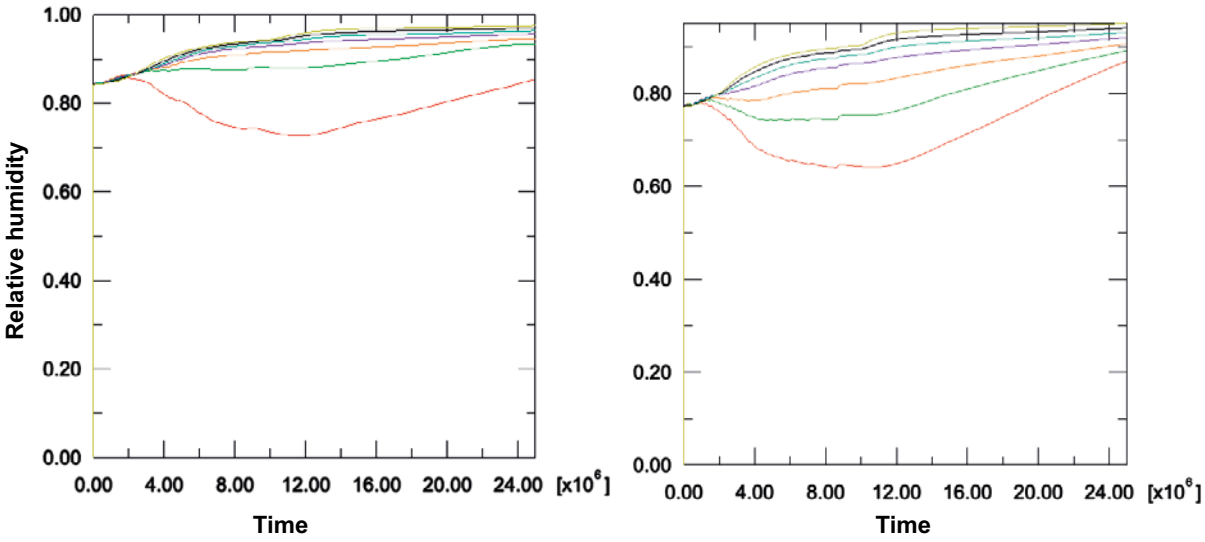

Figure 2-46. *Illustration of the influence of the retention curve on the RH development. Left diagram: Retention curve at 80 °C used. Right diagram: Retention curve at 20 °C used. The results are plotted at equal distances from the hot end (which corresponds to the red line).*

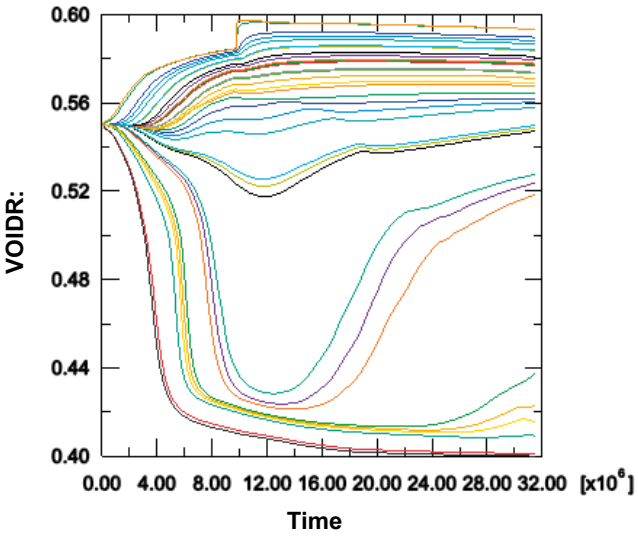

Figure 2-47. *Illustration of the modelled void ratio as a function of time (seconds) of the bentonite in cell 1. The results are plotted at equal distances from the hot end (which corresponds to the lower red and black lines).*

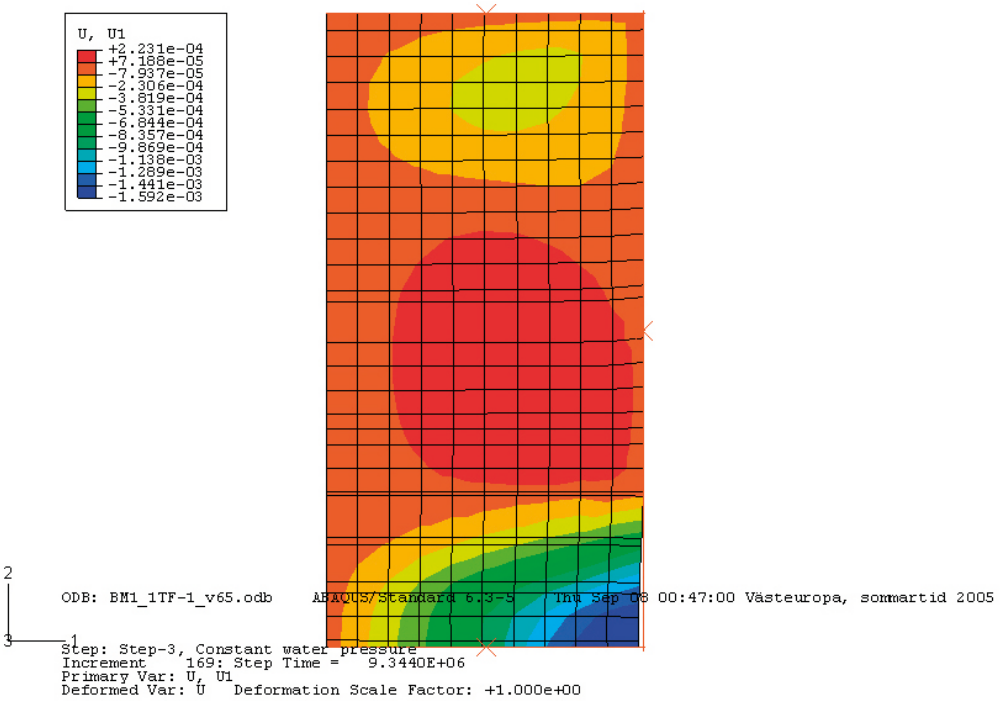

Figure 2-48. *Modelled radial displacements (m) of the sample at the end of the test. The gap at the bottom is also shown by the deformed mesh.*

2.4.6 Conclusions and comments

It is not easy to draw conclusions from the results. Some modeling results agree rather well, while others disagree substantially.

Cell 1

For Cell 1 measured and modeled RH and axial stress agree rather well (in spite of some overestimation of the stress), while radial stress and inflow disagree. For this cell it can rather easily be concluded that the latter measured results suffer from errors. The measured water inflow is higher than possible and the low radial stresses disagree with the much higher measured axial stress. It is difficult to measure total stress on a stiff material like the unsaturated bentonite blocks used in the test with such small transducers and the results were also questioned in the laboratory report.

The conclusion is thus that the hydraulic model is validated and partly also the mechanical although there are question marks.

Cell 2

For Cell 2 there was no good agreement for any of the measured results. RH differed a lot and especially the apparent steady state that was reached after half the test time was not predicted. This resulted also in a different mechanical behaviour since the measured axial stress ceased to increase after half the test time due to the lack in increased wetting. Only one of the radial pressure transducers showed after completed test time a significant pressure. The measured and calculated water ratio distribution differed substantially on the same reason. The measured water inflow could be concluded to be erroneous for this cell too since the measured water ratio distribution after termination of the test yielded a water uptake that was only a third of the measured.

The main uncertainty is the apparent steady state that occurred. Is it caused by leakage or an actual process that could not be modelled? This test could thus neither verify nor to reject the model.

3 BM 1.1.2 – Infiltration tests performed by CIEMAT

3.1 General

BM 1.1.2 includes two tests similar to the tests in BM 1.1.1 but with larger specimens and with another type of bentonite, namely the FEBEX bentonite used in the large scale in situ test in Grimsel.

3.2 Specifications

3.2.1 Introduction

Benchmark 1.1.2 is based on the large-cell experiments performed by CIEMAT in their laboratory in Madrid. One of the tests is kept under isothermal conditions whereas the second test is performed under a thermal gradient. At the time of the performed modelling, these test were still ongoing.

The large cell infiltration tests and the results are described in detail in the Technical Report CIEMAT/DMA/M2140/1/05 by Villar et al. (2005a) issued in April 2005 and made available to the modellers. The information most relevant to the Benchmark is reproduced (often *verbatim*) in the present document. More details are given in the CIEMAT document.

3.2.2 Description of the infiltration tests

General

Two infiltration experiments being performed in CIEMAT's large cells (Figure 3-1) have been selected; the first one is an isothermal test whereas the second one is a test with a thermal gradient applied. The material tested is FEBEX bentonite.

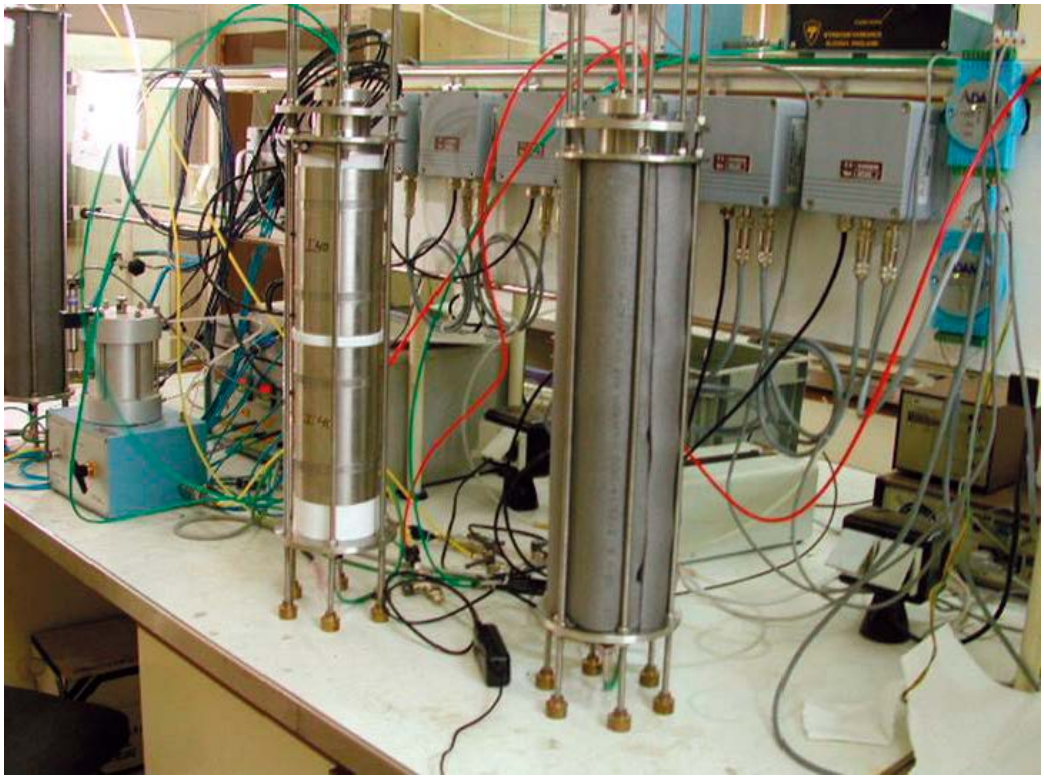

Figure 3-1. *Large infiltration cells: isothermal test (left) and thermal gradient test (right).*

The following parameters are measured during the tests:

- Temperatures
- Relative humidity
- Water intake

No mechanical parameters are measured during the test. As the experiments are still unfinished, no "post mortem" observations are available.

Apparatus and monitoring system

The infiltration tests are being performed in cylindrical cells enclosing a specimen 7 cm diameter and 40 cm long (Figure 3-2). The 15 mm thick cell wall is made of Teflon PTFE with a thermal conductivity of 0.25 W/mK. A 4 mm thick stainless steel shell provides mechanical reinforcement to resist the swelling pressures developed during the tests. The cell containing the thermal gradient test is additionally surrounded by a 15-mm thick foam layer with a thermal conductivity of 0.04 W/mK. Heat is applied to the bottom of the specimen. Hydration is performed from the top end of the specimen where a cooling system maintains the temperature constant.

Temperatures and relative humidity are measured inside the samples by means of sensors located at 30 cm (sensors RH1 and T1), 20 cm (sensors RH2 and T2) and 10 cm (sensors RH3 and T3) from the bottom end. The water intake into each of the experiments is also independently monitored. Further details of the equipment and monitoring system are presented in Villar et al. (2005a).

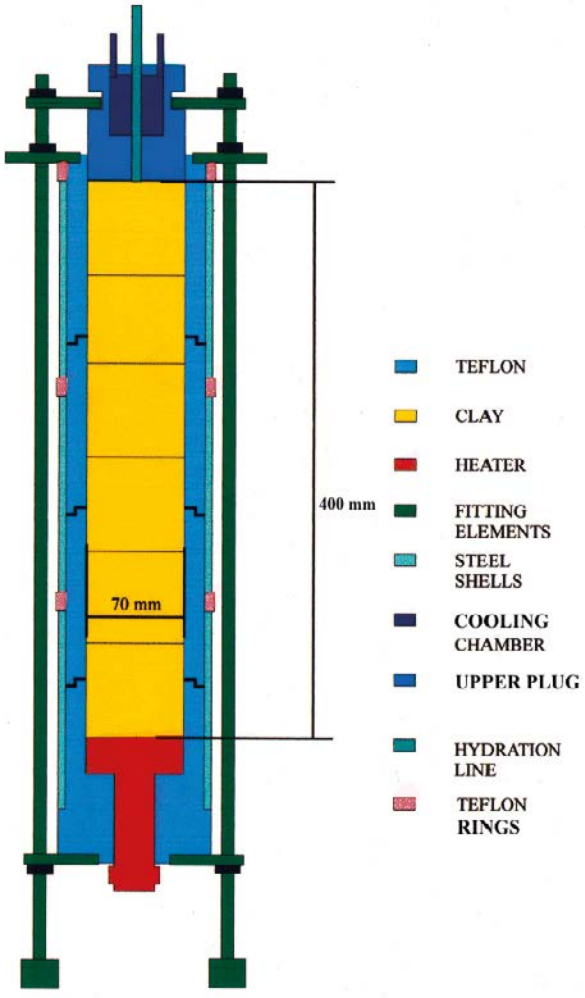

Figure 3-2. *Scheme of the large cells used in CIEMAT's infiltration tests.*

Material

The FEBEX bentonite has been used in the experiments. It is not a homoionic clay but it contains Na^+, Ca^{2+} and Mg^{2+} in significant and similar amounts. The material has been extensively tested in the framework of the FEBEX project and the main results are collected in ENRESA (1998, 2000), Villar (2002), Fernández (2003) and Lloret et al. (2004). A good summary is presented in Villar et al. (2005a) and the main THM properties are summarised in Appendix 4. Although a number of empirical laws are suggested in the Appendix, contributors may use alternative expressions, duly justified.

The clay was statically compacted (average compaction pressure of 30 MPa) at hygroscopic water content (around 13 %–14 % gravimetric water content) to a nominal dry density of 1.65 g/cm^3. The specimens were made up of five blocks; the three inner ones were 10 cm long whereas the two placed at the ends were 5cm long. Table 3-1 provides an indication of the possible heterogeneity by listing the measurements of dry density and water content made in a 10 cm long spare block.

Table 3-1. Results of the measurements performed in a 10-cm length spare block.

Position*	Dry density (g/cm^3)	Water content (%)
1.25	1.72	12.7
3.75	1.69	13.1
6.25	1.65	13.4
8.75	1.63	13.5

*Distance to the top of the block

Protocol of the experiments

Once the cell was assembled and the instrumentation installed in the *isothermal test* (*test* I40), the cooling system was set up and data acquisition was started. After 18 hours the hydration system was connected. The test was started on 15/01/2002 and the hydration stage on 16/01/2002.

In the *thermal gradient test* (*test* GT40), the cooling system and the heater were started simultaneously after cell assembly and instrument installation (initial phase). A temperature of 100 °C was applied at the bottom of the sample. After 65 hours of heating, hydration was started (second phase). The test began on 15/01/2002 and the hydration stage on 18/01/2002.

In both cases hydration was performed using low salinity water at a pressure of 1.2 MPa. The temperature applied by the cooling system corresponds to the ambient temperature of the laboratory and it undergoes some moderate variations. The temperatures recorded in the isothermal test can be used as reference values

Test results

The raw data obtained during the tests are collected in two Excel files, distributed within the EBS Task Force: *i40v.xls* (isothermal test I40) and *gt40v.xls* (thermal gradient test GT40). The raw results have been reviewed and selected by Villar et al. (2005a) to give a series of Tables of observed values that can be used directly for comparison with numerical analysis results.

Table 3-2 contains the observations of relative humidity, temperature and water intake of the isothermal test (test I40**)** from the time of start of hydration. The results of the thermal gradient test are presented in Table 3-3 and Table 3-4. Table 3-3 refers to the observations during the initial phase of the test, from the start of heating to the time of connecting the hydration system. Table 3-4 contains the results of the second stage of the experiment, from the time of the start of hydration. According to Villar et al. (2005a), the water intake data is not totally reliable and should be taken as indicative only. The actual water intake will be determined at the end of the test from the difference between final and initial weights.

Table 3-2. Isothermal test (test I40). Relative humidity (RH) and temperature (T) recorded by sensors after the initiation of hydration (sensor 1 placed at 30 cm from the bottom, sensor 2 at 20 cm and sensor 3 at 10 cm).

Time (h)	RH1 (%)	T1 (°C)	RH2 (%)	T2 (°C)	RH3 (%)	T3 (°C)	Water intake (cm^3)
0	42	20.6	41	20.7	42	20.5	0
1	42	20.9	42	20.9	42	20.7	
5	42	22.5	42	22.4	42	22.1	10
30	42	22.8	42	22.8	42	22.6	15
61	42	22.9	42	23.0	42	22.8	18
101	42	20.1	42	20.2	42	20.1	20
201	43	23.7	43	23.7	43	23.5	30
300	43	21.3	42	21.3	42	21.1	35
399	44	22.9	43	23.0	42	22.8	40
501	45	21.6	42	21.7	42	21.5	44
600	46	19.2	42	19.3	42	19.1	56
701	49	22.5	42	22.6	42	22.5	66
803	51	22.1	42	22.2	42	22.0	77
899	53	24.5	43	24.6	43	24.5	87
1001	55	23.3	43	23.4	42	23.2	97
1999	69	23.5	46	23.7	42	23.6	129
3001	76	24.0	51	24.3	43	24.2	147
4000	81	26.5	56	26.6	45	26.4	162
5001	84	28.7	61	28.7	48	28.6	172
10002	90	22.8	72	22.8	57	22.7	254
14997	92	24.9	77	25.0	66	24.9	317
19999	94	26.5	82	26.7	72	26.9	382
24998	94	22.7	83	22.9	76	22.9	443
28219	95	23.7	85	23.9	77	23.9	469

Table 3-3. Thermal gradient test (test GT40): Initial Phase. Relative humidity (RH) and temperature (T) recorded by sensors (sensor 1 placed at 30 cm from the bottom, sensor 2 at 20 cm and sensor 3 at 10 cm).

Time[1] (h)	RH1 (%)	T1 (°C)	RH2 (%)	T2 (°C)	RH3 (%)	T3 (°C)
0	42	21.9	42	21.7	42	21.4
1	42	22.5	42	22.3	43	23.3
2	42	22.6	43	22.5	44	27.5
3	42	22.7	43	23.0	45	30.9
4	43	22.9	43	24.4	47	36.6
5	43	23.1	44	26.1	48	40.5
6	43	23.5	44	27.6	49	43.2
7	43	24.0	45	28.9	50	45.1
8	43	24.5	45	30.0	50	46.4
9	43	24.9	45	30.8	50	47.3
10	43	25.3	45	31.4	51	47.9
20	44	27.1	46	33.5	52	49.1
30	45	29.2	47	35.6	52	50.9
40	44	28.2	47	34.9	53	50.1
49	44	29.2	47	35.7	53	51.1
60	45	29.1	48	35.5	54	50.8
65	45	28.6	48	35.1	54	50.5

[1]Time since start of heating.

Table 3-4. Thermal gradient test (test GT40): Second Phase. Relative humidity (RH) and temperature (T) recorded by sensors (sensor 1 placed at 30 cm from the bottom, sensor 2 at 20 cm and sensor 3 at 10 cm).

Time[1] (h)	RH1 (%)	T1 (°C)	RH2 (%)	T2 (°C)	RH3 (%)	T3 (°C)	Water intake (cm^3)
0	44	28.9	48	35.5	54	50.9	0.0
1	44	29.0	48	35.6	54	51.1	0.0
5	45	30.2	48	36.6	54	51.8	0.8
10	45	30.0	48	36.4	55	51.5	0.9
21	45	28.8	48	35.3	55	50.6	1.0
30	45	28.3	48	34.9	55	50.4	1.1
40	44	27.7	48	34.4	56	49.9	1.3
50	44	27.1	48	34.0	56	49.7	1.4
61	44	26.5	49	33.6	56	49.4	1.5
69	44	26.1	49	33.2	56	49.1	7
81	45	27.7	49	34.6	57	50.2	8
87	44	27.5	49	34.4	57	50.1	9
101	45	28.5	49	35.3	57	50.9	10
200	45	26.8	51	33.8	58	49.5	17
299	47	29.6	52	36.3	57	51.3	23
401	48	26.9	53	33.9	56	49.6	28
500	50	27.5	54	34.5	55	49.9	32
599	52	26.9	55	34.0	54	49.6	59
701	55	28.0	56	34.7	53	50	63
803	57	30.2	57	36.6	52	51.5	66
899	59	28.8	57	35.5	51	50.7	70
1 001	62	30.5	58	37.0	50	51.7	73
1 998	76	29.7	61	36.2	43	51.1	101
3 003	83	29.7	63	36.2	39	51.1	128
3 999	86	31.6	65	38.2	38	52.8	145
5 000	88	33.8	66	39.7	37	53.7	160
10 001	92	28.6	70	35.3	36	50.3	220
14 948	92	30.3	71	36.6	38	51.3	275
20 004	93	30.6	73	37.2	38	52.1	330
25 004	93	28.8	74	35.6	39	50.8	388
28 170	94	29.4	74	36.1	38	51.2	417

[1]Time since start of hydration.

3.2.3 Requested results

The following information was requested:

a) Main features of the analyses performed.

b) Results of the analyses and comparison with experimental results.

Main features of the analyses performed

This basic description should contain summarised information on:

- Geometry adopted for the analysis.
- Type of analysis (e.g. 1-D, 2-D, axisymmetric...).
- Element types used.
- Constitutive laws adopted (thermal, hydraulic, mechanical).
- Constitutive parameters used and procedure used in their determination or estimation.

- Boundary conditions (thermal, hydraulic, mechanical).
- Initial conditions (thermal, hydraulic, mechanical).
- Hypothesis adopted for gas pressure and gas flow.
- Any other features that are deemed important in the analysis.

Results of the analyses and comparison with experimental results

The following analysis results should be provided graphically together with comparison with observed data. The Excel files of the submitted graphs should also be made available. The date and hour taken as time origin should be indicated.

Isothermal test (test I40)

- Relative humidity vs. time for sensors HR1, HR2 and HR3.
- Water intake vs. time.

Thermal gradient test (test GT40). Initial phase

- Temperature vs. time for sensors T1, T2, T3.
- Relative humidity vs. time for sensors HR1, HR2, HR3.

Thermal gradient test (test GT40). Second phase

- Temperature vs. time for sensors T1, T2, T3.
- Relative humidity vs. time for sensors HR1, HR2, HR3.
- Water intake vs. time.

Although only TH parameters are provided for comparison, it is advised to adopt a full THM analysis whenever possible.

3.2.4 Properties of FEBEX bentonite

The properties of FEBEX bentonite are shown in Appendix 4.

3.3 Modelling results with Code Bright

3.3.1 Introduction

Section 3.3 presents the benchmark calculations made using Code Bright.

In Section 3.3.2 a brief description of the experimental setup is made. Section 3.3.2 presents a base case model and the results are compared with experimental data in Section 3.3.3. In Section 3.3.4 some discussion is made on difficulties that arose in the modeling work. Finally conclusions of the modeling calculations are made.

3.3.2 Model description

In this section the base case models employed to simulate the I40 and TG40 cells are presented. All modeling work was performed with the finite element program Code_Bright, version 2.2 (CIMNE 2000). Only thermal and hydrodynamic processes were included in the analysis (TH-model). As in the experimental setup, the model with isothermal conditions is referred to as I40, while the model of the thermal gradient setup is labeled TG40.

Geometry

In an attempt to correctly model the heat flow in TG40, both the clay itself as well as its container has been taken into account when choosing a suitable model geometry. Both the Teflon cap and the surrounding steel shell are accounted for.

The 2D axisymmetric geometry is pictured in Figure 3-3. Even though no heat transport is experienced in I40, an identical geometry is used for that model. In total the geometry consists of 1 424 rectangular shaped 2D-finte elements.

Boundary conditions

The thermal and hydrodynamic boundary conditions imposed on the systems are schematically pictured in Figure 3-3.

Temperature

I40 was made to follow seasonal variation of the environmental temperature by applying a thermal boundary protocol for the entire system. This protocol is based upon measured values and is found in Figure 3-4.

The same protocol is used as boundary condition for the upper edge in TG40 while the lower boundary of the model is held constant at 100 °C. To allow for thermal losses over the cylindrical surface of the setup, the heat transfer over this boundary is assumed proportional to the deviation from the environmental temperature (ΔT)

$$\vec{i}_{loss} = -\gamma \cdot \Delta T$$

with the choice of heat transfer coefficient $\gamma = 3$W/K.

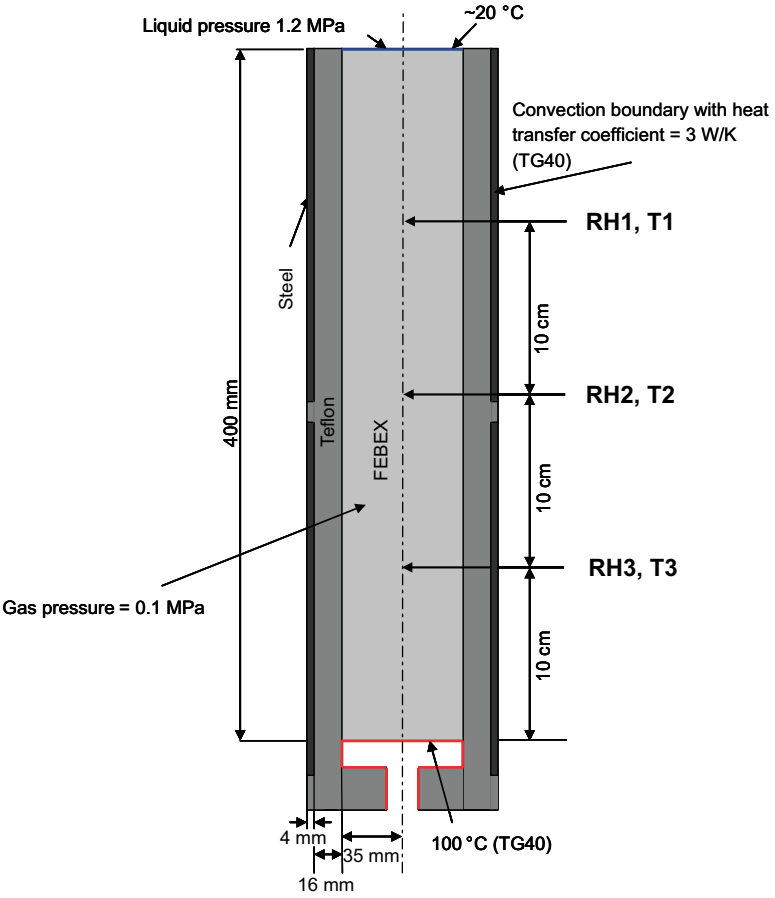

Figure 3-3. *Geometry and boundary conditions of the models. The location of the corresponding temperature and RH sensors are indicated.*

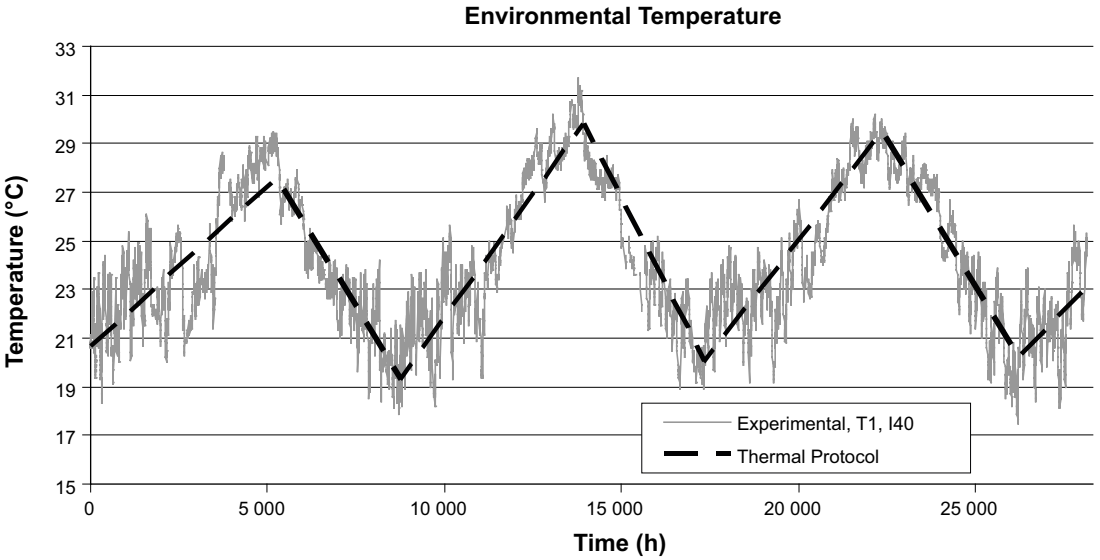

Figure 3-4. *Thermal protocol mimicking the environmental temperature. It is applied both to the top edge in TG40 and to the entire system in I40.*

Liquid pressure

In both of the models the top edge is exposed to a liquid pressure of 1.2 MPa while the other boundaries are kept impenetrable to liquid. The pressure is switched on after 65 hours in TG40 and after 16 hours in I40.

Gas pressure

The base case includes (uncontrolled) gas leaks by exposing the system to a volume boundary condition of atmospheric gas pressure (0.1 MPa).

Initial conditions

The modeled cells were prepared in accordance with the specifications for the present benchmark and relevant initial parameters are found in Table 3-5.

Table 3-5 Initial model parameters for the FEBEX bentonite.

Water ratio, w_{ini}	13.2	%
Dry density, ρ_{dry}	1.675	g/cm^3
Solid phase density, ρ_s	2.70	g/cm^3
Porosity, ϕ_{ini}	0.38	–
Saturation level, S_{ini}	58	%
Void ratio, e_{ini}	0.614	–
Temperature, T_{ini}	20.7	°C
Gas pressure, $P_{g,ini}$	0.1	MPa
Liquid pressure $P_{l,ini}$	−118	MPa

The values for the initial water ratio and dry density are produced by making an average of the values from the analysis made on a spare block, presented in the specification report (CIEMAT 2005).

In modeling the materials of the containing construction, physically reasonable values have been used for the heat transport parameters. Concerning the hydrodynamic processes, parameters have been chosen in order to suppress gas and liquid flow in this part of the structure. Relevant material parameters for Teflon and steel are listed in Table 3-6.

Table 3-6. Adopted material parameters for steel and Teflon.

	Stainless Steel L316	Teflon
Heat conductivity	16.3 W/mK	0.25 W/mK
Intrinsic permeability	10^{-30} m^2	10^{-30} m^2
Porosity	0.0001	0.01
Density	8.0 g/cm^3	2.3 g/cm^3
Specific Heat	0.5 J/(g K)	1.2 J/(g K)

Constitutive laws

The equations describing the thermal and hydrodynamic transport are listed together with relevant parameter values in Table 3-7.

Table 3-7. Hydrodynamic and thermal transport equations and associated parameters.

Darcy's law ***(Advective mass flow of gas and liquid)***

$$\vec{q} = \frac{k \cdot k_r}{\mu} \nabla P$$

Intrinsic permeability (isotropic) k =1.54 10^{-21} m^2

Liquid relative permeability $k_r = S^3$

Gas phase relative permeability $k_{rg} = 10^8(1-S)^3$

P and μ denotes pressure and viscosity respectively. S is the liquid saturation level.

Fourier's law ***(Conductive heat flow)***

$$\vec{i}_c = -\lambda \cdot \nabla T$$

Heat conductivity $\lambda = 0.47^{S} \cdot 1.15^{(1-S)}$ W/mK

T denotes temperature.

Fick's law ***(Diffusive vapour transport)***

$$\vec{i} = -\phi \cdot \tau \cdot D \cdot (1-S) \cdot \rho_g \cdot \nabla \omega_g^w$$

Diffusion coefficient

$$D = 5.9 \cdot 10^{-6} \frac{(273.15+T)^{2.3}}{P_g} \text{ m}^2/\text{s}$$

Tortuosity for vapor diffusion, $\tau = 0.8$

ρ_g and ω_g^w denotes gas phase density and mass fraction of vapor in gas, respectively. ϕ is the porosity.

The choice of intrinsic permeability deserves some comment. Relating the expression for the permeability, k_w, found in the specification report, to a value of k, used in Code_Bright (see Table 3-7) gives the value $k = 2.96 \times 10^{-21}$ m^2 (assuming a room temperature liquid viscosity of 0.96 mPa·s.). Using instead an expression relating permeability to porosity in FEBEX bentonite found in Sanchez (2004) gives $k = 1.54 \times 10^{-21}$ m^2. Preliminary test calculations indicated that the higher value of k gave a much too fast infiltration process as compared to experiment. Therefore the value $k = 1.54 \times 10^{-21}$ m^2 was adopted.

Table 3-8. Retention curve parameters.

P_0	132	MPa
λ	0.57	–
P_m	600	MPa
λ_m (not fitted)	1	–
σ_0 (not fitted)	0.072	N/m

The parameterization of the retention curve given in the specification report (Table A1.2) does not correspond to the values plotted in Figure A1.1 in that same document. Furthermore, only experimental points with a rather high water ratio are found in that diagram. Therefore a new fit was made to an extended van Genuchten model,

$$S_r = \left\{1+\left(\frac{P_g - P_l}{P_0 \dfrac{\sigma}{\sigma_0}}\right)^{\frac{1}{1-\lambda}}\right\}^{-\lambda} \cdot \left\{1-\frac{P_g - P_l}{P_m}\right\}^{\lambda_m},$$

where experimental points were "read off" of the diagram (Figure A1.1). Some additional points for low water ratio from Villar and Lloret (2004) were included as well. The fitted parameters are listed in Table 3-8 and Figure 3-5 displays the adopted retention curve.

3.3.3 Results

In this section the requested results on temperature, relative humidity and amount of injected water is presented and compared to experimental findings. Comments on the modeling procedure and discussion of the results are found in Section 3.3.4.

Temperatures

The calculated time evolution of the temperature at the three sensor locations (along the symmetry line, as seen in 3-3) is presented in Figure 3-6, Figure 3-7, and Figure 3-8.

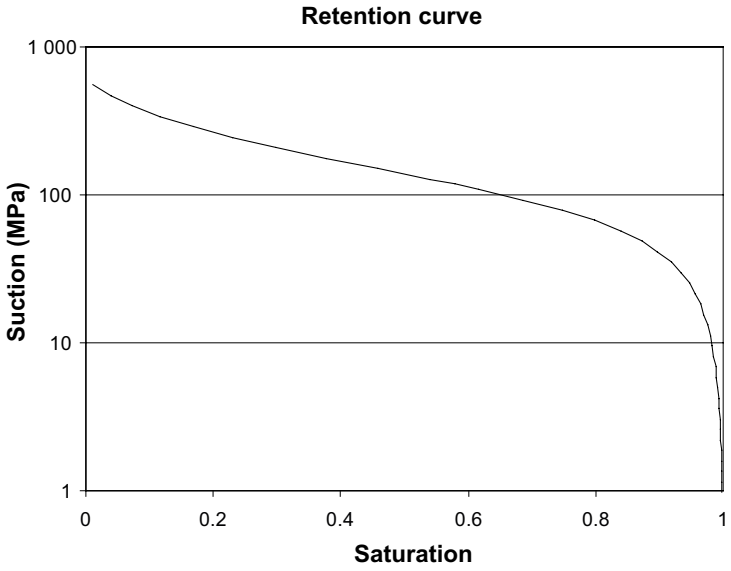

Figure 3-5. *Retention curve used in the modeling.*

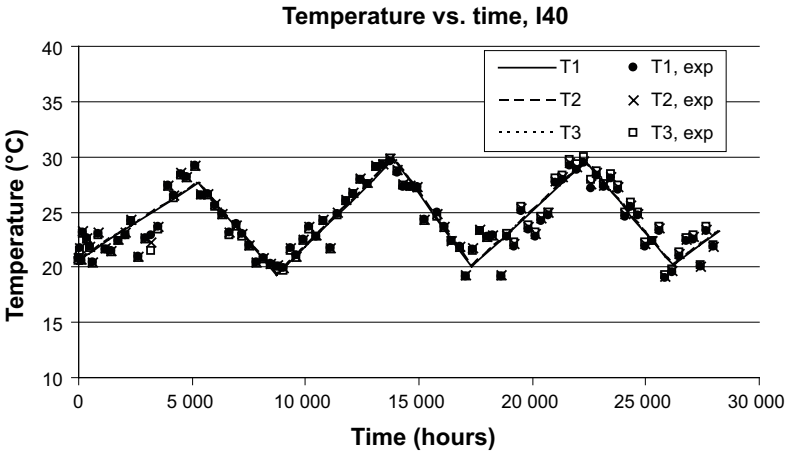

Figure 3-6. *Temperature vs. time for I40.*

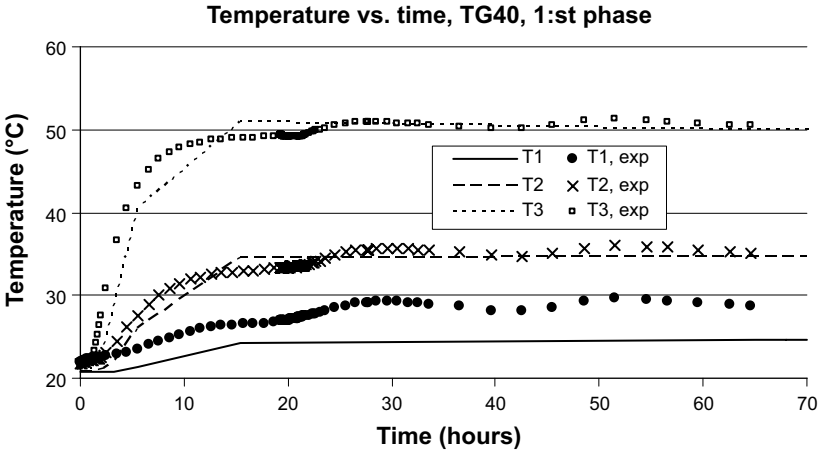

Figure 3-7. *Temperature vs. time in the first phase for TG40.*

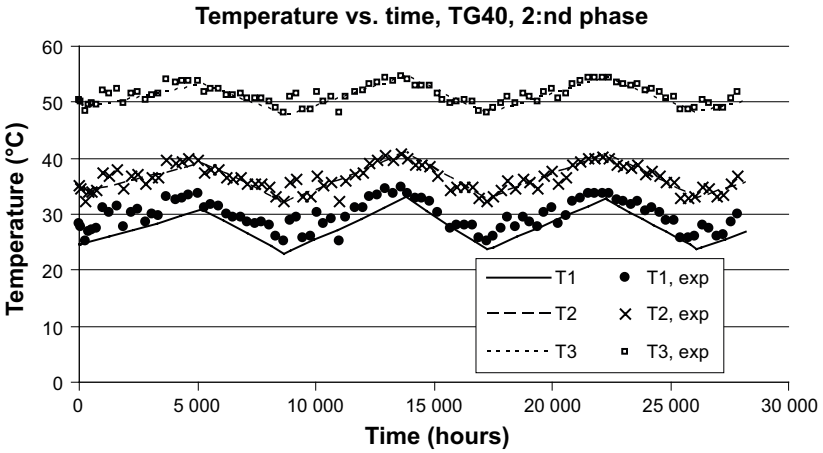

Figure 3-8. *Temperature vs. time in the second phase for TG40.*

Relative humidity

In Figure 3-9, Figure 3-10 and Figure 3-11 the time evolution of the relative humidity at the location for the three sensors (along the symmetry line) are presented and compared to experiment.

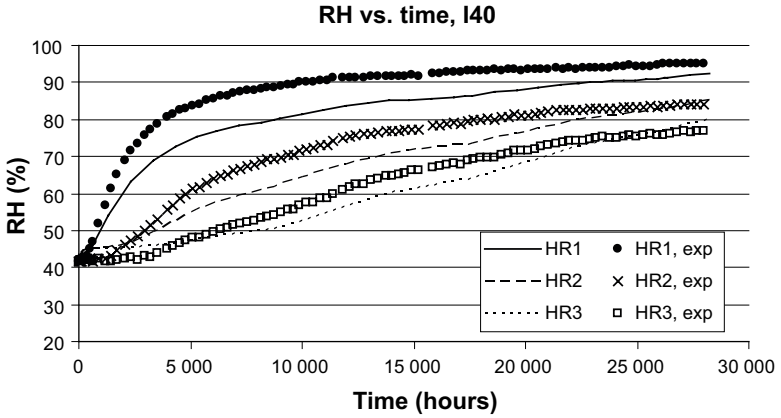

Figure 3-9. *Relative humidity vs. time for I40.*

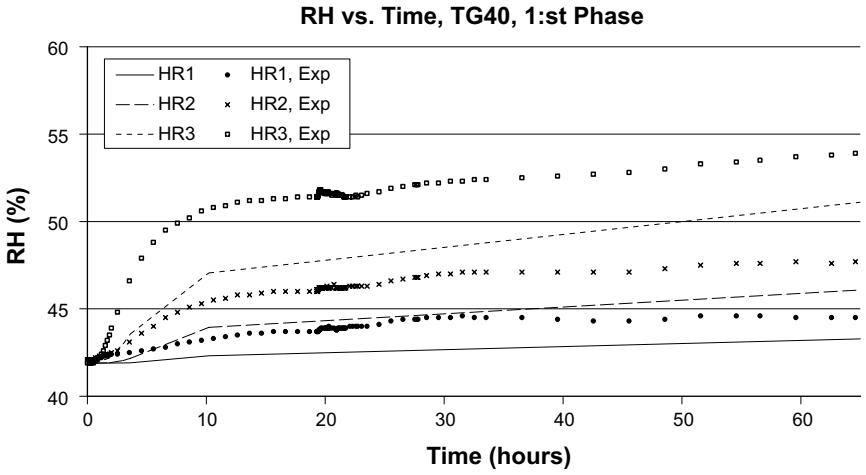

Figure 3-10. *Relative humidity vs. time in phase 1 for TG40.*

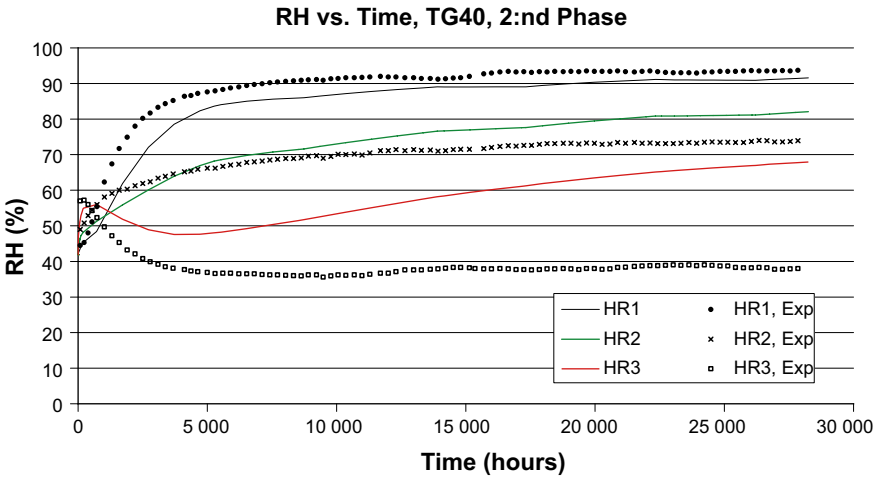

Figure 3-11. *Relative humidity vs. time in phase 2 for TG40.*

Water inflow

The calculated accumulated inflow of water in the models are presented and compared with measured data in Figure 3-12 and Figure 3-13.

From the data in Figure 3-3 and Table 3-5 the maximum volume of injected water could easily be calculated, assuming no leaks in the setup

$V_{\max} = \pi \cdot 3.5^2 \cdot 40 \cdot \phi_{ini} \cdot (1 - S_{ini})\ cm^3 = 245\ cm^3$.

Thus, the experimental values of over 400 cm^3 at the end of the considered time period hints that either leaks are present, as pointed out as a possibility in the test description (Villar et al. 2005a), or that the reliability of the inflow measurement itself is questionable.

Sensitivity Analysis

A small sensitivity analysis has been performed with focus on the interplay of the diffusion (tortuosity τ) and advective flow (intrinsic permeability k) parameters. No water mass conservation investigation has been done because the experiments only have a very short period where no extra water is injected. The base case value of the investigated parameters are $\tau = 0.8$ and $k = 1.54 \times 10^{-21}$ m^2 (Table 3-7). The analysis has been made focusing on the relative humidity evolution of TG 40.

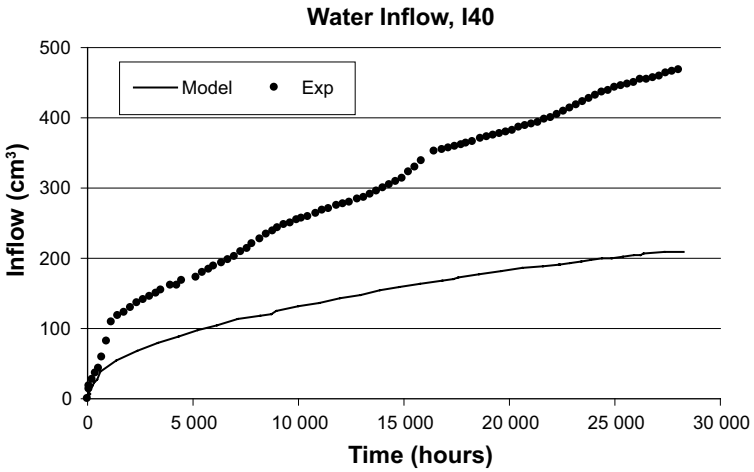

Figure 3-12. *Accumulated water inflow for I40.*

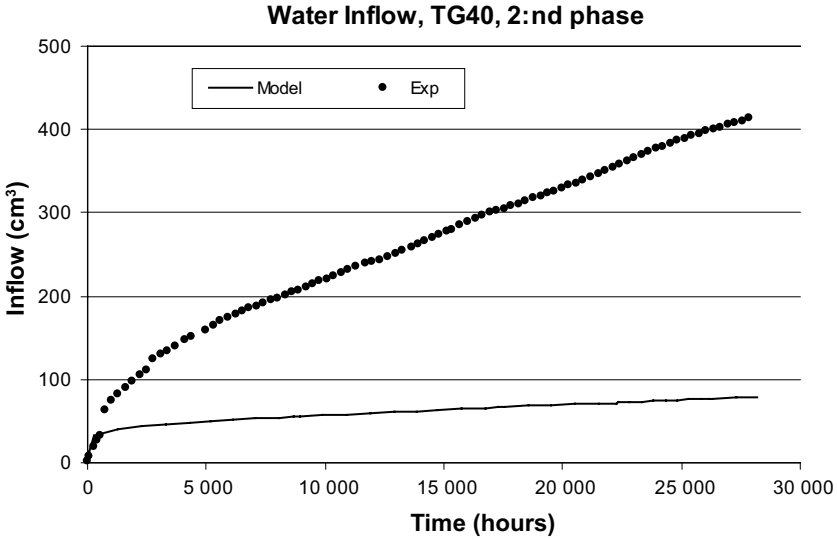

Figure 3-13. *Accumulated water inflow for phase 2 for TG40.*

In Figure 3-14, the RH-evolution of the sensor closest to the heater (HR3) in TG40 is plotted for various values of τ and k. It is seen that the infiltration speeds up as the tortuosity is lowered (while k is kept at its default value) and vice versa.

In order to investigate the importance of the individual parameters in contrast to the parameter ratio k/τ, the RH-evolution has been calculated for the same set of tortuosities but with k/τ fixed to its base case value. These results are also pictured in Figure 3-14. It is seen that a lower τ will give a lower infiltration speed in this case. Thus, the intrinsic permeability is more sensitive of the investigated parameters.

The results at the position of the other two RH sensors are similar to HR3 as can be seen for the case of HR1 in Figure 3-15. The difference being that a lowering of τ lowers the infiltration process also when using the base case value of k.

3.3.4 Discussion

We define the models presented in the last sections as our base cases (Table 3-7). During the work, several alternative models have been investigated. The need for these model examinations arose due to two major difficulties associated with the calculation of the TG40 system.

Temperature profile in TG40

The first problem concerns the temperature distribution. The experimental setup is covered with isolating foam to prevent thermal losses on the cylindrical surface of the steel shells.

In Figure 3-16 the temperature profile for several thermally isolated models are plotted together with experimental values and the base case. The model labeled “FEBEX only” considers only the bentonite (no Teflon or steel) and employs a larger dependence of the heat conductivity on the liquid saturation level compared to the default case. We see that even with this exaggerated saturation level dependence, the deviation from a linear profile is very small. The possibility that the measured profile is a result from intrinsic material properties of the bentonite is therefore excluded.

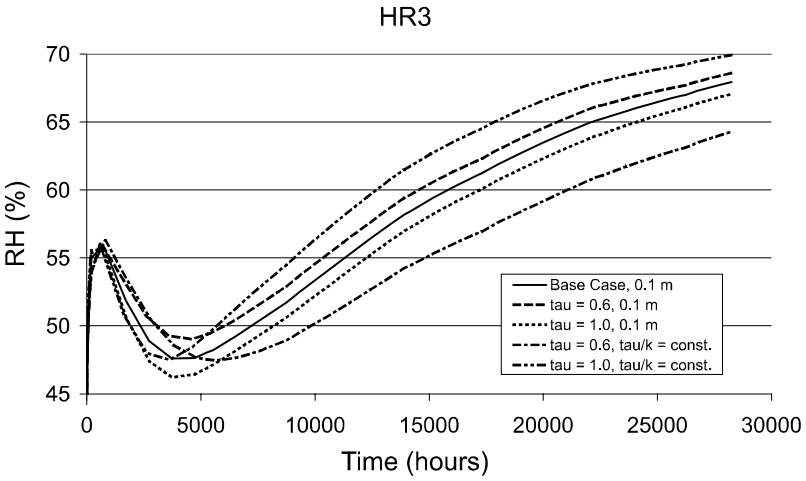

Figure 3-14. *RH-evolution for various values of tortuosity and intrinsic permeability at the position of the sensor closest to the heater in TG40.*

The two models labeled “Const. h.c.” examines the influence of the confinement structure. The models are similar to the base case except that the heat conductivity is made constant (and no heat loss occurs on the cylindrical surface, of course). The two constants of 1.3 W/mK and 0.2 W/mK are chosen as to correspond to exaggerated values for both saturated and (very) dry bentonite respectively. These curves show the tendency of the steel shells to flatten the temperature profiles. In the middle of the structure, where a teflon ring separates the two steel sections (see Figure 3-3), the temperature falls more rapidly. Even though the inclusion of the surrounding confinement gives a more non-linear behavior of the profile we note that the deviation from measured values is enormous (approximately 30 °C too high for the lowest sensor).

These three considered models give a fairly good estimate of the non-linearity of the temperature profile for a thermally isolated system. We conclude that it is impossible for a model which treats the interface between steel and foam as a thermally insulated boundary to reproduce the experimental temperature profile.

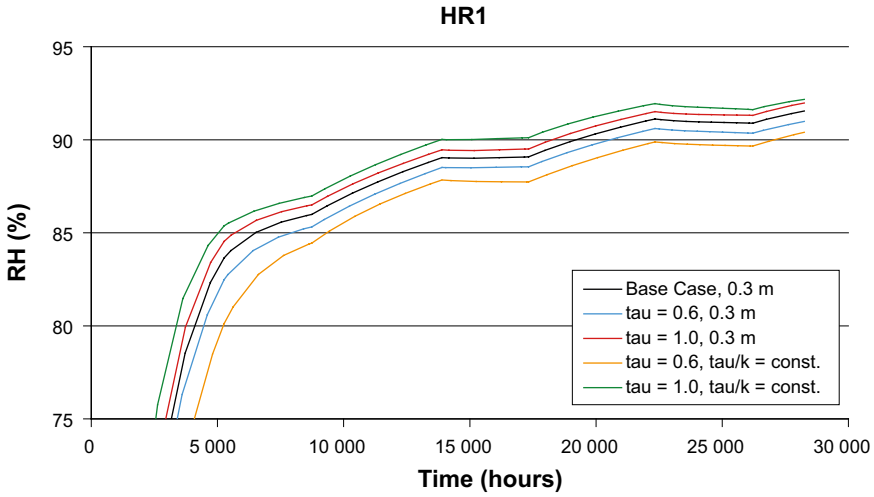

Figure 3-15. *RH-evolution for various values of tortuosity and intrinsic permeability at the position of the sensor closest to the top in TG40.*

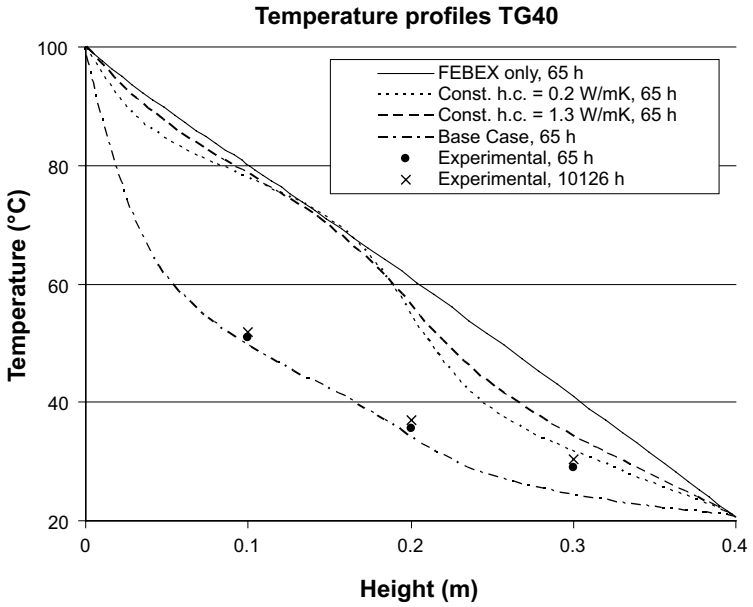

Figure 3-16. *Temperature profile for various models of the TG40 cell after 65 hours.*

The argument above does not exclude the possibility that the measured temperature profile should be an effect of heterogeneities within the clay sample, such as a crack or a gap. However, looking at how stable the temperature profile is as a function of time (it basically only varies with season) we doubt that this is the case.

The choice made in the base case is to assign a heat loss at the steel surface which is "tuned" in order to obtain a temperature profile in agreement with the experimental values.

Gas Phase

Another problem encountered during the modeling is the question of how to handle the gas phase. The problem has two sides to it. Firstly, it is uncertain if there are gas leaks present in the experimental set-up. If there are, these are obviously uncontrolled and will make a complete modeling (concerning boundary conditions, et. c.) unfeasible. The second issue concerns the way the gas phase transport should be described, i.e. what parameters to choose in Table 3-7. Obviously, the two issues are coupled – a faster gas transport will even out the gas pressure more effectively, as will a larger gas leak.

The RH-evolution of the sensor located closest to the heater (HR3) has been impossible to capture with a conventional model (i.e. with a continuous S^3-function for the relative permeability of water and with reasonable choices of parameters k and τ). Furthermore, with a completely gas tight model the gas pressure rises to over 4 atmospheres at the end of the considered infiltration process. A large gas pressure makes the diffusivity less efficient (see the expression for the diffusion coefficient in Table 3-7) which makes the infiltration process to appear even faster (specifically when looking at the lowest RH sensor). We therefore assume that the experimental setup is not gas-tight and that gas is transported out of the system to such an extent that the gas pressure stays close to the surrounding atmospheric pressure.

The choice made in the base case for the description of the gas phase is a rather radical one – we use a volume boundary condition to keep the gas pressure in the bentonite at 0.1 MPa during the entire calculation. The effect of such a treatment is to a high extent equivalent with a calculation where the gas phase logic has been turned off and the total gas pressure is treated as a constant. The major difference is that a (very) small amount of water is leaving the model in the case which includes gas logic.

3.3.5 Conclusions

The present report has presented models which resembles experimental findings rather well, both concerning temperatures and relative humidity (apart from the RH-evolution of the lowest sensor in the thermal gradient test). However, in order to achieve this resemblance several assumptions had to be made concerning the boundary conditions both for the hydraulic and the heat transport processes. This lack of boundary control makes any conclusions to be drawn about the systems less straightforward.

With this in mind we still conclude that thermal leaks are present in TG40. Also, our investigation suggests that gas leaks are present which equalizes the pressure in the setup with the surroundings. But even with atmospheric pressure the modeled vapor diffusion is not effective enough to maintain the steady-state like behavior of the lowest RH-sensor in TG40.

The conclusion regarding gas pressure should not be considered too rigorous, as it relies critically on the selected transport parameters (e.g. k and τ, Table 3-7) as well as the underlying conceptual model, which for instance assumes all moisture transport driven by the suction gradient to be in liquid form. Some further aspects of the underlying model is discussed in Section 2.3.5.

An indication on the quality of these assumptions could be found by looking at the results for I40. Even if the calculation produces RH-values in accordance with experiment at the end of the considered time period, the slope of the curves (Figure 3-9) is a little bit too steep while at the beginning of the infiltration, the simulation is a little bit too slow as compared to experiment. However, an alternative explanation for this mismatch might instead be found in the choice of transport and retention parameters (e.g. the adopted retention curve certainly have some uncertainty, see Section 3.3.2).

3.4 Modelling results with Abaqus

3.4.1 General

The tests in BM 1.1.2 have been performed on FEBEX bentonite, which has been used both in the in situ test in Grimsel and the full scale mock-up test. A material model for Abaqus has been derived in previous projects and used for modelling these tests. Several modelling calculations with the code Abaqus have thus been performed with the material model for FEBEX bentonite. The Abaqus model used for the tests in Benchmark 1.1.2 has thus been verified for both laboratory tests and large scale tests (see e.g. Börgesson et al. 2004). No changes and no calibration of this model have thus been done with the results in BM 1.1.2 but only comparison with measured results (validation calculations).

3.4.2 Material model and description

General

This chapter contains a description of the material models for the buffer material and the parameters included in the models. Since the model is basically the same as the model used for BM 1.1.1 the description will be brief.

Material models

The models and data used for the buffer are identical to the ones used in the FEBEX calculation (Börgesson et al. 2004).

Thermal flux from conduction

No thermal modelling was done for BM 1.2 (on the same reason as for BM 1.1) since the knowledge of the thermal properties of the apparatus, the insulation and the thermal power applied was insufficient.

Water liquid flux

The factor δ controlling the relation between hydraulic conductivity of unsaturated and saturated soil in Equation 3-1 (same as Equation 2-18) is the same as for MX-80:

$$K_p = (S_r)^{\delta} K \qquad (3\text{-}1)$$

$\delta = 3$

The *hydraulic conductivity* is a function of the temperature and the void ratios. Table 3-9 shows the values used in the model.

Table 3-9. Hydraulic conductivity K as a function of void ratio e and temperature T.

T °C	e	*K* m/s
20	0.47	0.048×10^{-13}
20	0.57	0.11×10^{-13}
20	0.69	0.25×10^{-13}
20	0.82	0.55×10^{-13}
50	0.47	0.07×10^{-13}
50	0.57	0.17×10^{-13}
50	0.69	0.37×10^{-13}
50	0.82	0.83×10^{-13}
70	0.47	0.10×10^{-13}
70	0.57	0.22×10^{-13}
70	0.69	0.49×10^{-13}
70	0.82	1.1×10^{-13}
90	0.47	0.12×10^{-13}
90	0.57	0.28×10^{-13}
90	0.69	0.6×10^{-13}
90	0.82	1.4×10^{-13}

Water vapour flux

The thermal vapour flow diffusivity D_{Tvb} and the parameters *a* and *b* according to Equations 3-2 to 3-5 (same as Equations 2-20 to 2-22) have been determined with calibration calculations (Börgesson et al. 2004).

$$q_v = -D_{Tv}\nabla T - D_{pv}\nabla p_v \qquad (3\text{-}2)$$

where

$$D_{Tv} = D_{Tvb} \qquad 0.3 \ S_r \ 0.7 \qquad (3\text{-}3)$$

$$D_{Tv} = D_{Tvb}\cdot\cos^{a}\left(\frac{S_r - 0.7}{0.3}\cdot\frac{\pi}{2}\right) \qquad S_r \ 0.7 \qquad (3\text{-}4)$$

$$D_{Tv} = D_{Tvb}\cdot\sin^{b}\left(\frac{S_r}{0.3}\cdot\frac{\pi}{2}\right) \qquad S_r \ 0.3 \qquad (3\text{-}5)$$

D_{pv} =0

$D_{Tvb} = 0.4\times10^{-11}$ –0.7×10^{-11} m^2/s, K

a = 6

b = 10

Hydraulic coupling between the pore water and the pore gas

The following water retention curve has been used (fitted to the modified van Genuchten expression in Equation 3-6).

$$S_r = S_{r_0} + \left(S_{r_{mas}} - S_{r_0}\right)\left[1+\left(s/P_0\right)^{1/(1-\lambda)}\right]^{-\lambda}\left[1-s/P_s\right]^{\lambda_s} \qquad (3\text{-}6)$$

where S_{r0} and S_{rmax} are the residual and maximum degree of saturation and P_0 (MPa), P_s (MPa), λ and χ_s are material parameters with the following values:

S_{r0} = 0.01

S_{rmax} = 1.00

P_0 = 3.5·10^4 (kPa)

P_s = 4.0·10^6 (kPa)

λ = 0.30

λ_s = 1.5

Figure 3-17 shows the relation.

The water transport in Abaqus is governed by the pore water pressure (u_w) but since the measurements and requested results are in relative humidity (R_h) a conversion from calculated negative pore water pressure to relative humidity has to be done. The same conversion according to Equation 3-7 as for BM 1.1 has been used.

$$R_h = exp(u_w/462T) \qquad (3\text{-}7)$$

where T = absolute temperature (t+273)

Mechanical behaviour of the structure

The *Porous Elastic Model* implies a logarithmic relation between the void ratio *e* and the average effective stress *p* according to Equation 3-8 (same as Equation 2-25).

$\Delta e = \kappa\Delta\ln p$ (3-8)

κ = 0.165

v = 0.4

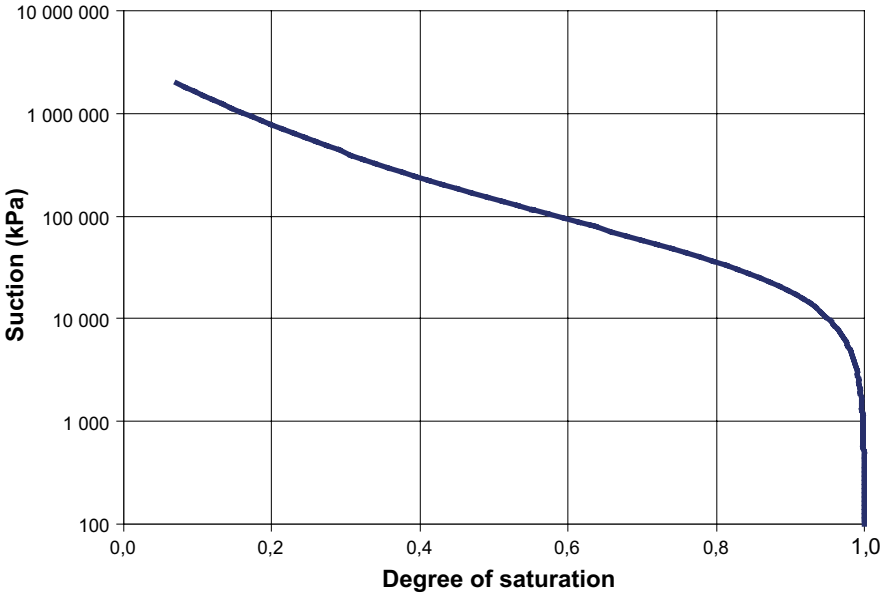

Figure 3-17. *The water retention curve used for FEBEX bentonite in BM 1.2.*

The following data was used for the *Drucker Prager Plasticity* model

$\beta = 17°$

$d = 100$ kPa

$\psi = 2°$

Table 3-10. Yield function.

q (kPa)	ε_{pl}
1	0
50	0.005
100	0.02
150	0.04
200	0.1

Thermal expansion

The volume change caused by the thermal expansion of water α_w and particles α_s are modelled with the following parameter values:

$\alpha_w = 3.0 \times 10^{-4}$

$\alpha_s = 0$

Mechanical behaviour of the separate phases

The water and the particles are mechanically modelled as separate phases with linear elastic behaviour. The pore air is not mechanically modelled. The following values have been used for the *properties of the water and solid phases*:

$B_w = 2.1 \times 10^6$ kPa (bulk modulus of water)

$B_s = 2.1 \times 10^8$ kPa (bulk modulus of solids)

$\rho_w = 1000$ kg/m^3 (density of water)

$\rho_s = 2750$ kg/m^3 (density of solids)

Mechanical coupling between the structure and the pore water

The mechanical behaviour is modelled to be governed by the effective stress theory and a procedure called moisture swelling.

Effective stress theory

The effective stress concept according to Bishop is used for modelling the mechanical behaviour of the water-unsaturated buffer material:

$$s_e = (s - u_a) + \chi(u_a - u_w) \qquad (3\text{-}9)$$

with

u_a = 0 (no account is taken to the pressure of enclosed air)

$\chi = S_r$

Moisture swelling

The shortcomings of the effective stress theory can be compensated in Abaqus by a correction called "*moisture swelling*". This procedure changes the volumetric strain ε_v by adding a strain that can be made a function of the degree of saturation S_r (see Chapter 4).

A similar evaluation of the data for this procedure has been done as for BM 1.1. Figure 3-18 shows the derived relation.

Required parameters

The required input parameters and initial conditions are the same as for BM 1.1.1 (see Section 2.4.2).

Calibration tests

Most of the required parameters were determined with direct measurements in the laboratory. Four different calibration calculations were performed for evaluating the additional parameters:

- Swelling pressure tests.
- Swelling tests.
- Water uptake tests.
- Temperature gradient tests.

These tests are described in the report about the modelling of the FEBEX test (Börgesson et al. 2005) and will not be dealt with here.

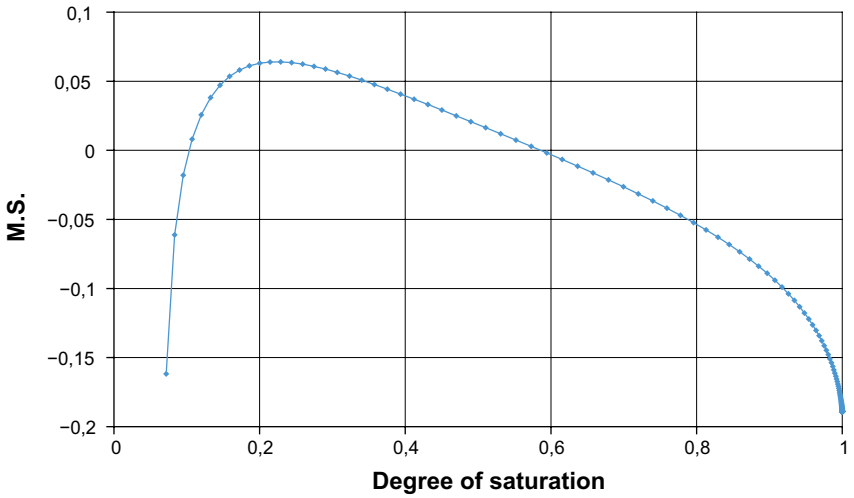

Figure 3-18. *Derived relation for the Moisture swelling procedure of the bentonite in BM 1.2.*

3.4.3 Finite element model

Element mesh

Only the bentonite sample and the boundaries to the cell were modelled. The element mesh consists of about 120 axial symmetric elements. The mesh is shown in Figure 3-19 together with the measuring points.

Boundary conditions

Thermal

The temperature of all points is defined according to the measurements. For cell I40 (isothermal test) the temperature was constant 24 °C during the entire test. For cell GT40 (thermal gradient test) the temperature was in phase 1 stepwise increased from 24 °C to the final temperature (Figure 3-20) during 30 hours and for phase 2 kept constant at the defined temperatures shown in Figure 3-20.

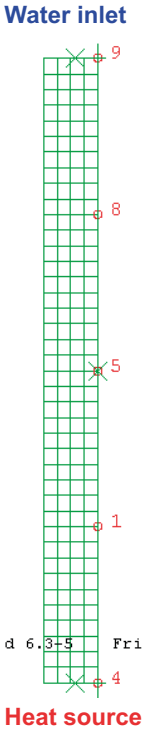

Figure 3-19. *Element mesh of BM 1.2. Axial symmetry around the left boundary. The location of measuring points are ring marked. RH is measured in points 1, 5, and 8 while temperature is measured in all 5 points.*

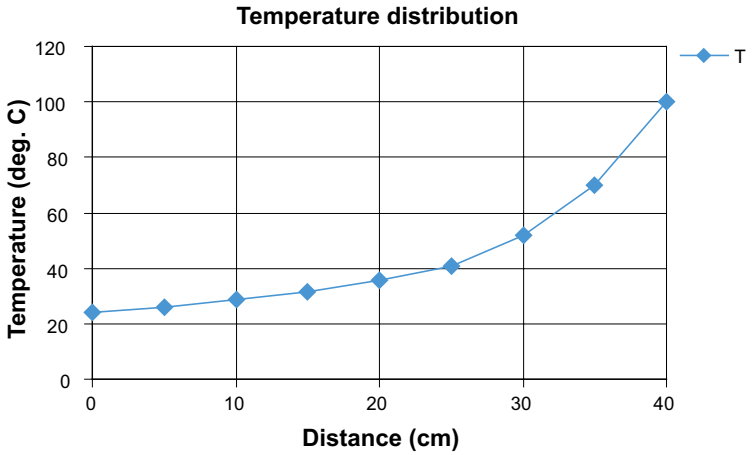

Figure 3-20. *Defined temperature as a function of the distance from the top of the sample for phase two of cell GT40.*

Hydraulic

The hydraulic history is divided into two phases:

- In phase 1 (first 30 hours) all boundaries are isolated.
- In phase 2 constant water pressure 1.2 MPa is kept in the top, while the other boundaries are isolated.

Mechanical

The mechanical boundary conditions are:

- Axial symmetry at the left boundary.
- Combined contact and friction elements at the other boundaries.

The contact elements allow the sample to release the contact with the boundary in case of tensile total stress that may occur during local shrinkage. The contact surface can slip during compression and has friction and cohesion defined by total stress.

$\phi = 5°$

$c = 50$ kPa

Initial conditions

The density and water ratio of the samples were the same in the two cells:

$\rho_\delta = 1\,650$ kg/m^3

$w = 13.4$ %

which yield the following input data:

$e_0 = 0.67$

$S_{r0} = 0.55$

$u_0 = -117\,000$ kPa

$p_0 = 64\,350$ kPa

$T_0 = 24$ °C

3.4.4 Calculation sequence

The modeling simulated the actual time history, with two phases. No thermal calculation was thus done. The motivation for this is that the thermal properties and the power applied to the bottom were not sufficiently well known.

Phase 1: The temperature of cell GT40 was increased in the bottom in steps from the initial value 24 °C to 100 °C in 30 days. The measured temperature distribution through the sample was followed and applied as input data.

Phase 2: Constant water pressure 1.2 MPa was applied and kept in the top boundary. The calculation was extended until full water saturation was reached.

3.4.5 Results

Cell I40 (isothermal test)

The results of the calculations for the isothermal test in cell I40 and comparison with measurements are shown in Figure 3-21and Figure 3-22.

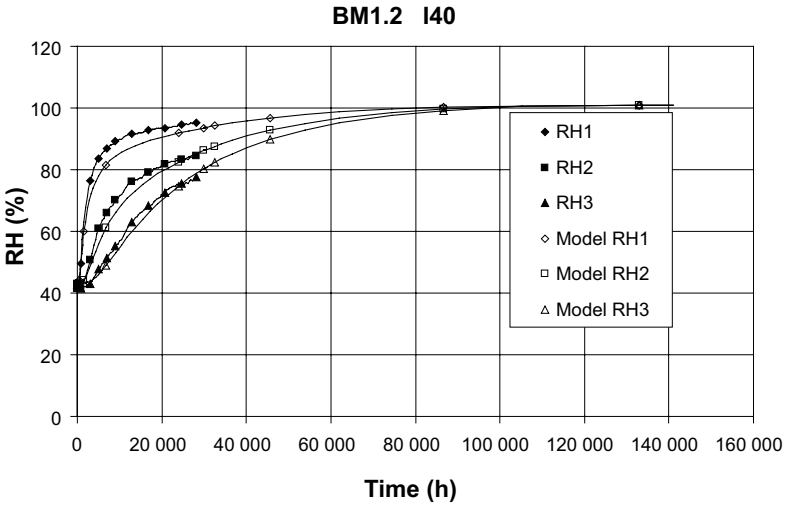

Figure 3-21. *Modelled and measured relative humidity in cell I40.*

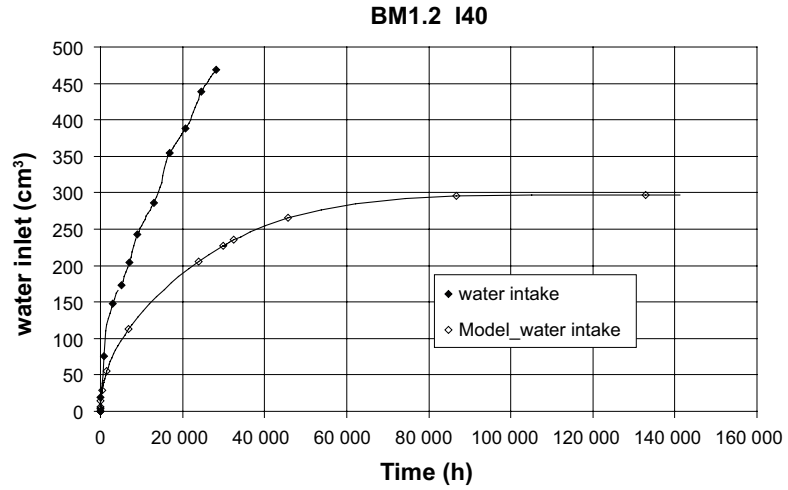

Figure 3-22. *Modelled and measured water inflow in cell I40.*

Relative humidity

Relative humidity is plotted as history plots in Figure 3-21. The agreement is very good.

Water inflow

The measured and modeled water inflow is shown in Figure 3-22. The agreement is poor, since the modeled water inflow is about half the measured. However, the figure also shows that the measured water inflow is much higher than the expected water inflow at full saturation, which shows that there must be leakage in the system.

Cell GT40 (thermal gradient test)

The results of the calculations for the thermal gradient test in cell GT40 and comparison with measurements are shown in Figure 3-23 to Figure 3-25.

Temperature

Figure 3-23 shows the measured and the applied temperature in the measuring points. The main difference is caused by the small deviation from the linear relation. The seasonal variation is not included in the model.

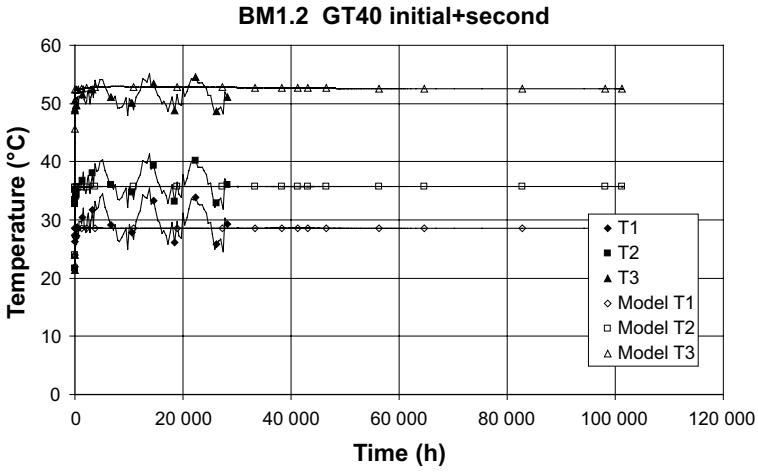

Figure 3-23. *Applied and measured temperature distribution in cell GT40 in the three measuring points.*

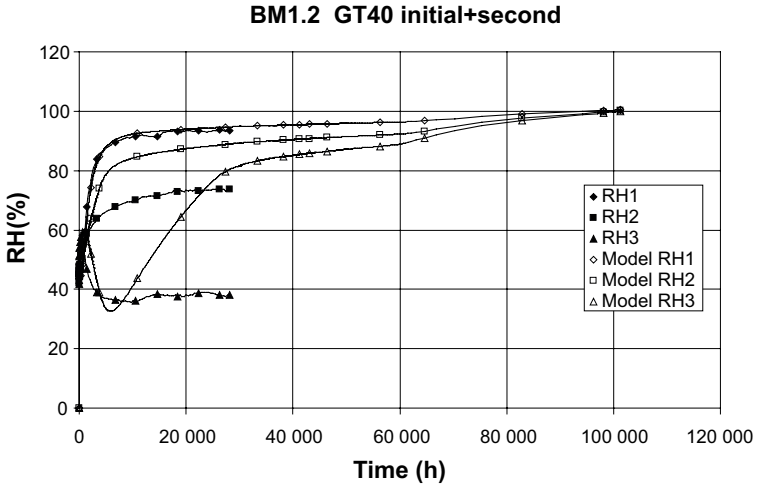

Figure 3-24. *Modeled and measured relative humidity in cell GT40.*

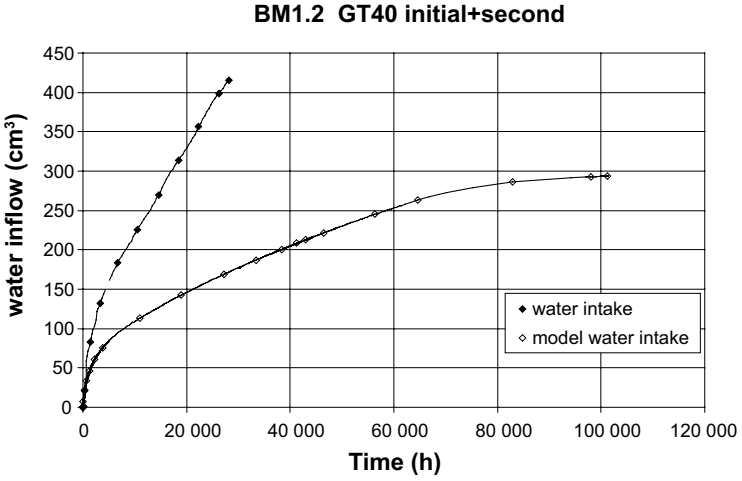

Figure 3-25. *Modelled and measured water inflow in cell GT40.*

Relative humidity

The measured and modelled relative humidity is plotted as history plots in Figure 3-24. The agreement is good for one point (RH1) but very poor for the other points since the measured steady state condition that seems to evolve rather soon is not modeled.

Water inflow

The measured and modeled water inflow is shown in Figure 3-25. The agreement is poor, since the modeled water inflow is less than half the measured. However, the figure also shows that in agreement with cell GT40 the measured water inflow is much higher than the expected water inflow at full saturation, which shows that there must be leakage in this cell as well.

Additional results and analyses

Influence of the thermal vapour flow diffusivity

The modeling results of GT40 stem from a model with the thermal vapour flow diffusivity $D_{Tvb} = 0.7 \times 10^{-11}$ m^2/s,K, which is higher than the originally derived value for the FEBEX test where $D_{Tvb} = 0.4 \times 10^{-11}$ m^2/s,K was used. The value was increased in order to see if the steady state could be achieved in the modelling. The influence of this value is illustrated in Figure 3-26, which shows the modelled RH for both these values. There is an obvious difference in drying on the hot side, but one cannot conclude that the higher diffusivity value is better since the difference from the measured results is too large and there are question marks about potential leakage in the cell.

Bentonite displacements

The mechanical model also yields the deformations of the bentonite sample. Figure 3-27 shows that there just as in BM 1.1.1 is an open slot between the bentonite sample and the steel tube. After 7 000 hours the slot starts 8 cm from the bottom and is 0.5 mm wide at the bottom.

3.4.6 Conclusions and comments

Just as for BM 1.1.1, it is not easy to draw conclusions from the results. Some modeling results agree rather well with measurements, while others disagree substantially.

For cell I40 the very fine agreement between modeled and measured RH seems to verify the water transport model. The impossible high measured inflow shows that there is a leakage in the cell or in the connected pressurizing equipment.

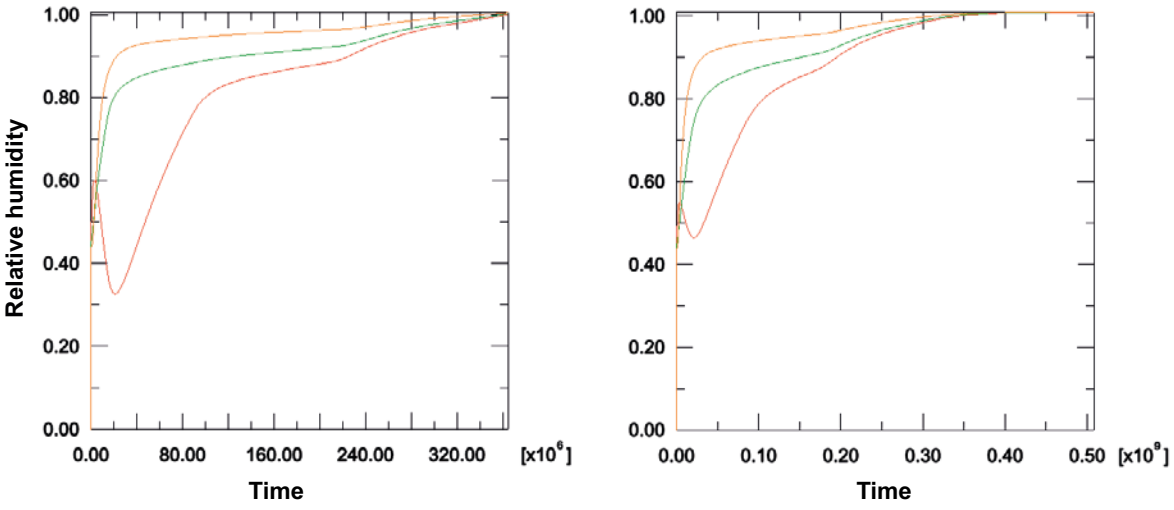

Figure 3-26. *Illustration of the influence of the thermal vapour flow diffusivity on the RH development. Left diagram: DTvb = 0.7×10^{-11} used. Right diagram: DTvb = 0.4×10^{-11} used.*

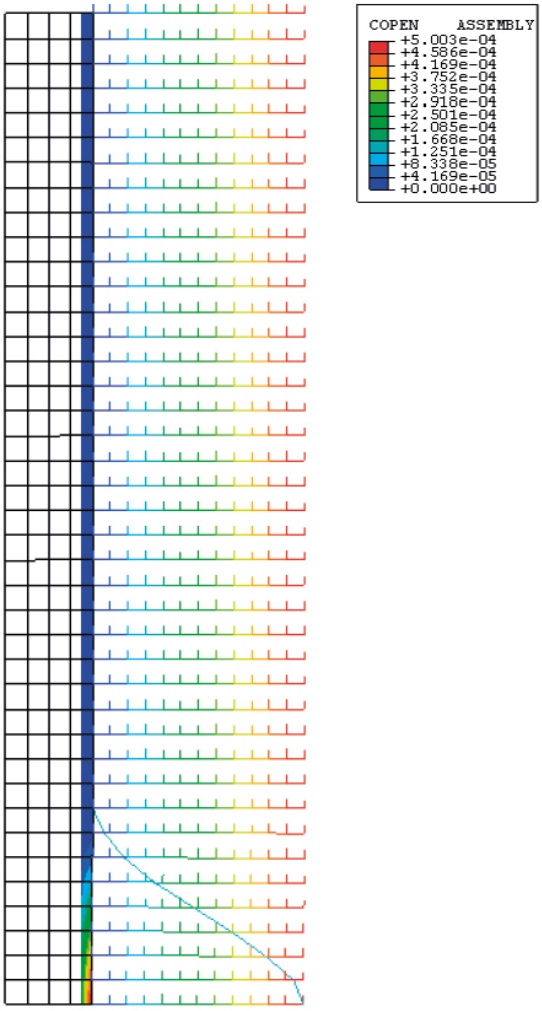

Figure 3-27. *Modelled radial displacements (m) of the contact element after 2.54×10^7 s (about 7000 hours). The light blue curve represents the gap between the sample and the tube and is scaled along the x-axis according to the colours in the labels. The curve shows that the sample and the tube have lost contact about 8 cm from the bottom and that the gap is 0.5 mm at the bottom.*

Cell GT40 is more difficult to analyze. The measured inflow is obviously erroneous for this cell too. The strong deviation between measured and modeled RH can either be caused by a shortcoming in the model, erroneous measuring results or leakage of vapour in the cell. Excavation and recalibration can answer if the measurements are correct but a possible leakage is probably difficult to detect. However, the model has been calibrated against other laboratory tests and yielded reasonable results for both FEBEX mock-up test and FEBEX field test so it is difficult to understand why this test cannot be modeled. The most probable explanation seems to be vapour leakage.

4 BM 1.1.3 – Heating test performed by UPC

4.1 General

Benchmark 1.1.3 is based on a heating test with no water infiltration performed in the UPC laboratory. The material tested was compacted FEBEX bentonite. The test includes a temperature gradient applied along two specimens with constant water content and no mechanical confinement.

4.2 Specifications

4.2.1 Description of the UPC test

General

Conceptually, the test is depicted in Figure 4-1. Two cylindrical samples of compacted FEBEX bentonite are subjected to a prescribed heat flow from one end. The temperature is kept constant at the other end. The two specimens are symmetrically placed with respect to the heater.

The following parameters are measured:

- Temperatures at various points throughout the test.
- Water content at the end of the test.
- Specimen diameter at the end of the test.

Apparatus and monitoring system

The apparatus used for performing the test is depicted in Figure 4-2. The two cylindrical specimens (38 mm diameter, 76 mm height) are placed vertically in the apparatus, with the heater located between them. A latex membrane that allows deformation and keeps constant the overall water content and a layer (5.5 cm thick) of heat insulating material (composed of deformable foam, expanded polystyrene and glass fibre) surround the specimen. The ensemble is contained in a perspex tube. It has been determined that the diffusion water loss from the specimens during the test was less than 0.1 g/day. From the backanalysis of experiments, a value of thermal conductivity of the insulating layer of 0.039 W/mK has been estimated.

The heater is a copper cylinder (38 mm diameter, 50 mm height) with five small electrical resistances inside. The resistances are connected to an adjustable source of direct current that allows the control of input power from 0 to 5 W. At the cool ends, a constant temperature is maintained by flowing water through a stainless steel cap in contact with the soil. A temperature regulation system keeps the temperature of the contact between the cap and the soil practically constant, with variations smaller than 0.5 °C. In order to ensure a good contact between the caps and the samples, a light stress (about 0.05 MPa) was applied on top of the test ensemble.

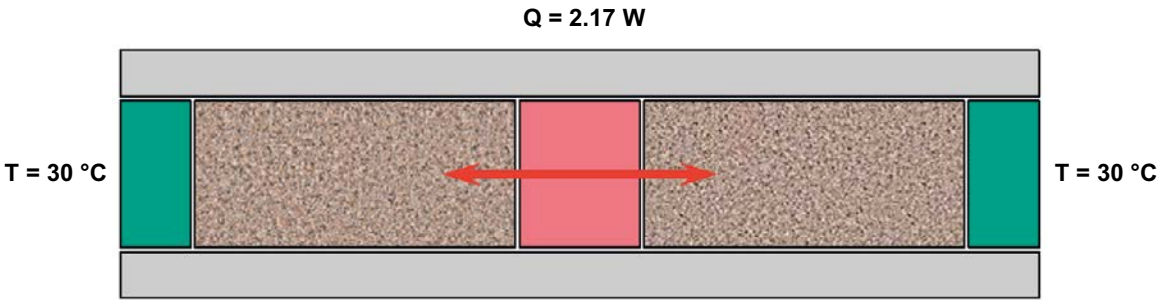

Figure 4-1. *Conceptual scheme of the UPC heating test.*

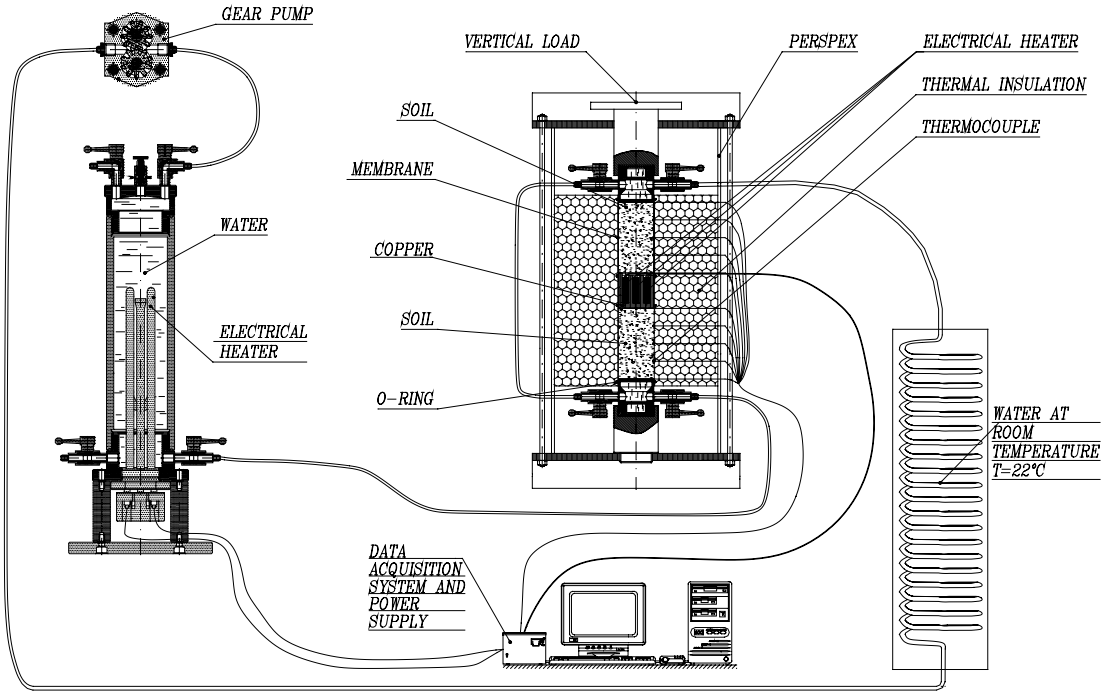

Figure 4-2. *Scheme of the UPC experimental device.*

Only temperatures were measured during the test. Temperatures measurements were concentrated in one of the specimens; three measurements were made in the inside of the sample and two more on the hot and cool ends of the specimen. In the second sample, only one inside temperature measurement was made in the centre of the specimen that confirmed the symmetry of the temperature distribution.

Material

The FEBEX bentonite has been used in the experiments. Information on the characteristics and properties of this bentonite has already been given in the specifications of benchmark THM 1.2. The bentonite has been compacted at a dry density of 1.63 g/cm^3 and with a water content of 15.33 % (degree of saturation of 0.63).

Protocol of the experiments

A constant power of 2.17 W was supplied by the heater during 7 days whereas at the opposite ends of the specimens a temperature of 30 °C was maintained. Initial temperature of the bentonite was 22 °C.

At the end of the 7 days, the heaters were switched off, the apparatus dismantled and the diameter and water content at different points of the specimens determined. The diameter of the specimen was measured at 7 sections in each specimen with an accuracy of 0.01 mm. To obtain the distribution of water content, each specimen was cut into six small cylinders, and the water content of each cylinder was determined.

Test results

The data obtained during the tests are collected in a file *UPC heating test. Xls* made available for the modellers.

4.2.2 Requested results

The following information is requested:

a) Main features of the analyses performed.

b) Results of the analyses and comparison with experimental results.

Main features of the analyses performed

This basic description should contain summarised information on:

- Geometry adopted for the analysis.
- Type of analysis (e.g. 1-D, 2-D, axisymmetric...).
- Element types used.
- Constitutive laws adopted (thermal, hydraulic, mechanical).
- Constitutive parameters used and procedure used in their determination or estimation.
- Boundary conditions (thermal, hydraulic, mechanical).
- Initial conditions (thermal, hydraulic, mechanical).
- Hypothesis adopted for gas pressure and gas flow.
- Any other features that are deemed important in the analysis.

Special attention should be given to the information involved in water transfer (vapour diffusion, including tortuosity if used, and permeability and hydraulic conductivity) and in thermal diffusion (thermal conductivity and specific heat).

Results of the analyses and comparison with experimental results

The following analysis results should be provided graphically together with comparison with observed data. The Excel files of the submitted graphs should also be made available.

Temperatures

- Evolution of temperatures vs. time at x= 0 mm, 20 mm, 38 mm, 60 mm, 76 mm throughout the test (coordinate x is the distance to the heater).
- Distributions of temperatures at the following times: 0.292 hours, 1.446 hours, 3.161 hours, 100.609 hours.

Water content

- Distribution of water content along the specimen at the end of the test.

Sample diameter

- Distribution of diameter increment along the specimen at the end of the test.

4.3 Modelling results with Code Bright

4.3.1 Introduction

Section 4.3 presents the benchmark calculations made with Code_Bright on BM system 1.1.3. The task is described in the specifications of Section 4.2.

4.3.2 Model description

Geometry

The experiment was modeled as a 2D axis-symmetric THM problem with a symmetry line through the mid-section of the heater and with constant atmospheric gas pressure. The modeling work was performed with the finite element program Code_Bright, version 2.2 (CIMNE 2000). The bentonite sample, the heater and the insulation was modeled explicitly. This was found necessary to capture the temperature development. No attempt to include any further details of the experiment was made.

Boundary and initial conditions

The applied thermal and mechanical boundary conditions are shown in Figure 4-3. A no liquid-flow condition was prescribed on all boundaries. The temperature at the circumferential boundary of the insulation was kept constant at 22 °C throughout the calculation. The cold side of the bentonite sample was ramped from 22 to 30 °C during the first 0.15 h of the test, and was thereafter kept constant (Figure 4-4). The heat load, corresponding to half the value of the actual heat load, was applied as a point source in the interior of the heater.

The movement of the bentonite was restrained by a roller boundary at the hot side. This boundary was extended at the same level through the insulation. This approach was chosen in order to minimize the mechanical interference of the heater and the insulation, which were modeled with a low stiffness (see below). The axial confinement was modeled as a 0.05 MPa compressive boundary stress, which was ramped from zero during one hour prior to the actual start of the test (Figure 4-4).

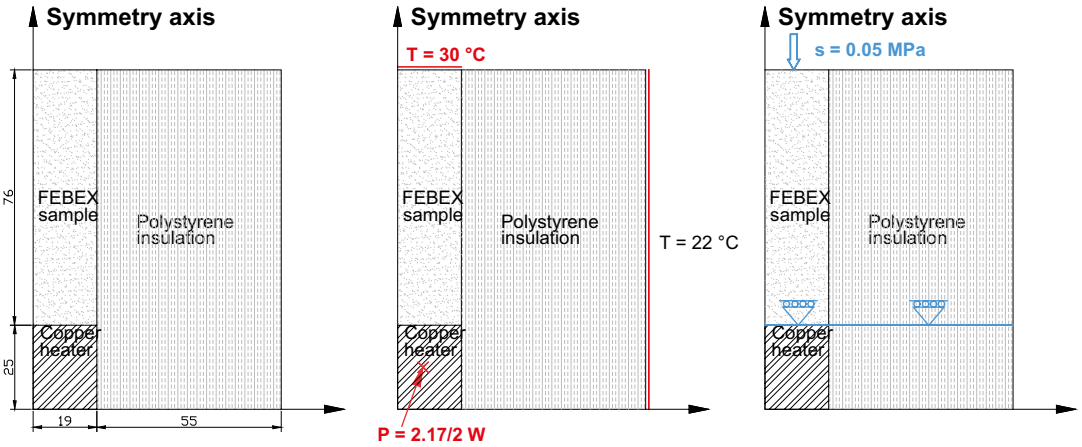

Figure 4-3. Model geometry (left), thermal (middle) and mechanical (right) boundary conditions.

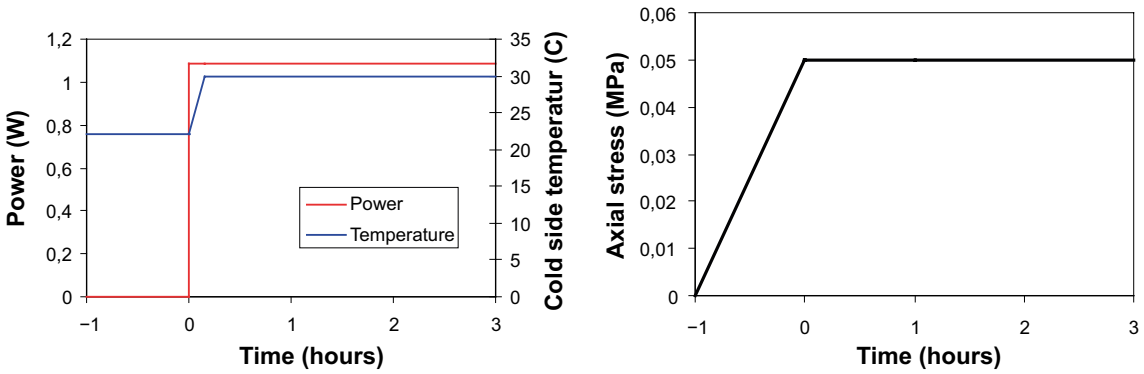

Figure 4-4. Ramping of thermal (left) and mechanical (right) boundary conditions.

Table 4-1. Initial model parameters for the different materials.

	FEBEX Bentonite	Copper heater	Polystyrene insulation	
Porosity, φ_{ini}	0.396	0.01	0.9	–
Saturation level, S_{ini}	63.1	~100	~ 0	%
Temperature, T_{ini}	22	22	22	°C
Liquid pressure, $P_{l,ini}$	−103	−103	−103	MPa
Init. stresses, σ_x, σ_y, σ_z	(0,0,0)	(0,0,0)	(0,0,0)	MPa

The modeled bentonite sample was defined in accordance with the specifications given for the present benchmark and relevant initial parameters are found in Table 4-1. The bentonite had been compacted to a dry density of 1.63 g/cm^3 (corresponding to a void ratio of 0.656) and with a water content of 15.33 %.

Constitutive laws and material data

Solid phase properties and transport coefficients

Solid phase densities and specific heat values are shown in Table 4-2. The FEBEX solid phase density was taken from CIEMAT (2005), whereas the specific heat value was taken from models with MX-80 (Åkesson 2006). Values for copper and polystyrene were taken from standard tables.

Heat transport is described by Fourier's law:

$$\vec{i}_c = -\lambda \cdot \nabla T \tag{4-1}$$

Values of heat conductivities are listed for the different materials in Table 4-2. The saturation-dependent function for FEBEX was taken from CIEMAT (2005). The value for copper was taken from a standard table, whereas the value for the insulation was taken from the specifications for benchmark 1.3 (UPC 2006).

The hydrodynamic transport is described by Darcy's law:

$$\vec{q} = -\frac{k \cdot k_r}{\mu} \nabla P \tag{4-2}$$

The permeability of the bentonite sample is also modeled as porosity dependent and following Kozeny's law:

$$k(\phi) = k_0 \frac{\phi^3}{(1-\phi)^2} \frac{(1-\phi_0)^2}{\phi_0{}^3} \tag{4-3}$$

The vapor diffusion follows Fick's law:

$$\vec{i} = -\phi \cdot \tau \cdot D \cdot (1 - S_r) \cdot \rho_g \cdot \nabla \omega_g^w \tag{4-4}$$

in which the diffusion coefficient is calculated as:

$$D = 5.9 \cdot 10^{-6} \frac{(273.15 + T)^{2.3}}{P_g} \tag{4-5}$$

Values of intrinsic permeability, liquid relative permeability relations and vapor diffusion tortuosity values are listed in Table 4-2. The FEBEX bentonite intrinsic permeability value for the reference porosity was taken from Sánchez (2004). The FEBEX bentonite vapor diffusion tortuosity value was taken from the Benchmark 1.2 specifications (CIEMAT 2005). Parameter values for the adjacent materials have been chosen in order to eliminate liquid flow and vapor diffusion in these materials.

Table 4-2. Solid phase properties and transport parameters for the materials.

	FEBEX Bentonite	Copper heater	Polystyrene insulation	
Solid phase density, ρ_s	2.70	8.93	0.1	g/cm^3
Specific heat	0.8	0.39	1.3	J/gK
Heat conductivity, λ	$0.47^{(1-S)}1.15^{S}$	390	0.039	W/mK
Intrinsic permeability, k	1.9×10^{-21}	10^{-30}	10^{-30}	m^2
Liquid rel. permeability, k_r	S_r^3	S_r^3	S_r^3	–
Tortuosity for vapor diffusion, τ	0.8	10^{-25}	10^{-25}	–

Retention properties

The porosity-dependent expression for the retention properties, provided in Code_Bright, was used to describe the bentonite sample:

$$S_r(\phi) = \left(1+\left(\frac{s}{P_o(\phi)}\right)^{\frac{1}{1-\lambda(\phi)}}\right)^{-\lambda(\phi)} \qquad \begin{aligned} P_0(\phi) &= 58\cdot\exp\left(15\cdot(\phi_0-\phi)\right) \\ \lambda(\phi) &= 0.37\cdot\exp\left(2\cdot(\phi_0-\phi)\right) \end{aligned} \tag{4-6}$$

The parameter values were derived by choosing three reference points (Figure 4-5, left). These points represent the initial condition and the approximate end points after the dismantling of the experiment. A set of relations were derived from these points for different void ratios (Figure 4-5, right), under the assumption that suction is constant for a given water content. The parameters in Equation 4-6 were thereafter calibrated in order to get a close match between experimental data and the model.

The saturation limit parameters in the standard retention law were utilized to describe the adjacent materials (Equation 4-7). Values were chosen to keep the degree of saturation of the heater and the insulation close to 100 and 0 %, respectively (Table 4-3):

$$\frac{S_r - S_{rl}}{S_{ls} - S_{rl}} = \left(1+\left(\frac{s}{P_o}\right)^{\frac{1}{1-\lambda}}\right)^{-\lambda} \tag{4-7}$$

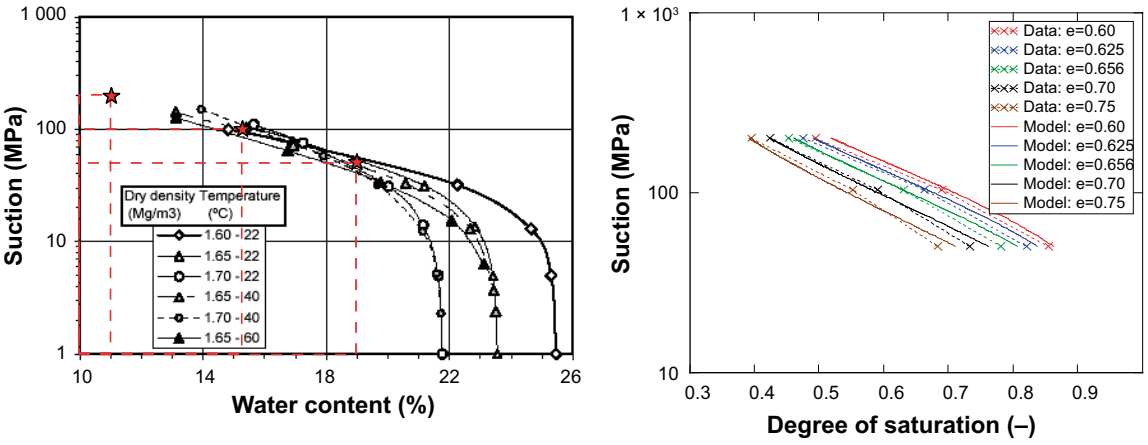

Figure 4-5. *Retention data for FEBEX bentonite (Villar et al. 2005b) and chosen reference points (left), adoption of porosity dependent retention curve (right).*

Table 4-3. Retention parameters for the heater and the insulation.

	Copper heater	Polystyrene insulation	
P_0	1000	0.1	MPa
λ	0.3	0.3	–
S_{rl}	0.99	0	–
S_{ls}	1	0.01	–

Mechanical parameters

The bentonite sample was mechanically modeled with the thermo-elastoplastic (TEP) constitutive laws implemented in Code_Bright. Given the low stress level and modest moisture redistribution, only elastic strains were allowed. The elastic volumetric strain ($d\varepsilon_v^e$) is according to BBM calculated as:

$$d\varepsilon_v^e = \frac{\kappa_i(s)}{1+e}\frac{dp'}{p'} + \frac{\kappa_s(p',s)}{1+e}\frac{ds}{s+0.1} + (\alpha_0 + \Delta T\alpha_2)dT \tag{4-8}$$

The parameters used are shown in Table 4-4. The approach used for the mechanical stiffness (κ_i, K_{min}), Poisson's ratio (ν) and the thermal expansion (α_0, α_2) have earlier been used for MX-80 (Åkesson 2006), but are actually of minor importance in this type of experiment. The controlling process in this case is the swelling and shrinkage process which is described by κ_s. Parameter values for this process were derived from experimental data (see Figure 4-6). The following expression was used to calibrate the κ_s parameters:

$$e(s_1) = e_0 - \int_{s_0}^{s_1} \frac{\kappa_{s0}}{2} \cdot \exp(\alpha_{ss} \cdot s) \cdot \frac{ds}{s+0.1} \tag{4-9}$$

It should be observed that the denominator value of 2 is a consequence of the uniaxial strain conditions and is given by $3(1-\nu)/(1+\nu)$, which is the same as the ratio between the oedometer- and the bulk moduli.

Table 4-4. TEP parameters for the FEBEX bentonite.

$\kappa_i = 0.25 \cdot [1 - 0.01 \cdot s]$ K_{min}=10 MPa	$\kappa_s(s) = 0.3 \cdot e^{-0.01s}$	$\nu = 0.2$	$\alpha_0 = 3 \times 10^{-6}$; $\alpha_2 = 0$

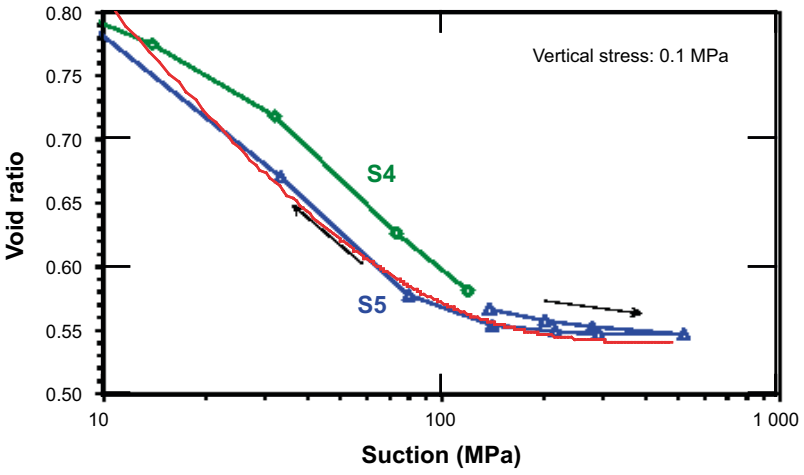

Figure 4-6. *Swelling data for FEBEX bentonite (from Sánchez 2004). Red line corresponds to calibrated BBM model.*

The materials for the heater and the insulation was modeled as linear elastic with a low Young modulus (E = 5 MPa) and a high Poisson's ratio (ν = 0.4999). No thermal expansion was applied. This approach was chosen for minimizing the mechanical interference with the bentonite sample and at the same time to ensure numerical stability.

4.3.3 Results

Experimental water contents and diameter increments are compared with model values for the time of dismantling (t = 168 h) in Figure 4-7. A comparison between the temperature evolution in the experiment and in the model at the five thermocouple positions is also shown. Temperature scan-lines for points in time requested in the benchmark specification are shown in Figure 4-8. Finally, the long-term development of the degree of saturation at the hot and cold ends is shown in Figure 4-9.

All model data for temperature, porosity and degree of saturation were taken from the model along the symmetry axis, whereas the radial displacements were taken along the circumferential boundary.

4.3.4 Concluding remarks

The model appears to capture the final distributions of water content and diameter increment as well as the development of temperature satisfactorily (Figure 4-7). The model also indicates that the moisture redistribution had not reached steady-state at the time of dismantling (Figure 4-9).

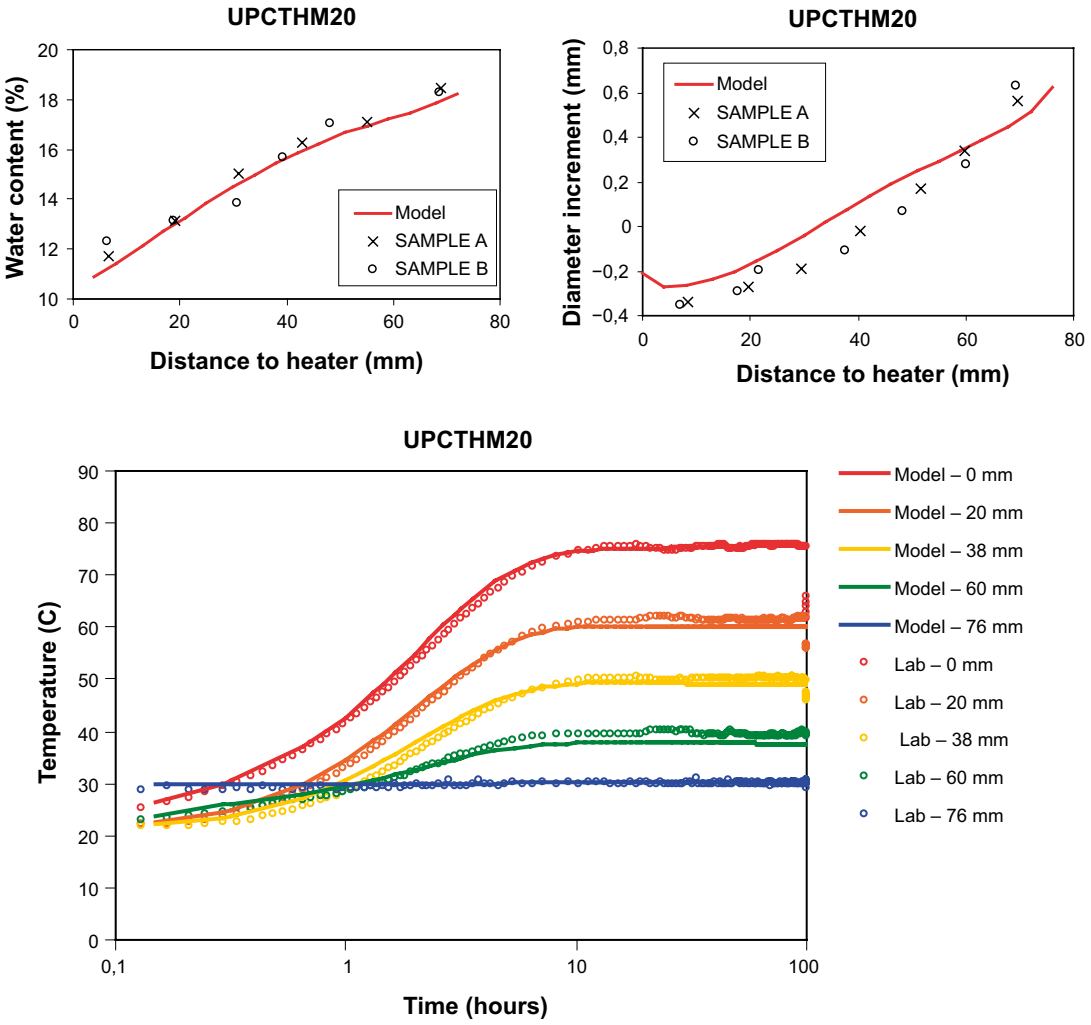

Figure 4-7. *Comparison of experimental and model results: Water content at t = 168 h (upper left); Diameter increment at t = 168 h (upper right); and development of temperature during the first 100 hours at five different thermocouple positions (lower).*

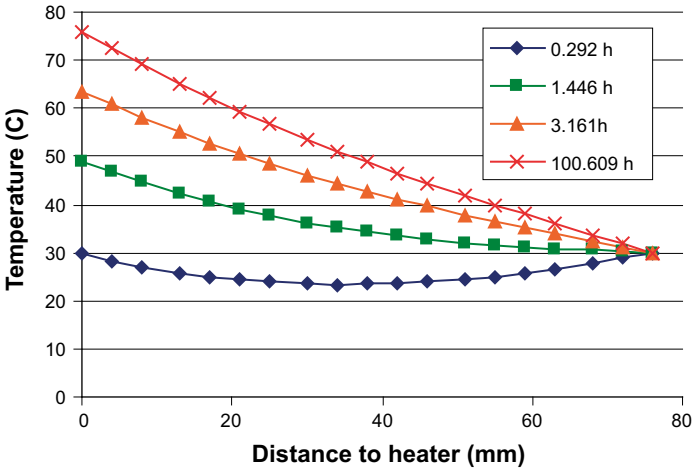

Figure 4-8. *Scan-lines of temperature at different points in time.*

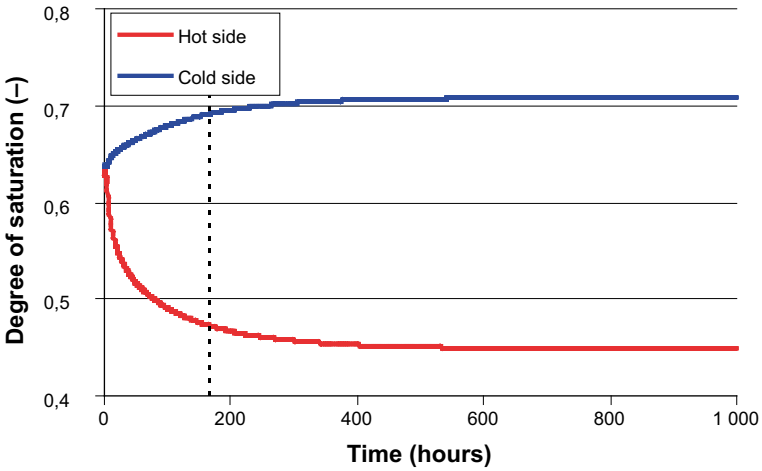

Figure 4-9. *Long-term trends of degree of saturation at hot and cold end. The time of dismantling (t = 168 h) is annotated.*

The model was made in accordance with the material specifications. In addition, efforts were made to follow reported data for FEBEX bentonite with respect to retention- and swelling properties in a physically consistent way. The TEP constitutive laws are apparently well suited for this type of problem, with a low and static stress level and therefore effectively independent of the mechanical stiffness of the material. The porosity dependence of the retention curve implemented in the code also appears to be adequate for unconfined conditions with modest moisture redistribution.

The main difficulty of this work was the absence of friction elements in the code. The stiffness of the adjacent materials will inevitably interfere mechanically with the bentonite sample. This effect can be noticed in the diameter increments shown in Figure 4-7. The measures taken to minimize this effect, the lower roller boundary in Figure 4-3 and the low stiffness, had some effect but did not eliminate the difficulty. The mechanical analysis would be significantly simplified if the sample were modeled without account of the interaction with the adjacent materials. This would on the other hand increase the complexity of the thermal problem.

4.4 Modelling results with Abaqus

4.4.1 General

Benchmark 1.1.3 is a laboratory test that has been performed on FEBEX bentonite by Xavier Pintado at UPC (Pintado and Lloret 2006). Specifications of the task are given in Section 4.2 and an Excel file with measurement results has been provided.

4.4.2 Test description

The test and the requested results are described in Section 4.2.

4.4.3 Material model

FEBEX bentonite was used in the test and the material model is identical to the material model of FEBEX bentonite described in Section 3.4. Some attempts to improve the results by changing the parameters in the material model have been done.

4.4.4 Finite element model

The element mesh consists of about 2200 axial symmetric elements with four different properties. The mesh is shown in Figure 4-10.

4.4.5 Boundary conditions

A fully coupled thermo-hydro-mechanical calculation was done but the insulation, the cooler and the heater were only included in the thermal part.

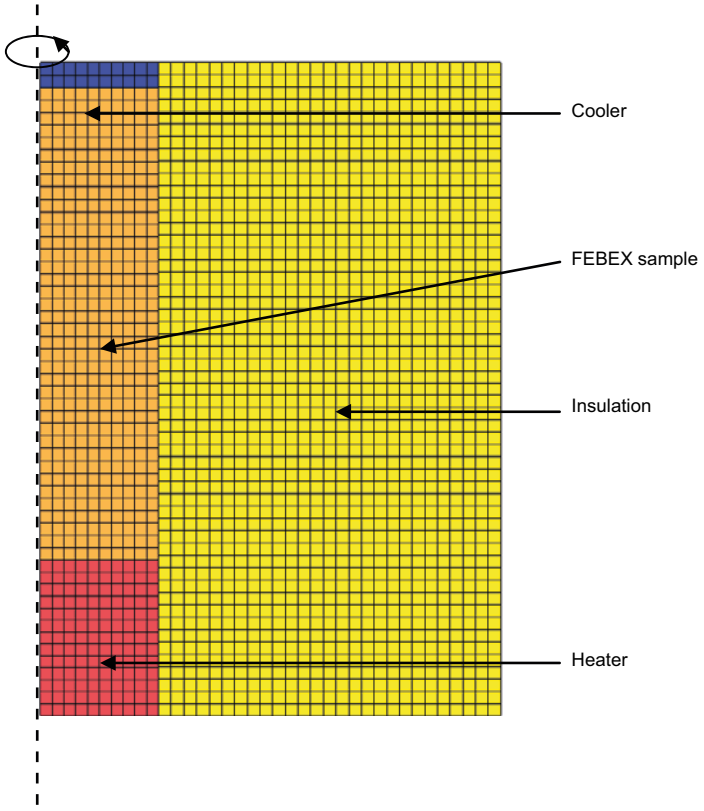

Figure 4-10. *Element mesh of BM 1.1.3. Rotational symmetry around left boundary.*

Thermal boundary conditions

A constant temperature of 30 °C was applied in the cooler.

A constant power of 2.17 W was applied in the heater.

A heat transfer coefficient of c=10 W/m^2,K was applied on the upper and right boundaries together with a constant temperature of 22 °C.

Symmetry conditions (no flow boundaries) were applied on the left and bottom boundaries.

Hydraulic boundary conditions

No flow conditions were applied on all FEBEX sample boundaries.

Mechanical boundary conditions

The FEBEX sample was mechanically free to move in radial and axial direction except for the symmetry plane that was constrained radially.

4.4.6 Initial conditions

The initial dry density and water ratio of the samples were

ρ_δ = 1 630 kg/m^3

w = 15.3 %

which yield the following input data using the density of particles ρ_δ = 2 730 kg/m^3:

Void ratio: e_0 = 0.67

Degree of water saturation: S_{r0} =0.62

Pore water pressure: u_0 = −81 000 kPa

Average effective stress: p_0 = 51 030 kPa

The initial temperature was T_0 = 22 °C

4.4.7 Calculation sequence

The calculation was done with a staggered coupling between temperature calculations and hydro-mechanical calculations in the following way:

1. A temperature calculation is performed with the initial temperature 22 °C in the entire mesh and 30 °C in the cooler. The initial values of void ratio and degree of saturation are used throughout the calculation.
2. The temperature evolution is used for a hydro-mechanical calculation. In this calculation only the mesh of the bentonite is used.
3. The results from the hydro-mechanical calculation (evolution of void ratio and degree of saturation) are used in a new temperature calculation
4. Steps 2 and 3 are repeated until no change in solutions appears. Two iterations were enough since the influence of the changes in void ratio and degree of saturation on the temperature evolution is small.

4.4.8 Results

Requested results

Figure 4-11 to Figure 4-14 show the requested results together with measured. Figure 4-11 shows the temperature evolution in the measuring points. The measured temperature is slightly higher than the calculated. The reason is not clear but the difference could be explained by that a slightly too high

thermal conductivity of the insulation is used. Figure 4-12 shows the temperature paths at different times. The modeled temperature in the centre of the sample is slightly underestimated.

Figure 4-13 shows the distribution of the water ratio along the sample. A comparison between measured and calculated values shows a fair agreement although the shapes of the curves differ slightly. Figure 4-14 shows the change in diameter. The comparison shows that the calculated change in diameter is much smaller than the measured change (a factor of at least 5).

Other results

The calculation was run longer than to the end of the test in order to study when steady state was reached. Figure 4-15 shows the evolution of water ratio and diameter of the sample until 1 000 hours. The results show that steady state is far away and that both the redistribution of water ratio and sample diameter continued when the test was terminated.

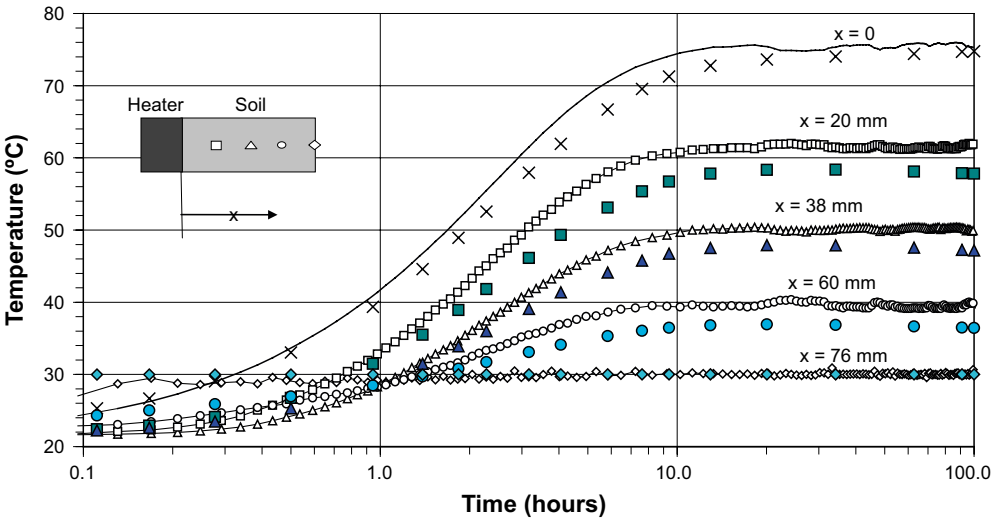

Figure 4-11. *Measured and modelled temperature evolution. Crosses and filled symbols are modelling results.*

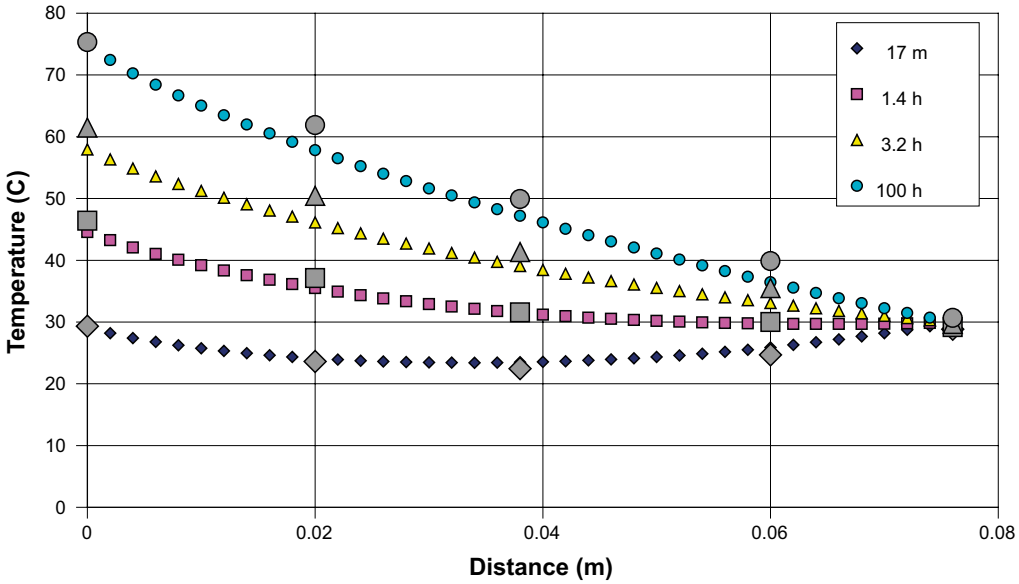

Figure 4-12. *Measured and modelled temperature paths at different times. Large grey symbols are measured results.*

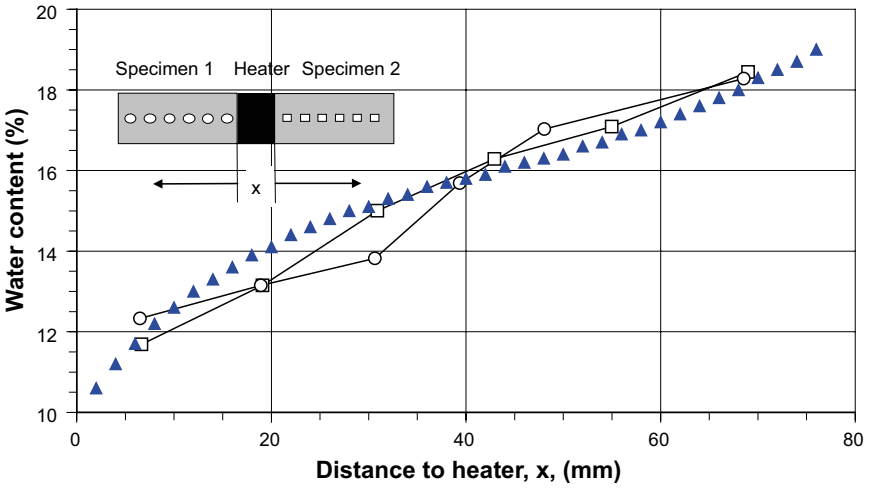

Figure 4-13. *Measured and modelled paths of water ratio at end of test. Blue filled symbols are modelling results.*

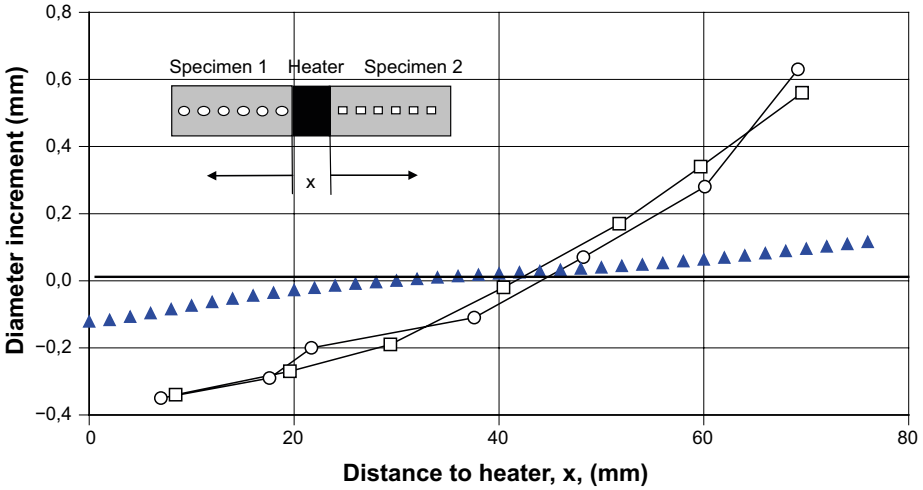

Figure 4-14. *Measured and modelled paths of diameter increment at end of test. Blue filled symbols are modelling results.*

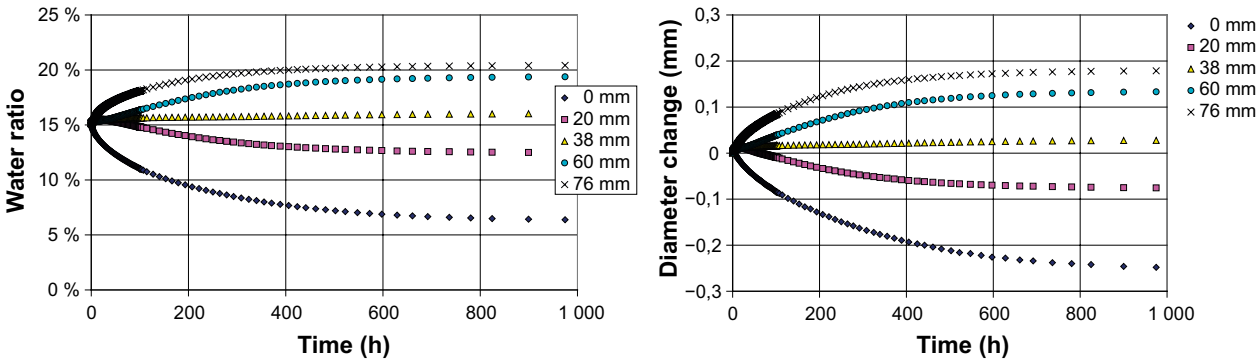

Figure 4-15. *Calculated evolution of water ratio and sample diameter increment beyond the end of test time.*

Another interesting result that the staggered calculation yielded is the difference in temperature between the first iteration when the initial water ratio and density of the sample were used in the temperature calculation and the final one when the water redistribution was taken into account. Figure 4-16 shows a comparison. There is a difference and obvious influence of the moisture redistribution but it is not strong. This shows that (in this case) the thermal behaviour is dominated by the insulation. An odd observation is that the temperatures derived from the incorrect initial conditions agree better with the measurements.

Improvement of material models

The material models of Abaqus have some drawbacks. One is that the gas is not modeled as a separate phase but only as degree of saturation. Vapour is not modeled as being driven by vapour pressure but as being driven by a thermal gradient. The other drawback is that Abaqus uses the effective stress theory also in unsaturated state, which is not correct since in unsaturated state two variables are required. In Abaqus this is taken care of by a procedure called "moisture swelling". With this procedure the swelling can be controlled by adding a volume change as a function of the degree of saturation. This works rather well at constant volume (where the volume change is transformed to a change in total stress according to the stiffness of the material) but if the volume can change the model gets increasingly incorrect since both the "moisture swelling" procedure and the retention curve are only functions of the degree of saturation and are thus only valid for a specific void ratio.

The problems with the vapour flux are the reason for the small difference in the solution of the water ratio distribution compared to the measured values. There is some diffenece in shape of the curves and the shape is controlled by the diffusion coefficient D_{Tv} which is a function of the degree of saturation S_r at $S_r < 0.3$ and $S_r > 0.7$ (see Equations 3-3 to 3-5). The shape can thus be controlled by these functions but attempts to improve them failed although the difference between measurements and calculations is rather small. The reason is most likely that the volume of the sample changes and the diffusion coefficient cannot be made a function of the void ratio – only the degree of saturation.

The problems with the volume change are more obvious and are the reason for the disagreement between measured and modelled change in diameter of the sample. Attempts to increase the volume change failed since the code cannot handle the influence of changed void ratio on the "moisture swelling" procedure and on the retention curve. Figure 4-17 and Figure 4-18 illustrate the problem.

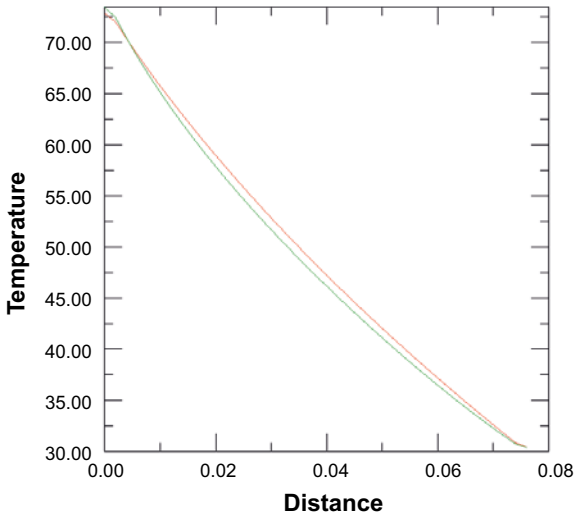

Figure 4-16. *Temperature distribution along the sample when the initial conditions (red line) and the final conditions (green line) are used in the calculation.*

Figure 4-17 shows that the increase in degree of saturation ceases in the cold part at distances above 50 mm from the heater in spite of that the sample increases its volume strongly all the way. Figure 4-18 shows why. Above the water ratio 16 % the sample swells without increasing the degree of saturation. The sample does not approach the saturation line when the sample increases the water ratio (rather the reverse).

The conclusion is thus that swelling of a bentonite cannot be coupled to the degree of saturation since there is no single relation.

4.4.9 Conclusions and comments

Benchmark 1.1.3 yields a fine opportunity to check and improve the THM models in general and the vapour flux processes in particular. The test is well defined and the water balance is well controlled due to that no water was allowed to leave or enter the samples.

However, since no measurements (except temperature) are available during the test, the question arises of how far from steady state regarding water ratio distribution the sample was at termination. According to the Abaqus modeling the moisture redistribution is still far from steady state.

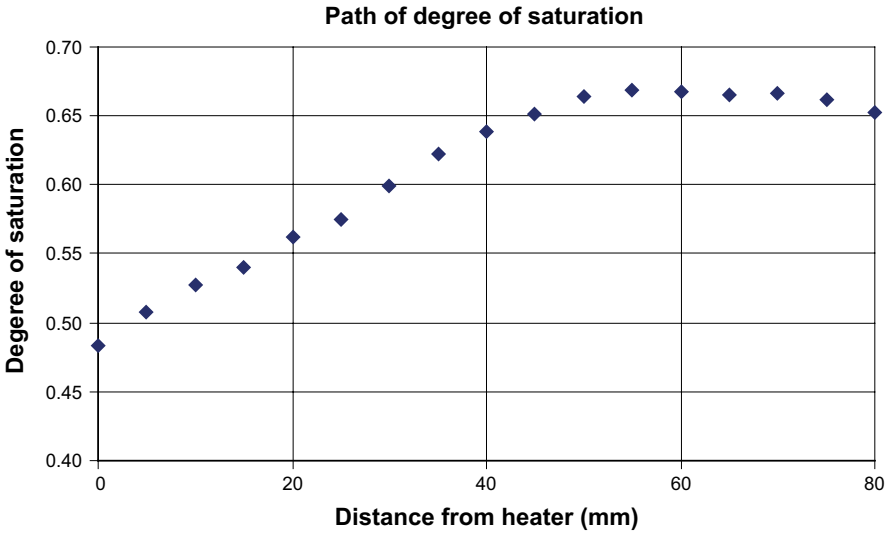

Figure 4-17. Degree of saturation in the sample as function of the distance from the heater.

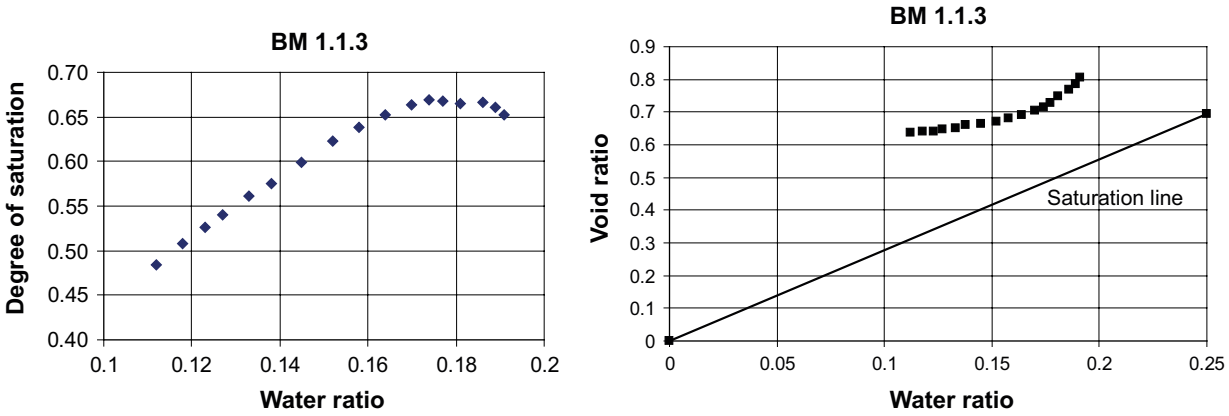

Figure 4-18. Degree of saturation and void ratio as functions of water ratio evaluated from the measurements of the sample after end of test.

While both temperature and water ratio distributions were rather well modeled the diameter change was obviously not well modeled. The modeled change in diameter was about a factor 5 too small. Attempts to improve the mechanical model failed. This problem illustrates a disadvantage in the way Abaqus handles mechanics in unsaturated media. The combination of the effective stress theory and the "moisture swelling" procedure is not enough to handle the mechanical behaviour at free swelling of an unsaturated bentonite in contrast to at constant volume when the model works much better. In addition the retention curve and the "moisture swelling" procedure can only be made functions of the degree of saturation and cannot take the change in void ratio into account, which means that the observed swelling without increased degree of saturation cannot be accurately modeled.

5 BM 1.2 – Gas migration tests in compacted bentonite performed by BGS

5.1 General

Gas tests on water saturated highly compacted bentonite have been performed by BGS for many years. Some of them are well defined and suited for modelling. Tests with two types of geometry of the confining cell have been used to define BM 1.2.1 and 1.2.2. The specifications are provided by John Harrington.

5.2 Specifications

5.2.1 Specification of BM 1.2.1

This section contains the specifications of Benchmark 1.2.1 of the Task Force on Engineered Barrier System. Benchmark 1.2.1 is based on the tests performed by BGS (British Geologic Survey). Tests were performed on cylindrical specimens of compacted MX-80 bentonite subjected to isotropic stress states. Gas flow geometry was linear, i.e. gas was injected at one end of the sample and it was allowed to escape at the other end.

Tests and the results are analysed in Horseman et al. (1999).

Description of the gas migration tests

General

Seven gas migration tests were performed on cylindrical samples of compacted MX-80 bentonite. Samples were divided in two groups, HS (high swelling, 4 samples) and MS (medium swelling, 3 samples).

First, samples were saturated and consolidated under different values isotropic confining stress and a water backpressure of 1MPa. Afterwards, gas injection started at different values of constant flow rate.

The following parameters were measured during the tests:

- Injection pressure.
- Flow rate out of specimen.

Apparatus and monitoring system

The samples have a diameter and a height of 49mm. The specimens were tested in a cell under isotropic stress conditions. The apparatus is described in detail Harrington and Horseman (1999). Figure 5-1 shows a diagram of the test vessel. The scheme of the complete experimental set-up is shown in Figure 5-2.

Material

Compacted MX-80 bentonite has been used to manufacture the specimens tested. The characteristics of the material prior to be tested are given in Table 5-1. Swelling pressures and intrinsic permeabilities were estimated from published trends (Börgesson et al. 1995).

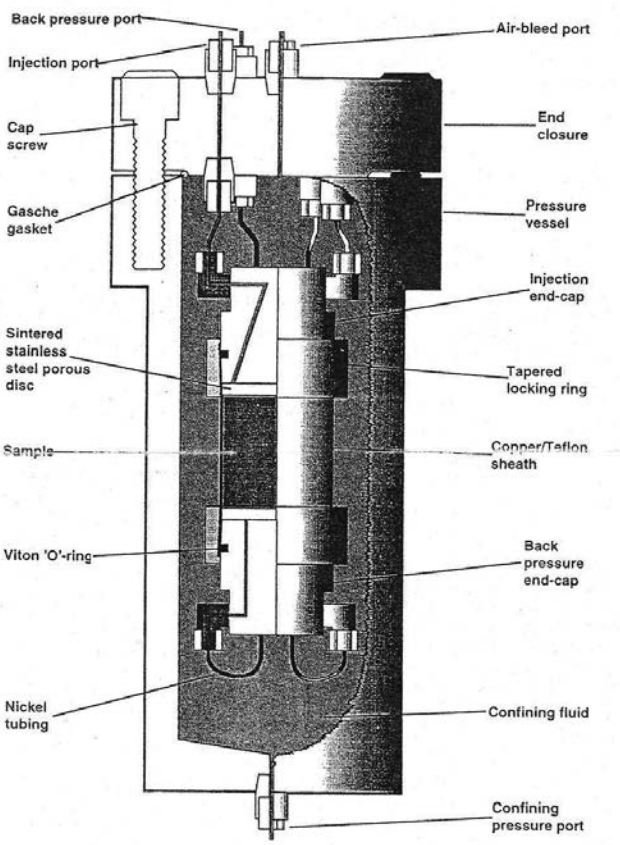

Figure 5-1. *Diagram of the test vessel.*

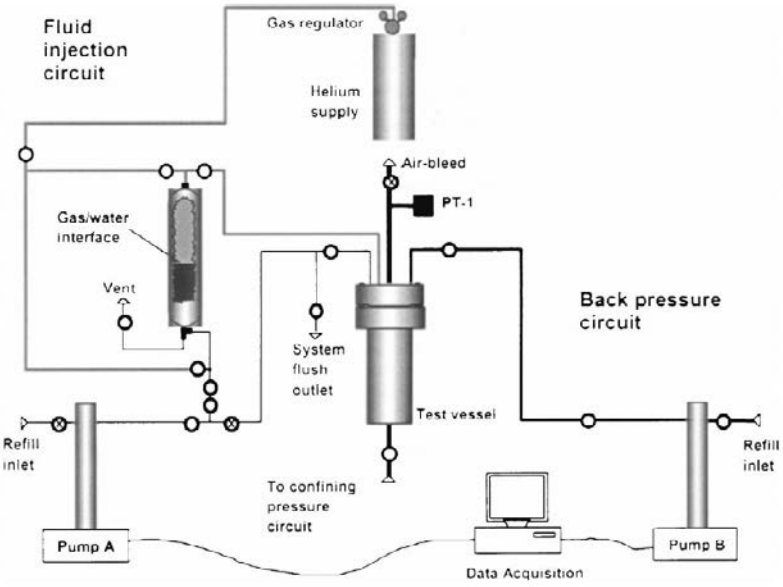

Figure 5-2. *Layout of the experimental set-up.*

Table 5-1. Characteristics of the MX-80 samples.

Test number	Batch	Water content (wt%)	Bulk density (Mg m^{-3})	Dry density (Mg m^{-3})	Void ratio	Swelling pressure (MPa)	Intrinsic permeability (m^2) / 10^{-20}
MX80-1	HS	23.5	2.072	1.678	0.651	15.7	0.6
MX80-2	HS	23.5	2.072	1.678	0.651	15.7	0.6
MX80-3	HS	23.1	2.079	1.689	0.640	17.1	0.5
MX80-4	HS	23.8	2.067	1.669	0.659	14.8	0.6
Averages		**23.5**	**2.073**	**1.678**	**0.650**	**15.8**	**0.6**
MX80-5	MS	28.2	1.994	1.555	0.781	6.4	1.0
MX80-6	MS	26.2	2.026	1.605	0.726	9.3	0.9
MX80-7	MS	27.5	2.004	1.572	0.762	7.3	1.0
Averages		**27.3**	**2.008**	**1.577**	**0.756**	**7.7**	**1.0**

Protocol of the experiments

Specimens were fully saturated (Sr > 99 %) and equilibrated under confining stress with a backpressure (i.e. water pressure) of 1.0 MPa applied at both ends. Net flows were monitored to establish the point of equilibration. Helium gas was injected at constant flow rate.

The volumetric flow rate of the injected fluid and the pressure of the downstream fluid were controlled using two syringe pumps. A pressure transducer monitored the outgoing pressure. Injection pressure and outgoing flux were recorded.

Four experiments provided data amenable to quantitative interpretation. Test on specimen Mx80-4A is representative of the experimental findings. Applied confining stress was 16.0 MPa. In this test gas was first injected at a volumetric flow rate of 375 μl/h. A gas breakthrough event was detected approximately at day 7. Gas injection was stopped at day 14 and the shut-in transient was monitored. Gas injection was restarted at day 30 at the same value of flow rate. After the second gas injection stage the specimen was subjected to a decreasing history of pumping rates: 180, 90, 45 and 0 μl/h. Table 5-2 summarizes the pumping rate history.

Table 5-2. Protocol for gas injection for experiment Mx80-4A.

Initial time (day)	Final time (day)	Injection flow rate (μl/h)
0	14	375
14	30	0
30	36	375
36	39	180
39	42	90
42	46	45
46	70	0

Test results

Figure 5-3 shows the first stage of test Mx80-4A. Confining stress and backpressure were 16.0 and 1.0 MPa, respectively. Initially gas was injected at a pumping rate of 375 µl/h. Gas breakthrough (sudden and sharp increase in flow rate out of the sample) occurs at gas injection pressure of 16.2 MPa. Peak injection pressure is slightly higher, 16.3 MPa. After the peak the gas pressure decreases to a steady state value of 15.22 MPa. Then gas injection is stopped.

Figure 5-4 shows the injection flow rate, injection pressure and outgoing flux during the remaining stages of the test. In the second injection stage the increase in flow rate out of the sample starts just as the injection pressure increases. No breakthrough pressure was determined. The peak pressure (15.25 MPa) is lower than in the first stage, but it is very close to the previous steady-state pressure.

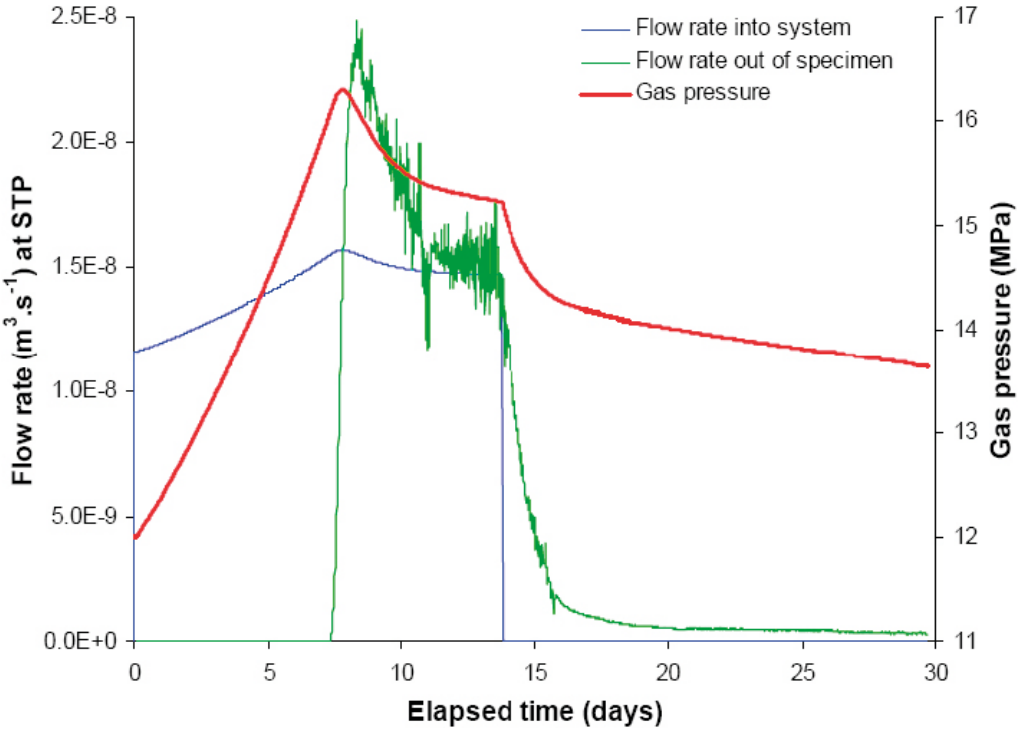

Figure 5-3. *Evolution of flow rate into system, injection pressure and outgoing flux during the first injection and shut-in stage.*

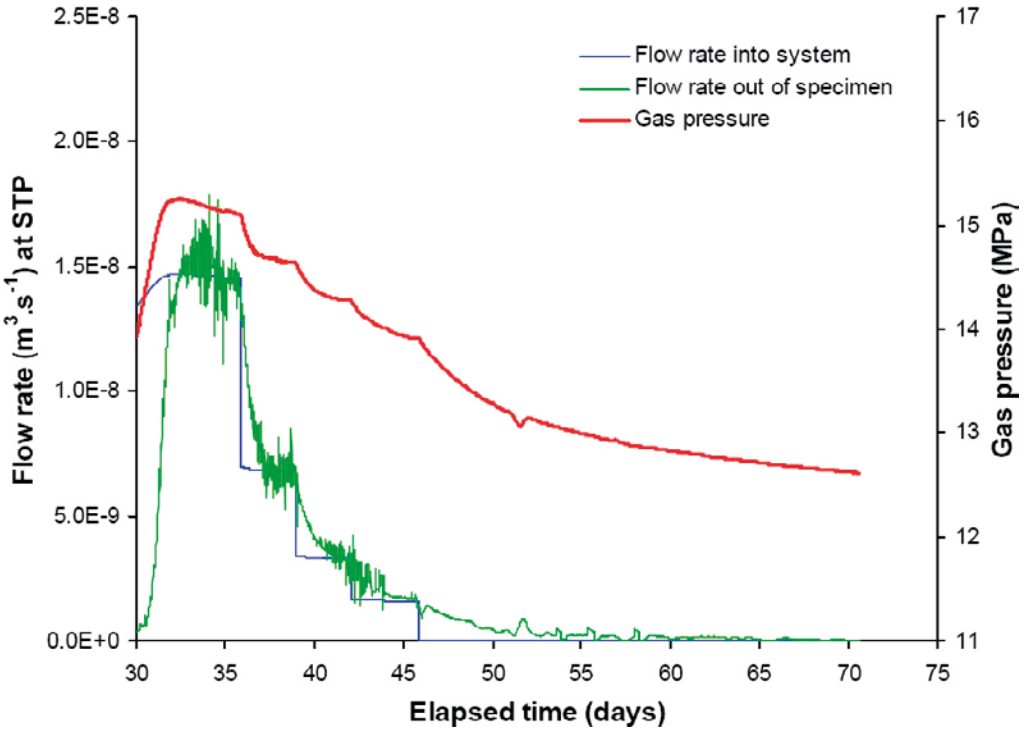

Figure 5-4. *Evolution of flow rate into system, injection pressure and outgoing flux during the remaining stages.*

Table 5-3 shows the gas pressures recorded during the different stages of the test at breakthrough, peak and steady-state.

Table 5-3. Gas pressures during test stages.

Injection flow rate (μl/h)	Gas pressure (MPa)		
	Breakthrough	Peak	Steady-state
375	16.19	16.3	15.22
375	–	15.25	15.11
180	–	–	14.64
90	–	–	14.27
45	–	–	13.91

An excel file distributed within the EBS Task Force (Excel files for THM2-1.xls) includes a discretization of the two test stages and associated plots of the evolution of flow rates and gas pressures.

Figure 5-5 shows the relation between calculated gas permeability and net mean effective stress during the different stages of test Mx80-4A. Gas permeability was calculated using the following relationship (laminar flow of a gas):

$$Q_{st} = \frac{v_{mst} k_g A_s}{2\mu_g L_s RT}\left[p_{gi}^2 - \left(p_{wo} + p_{co} \right)^2 \right]$$

where Qst ($m^3.s–1$) is the post-breakthrough volumetric flux of gas at standard temperature and pressure (STP), $vmst$ ($m^3 \cdot mol^{-1}$) is the molar volume of the gas at STP, μg (Pa·s) is the dynamic viscosity of the gas, R ($J \cdot mol^{-1} \cdot K^{-1}$) is the gas constant, T (K) is the absolute temperature, pgi (Pa) is the upstream gas pressure, pwo (Pa) is the downstream water pressure, and As (m^2) and Ls (m) are the cross-sectional area and length respectively of the test specimen. Parameter pco (Pa) was termed the apparent capillary pressure and defined as the pressure difference between gas and water at the

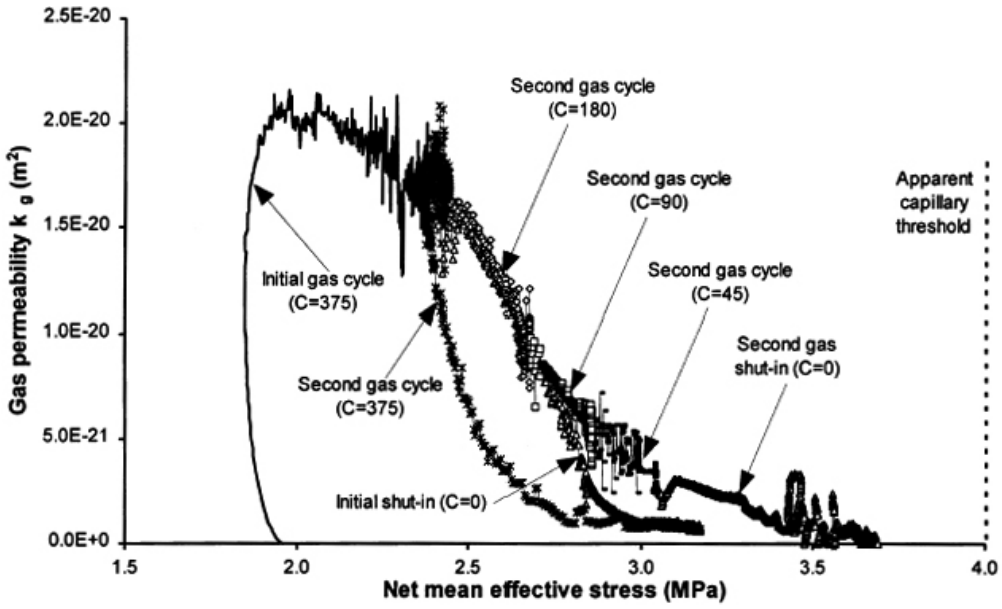

Figure 5-5. *Calculated gas permeability against net mean stress during test Mx80-4A.*

downstream end of the specimen. Permeability values calculated in this way are somewhat model dependent (Harrington and Horseman 2003).

Requested results

The following information was requested:

- Main features of the analyses performed.
- Results of the analyses and comparison with experimental results.

Main features of the analyses performed

This basic description should contain summarised information on:

- Geometry adopted for the analysis.
- Type of analysis (e.g. 1-D, 2-D, axisymmetric...).
- Element types used.
- Constitutive laws adopted (thermal, hydraulic, mechanical).
- Constitutive parameters used and procedure used in their determination or estimation.
- Boundary conditions (thermal, hydraulic, mechanical).
- Initial conditions (thermal, hydraulic, mechanical).
- Hypothesis adopted for gas flow.
- Any other features that are deemed important in the analysis.

Results of the analyses and comparison with experimental results

The following analysis results should be provided graphically together with a comparison with observed data. The Excel files of the submitted graphs should also be made available.

- Injection pressure evolution (0–70 days).
- Outgoing gas flow rates (0–70 days).
- Calculated permeability versus net mean stress. (Figure 5-5).

5.2.2 Specification of BM 1.2.2

This section contains the specifications of Benchmark 1.2.2 of the Task Force on Engineered Barrier System. Benchmark 1.2.2 is based on a second series of gas migration tests performed by BGS (British Geologic Survey). Tests were conducted using a new apparatus named CVRF (constant volume radial flow) permeameter, designed by BGS, in an effort to reproduce the expected conditions in the EBS bentonite buffer.

The gas migration tests and the results are described in detail in the technical report by Harrington and Horseman (2003). The information most relevant to the Benchmark is reproduced in the present document.

Description of the gas migration test

General

Two gas migration tests (Mx80-8 and Mx80-10) were conducted under constant volume conditions on saturated MX-80 bentonite samples using a new experimental device (CVRF).

The following parameters are measured during the tests:

- Injection pressure.
- Flow rate out of specimen (3 radial sink arrays).

- Porewater pressure (1 sensor).
- Radial stress (3 sensors).
- Axial stress (2 sensors).

Apparatus and monitoring system

The samples have a diameter of 60 mm and a height of 120mm. The specimens were tested in the CVRF cell. Figure 5-6 shows a diagram of the apparatus, which has six main components: a thick-walled, dual-closure pressure vessel; an injection pressure system; three independent backpressure systems; total stress gauges (2 axial, PT1 and PT2; 3 radial, PT3, PT5, PT6); a water pressure monitoring system (PT4); and the data acquisition system. Sensors PT1, PT5 and PT6 were added after test Mx80-8.

Fluid (either gas or water) can be injected using a syringe pump at the middle of the specimen by a filter embedded at the end of a 6.4mm diameter stainless steel tube. When gas is injected, helium is displaced by water form a pre-charged vessel. Fluid is allowed to flow out the cell through 12 stainless steel radial filters, which are grouped in 3 sink arrays. Outgoing fluxes are monitored in these 3 sink arrays by 3 syringe pumps.

Material

Compacted MX-80 bentonite was used to manufacture the specimens tested. The characteristics of the material prior to be tested are given in Table 5-4.

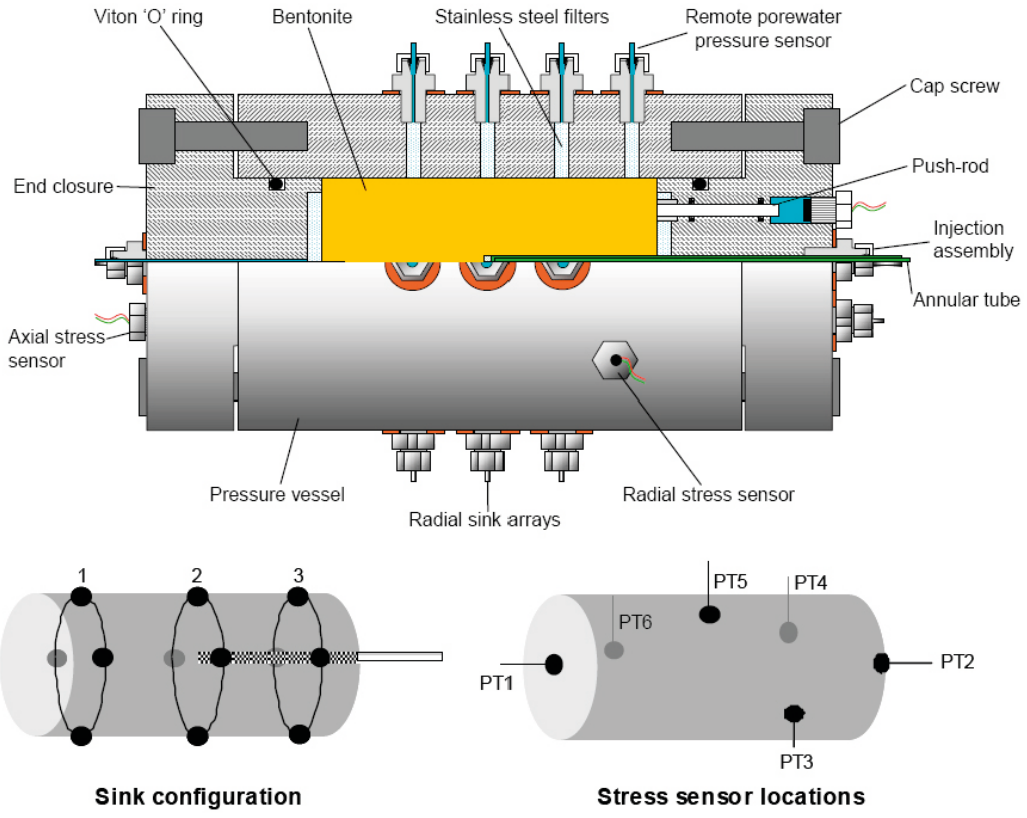

Figure 5-6. *Layout of the experimental cell.*

Table 5-4. Initial conditions of the samples tested.

Test	w	Bulk density (g/cm^3)	Dry density (g/cm^3)	e	Sr
Mx80-8	0.267	1.997	1.577	0.756	0.976
Mx80-10	0.267	2.005	1.582	0.751	0.986

Protocol of the experiments

The test selected for the benchmark is MX80-8. However, during the hydration stage of test Mx80-8 stress sensors (PT2 and PT3) did not capture the increase in total stress (although they were in operation during the gas injection phase). This information may be obtained from the initial saturation stage of the test MX80-10. In fact, in the two tests samples were saturated before gas testing by applying backpressure using de-aired and distilled water, obtaining degrees of saturation close to 1. The pressure cells in test Mx80-10 allowed measuring the development of the swelling pressure and the variation of total stresses with the applied backpressure. This information is given first and subsequently the results of the gas injection test on MX80-8 are presented. Table 5-5 provides the history of applied backpressure to all the filters in test Mx80-10.

Table 5-5. Backpressure history during Mx80-10 hydration stage.

Initial time (day)	Final time (day)	Backpressure (MPa)
0	18	1
18	26	2
26	39	3
39	46	4
46	56	5
56	64	6
64	71	7
71	78	4
78	91	1

After the hydration phase, gas was injected into the MX80-8 sample at controlled flow rate. Injection pressure, outgoing flow rates at the 3 sink arrays, total stresses and water pressure were monitored during gas injection.

Table 5-6 shows the history of gas injection flow rates for test Mx80-8.

Table 5-6. Gas injection history. Mx80-8 test.

Initial time (day)	Final time (day)	Injection flow rate (µl/h)
0	53	375
53	121.3	0
121.3	132.3	375
132.3	225	0

Test results

Test Mx80-10. Initial hydration stages

Figure 5-7 shows the (total) stresses measured during the first hydration stage of test Mx80-10. Figure 5-8 shows the evolution of measured total stresses during the subsequent stages characterized by an increasing application of backpressure and a final reduction. The pressure values obtained at the different sensors for each stage are given in Table 5-7.

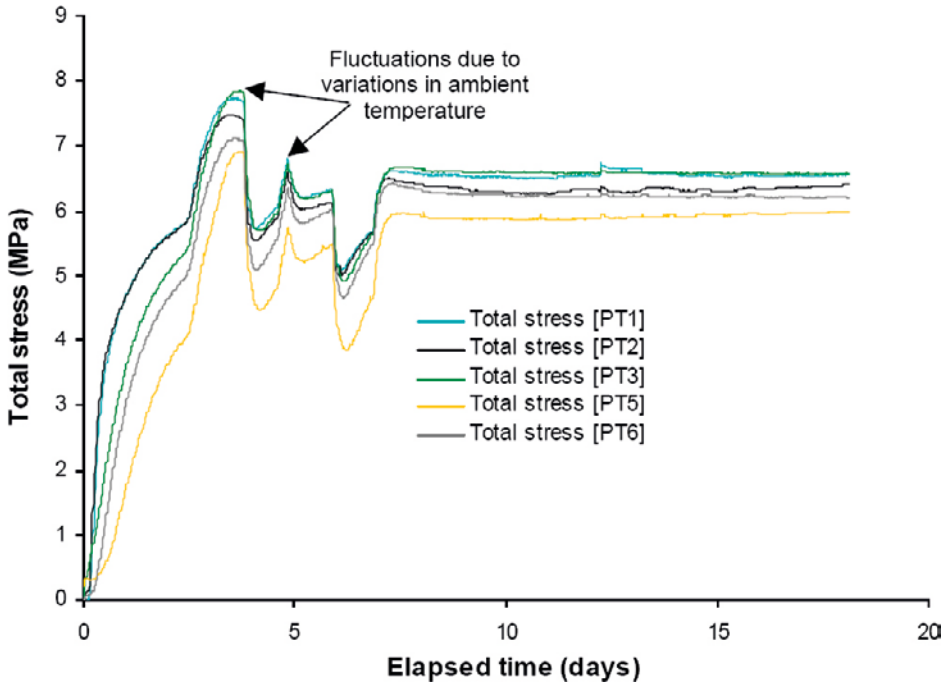

Figure 5-7. *Total stresses during initial hydration stage of test Mx80-10.*

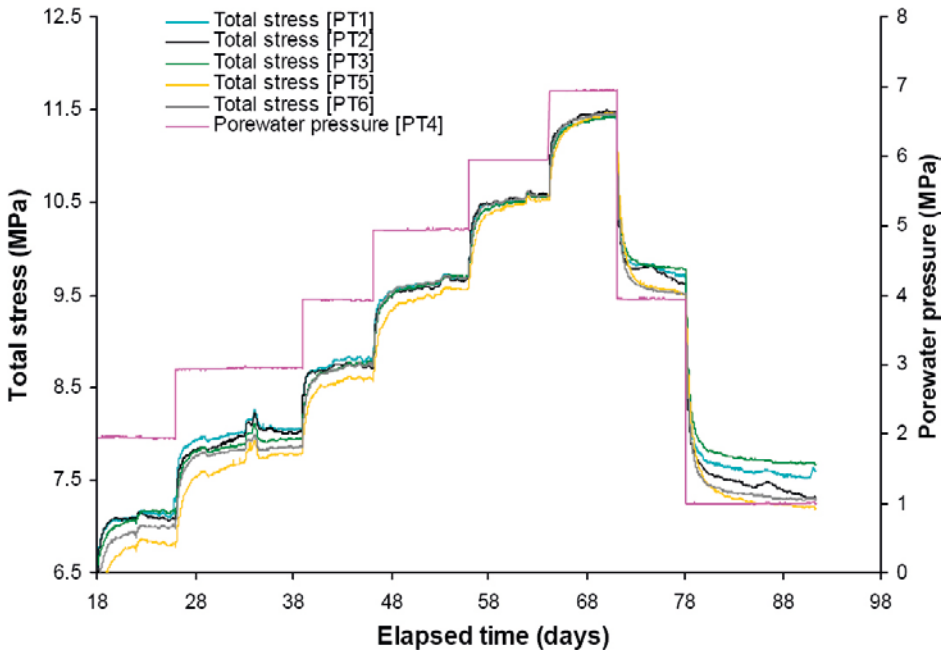

Figure 5-8. *Changes in total stress during backpressure history of test Mx80-10.*

Table 5 7. Axial and radial total stresses. Mx80-10 test backpressure history.

Backpressure (MPa)	Axial backpressure end-cap [PT1]	Axial injection end-cap [PT2]	Total stress (MPa)			
			Radial injection end [PT3]	Radial middle [PT5]	Radial back-pressure end [PT6]	Average
1.0	6.56	6.41	6.57	5.98	6.21	6.35
2.0	7.27	7.07	7.12	6.76	6.97	7.04
3.0	8.06	8.02	7.94	7.79	7.86	7.93
4.0	8.77	8.70	8.75	8.57	8.73	8.70
5.0	9.71	9.70	9.71	9.57	9.69	9.68
6.0	10.56	10.58	10.56	10.53	10.57	10.56
7.0	11.42	11.48	11.44	11.48	11.46	11.46
4.0	9.72	9.64	9.78	9.50	9.51	9.63
1.0	7.59	7.31	7.67	7.19	7.29	7.41

Test Mx80-8. Gas injection results

Figure 5-9 shows the complete history of injection pressure, total stresses (PT2 and PT3 sensors) and water pressure (PT4 sensor) for test Mx80-8. Figure 5-10 shows the first gas injection stage, including the outgoing flow rate from sink array 1 (which measured 99 % of the outgoing fluxes). Table 5-8 shows the values of injection gas pressure and axial total stress at the most relevant events of every gas injection stage.

Table 5-8. Gas pressures and axial stress during test stages (MX80-8).

Gas injection stage	Injection flow rate (µl/h)	Gas pressure (MPa)				Axial stress (MPa) (PT2)
		Breakthrough	Peak	Steady-state	Shut-in (asymptote)	Breakthrough-Peak
1 (0–53 days)	375	18.9	19.4	11.2	8.0	18.3
2 (121.3–132.3 days)	375	9.4	–	11.5	8.0	–

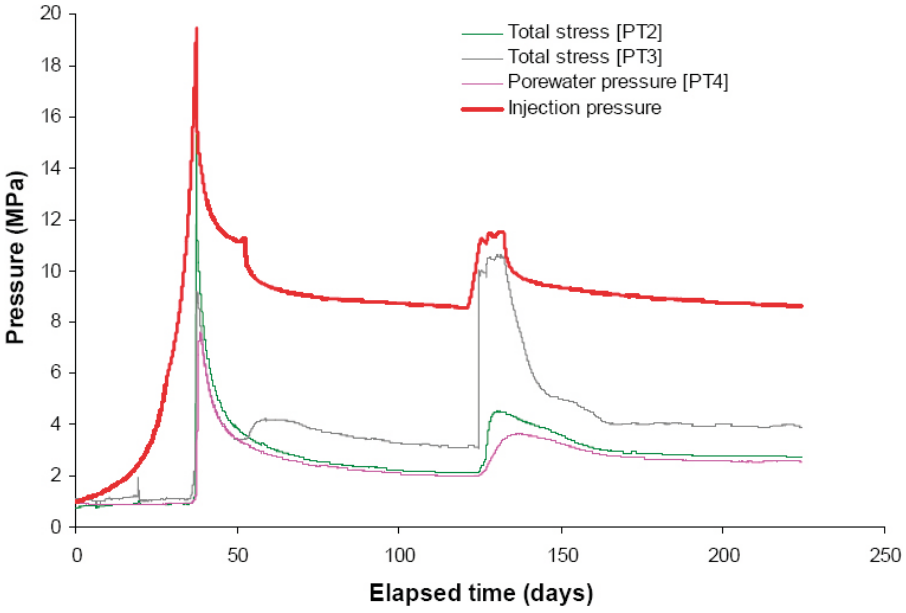

Figure 5-9. *Complete history of gas injection test Mx80-8. Evolution of gas injection pressure, total stresses and water pressure.*

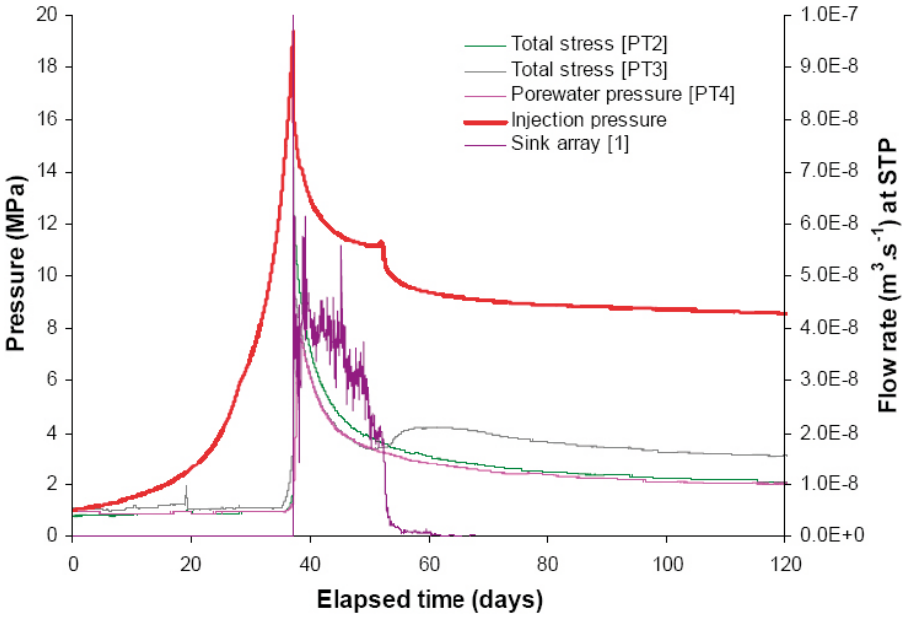

Figure 5-10. *First stage of gas injection (test Mx80-8). Evolution of gas injection pressure, total stresses, water pressure and outgoing flow rate from sink array 1.*

Figure 5-11 shows the evolution of outgoing fluxes through sink arrays 2 and 3 during the first stage of gas injection. The measured flows seem to be mainly water (Harrington and Horseman 2003).

Figure 5-12 shows the second gas injection phase. Injection pressure, injection flow rate at STP and outgoing fluxes at the three sink arrays are plotted. In this case the main gas discharge was recorded in sink array 3, at a breakthrough pressure of 9.4MPa. There is not a clearly defined pressure peak. The evolution of outgoing flows from sink 3 to sinks 1 and 2 is indicative of the existence of multiple gas pathways (Harrington and Horseman 2003). Gas injection pressure evolves almost to the same steady-state value as in first injection stage.

An excel file distributed within the EBS Task Force (Excel files for THM2-2.xls) includes a discretization of the hydration stage of test MX80_10 and the two gas test stages of test Mx80-8 and associated plots. Discretized data for applied gas pressure, flow rates in and out of the cell, measured total stresses on PT2 and PT3 and pore water pressure at PT4 are given.

Requested results

The following information was requested:

a) Main features of the analyses performed.

b) Results of the analyses and comparison with experimental results.

Main features of the analyses performed

This basic description should contain summarised information on:

- Geometry adopted for the analysis.
- Type of analysis (e.g. 1-D, 2-D, axisymmetric...).
- Element types used.
- Constitutive laws adopted (thermal, hydraulic, mechanical).
- Constitutive parameters used and procedure used in their determination or estimation.
- Boundary conditions (thermal, hydraulic, mechanical).
- Initial conditions (thermal, hydraulic, mechanical).

- Hypothesis adopted for gas flow.
- Any other features that are deemed important in the analysis.

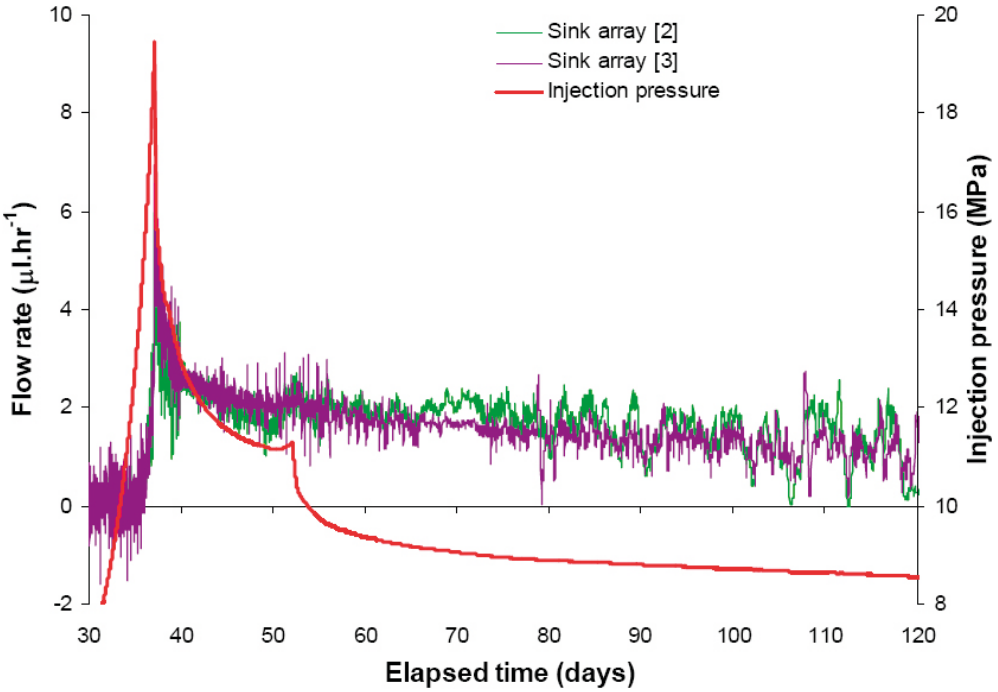

Figure 5-11. *Outgoing fluxes from sink array 2 and 3 during first gas injection stage. Test Mx80-8.*

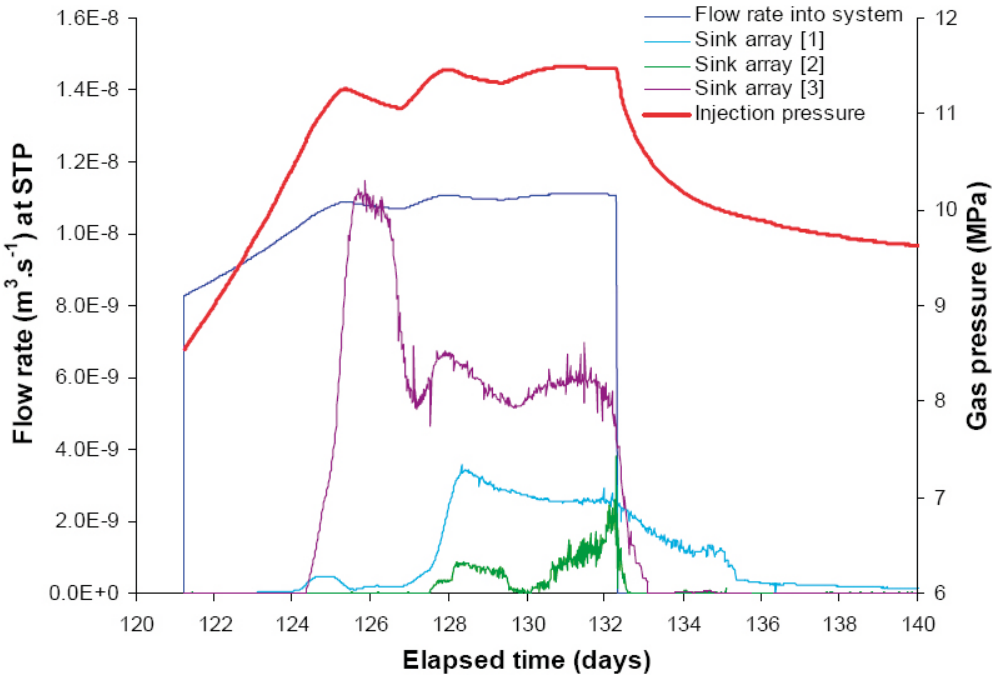

Figure 5-12. *Second stage of gas injection (test Mx80-8). Evolution of gas injection pressure and outgoing fluxes.*

Results of the analyses and comparison with experimental results

The following analysis results should be provided graphically together with comparison with observed data. The Excel files of the submitted graphs should also be made available.

Hydration stages of test Mx80-10

- Total stress evolution at sensor PT2 (axial stress) and PT5 (radial stress).

Gas migration test Mx80-8

- Injection pressure evolution,
- outgoing flow rates (gas/water) at each sink array,
- total (axial and radial) stresses evolution at sensors PT2 and PT3 (from 0 to 240 days),
- porewater pressure evolution at PT4 (from 0 to 240 days).

5.3 Modelling results with Code Bright and analytical solutions

5.3.1 Introduction

This section presents the calculations made by SKB Team 1 on benchmarks 1.2 – Gas migration experiments performed by British Geological Survey (BGS).

In Sections 5.3.2 and 5.3.3 the experiment is briefly described and analysed and include a theoretical discussion where specific retention properties of saturated bentonite, used in the present calculations, are derived. In Section 5.3.4 the modeling is described. An analytical treatment of the initial part of the experiments is presented as well as H- and HM-models calculated with Code_Bright. Finally a discussion of the modeling and its results are made (Section 5.3.5).

5.3.2 Experimental background

This section briefly describes the experiments which have been modeled. A more thorough description is found in the benchmark specifications (Section 5.2).

The experiment underlying benchmark 1.2.1 is a test of gas migration through a water saturated sample of MX-80 bentonite confined at constant pressure. The set-up is schematically pictured in Figure 5-13. A vessel filled with helium gas is attached to one side of the bentonite specimen. The gas is compressed by applying a controlled water flow of 375 µl/h into the vessel. After a pressure build-up period, a distinct breakthrough event occurred where gas flow was detected on the outlet side of the bentonite sample. Simultaneously the vessel pressure dropped. The constant water inflow was kept also after break-through until an approximate steady-state, with constant vessel pressure and outflow rate, was reached. In a next stage, the water inflow was turned off, gas outflow ceased and a shut-in pressure was registered. During the entire test period a water (back)pressure of 1 MPa was kept on the outlet side. In total, 7 different bentonite samples where tested. The sample singled out for benchmark modeling had a dry density of 1.669 g/cm^3 and a swelling pressure of 14.8 MPa. The vessel pressure and the outflow rate for the first 17 days of this sample are pictured in Figure 5-14. The experiment was run for another 53 days with various rates of water inflow, but the modeling will only focus on the first cycle of pressure build-up, breakthrough and shut-in.

Benchmark 1.2.2 models an experiment similar to the one just described, the main difference being that the clay specimen was kept at constant volume rather than constant pressure (Harrington and Horseman 2003). Gas was injected in the middle of a cylindrically contained bentonite sample (by the same technique as pictured in Figure 5-13) and outflow was detected in sinks on the outer cylindrical side. Vessel pressure, pore pressure and outflow were sampled as well as axial and radial stresses. Also in this experiment a distinct break-through event was recorded. Two samples where tested and the one singled out for benchmark modeling had a dry density of 1.577 g/cm^3 and swelling pressure of 6.7 MPa. The modeling will also in this case only concern the first cycle of pressure build-up, breakthrough and shut-in.

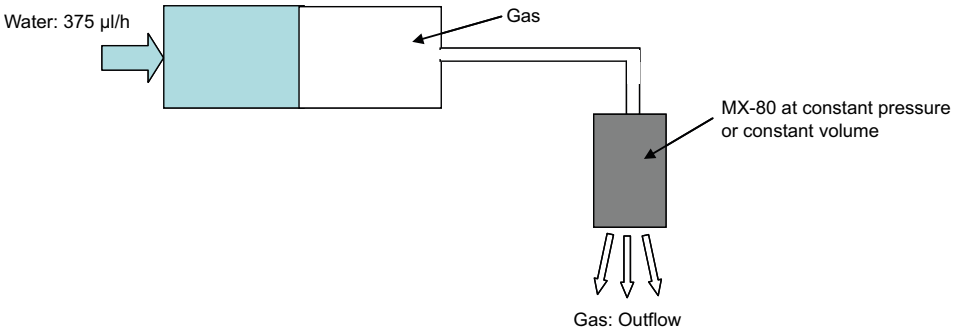

Figure 5-13. *Schematics of the performed gas migration tests.*

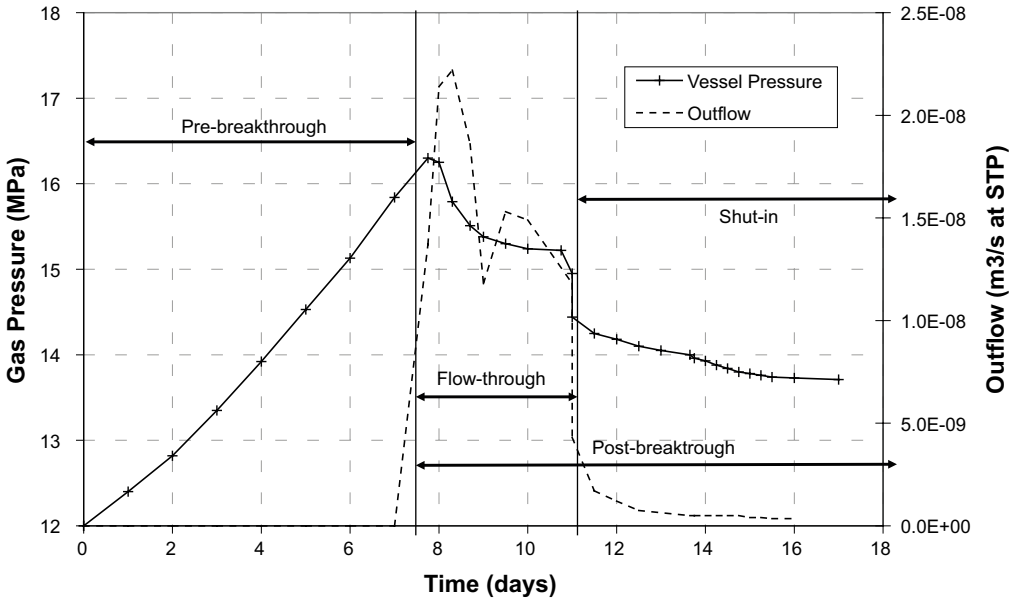

Figure 5-14. *Results of the first 17 days of BM 1.2.1. A pressure build-up phase is followed by a break-through event where a sudden raise of the outflow is detected. After achieving an approximate steady state (constant pressure and outflow) the water inflow is shut off and the outflow again falls to zero.*

In both of the experiments (and models) it is fruitful to divide the time period of testing into different parts

- Pre-breakthrough: From beginning of test to the breakthrough event (when a huge increase in outflow is detected).
- Flow-through: From breakthrough until the water inflow is shut off.
- Post-breakthrough: The period after the breakthrough event.
- Shut-in: The period after which the water inflow have stopped.

These time periods are indicated in Figure 5-14 for the case of BM 1.2.1.

5.3.3 Theoretical aspects

Total pressure in a confined montmorillonite system

If hysteresis effects are neglected, there is a one-to-one correspondence between water content and water (chemical) activity in unconfined montmorillonite. This retention property could be represented by the equilibrium relative humidity for a given water ratio, $RH(w)$.

Using this function, the chemical potential of clay water confined at (hydrostatic) pressure P can be written

$$\mu_{clay}(w) = \mu_{p.w.} + RT \ln RH(w) + P \cdot v_w \quad (5\text{-}1)$$

where $\mu_{p.w.}$ denotes the chemical potential of pure water, R is the universal gas constant and T the absolute temperature. The last term represents the contribution from mechanical work due to the external pressure, v_w denotes the molar volume of water (assumed constant).

In a confined system, specified by e.g. a void ratio, $e = V_{void}/V_{solid}$, the water ratio has an upper limit

$$w_{sat} = \frac{e}{\rho_s} \quad (5\text{-}2)$$

where ρ_s is the solid density (water density is assumed to be 1 g/cm^3). From Equation 5-1 it is seen that such a system in equilibrium with pure water ($\mu_{clay}(w_{sat}) = \mu_{p.w.}$) will exercise a swelling pressure

$$P_s = -\frac{RT}{v_w} \ln RH(w^{sat}). \quad (5\text{-}3)$$

By defining negative liquid pressures at relative humidity less than 100 % as

$$P_l \equiv \frac{RT}{v_w} \ln RH < 0, \quad RH < 100\ \%\ ,$$

the chemical potential of water is written $\mu = \mu_{p.w.} + P_l \cdot v_w$ and total pressure of the confined clay system at saturation can formally be expressed using Equation 5-1

$$P_{TOT} = P_s + P_l, \text{ (saturated system)} \quad (5\text{-}4)$$

By definition, an unsaturated state contains a gas phase. At equilibrium, the pressure of this phase must equal the total pressure of the system,

$$P_{TOT} = P_g. \text{ (unsaturated system)} \quad (5\text{-}5)$$

Finally, since $P_g \le P_{TOT}$ generally, Equation 5-1 also gives the criterion for saturation

$$s \le P_s\ ,$$

where

$$s \equiv P_g - P_l$$

defines suction.

To summarize, the total pressure of a confined isotropic montmorillonite system at equilibrium depends on liquid and gas pressure as

$$P_{TOT}(P_g, P_l) = \begin{cases} P_s + P_l, & s \le P_s \quad (saturated) \\ P_g, & s > P_s \quad (unsaturated) \end{cases} \quad (5\text{-}6)$$

Completely homogenized model (CHM)

The stress response of an unsaturated confined bentonite sample which takes up water is experimentally seen to differ from what is stated by Equation 5-6 (Dueck 2004). The reason for this is that the system will be locked in meta-stable states due to internal friction between separate swelling bentonite grains. Here the term meta-stable is used in the sense that the built-up stress can be made to vanish by a re-compaction of the sample at the new water ratio.

In this sense, complete thermodynamic equilibrium, which Equation 5-6 describes, is not achieved in experiments of this kind. The detailed description of such a stress build-up is very complicated, it must e.g. depend on initial grain size distribution, initial water ratio, sample compaction history etc. (Dueck 2004, Åkesson and Hökmark 2007, Alonso et al. 1990) and will not be further discussed here.

However, another experimental fact is that *at saturation*, swelling pressure is given by Equation 5-3 (Karnland et al. 2005, Dueck 2004) and Bucher and Müller-Vonmoos (1989). This fact indicates that the combination of stresses built up during infiltration in and lowering of the internal friction as the sample takes up water is capable of homogenization to a state of complete, or near complete thermodynamic equilibrium at saturation.

As the initial state in gas injection experiments is saturated it is reasonable to adopt a completely homogenized model (CHM) of the bentonite in these cases. In this model, all montmorillonite of the bentonite is assumed to be equally hydrated while the accessory minerals are playing a completely passive role and only contribute by occupying some of the available volume. All water is assumed located in interlayer spaces. By redefining the total volume to be only the volume occupied by montmorillonite and water, the CHM is therefore completely specified by a $RH(w)$-function and water ratio at saturation, w_{sat}.

The total pressure experienced in the CHM will obey Equation 5-6 at any state of saturation. Pressure build-up paths during hydration ($P_l \rightarrow 0$, from negative values) are pictured in Figure 5-16 for different constant values of P_g.

Figure 5-16 also shows a schematic hydration path of an unsaturated sample for the more experimentally realistic case where total equilibrium in the unsaturated state is not achieved ($P_g = 0$ for this path). Note that any CHM path with $P_g \leq P_s$, as well as the "realistic" path, end up at $P_{TOT} = P_s$ as $P_l \rightarrow 0$ (Equation 5-3), indicated by the ring in Figure 5-16. As we assume a complete homogenization in this point also for the "realistic" case, dehydration from this state will follow a CHM path. Thus, any system with $P_{TOT} = P_s$ at $P_l = 0$ will stay at this total pressure for any value of P_g between 0 and P_s. When $P_g > P_s$, dehydration occurs. This is of course consistent with the general CHM criterion for dehydration, $s > P_s$, and corresponds physically to the fact that consolidation of a homogeneous montmorillonite system can only be achieved after the swelling pressure is surpassed.

A CHM path will also be followed if the dehydration is performed by lowering P_l (e.g. by an external salt solution or by freezing the sample) rather than raising P_g. Assuming $P_g = 0$, P_l has to be lower than $-P_s$ before hydration takes place. At this point ($P_l = -P_s$) the total pressure is completely lost.

Experimental verification of the completely homogenized model

The swelling pressure measurements in both of the considered experiments can be used for additional verification of Equation 5-3. Calculated swelling pressures, using the $RH(w)$-curve for MX-80 from (Dueck 2004) and the specified water ratios at saturation, is presented and compared to measured values in Table 5-9. Considering the rather large uncertainties involved in both swelling pressure measurements and in obtaining the $RH(w)$-curve (e.g. from hysteresis effects), the validation of Equation 5-3 is very good.

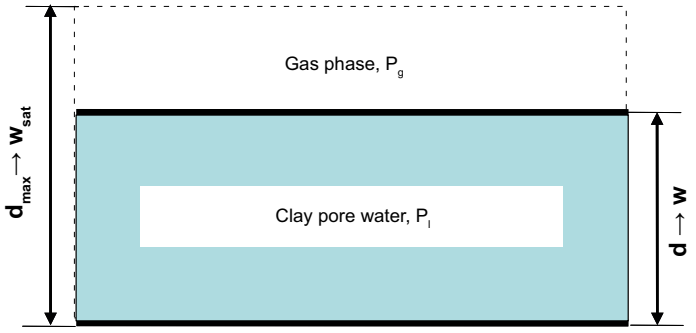

Figure 5-15. *In the completely homogenized model (CHM) all clay surfaces are equally hydrated, corresponding to a (mean) interlayer distance d (and a corresponding water ratio w). The gas phase is only specified by its total volume and no assumptions are made regarding the distribution of this volume other than that it is excluded from interlayer spaces.*

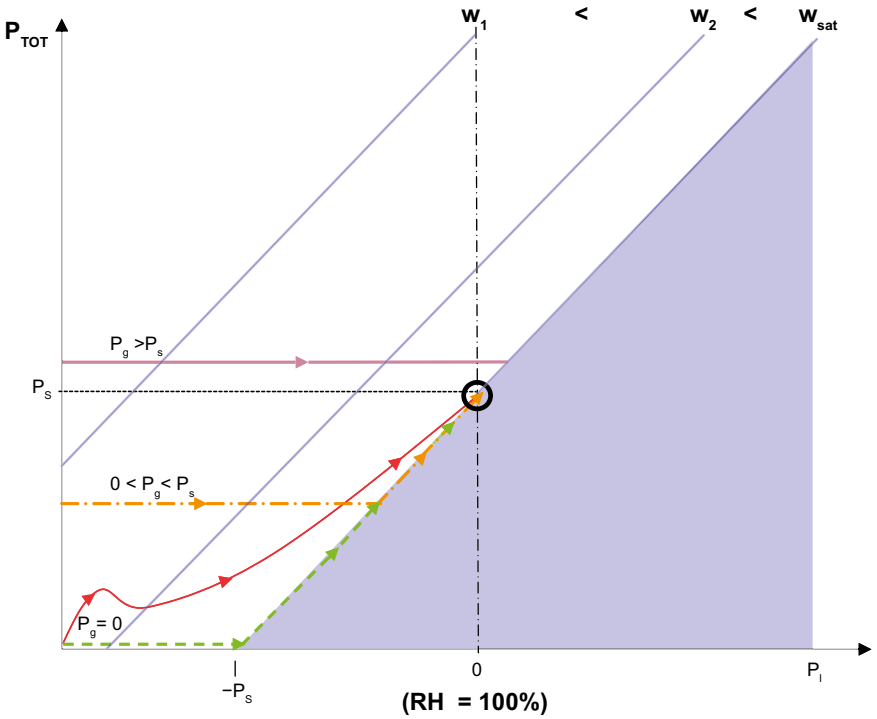

Figure 5-16. *Pressure path-ways during infiltration in the completely homogenized model for three different constant gas pressures (thick lines). At the edge of the filled space, the sample is saturated. Lines of constant water ratio are indicated. Also pictured is a more "realistic" path of an infiltration experiment where complete thermodynamic equilibrium is not established at each value of the increasing water pressure (thin line, P_g=0). The w-values do not strictly apply for this path.*

Table 5-9. Summary of evaluated swelling pressures in the two considered experiments.

	BM 1.2.1	BM 1.2.2
w_{sat}	0.238	0.267
$RH(w_{sat})$ [1)]	90 %	94 %
P_s, theory[2)] (MPa)	14.5	8.5
P_s, measured (MPa)	14.8	6.7[3)]

[1)] From Dueck (2004)
[2)] Using Equation 5-3
[3)] Extrapolation of P_{TOT}-vs-P_l curves to P_l = 0 for decreasing P_l. P_l from 7 to 1 MPa.

In BM 1.2.1 no liquid pressure data is available, making it impossible to evaluate the value of suction during flow-through. In BM 1.2.2 however, liquid pressure was measured at one point inside the sample, allowing for an approximate evaluation of suction by

$$s_{approx} = P_g^{vessel} - P_l^{inside} \qquad (5\text{-}7)$$

Note that a completely correct definition of suction would require gas and liquid pressures to be measured in the same point.

A plot of this approximate suction as a function of time is found in Figure 5-17. In this figure it is seen that throughout the entire flow-through phase, the value of suction lies slightly above the measured swelling pressure (6.7 MPa). As the water inflow is shut of at day 51, outflow ceases and suction is seen to fall just below the value of swelling pressure. This behavior is in total agreement with a CHM interpretation, where suction must reach a value above the swelling pressure in order to consolidate the sample and establish the gas phase. In Figure 5-18 the pressure-path in a $P_{TOT} - P_l$-diagram (Figure 5-16) at post-breakthrough for the first cycle of BM 1.2.2 is illustrated.

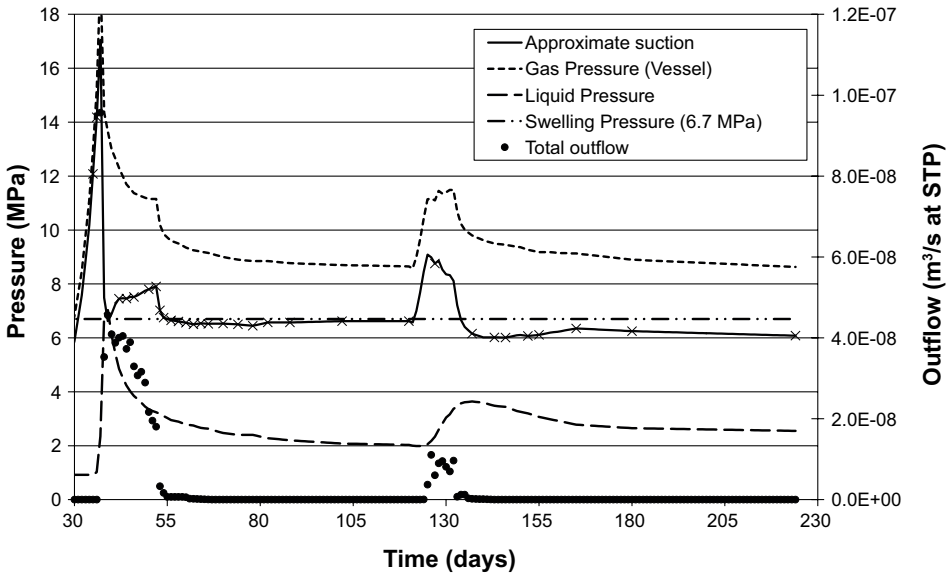

Figure 5-17. *Gas pressure, liquid pressure, total outflow and approximate suction during both pumping cycles in BM 1.2.2 as given by Equation 5-7. The suction-curve is produced by subtracting time-interpolated values of gas and liquid pressure. Points where these pressures are measured at the same time are indicated by ×. Notice how outflow strictly occur only where suction exceeds the swelling pressure.*

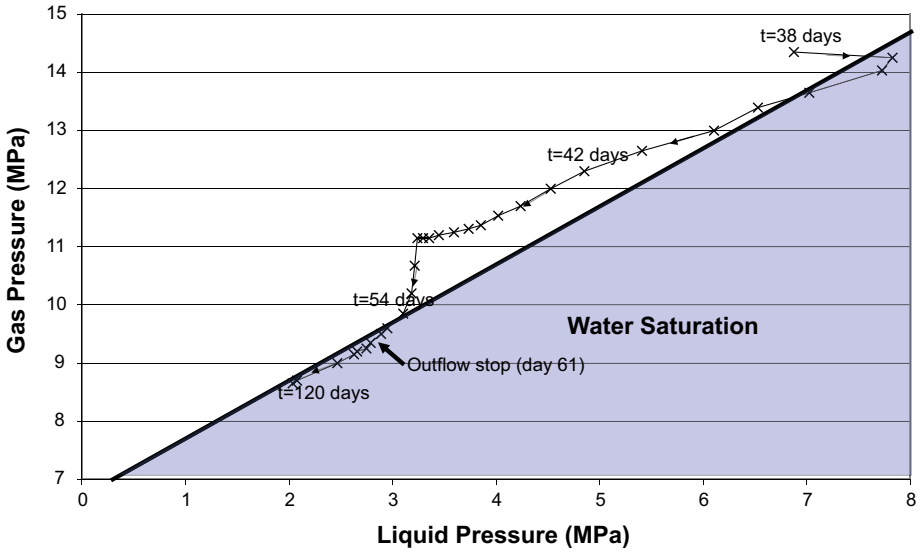

Figure 5-18. *Pressure-path for the first flow through cycle in BM 1.2.2. The result is in good agreement with a CHM interpretation (compare Figure 5-16).*

The absolute values of gas pressure at the different stages of a migration test on the other hand, such as peak- and shut in- pressures, do not characterize the sample in the same fundamental way, as they depend on set-up specific parameters such as initial gas volume and water inflow rate. A very (infinitely) large gas reservoir, for example, would give a constant gas pressure throughout the entire flow-through period.

Gas entry value (GEV) retention curves

When modeling hydraulic processes in unsaturated bentonite it is common to express the level of saturation as a function of suction only, $S_l = S_l(s)$. When describing infiltration of initially unsaturated samples, this function is "conventionally" put to 1 only at zero suction. This is consistent with the behavior of the "realistic" hydration path in Figure 5-16.

When adopting a CHM in the case of dehydrating a saturated state however, it follows from the discussion above that $S_l(s) = 1$ for all $s \leq P_s$. Such a function will in the following be referred to as a gas entry value (GEV) retention curve. This should not be confused with the ordinary two-phase view of gas entry values (or air entry values, see e.g. Bear 1972), where liquid is expelled by gas in a pre-existing and common pore system. Instead, in this context the GEV gives the suction threshold for consolidating the sample and thus *creating* a pore system for the gas. A "conventional" and a GEV retention curve (functions $S_l(s)$) is schematically illustrated in Figure 5-19.

5.3.4 Modeling

Modeling of the two experiments will focus on the first cycle of pressure build-up, breakthrough and shut-in. In BM 1.2.1 this means that the first 30 days of the experiment will be modeled, while the focus will be between day 28 to 70 in BM 1.2.2. In what follows, the time scale referred to in BM 1.2.2. will be shifted by 28 days compared to experiment. I.e. day 0 in the model will correspond to day 28 of the experiment.

First an analytical investigation of the pressure build-up phase is presented, followed by calculations made by the finite element code Code_Bright version 2.2 to model the entire cycle. With this tool both a pure hydraulic model (H) and a coupled hydraulic-mechanical model (HM) has been developed.

Analytical solution of the pre-breakthrough phase

In both of the experiments, no or very small amounts of outflow is detected during pre-breakthrough. In BM 1.2.2, where volume is kept constant, this implies that only a negligible amount of gas is leaving the vessel on the inflow side. Also in BM 1.2.1, where sample pressure is constant, we expect volumetric changes to be small and basically all gas to be kept in the vessel during pre-breakthrough. With the further assumption of ideal gas conditions the pre-breakthrough gas compression could be studied analytically. However, to get a well defined problem the initial gas volume is required. This quantity is not specified and need to be evaluated from the pressure build-up data.

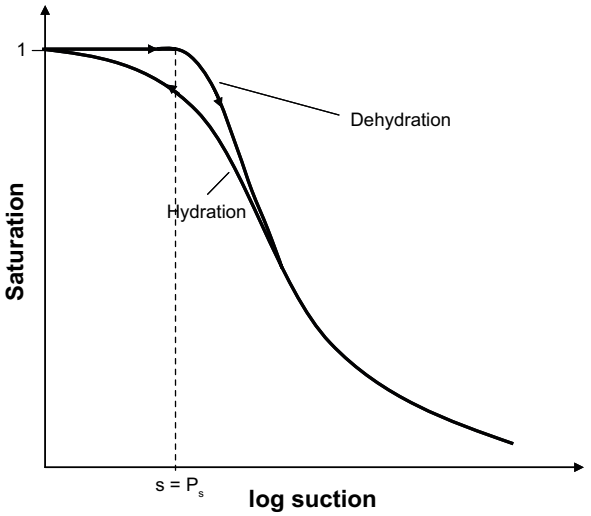

Figure 5-19. *Retention curves corresponding to hydration of an initially unsaturated sample ("conventional" type) and dehydration of an initially saturated sample (GEV retention curve) respectively.*

Equation for pressure build-up

With the above mentioned assumptions, pre-breakthrough pressure build-up is described by

$$dP = -\frac{1}{V^2} NRT dV = -\frac{P^2}{NRT} dV \qquad dV = -Q dt \tag{5-8}$$

where P denotes gas pressure in vessel, V is the vessel gas volume, N the constant amount of gas in moles, T the absolute temperature and Q = 375 µl/h is the constant water inflow velocity. Solving the resulting differential equation gives

$$P(t) = \frac{P_0}{1 - Qt/V_0} \,. \tag{5-9}$$

The initial volume, V_0 is evaluated using two values of vessel pressure at different times, here chosen as $P_0 = P(t=0)$ and $P_{168} = P(t=168)$ for both benchmarks (note that this refers to the shifted time scale in BM 1.2.2, time unit is hours),

$$V_0 = \frac{NRT}{P_0} = \frac{168Q}{1 - P_0/P_{168}} \,. \tag{5-10}$$

Values of P_0, P_{168} and V_0 in the two different experiments are given in Table 5-10.

Table 5-10. Specified pressure values and evaluated initial gas volumes.

	BM 1.2.1	BM 1.2.2
P_0 (MPa)	12.0	5.8
P_{168} (MPa)	15.8	13.0
V_0 (cl)	26.0	11.4

Results

The pressure build-up, Equation 5-9, is plotted together with experimental data in Figure 5-20 and Figure 5-21. It is seen that the agreement is basically perfect, which confirms the notion that gas is only being compressed in the vessel during pre-breakthrough, without any significant loss into the clay. For BM 1.2.1, the good agreement also confirms the notion that any volume changes of the clay are minor.

In Figure 5-21 is the available gas volume in the vessel as a function of time in BM 1.2.2 also plotted. Notice that the available gas volume will be depleted after approximately 300 hours. As the water pumping is reported to continue beyond this point, the vessel obviously must have been refilled at some time during the post-breakthrough period, a fact not found in the report on the experiment.

Numerical modeling: H-model

This section presents modeling of the two experiments using only the hydraulic part of Code_Bright, i.e. only advection- and diffusion- equations for gas and liquid phases are solved and no explicit mechanical model of bentonite is involved. The only mechanical coupling enters via the use of GEV retention curves.

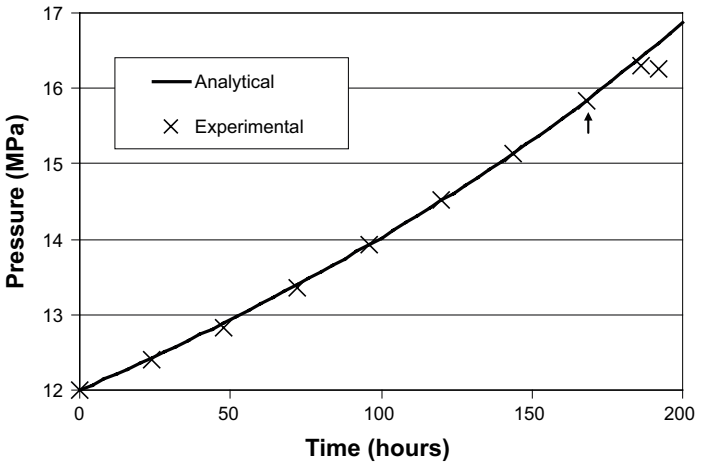

Figure 5-20. *Analytical solution of the pressure build-up in the pre-breakthrough phase for BM 1.2.1. (line) together with experimental values (×). The arrow indicates the pressure value used to evaluate the initial gas volume, V0 (together with the pressure at zero hours). The good agreement between analytical solution and experiment confirms that volume changes of the clay specimen are only minor during this phase of the test.*

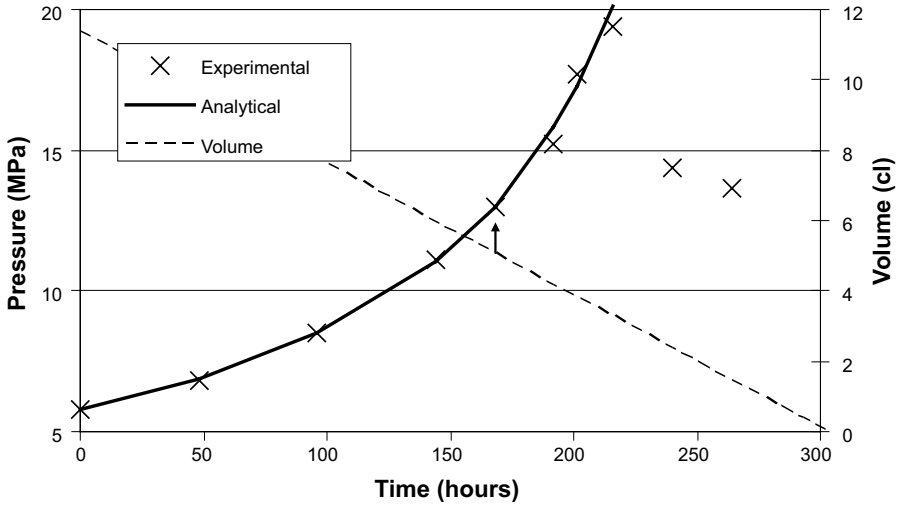

Figure 5-21. *Analytical solution of the pressure build-up in the pre-breakthrough phase for BM 1.2.2. (solid line) together with experimental values (×). Time scale is shifted −672 hours (−28 days)as compared to experiment. The arrow indicates the pressure value used to evaluate the initial gas volume, V0 (together with the pressure at zero hours). The vessel volume remaining as a function of time, V(t), is also plotted (dashed line). Note that V(t)=0 at approximately 300 h. As the water inflow was reported to continue for another 168 hours, the vessel must have been refilled (with gas) somewhere during post-breakthrough.*

Constitutive equations

The models consider simultaneous advective flow of liquid (water) and gas (helium) as well as diffusion of dissolved gas in the liquid phase. The advective flow for a given phase (gas or liquid) is described by Darcy's law

$$\vec{q} = \frac{\vec{k} \cdot k_r}{\mu} \nabla P, \qquad (5\text{-}11)$$

where $\vec{q}$ denotes flow velocity (m/s), $\vec{k}$ and k_r are the intrinsic and relative (phase dependent) permeabilities respectively, μ is the dynamic viscosity and ∇P the pressure gradient. The models use a default expression for water viscosity while helium viscosity is kept constant at 1.863×10^{-11} MPa·s (Ingelstam et al. 1982).

Gas diffusion is described by Fick's law

$$\vec{i} = -\phi \cdot \tau \cdot D \cdot S_l \cdot \rho_l \cdot \nabla \omega_l^a , \qquad (5\text{-}12)$$

where ϕ is porosity, τ tortuosity, D the diffusion constant, S_l liquid saturation, ρ_l liquid density and $\nabla \omega_l^a$ the mass fraction gradient of dissolved gas in the liquid phase. As the experiments were performed isothermally at room temperature, the mass fraction of water vapor in the gas phase is considered negligible and vapor diffusion is not considered in the models. This is done by setting the tortuosity factor for vapor to a very low value (10^{-5}).

Heat transport is not involved in the models and all equations are evaluated at 20 °C.

Geometries and boundary conditions

As described in Section 2.3.2, it is the compression rate of the gas on the injection side of the sample which is controlled rather than the actual gas flow into the bentonite. Code_Bright, on the other hand, is not able to handle boundary condition of this "moving piston"-type. For a satisfying description, the only option is to explicitly include the gas vessel in the model and adopt a liquid flux boundary condition for the water inflow.

Consequently a "vessel" material must be defined. This material is made to mimic a void space by giving it unit porosity (i.e. no soil mass), high permeability and weak retention properties. By assigning the vessel an appropriate volume (Table 5-10), and applying the constant water flow at its boundary, the gas compression can be correctly simulated. Furthermore, to get a sharp water front a large exponent is used in the expression for the liquid relative permeability.

It is also necessary to define a "valve" material at the interface between vessel and bentonite. By suppressing liquid permeability in this material, it acts as a valve, making sure that water in the saturated bentonite does not leak out into the empty vessel. The vessel model for BM 1.2.1 is pictured in Figure 5-22.

In order to speed up the transport parameter evaluation, a smaller model has been used which is also pictured in Figure 5-22. This model considers only the bentonite, and a gas pressure boundary condition is imposed on the upper side which follows the experimental pressure buildup. Of course, this model has no relevance after breakthrough.

Table 5-11 lists the chosen characterizing parameter values for the involved materials. It should be emphasized that the transport parameters in the "vessel" and "valve" materials are chosen for convenience only, and do not relate to any experimental data, e.g. the gas permeability is made very large for a complete gas pressure homogenization to occur at all times. The data for MX-80 are primarily taken from the benchmark specifications (see Section 5.2), and some parameter choices are based on the modelling performed in Section 2.3.

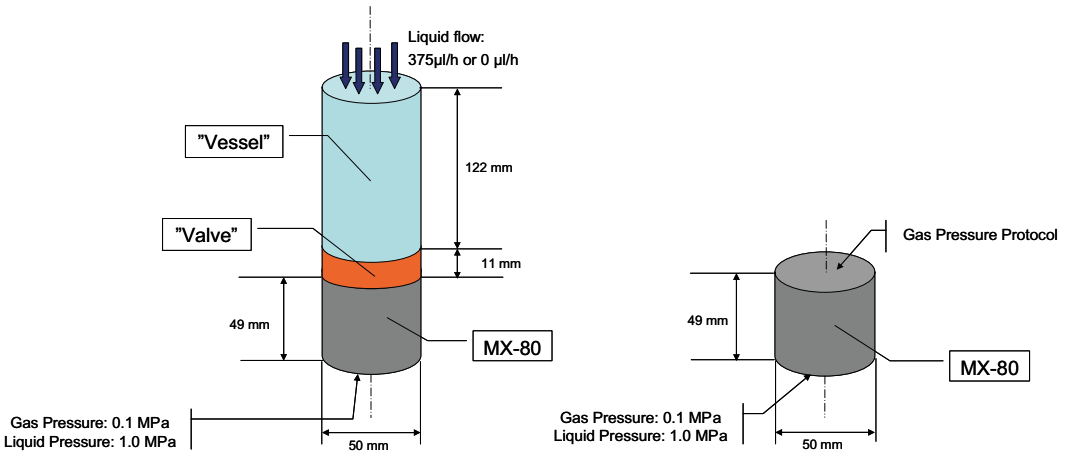

Figure 5-22. *Geometry and boundary conditions of a) the vessel model, b) parameter evaluation model.*

Table 5-11. Material Parameters.

	"Piston"	"Valve"	MX-80 BM 1.2.1	MX-80 BM 1.2.2
Intrinsic permeability, k	$5 \times 10^{-18} m^2$	$5 \times 10^{-18} m^2$	$4 \times 10^{-21} m^2$	$6 \times 10^{-21} m^2$/ $0.5 \times 10^{-21} m^2$
Liq. rel. permeability, k_{rl}	S^4	$10^{-25}\ S$	S^3	S^3
Gas rel. permeability, k_{rg}	$10^{11}\ (1-S)^3$	$10^{11}\ (1-S)^3$	varied	varied
Gas diffusion coefficient, D	4.635×10^{-9} m^2/s	4.635×10^{-9} m^2/s	4.635×10^{-9} m^2/s	4.635×10^{-9} m^2/s
Gas diffusion tourtuosity, τ	10^{-5}	10^{-5}	1.0	1.0
Porosity, ϕ	1.0	1.0	0.397	0.43
Void ratio, e	–	–	0.659	0.756
Solid phase density, ρ_s	not present	not present	2.78	2.78
Dry density, ρ_{dry}	–	–	1.677	1.58

A vessel model was also applied for BM 1.2.2. This has a slightly more complex geometry as can be seen in Figure 5-23. In the experimental set-up there are 12 outflow sinks placed at 90° angles in three groups on the outer cylindrical surface of the bentonite container. In the model, these have been replaced by three thin bands in order to preserve the axial symmetry. Modeling of BM 1.2.2 will be limited to approximately 300 hours of the test as the vessel gets water saturated as noted in the analytical treatment of the pre-breakthrough pressure build-up. Since the refilling of the vessel is undocumented, both concerning amount of gas and at what time, it is impossible to further model the experiment. Furthermore, when comparing the model to experiments after breakthrough it should be kept in mind that the experimental conditions changes at some (unidentified) point.

For both benchmarks a thorough investigation on convergence in mesh-size has been performed. In BM 1.2.1 a mesh of 4×31 rectangular 2D-elements was used, i.e. in total 124 elements. In BM 1.2.2 the mesh consists of 358 2D-elements in total. All models utilize axisymmetry (the symmetry axes are indicated in Figure 5-22 and Figure 5-23).

Initial conditions

Table 5-12 and Table 5-13 list relevant initial values for both the designed "vessel" and "valve" materials as well as for MX-80. The liquid pressure in the "valve" material is kept constant via a boundary condition throughout the entire simulations. In principle, this condition could "create" or "destroy" some water in the model. In practice this is not a problem, however, since the water conductivity is hugely supressed in this material.

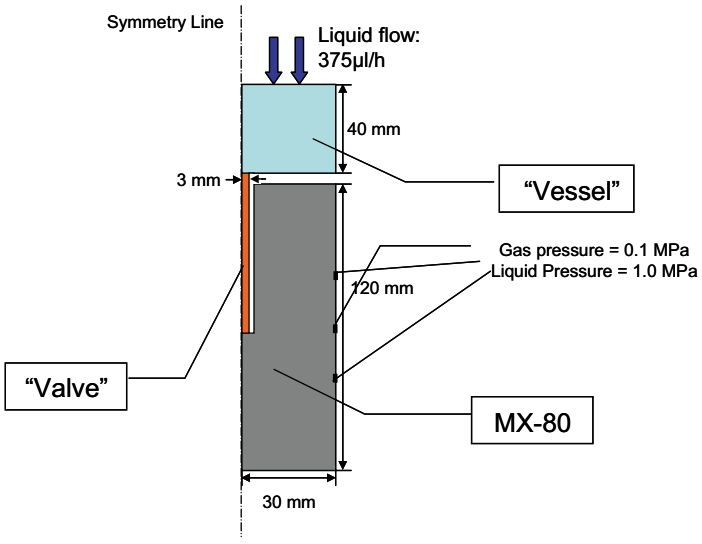

Figure 5-23. *Geometry and boundary conditions for the BM 1.2.2 vessel model.*

Table 5-12. Initial model parameters for the parts of the BM 1.2.1 vessel model.

	"Piston"	"Valve"	MX-80
Saturation level, S_{ini}	0 %	0 %	100 %
Gas pressure, $P_{g,ini}$	12 MPa	12 MPa	0.1 MPa
Liquid pressure $P_{l,ini}$	1 MPa	1 MPa (fixed)	1 MPa

Table 5-13. Inital parameter values in the BM 1.2.2 vessel model.

	"Piston"	"Valve"	MX-80
Saturation level, S_{ini}	0 %	0 %	100 %
Gas pressure, $P_{g,ini}$	5.8 MPa	5.8 MPa	0.1 MPa
Liquid pressure $P_{l,ini}$	1 MPa	1 MPa (fixed)	1 MPa

Retention curve parameters

Retention properties for a given material in Code_Bright are handled by specifying $S_l(s)$ as a constitutive equation. None of the available forms of $S_l(s)$ allows for a GEV type of retention curve. However, by using the standard van Genuchten parameterization

$$S_l = \left\{1 + \left(\frac{s}{P_0 \frac{\sigma}{\sigma_0}} \right)^{\frac{1}{1-\lambda}} \right\}^{-\lambda} \tag{5-13}$$

with a value of λ close to one (0.99), it is possible to mimic a threshold behavior, as pictured in Figure 5-24. As such a curve will be almost vertical for a large range of saturation values, it will only have relevance close to saturation. The present modeling will always stay close to saturation (see e.g. the suction in Figure 5-17) and therefore this form of parameterization is acceptable as representing a GEV retention curve.

BM 1.2.1 has also been modeled with a "conventional" retention curve of the extended van Genuchten type

$$S_l = \left\{1 + \left(\frac{s}{P_0 \frac{\sigma}{\sigma_0}} \right)^{\frac{1}{1-\lambda}} \right\}^{-\lambda} \cdot \left\{1 - \frac{s}{P_m}\right\}^{\lambda_m} \tag{5-14}$$

(with λ *not* close to 1) in order to evaluate the effect of using a GEV retention curve for gas migration modeling and to evaluate how reasonable a two phase formulation is for the process under study. The parameters for the "conventional" curve are taken to be identical to the ones used for MX-80 in BM 1.1.1 (Section 2.3). This curve is shown and compared to the GEV type in Figure 5-24.

The retention parameterization chosen for the "vessel" material utilizes a standard Van Genuchten curve while the "valve" material has a linear retention curve

$$S_l = 1 - \frac{s}{P_0}. \tag{5-15}$$

However, the latter material is basically restricted to zero saturation by defining a very low upper limit. As with all other material specific parameters for "vessel" and "valve", the retention properties are chosen for convenience. All retention curve parameters are listed in Table 5-14.

Table 5-14. Retention curve parameters.

	MX-80 BM 1.2.1 "Conventional"	MX-80 BM 1.2.1 GEV	MX-80 BM 1.2.2 GEV	"Piston"	"Valve"
Type	Ext. Van G.	Van G.	Van G.	Van G.	Linear
P_0	98 MPa	16,15,14 MPa	6.7 MPa	10 MPa	30 MPa
σ_0	0.072 N/m	0.072 N/m	0.072 N/m	0.072 N/m	–
λ	0.35	0.99	0.99	0.99	–
P_m	417 MPa	–	–	–	–
λ_m	1	–	–	–	–
Max S	1	1	1	1	0.01
Min S	0	0	0	0	0

It should be noticed that the parameter P_0 in the GEV retention curves does not equal the gas entry value. E.g. the retention curve with $P_0 = 16$ MPa has a gas entry value of approximately 15 MPa, as seen in Figure 5-24.

Results

"Conventional" Retention Curve (BM 1.2.1)

Modeling results for BM 1.2.1 in the case of a "conventional" form of retention curve is presented in Figure 5-25. Four different models, with varying pre-factor, *A,* in the expression for the gas phase relative permeability,

$$k_{rg} = A \cdot (1 - S_l)^3, \qquad (5\text{-}16)$$

have been calculated. The models are listed in Table 5-15.

The functional form of k_{rg} as a function of saturation is not very well determined experimentally. It has however been established that a gas phase is several orders of magnitude more conductive at a given level of saturation as compared to water , motivating a value of $A \geq 10^6$ (Villar et al. 2005c). A pre-factor of this magnitude has also been validated in earlier modeling work – using $A = 10^8$ for the gas description in BM 1.1.1 (Section 2.3) gave pressure profiles consistent with experimental data in a sample with initial constant liquid saturation level of 82 %.

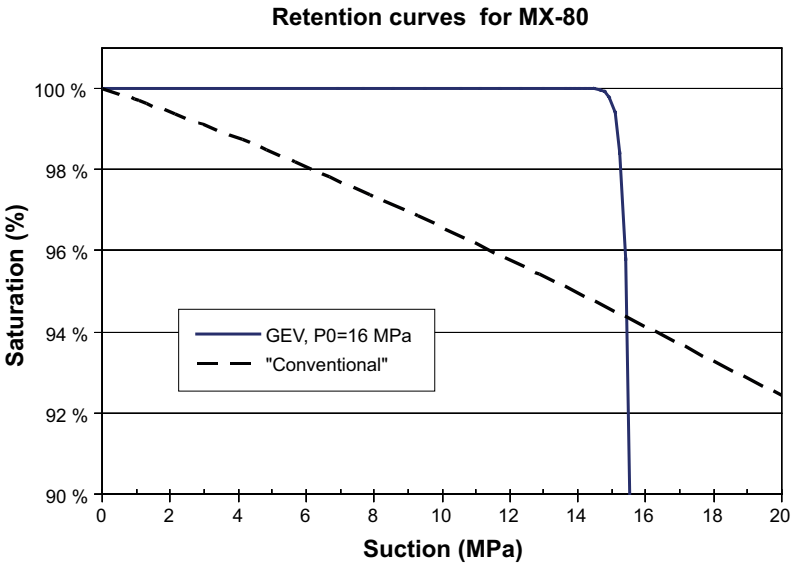

Figure 5-24. *"Conventional" and GEV form of retention curves.*

Table 5-15. Values of the prefactor in the relative permeability for gas in the considered models.

Model	A
BM 1.2.1_Conv_1e6	1×10^6
BM 1.2.1_Conv_1e5	1×10^5
BM 1.2.1_Conv_5e4	5×10^4
BM 1.2.1_Conv_1e4	1×10^4

As the models with "conventional" retention curve lacks a threshold behavior, the gas phase immediately starts to expel water, creating a front which moves through the sample at a speed determined by k_{rg}. In the model using $A = 10^6$ this front reaches the outlet side of the sample in just the first couple of hours of simulation after which an efficient transport channel is opened and the pressure drops. Thus, this model fails badly in reproducing experimental pressure evolution data.

In the other models presented in Figure 5-25 the speed of the gas transport is suppressed by choosing lower values of the A-parameter. In this way, the pressure-buildup phase can be reproduced by making A small enough (~10^4, model BM 1.2.1_Conv_1e4). However, based on the discussion above it is hard to justify such a low value. Furthermore, as seen in Figure 5-25 no abrupt breakthrough behavior can be captured. Also, looking at the gas flow in BM 1.2.1_Conv_1e4 it is seen that outflow appears already after 1.5 days in strong contrast to what is seen experimentally (~7 days, see e.g. Figure 5-13). The reason for a continued vessel pressure build-up after the gas front has reached the outlet side in this particular model is that the gas transport is made (unrealistically) inefficient. The overall conclusion is that it is impossible to model a breakthrough event using a pure H-model and a "conventional" retention curve.

Gas Entry Retention Curve (BM 1.2.1 and BM 1.2.2)

The models presented in Figure 5-26 and Table 5-16 utilize a GEV retention curve for modeling of BM 1.2.1. Three different retention curves have been used where the P_0-parameter, and thus the GEV, has been varied (see section on retention curve parameters above). For each model the A-parameter in the expression for the gas phase relative permeability (Equation 5-16) is tuned to a best possible experimental fit.

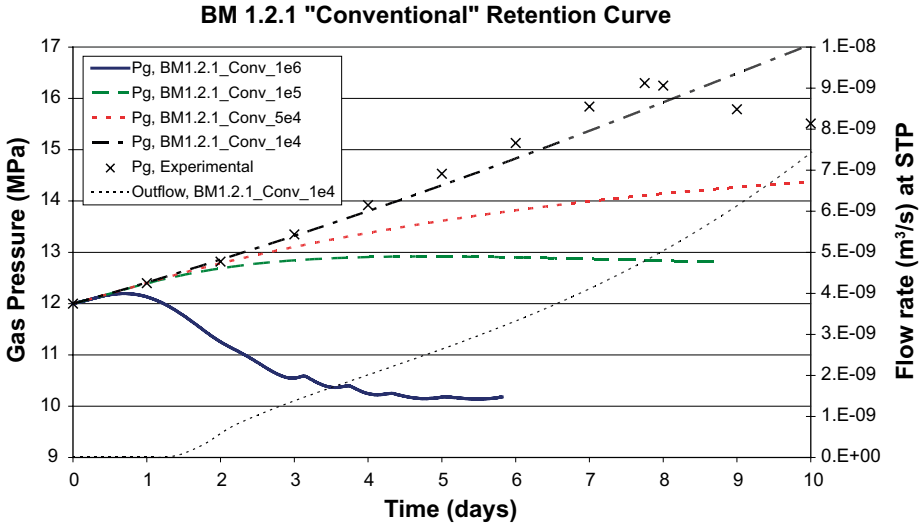

Figure 5-25. *Gas pressure build-up during the first 10 days in models using the "conventional" retention cure in BM 1.2.1. For model BM 1.2.1_Conv_1e4 also the gas outflow is plotted.*

Table 5-16. P_0- GEV- and corresponding A-parameter values in the gas entry value models for BM 1.2.1.

Model	P_0 (MPa)	GEV[1)] (MPa)	A
1.2.1_GEV_16	16	14.8	10^{12}
1.2.1_GEV_15	15	13.9	10^{9}
1.2.1_GEV_14	14	13.0	5×10^{7}

[1)] This value is taken to be s(0.999) of the retention curve. Since we are forced to use a van Genuchten parameterization it is not completely unambiguous. See earlier discussion.

With this type of retention curve it is possible to capture an abrupt breakthrough event in a pure H-model and a rather good agreement with experiment can be achieved for both pressure- and gas outflow evolution, as seen in Figure 5-26.

The model with the largest GEV-value, BM 1.2.1_GEV_16, has a very fast moving gas phase. This means that as soon as the criterion for breakthrough is fulfilled, the gas migrates through the clay almost instantly and a steady-state is quickly established. The noisy character of the outflow curve for this model is an artifact from using the van Genuchten type of retention curve. As the gas moves fast, a very small amount of desaturation is obtained, and this close to saturation the slope of the retention curve is almost vertical giving huge differences in suction at almost no change in saturation.

With a smaller GEV-value, the gas transport is adjusted to be slower (but still rather fast) which prolongs the time it takes to reach steady state. The increasing delay of the process can also be seen in the gas outflow curves, whose maxima is shifted towards larger times as the GEV is made lower.

Looking only at the pre-breakthrough and flow-through phases, BM 1.2.1_GEV_15 gives the best resemblance to experiment. This model has a GEV of 13.9 MPa, which is a bit lower than the measured swelling pressure of 14.8 MPa.

In the shut-in period the pressure is seen to drop much more in the experiment as compared to any of the models. In the experiment, it is seen that there is a small outflow for rather long times after the pumping is shut off. Thus, the sealing of the bentonite in the shut-in phase is not as efficient as in the models. It is likely that a detailed description of the gas phase distribution and how it couples e.g. to the transport of water is necessary to explain this difference. It should also be kept in mind that the model assumes volume conservation, while the experiment was performed under constant sample pressure.

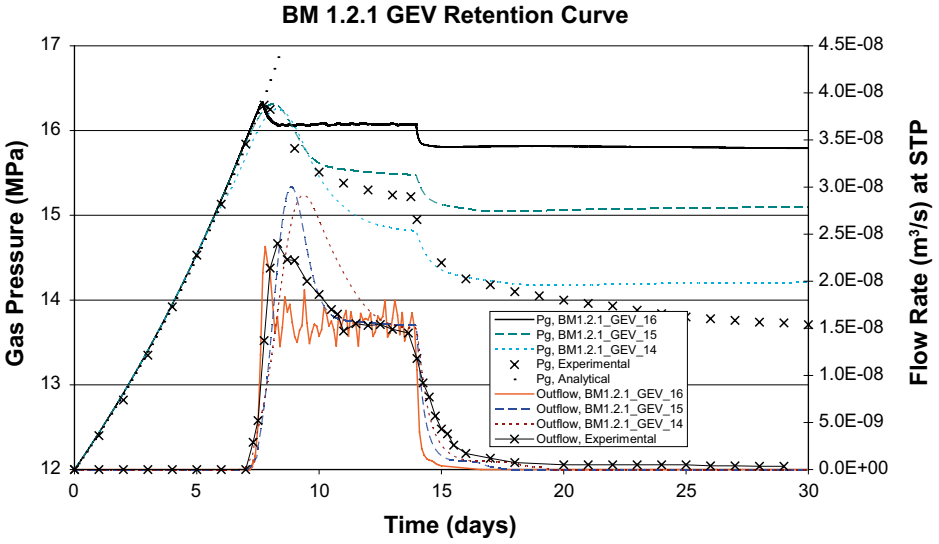

Figure 5-26. *Gas pressure build-up and gas outflow from gas entry value models and experiment during the first 30 days of BM 1.2.1.*

Figure 5-27 shows the pressure build-up for BM 1.2.2 using a GEV retention curve (specified in Table 5-14). It is seen that it is possible also in this case to model an abrupt breakthrough behavior. Two models with different choices of intrinsic permeability and gas transport parameters have been calculated. The two values of intrinsic permeability corresponds to what is expected from the density of the sample (Börgesson et al. 1995) and what has been evaluated in the report on the experiment respectively. As in the modeling of BM 1.2.1, the *A*-parameter has been tuned in order to get the best possible experimental fit. The parameters for each model are presented in Table 5-17.

As Figure 5-27 shows, the two parameter choices gives very similar results, indicating that the Code_Bright model in the present CHM-interpretation has too many parameters for specifying the system. On the other hand, BM 1.2.2_GEV_3.5e6 has a slightly better fit, and also a high enough value on the *A*-parameter to be compatible with the discussion on gas transport from above.

Table 5-17. Values of intrinsic permeability and A-parameter in the models.

Model	Intrinsic permeability, k (m^2)	A
BM 1.2.2_GEV_3.5e6	0.5×10^{-21} [1)]	3.5×10^{6}
BM 1.2.2_GEV_5e2	6×10^{-21} [2)]	5×10^{2}

[1)] The lowest value evaluated in Harrington and Horseman (2003)
[2)] From Börgesson et al. (1995)

Outflow is only detected at one of the sinks in the experiment during the modeled flow-through, clearly demonstrating that the process is not spatially symmetric. The models on the other hand are strictly radial symmetric with outflow occurring in all sinks (or bands rather, as discussed in the section on boundary conditions above) and obviously there is no possibility to get an agreement between model and experiment for the outflow in this case. To be able to capture the observed behavior, a detailed description of the gas distribution in the clay is needed. This is a very difficult task, and no attempts have been done in the present modeling. This topic if further discussed in the conclusions section.

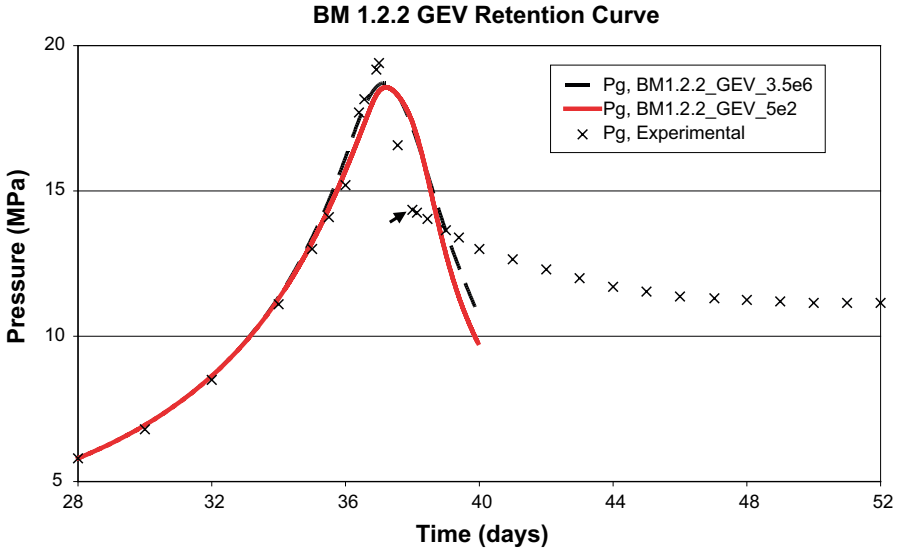

Figure 5-27. *Pressure-build up for the two considered models and experimental values in BM 1.2.2 (experimental time scale). The models have not been able to be calculated for times after 40 days, due to an uncontrolled refill of the vessel in the experiment. The arrow indicates a guess where this refill might have taken place.*

As already pointed out, it has only been possible to model the first 300 hours in BM 1.2.2 due to an uncontrolled vessel refill. Looking at the behavior of the experimental pressure-curve in Figure 5-27, it could be speculated that this refilling has occurred where an abrupt change of slope of this curve is seen in the post-breakthrough phase, indicated by an arrow. After a refill of the vessel, the experimental pressure response should be much less steep and could of course not be compared with the model.

Numerical Modeling: HM-model (BM 1.2.1)

Attempts have been made to find an explicit mechanical approach to capture a gas breakthrough, i.e to include the clay displacement field as variables in the problem formulation and adopt a mechanical model of the additional constitutive laws.

The avenue followed here, that the bentonite tensile strength governs the breakthrough level, has been addressed in previous studies (Harrington and Horseman 2003, Hoch et al. 2004) and can to some extent be modeled with Code_Bright. Focus has been entirely on BM 1.2.1.

The two main processes used to model this mechanism are:

- Through the reduction of the net mean stress (p) at constant mean total stress (σ_m, defined as positive for compressive stresses) and at increasing gas pressure (P_g) due to the relation $p = \sigma_m - P_g$.
- Through activation of plastic dilations when p reaches the lower boundary (p_s) of the yield locus. For given water content, these dilations will result in unsaturated conditions and will therefore enable the development of a path for gas migration.

Modeling was made under the assumption that a preferential path develops between the bentonite sample and the sheath in BM 1.2.1. This path was therefore modeled as a specific material with the only difference that the tensile strength was set to zero (see Figure 5-18).

Boundary conditions, initial conditions and retention parameters

Figure 5-29 a shows the model geometry, which is an extension of the parameter evaluation model from Figure 5-22. The sample was confined with roller boundaries at the top and lower boundary and with a constant pressure at the circumferential boundary. The gas and liquid pressure were held constant at the lower boundary while the gas pressure at the top boundary followed a simple ramping scheme (Figure 5-29 b). The initial conditions are shown in Table 5-18.

$$S_l = \left[1 + \left(\frac{s}{P_0}\right)^{\frac{1}{1-\lambda}}\right]^{-\lambda} \qquad P_0(n) = 50 \cdot e^{10\cdot(n_0 - n)} \qquad \lambda = 0.9$$

As in the H-models described earlier, the chosen retention curve for the HM-model also exhibited an apparent GEV, in this case however with a higher threshold value than the cell pressure and with a not as extreme value of the parameter λ (see Figure 5-30). The curve was also given a porosity dependence in order to enhance the desaturation effect during dilation.

Table 5-18. Initial conditions for HM-model.

Porosity, ϕ_{in}	0.397
Void ratio, e_{ini}	0.658
Liquid pressure,$P_{l,ini}$	1 MPa
Gas pressure, $P_{g,ini}$	0.1 MPa
Stress $\sigma_{x,ini}/\sigma_{y,ini}/\sigma_{z,ini}$	−16/−16/−16 MPa

No attempts have been made to explicitly include the gas vessel in the HM-modeling as it has been judged to become too cumbersome. Already in the approach described here, numerous numerical difficulties were experienced. Inclusion of the gas vessel is necessary in order for experimental comparison at post-breakthrough (see Figure 5-22), which is not intended in the present modeling.

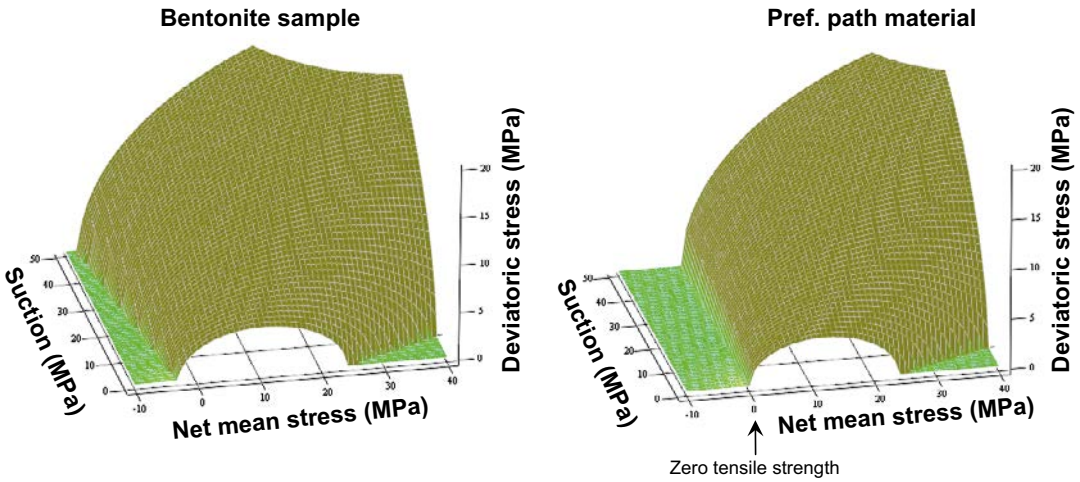

Figure 5-28. *Yield loci in (p,q,s)-space for bentonite sample and preferential path material.*

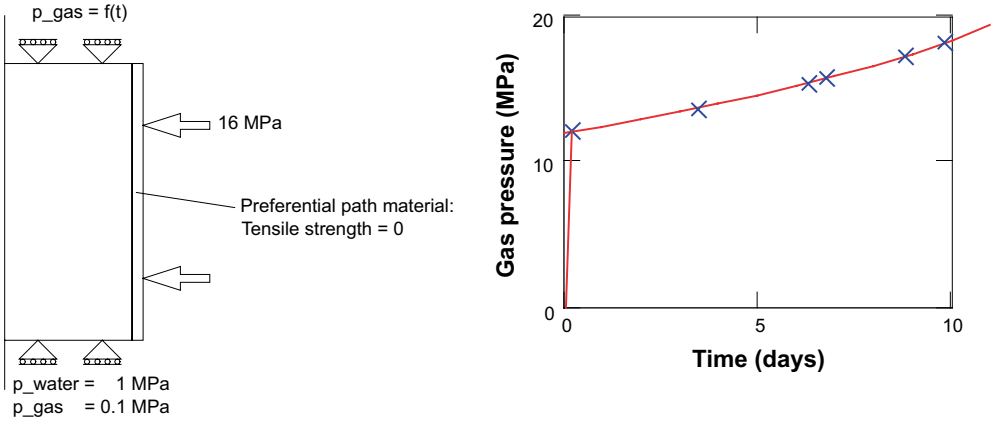

Figure 5-29. *Model geometry and boundary conditions (a) and gas pressurization scheme (b).*

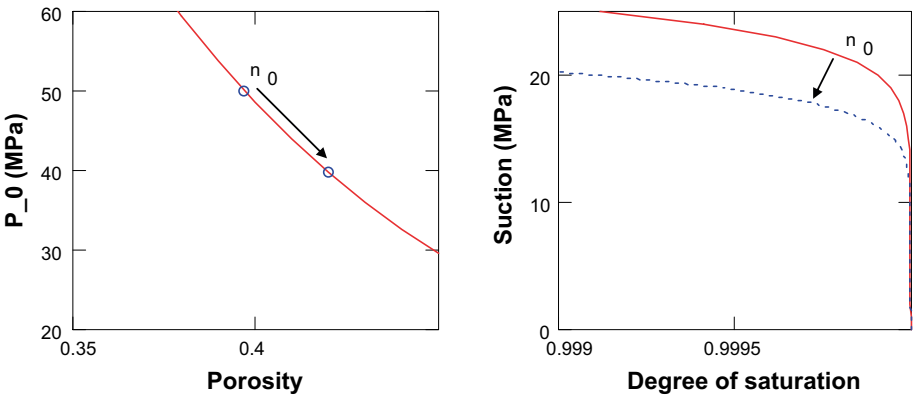

Figure 5-30. *Porosity dependent retention curve.*

Constitutive equations

Chosen hydrodynamic transport parameters is shown in Table 5-19. In general, the setting follows the conventional description, with the exception for the vapor diffusion tortuosity which was given a low value in order to suppress this process, just as in the case of the H-models.

Table 5-19. Hydrodynamic parameters.

Intrinsic permeability, k	1.6×10^{-21} m^2 *
Liquid relative permeability, k_{rl}	$1 \cdot S_l^3$
Gas relative permeability, k_{rg}	$10^4 \cdot S_g^3$
Gas diffusion tourtuosity, τ	1

* 40 % of value used in H-model

The mechanical model used is the thermoelastoplastic model for soils (based on the Barcelona Basic Model, Alonso et al. (1990)), available in Code_Bright. The setting of elastic parameters is shown in Table 5-20. It can be seen that all elastic modules represent a stiff, non-swelling material. The reason for this is that the build-up of a high gas pressure and a reduction of net mean stress is equivalent with an unloading of the sample. If "true" parameter values would have been chosen, this would lead to an elastic dilation throughout the pressurization.

Table 5-20. Elastic parameters.

Porous elastic module, κ_i	$0.005 \cdot (1 - 0.022 \cdot s)$
Minimum bulk modulus, K_{min}	100 MPa
Elastic module due to suction variation, κ_s	$0.005 \cdot [1 - 0.18 \cdot \ln(p/0.1)]$
Poisson ratio, ν	0.45

The plastic parameter values are shown in Table 5-21. As noted above, the main difference between the bentonite sample material and the preferential path material is the tensile strength (p_s).

Table 5-21. Plastic parameters.

	Bentonite	Pref. path material
Saturated pre-consolidation mean stress, p_0^*	24 MPa	
Apparent consolidation modulus, λ	$1.5 \cdot [0.25 \cdot e^{-0.05 \cdot s} + 0.75]$	
Critical state line parameter, M	0.36	
Tensile strength, p_s	$3 + 0.1 \cdot s$ MPa	0 MPa (no tensile strength)

Results

As mentioned, during the course of this work a lot of numerical difficulties were experienced and a large number of model versions were tested. Also the present model was not able to finish completely, but some features was captured which are presented here.

Stress paths for the three nodes at the upper boundary are shown in Figure 5-31. The paths follows the same course from the initial (p,s) point at (15, −0.9) to a point at the yield locus at (0, 17). After this point the paths diverge so that the nodes at the preferential path material follow the yield locus while the node in the sample material continues on the negative side with tensile stresses.

Contour plots of the plasticity flag (HV3), porosity and liquid saturation are shown in Figure 5-32. For elastic conditions the HV3 flag has the value of 1, but this is changed to −1 whenever the yield surface is reached. In these plots, it can be noted that plastic strains have spread down to the fourth element. As a result the porosity as well as the gas content has increased in these elements.

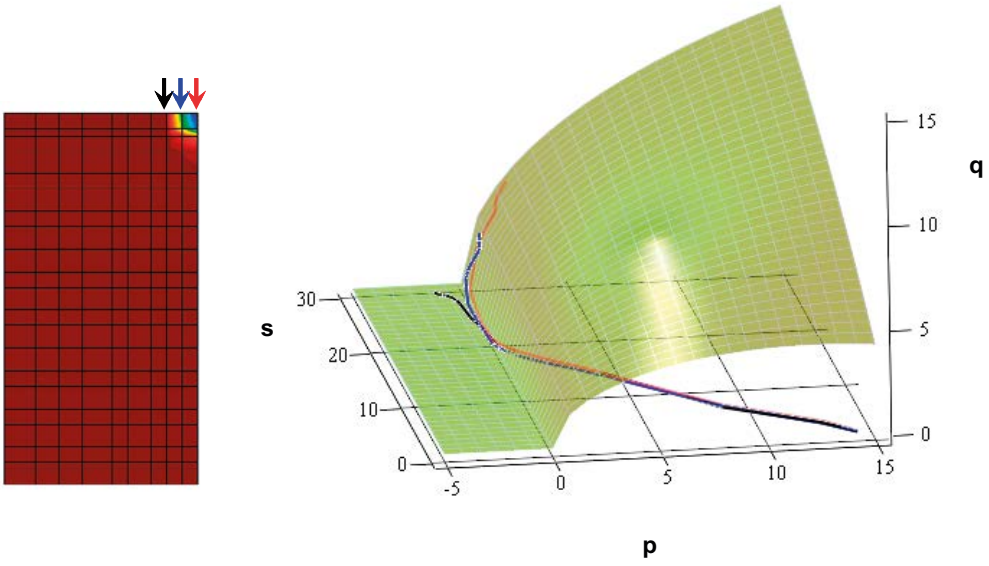

Figure 5-31. *Stress paths in (p,q,s)-space for three nodes at the upper boundary.*

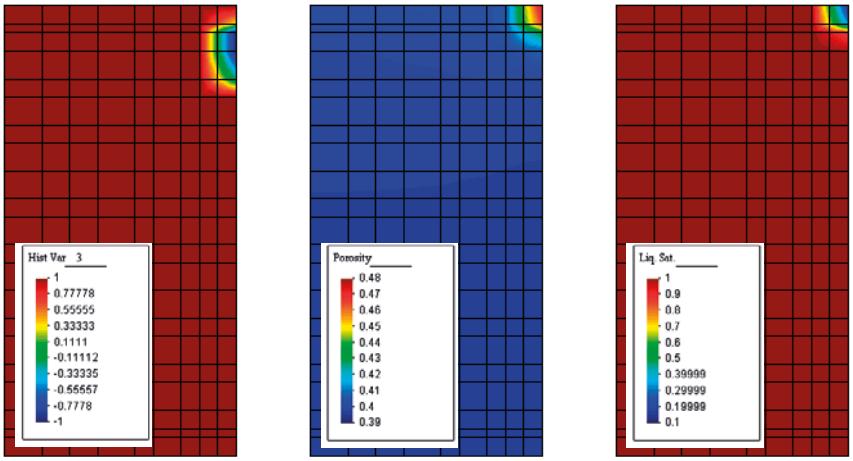

Figure 5-32. *Contour plot of HV3, porosity and liquid saturation at a boundary gas pressure of 17.3 MPa. The HV3-variable indicates plasticity (−1).*

Comments on HM approach

Even if the approach appears to capture the initiation of a preferential path, two remarks can be made:

- The mechanism relies on the buildup of a gas pressure in the water saturated sample, and thus in turn on the diffusion of dissolved gas into the sample. A high gas *pressure* is a precondition for the reduction of the net stress and the development of a gas *phase*. If the gas would not be allowed to diffuse into the sample, then the net stress could not be reduced to tensile levels.
- An increasing gas pressure is apparently equivalent with the unloading of the sample. If the sample has a low stiffness, it will dilate (elastically) as soon as the gas pressure increases. To suppress this effect a high stiffness has to be chosen.

A more consistent HM description of the development of a preferential path appears to require the option of gas-filled *contact elements*. Water saturated bentonite could in this case be described by: $\sigma_m = p + P_l$, whereas the gas-filled contact elements would be described by $\sigma_m = P_g$ (see Figure 5-33). Such a description would follow Equation 5-6 derived in Section 5.3.3. In addition, the mechanical laws applied for a work like that should be able to reproduce the relation between the void ratio and the swelling pressure, and thereby capture the *consolidation process*. The development of preferential paths would however still, at least to some extent, rely on the *strength* of the bentonite material. Considerable amount of code development is obviously needed before this option can be implemented and tested.

5.3.5 Conclusions

It has been shown that treating the mechanical response of the clay by use of a GEV retention curve only, the gas migration modeling gives results in rather good quantitative agreement with experiments. This form of retention curve is in turn motivated by a completely homogenized model of bentonite relating the GEV to the swelling pressure at saturation. The adoption of such a model for treating initially saturated systems is supported experimentally.

The physical interpretation which follows is that a gas phase with a pressure large enough for suction ($P_g - P_l$) to exceed the swelling pressure consolidates the clay, thereby generating the pore space through which the gas migrates. The details of the distribution and the dynamical evolution of this pore space are very complicated and have not been accounted for in the present modeling, except for the assumption that gas does not occupy interlayer pores. Several mechanisms for migration have been proposed, such as fracturing or development of micro fissures (Rodwell 2005). It cannot be ruled out that more than one mechanism is involved which might be of different importance depending on situation specific details such as gas pressure evolution and clay geometry.

The consolidation interpretation of the process is not compatible with the ordinary two-phase view of transport through a porous medium. In the latter view, on which Code_Bright is based, gas and liquid compete for volume in one and the same pre-existent pore structure. However, when implementing a pure H-model (no explicit mechanics) it is possible to reinterpret the Code_Bright model as the details of the gas phase volume distribution in this case is of less importance. Thus the gas can be considered contained in a separate pore system with porosity $S_g \cdot \phi$, where S_g is the saturation level for gas and ϕ the overall porosity. This reinterpretation is illustrated in Figure 5-34. As the details of the migration process are unknown and may vary between different experimental set-ups, it is however difficult to judge what values of the relative permeability of the gas phase (Equation 5-16) are "realistic". Another consequence of the Code_Bright formulation is that the gas phase inevitable will propagate through the sample as soon as the GEV is reached.

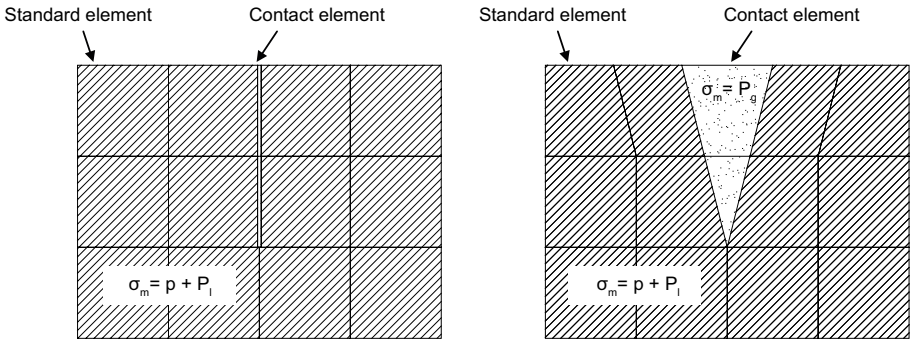

Figure 5-33. *Proposed development of a preferential path through predefined contact elements.*

In an explicit mechanical Code_Bright model, both gas and liquid do work on the solid phase in an equivalent manner, seen e.g. in the expression for effective mean stress

$$p = \sigma_m - \max\left(P_l, P_g\right)$$

Thus the problem formulation demands gas and liquid to share the same pore system and any interpretation besides the ordinary two-phase view becomes impossible (see Figure 5-34). A more consistent HM description of the development of a preferential path appears to require the separation of the two phases in different types of elements.

In many interpretations and discussions on gas migration experiments on compacted bentonite, focus has been on various defined pressure levels, such as

- breakthrough pressure – pressure at which outflow is detected,
- peak pressure – highest pressure level during flow-through,
- shut-in pressure – pressure when pumping is shut off and outflow has ceased.

As has been shown in this report and in terms of the present discussion, pressure levels like these lack fundamental importance as material characterizing parameters. On the contrary, they all depend strongly on the details of the experimental set-up, e.g. on the amount of gas which is being compressed as well as on the rate of compression.

An interesting experiment would be to apply different *constant* gas pressures to a set of identical samples. Pressures should be chosen to give suction values above, at and below the swelling pressure.

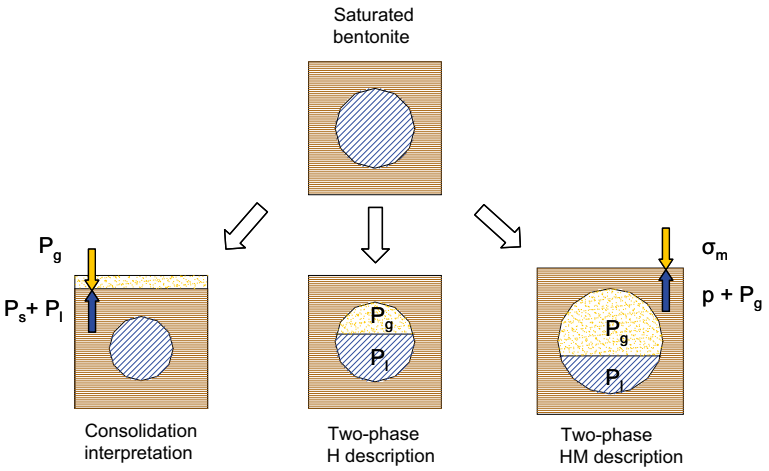

Figure 5-34. *Distinctions between the consolidation interpretation and the two-phase descriptions. At consolidation (left), a new pore-space is formed with a gas pressure balancing the total pressure in the bentonite. The same gas- and liquid-filled pore volumes can be handled in a two-phase H description (centre) by a GEV retention curve, and thereby be consistent with a consolidation interpretation. In a HM description (right), a gas pressure will unload the bentonite and thereby increase the total pore volume.*

References

SKB's (Svensk Kärnbränslehantering AB) publications can be found at www.skb.com/publications.

Alonso E E, Gens A, Josa A, 1990. A constitutive model for partially saturated soils. Géotechnique 40, 405–430.

Bear J, 1972. Dynamics of fluids in porous media. Mineola, NY: Dover.

Bucher F, Müller-Vonmoos M, 1989. Bentonite as a containment barrier for the disposal of highly radioactive wastes. Applied Clay Science 4, 157–177.

Börgesson L, 2001. Compilation of laboratory data for buffer and backfill materials in the Prototype Repository. SKB IPR 01-34, Svensk Kärnbränslehantering AB.

Börgesson L, Hernelind J, 1999. Coupled thermo-hydro-mechanical calculations of the water saturation phase of a KBS-3 deposition hole. Influence of hydraulic rock properties on the water saturation phase. SKB TR-99-41, Svensk Kärnbränslehantering AB.

Börgesson L, Hökmark H, Karnland O, 1988. Rheological properties of sodium smectite clay. SKB TR 88-30, Svensk Kärnbränslehantering AB.

Börgesson L, Johannesson L-E, Sandén T, Hernelind J, 1995. Modelling of the physical behavior of water saturated clay barriers. Laboratory tests, materal models and finite element application. SKB TR 95-20, Svensk Kärnbränslehantering AB.

Börgesson L, Hernelind J, Ludvigsson J-E, 2004. Äspö Hard Rock Laboratory. DECOVALEX III, Task 1. Modelling of FEBEX in-situ test. Coupled thermo-hydro-mechanical analyses of the buffer and the rock. SKB IPR-08-12, Svensk Kärnbränslehantering AB.

Börgesson L, Åkesson M, Kristensson O, Malmberg D, Dueck A, Hernelind J, 2016. EBS TF – THM modelling of BM 2: Large scale field tests. SKB TR-13-07, Svensk Kärnbränslehantering AB.

CEA, 2005. Specification of Benchmark THM 1.1 – Bentonite THM Mock-Up Experiments preformed by CEA. CEA, France.

CIEMAT, 2005. Specification of benchmark THM 1.2 – Infiltration Tests Under Isothermal Conditions and Under Thermal Gradient Performed by CIEMAT. CIEMAT, Spain.

CIMNE, 2000. CODE_BRIGHT. A 3-D program for thermo-hydro-mechanical analysis in geological media. Departamento de Ingeneria del Terreno; Cartgrafica y Geofisica, UPC, Barcelona, Spain.

Dang K D, Robinet J-C, 2004. Thermo-hydro-mechanical behaviour of MX80 bentonite for temperature ≥ 100 °C. Final Report. ANDRA report C.RP.0EUG.02.008, ANDRA, France.

Dueck A, 2004. Hydro-mechanical properties of a water unsaturated sodium bentonite: laboratory study and theoretical interpretation. PhD thesis. Lund University.

Dueck A, 2010. Thermo-mechanical cementation effects in bentonite investigated by unconfined compression tests. SKB TR-10-41, Svensk Kärnbränslehantering AB.

ENRESA, 1998. FEBEX. Bentonita: origen, propiedades y fabricación de bloques. Publicación Técnica 04/98, ENRESA, Spain. (In Spanish.)

ENRESA, 2000. FEBEX Project. Full-scale engineered barriers experiment for a deep geological repository for high level radioactive waste in crystalline host rock. Final Report. Publicación Técnica 1/2000. ENRESA, Spain.

Fernández A M, 2003. Caracterización y modelización del agua intersticial en materiales arcillosos. Estudio de la bentonita de Cortijo de Archidona. PhD thesis. Universidad Autónoma de Madrid. (In Spanish.)

Fredlund D G, Rahardjo H, 1993. Soil mechanics for unsaturated soils. New York: Wiley.

Gatabin C, Billaud P, 2005. Bentonite THM mock up experiments. Sensors data report. Rapport NT-DPC/SCCME 05-300-A, CEA, France.

Gens A, 2016. Äspö Hard Rock Laboratory SKB Task Force on Engineered Barrier System (EBS) Task 1: Laboratory tests. Report of phase 1 of the EBS THM Task Force. SKB TR-14-24, Svensk Kärnbränslehantering AB.

Harrington J F, Horseman S T, 1999. Gas transport properties of clays and mudrocks. In Aplin A C, Fleet A J, Macquaker J H S (eds). Muds and mudstones: physical and fluid-flow properties. Bath: Geological Society. (Special publication 158), 107–124.

Harrington J F, Horseman S T, 2003. Gas migration un KBS-3 buffer bentonite. Sensitivity of test parameters to experimental boundary conditions. SKB TR-03-02, Svensk Kärnbränslehantering AB.

Hoch A R, Cliffe K A, Swift B T, Rodwell W R, 2004. Modelling gas migration in compacted bentonite: GAMBIT club phase 3. Final report. Posiva 2004-02, Posiva Oy, Finland.

Horseman S T, Harrington J F, Sellin P, 1999. Gas migration in clay barriers. Engineering Geology 54, 139–149.

Imbert C, Billaud P, Touze G, Dang K D, 2004. Comportement thermo-hydro-mécanique d'une argile gonflante méthodologique en situation de stockage. Rapport RT-DPC/SCCME 04-677-A, CEA. (In French.)

Ingelstam E, Rönngren R, Sjöberg S, 1982. TEFYMA: handbok för teknisk fysik, fysik och matematik. Bromma: Sjöberg. (In Swedish.)

Kahr G, Kraehenbuehl F, Stoeckli H F, Müller-Vonmoos M, 1990. Study of the water-bentonite system by vapour adsorption, immersion calorimetry and X-ray techniques: II. Heats of immersion, swelling pressures and thermodynamic properties. Clay Minerals 25, 499–506.

Karnland O, Muurinen A, Karlsson F, 2005. Bentonite swelling pressure in NaCl solutions – Experimentally determined data and model calculations. In Alonso E E, Ledesma A (eds). Advances in understanding engineered clay barriers: Proceedings of the International Symposium on Large Scale Field Tests in Granite, Sitges, Barcelona, Spain, 12–14 November 2003. London: Taylor & Francis.

Karnland O, Olsson S, Nilsson U, 2006. Mineralogy and sealing properties of various bentonites and smectite-rich clay material. SKB TR-06-30, Svensk Kärnbränslehantering AB.

Lajudie A, Raynal J, Petit J-C, Toulhoat P, 1994. Clay based materials for engineered barriers. A review. In Murakami T, Ewing R C (eds). Scientific basis for nuclear waste management XVIII: symposium held in Kyoto, Japan, 23–27 October 1994. Pittsburgh, PA: Materials Research Society. (Materials Research Society Symposium Proceedings 353), 221–230.

Lloret A, Romero E, Villar M V, 2004. FEBEX II Project Final report on thermo-hydro-mechanical laboratory tests. Publicación Técnica 10/04. ENRESA, Spain.

Pintado X, Lloret A, 2006. Thermohydraulic test on bentonite. Journal of Thermal Analysis and Calorimetry 84, 325–330.

Pintado X, Ledesma A, Lloret A, 2002. Backanalysis of thermohydraulic bentonite properties from laboratory tests. Engineering Geology 64, 91–115.

Rodwell W R, 2005. Summary of a GAMBIT club workshop on gas migration in bentonite, Madrid 29–30 October, 2003. A report produced for the GAMBIT club SKB TR-05-13, Svensk Kärnbränslehantering AB.

Sánchez M, 2004. Thermo-hydro-mechanical coupled analysis in low permeability media. PhD thesis. Universitat Politècnica de Catalunya.

Tang A-M, Cui Y-J, 2005. Controlling suction by the vapour equilibrium technique at different temperatures and its application in determining the water retention properties of MX80 clay. Canadian Geotechnical Journal 42, 287–296.

UPC, 2006. Specification of benchmark THM 1.3 – Heating tests with no water.

Villar M V, 2002. Thermo-hydro-mechanical characterisation of a bentonite from Cabo de Gata. A study applied to the use of bentonite as sealing material in high level radioactive waste repositories. Publicación Técnica 01/2002, ENRESA, Spain.

Villar M V, Lloret A, 2004. Influence of temperature on the hydro-mechanical behaviour of a compacted bentonite. Applied Clay Science 26, 337–350.

Villar M V, Martín P L, Barcala J M, 2005a. Infiltration tests at isothermal consitions and under thermal gradient. Technical Report CIEMAT/DMA /M2140/1/05, CIEMAT, Spain.

Villar M V, Martin P L, Lloret A, 2005b. Determination of water retention curves of two bentonites at high temperature. Proceedings of an International symposium on Advanced Experimental Unsaturated Soil Mechanics in Trento, Italy. 77–82.

Villar M V, Romero E, Lloret A, 2005c. Thermo-mechanical and geochemical effects on the permeability of high-density clays. In Alonso E E, Ledesma A (eds). Advances in understanding engineered clay barriers: Proceedings of the International Symposium on Large Scale Field Tests in Granite, Sitges, Barcelona, Spain, 12–14 November 2003. London: Taylor & Francis.

Åkesson M (ed), 2006. Äspö Hard Rock Laboratory. Temperature Buffer Test. Evaluation modeling – Mock-up test. SKB IPR-06-11, Svensk Kärnbränslehantering AB.

Åkesson M, Hökmark H, 2007. Mechanical model for unsaturated MX80. In Schanz T (ed). Theoretical and numerical unsaturated soil mechanics. Berlin: Springer. (Springer Proceeding in Physics 113), 3–10.

Appendix 1

Location of the sensors

The vertical location of the various sensors is given in the following Tables.

Table A1-1. Temperature sensors.

Sensor	Y (mm)
T 0	0
T 1	2.5
T 2	18.75
T 3	35.0
T 4	51.25
T 5	67.5
T 6	83.75
T 7	100
T 8	116.25
T 9	132.5
T 10	148.75
T 11	165
T 12	181.25
T 13	197.5
T 14	206*

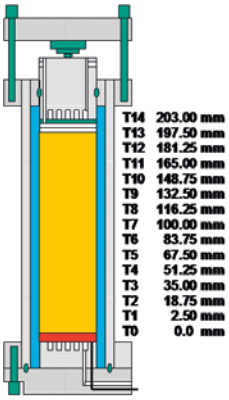

* Taking into account a 3-mm stainless-steel plate.

Table A1-2. Relative humidity sensors.

Relative-humidity sensor	Temperature sensor	Y (mm)
HR1	HRT1	22.5
HR2	HRT2	37.5
HR3	HRT3	52.5
HR4	HRT4	72.5
HR5	HRT5	92.5
HR6	HRT6	112.5
HR7	HRT7	132.5

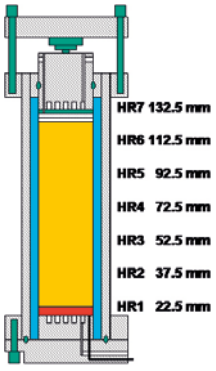

Table A1-3. Pore pressure sensors.

Sensor	Y (mm)
PI1	20.0
PI2	52.0
PI3	84.0
PI4	116.0

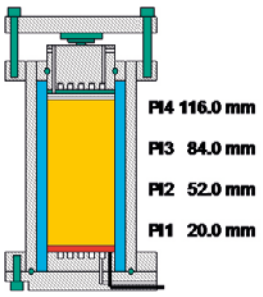

Table A1-4. Radial stress sensors.

Sensor	Y (mm)	
PT1	15.0	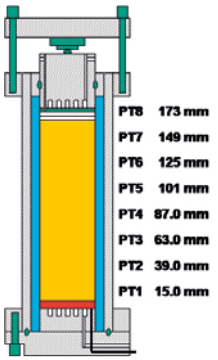
PT2	39.0	
PT3	63.0	
PT4	87.0	
PT5	101.0	
PT6	125.0	
PT7	149.0	
PT8	173.0	

Appendix 2

Properties of MX-80 bentonite

In this Appendix, some information on THM properties of MX-80 bentonite obtained in previous investigations is collected. The sources of the various results presented are indicated in each case. More detailed information may be found in other references.

A2.1 Physical properties

MX-80 has a solid grain density equal to 2.82 g/cm^3 (Villar 2002). Note that this value is different from the 2.65 g/cm^3 used in the reporting of the experiments (Gatabin and Billaud 2005).

A2.2 Retention curve

Figure A2-1 shows experimental results obtained for the retention curve of pure MX-80 bentonite at several dry densities. Data provided by EUROGEOMAT were found in Dang and Robinet (2004). The other data are from internal reports.

Villar (2002) presents data obtained on MX-80 compacted at 1 600 kg/m^3 using water with 3 salt concentrations: 0, 0.5 and 1.2 %. Results are shown in Figure A2-2. Water salinity appears to have little influence on the retention curve for suctions above 20 MPa. No data are available for lower suctions.

A2.3 Permeability

Figure A2-3 shows the variation of the intrinsic permeability with porosity as obtained by several laboratories on water saturated MX-80 samples. Intrinsic permeability obtained in compacted samples is systematically one order of magnitude higher than intrinsic permeability obtained in bentonitic slurries.

A2.4 Swelling properties

A2.4.1 Swelling pressure

Data on swelling pressure reported by Börgesson et al. (1995), Lajudie et al. (1994) and Imbert et al. (2004) are compiled in Figure A2-4.

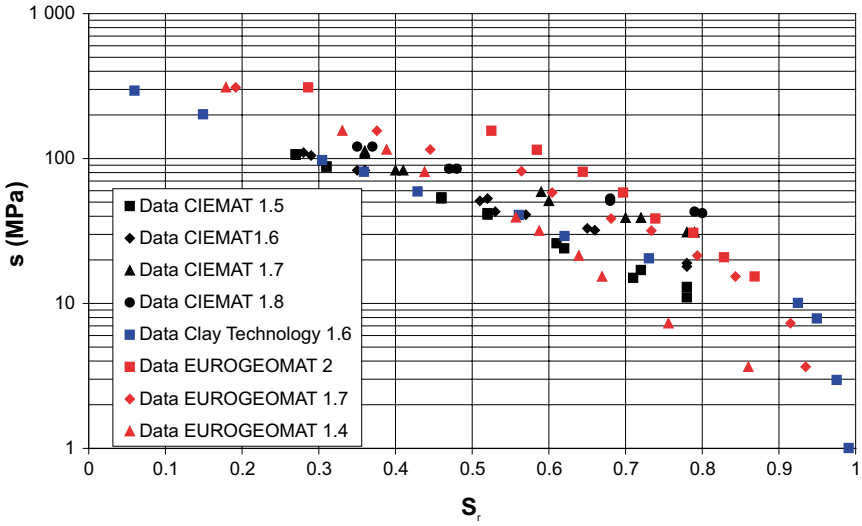

Figure A2-1. *Retention of MX-80 at constant volume and several dry densities.*

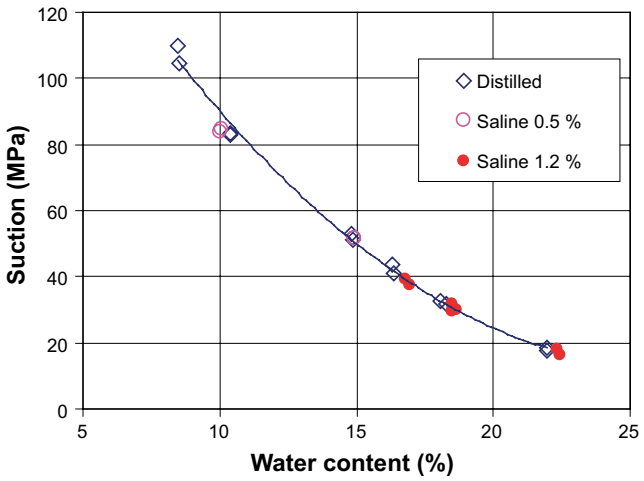

Figure A2-2. *Suction/water content relation for MX-80 clay compacted at dry density 1 600 kg/m³ and in presence of 3 water salinities (Villar 2002).*

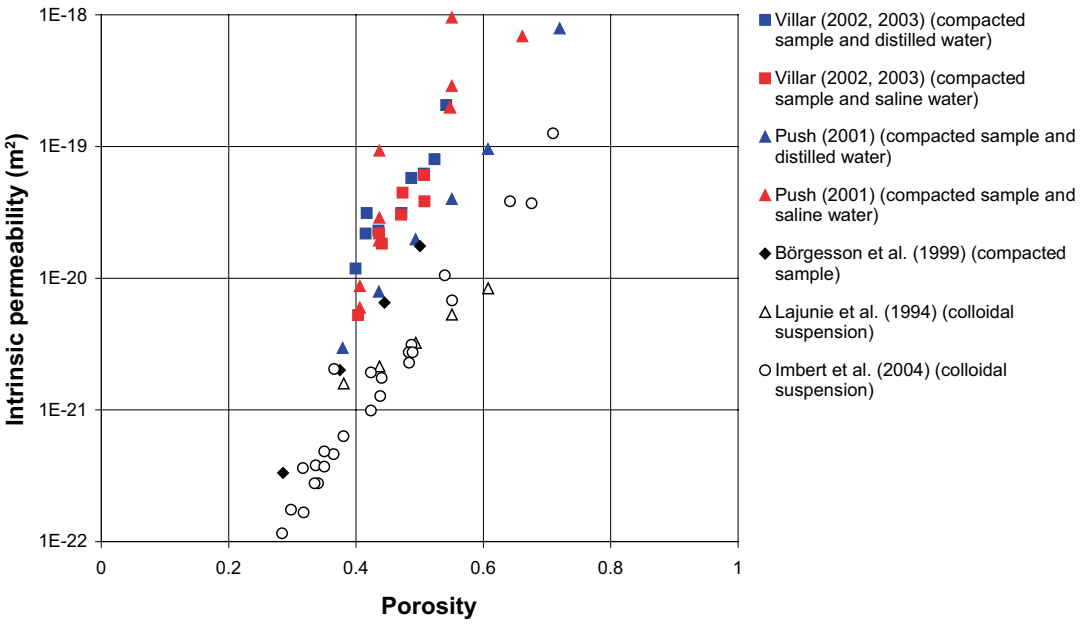

Figure A2-3. *Variation of intrinsic permeability with porosity as obtained by several laboratories in water-saturated samples.*

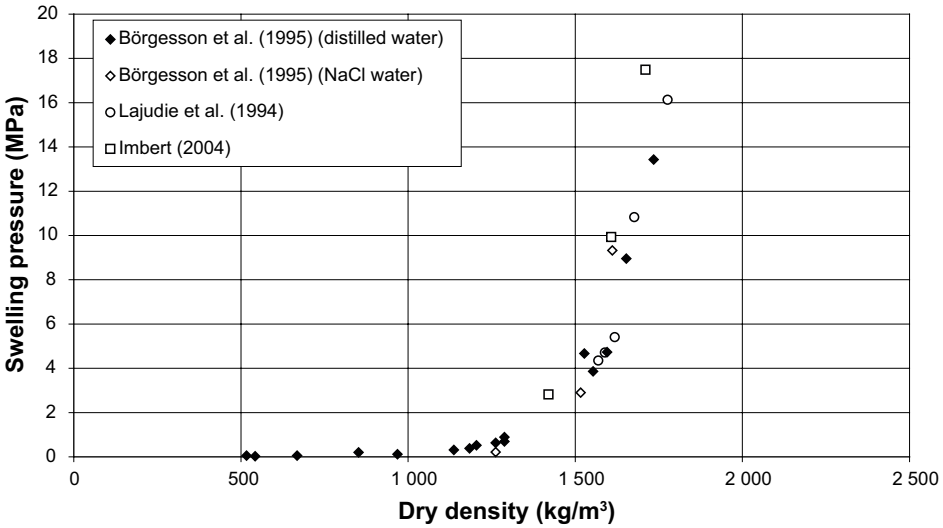

Figure A2-4. *Swelling pressure vs dry density as obtained by different laboratories.*

Especially relevant are the results reported by Imbert et al. (2004) from tests performed in the CEA laboratory on samples compacted uniaxially:

Table A2-1. Swelling pressure of uniaxially compacted MX-80 samples

Specimen	Water content (%)	Compaction pressure (MPa)	Initial dry density (g/cm³)	Final dry density (g/cm³)	Swelling pressure (MPa)
1741u	14.25	10	1.490	1.485	4.20
1726u	14.25	20	1.639	1.632	9.93
1727u	14.25	40	1.770	1.749	19.98
1729u	14.25	60	1.823	1.798	26.06
1730u	14.25	100	1.858	1.836	29.73
1740u	14.25	181.5	1.888	1.863	36.49

A2.4.2 Swelling strains

Villar (2002) performed 4 swelling tests (EDN_4_9, EDN_4_10, EDN_2_13 and EDN_2_14) under constant load (0.1 MPa) in the oedometer cell. Tests EDN_4_9 and EDN_4_10 have an initial density equal to 1 666 kg/m³ and tests EDN_2_13 and EDN_2_14 to 1 790 kg/m³. Hydration was achieved by applying 6 suction reduction steps (to 14 MPa, 8 MPa, 5 MPa, 1.5 MPa, 0.5 MPa and 0.1 MPa). Equilibration time after each step lasted more than 40 days. Tests EDN_4_10 and EDN_2_14 were performed controlling suction by nitrogen pressure (labelled *nit* in Figure A2-5) and tests EDN_4_9 and EDN_2_13 by a solution of sulphuric acid (labelled *sulf* in Figure A2-5).

Void ratios at the end of the equilibration stage of each suction step are shown in Figure A2-5 for all tests. Transient evolution of vertical strain during equilibration phases of test EDN_4_10 is presented in Figure A2-6.

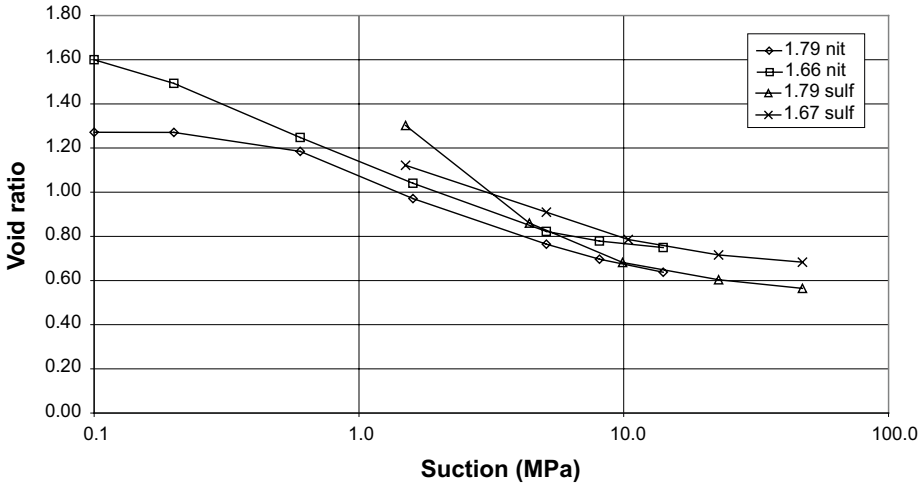

Figure A2-5. *Evolution of void ratio with applied suction during a wetting path performed in an oedometer cell under a constant load of 0.1 MPa.*

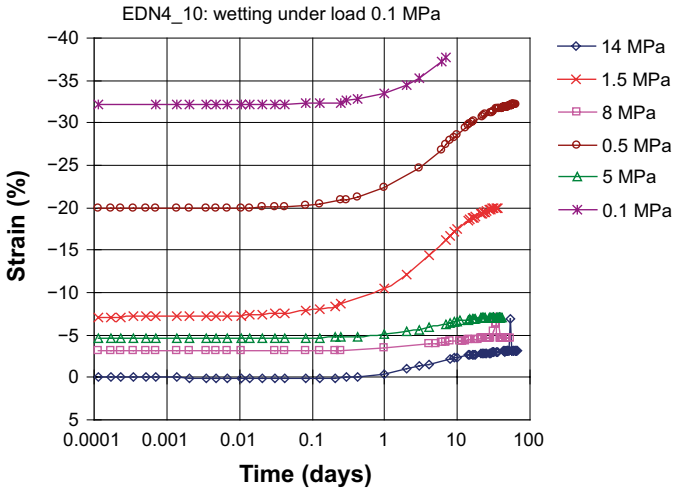

Figure A2-6. *Evolution of vertical strain with time during test EDN_4_10 (Villar 2002).*

A2.5 Mechanical response of saturated MX-80

Once brought to saturation, samples in tests EDN_4_9, EDN_4_10, EDN_2_13 and EDN_2_14 were further loaded in oedometer conditions. Figure A2-7 shows the compression lines obtained for each test.

A2.6 Thermal conductivity

The variation of thermal conductivity with degree of saturation was determined by Börgesson et al. (1995). The results are shown in Figure A2-8.

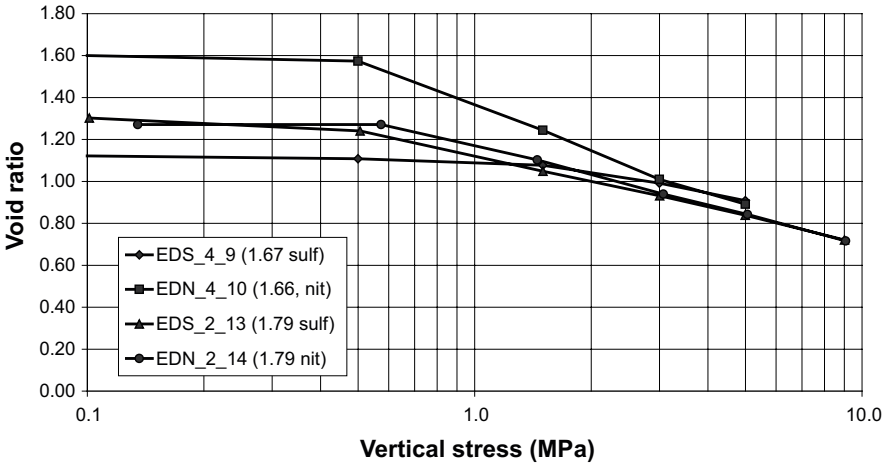

Figure A2-7. *Compression lines obtained during the drained loading following the saturation stage for samples EDN_4_9, EDN_4_10, EDN_2_13 and EDN_2_14.*

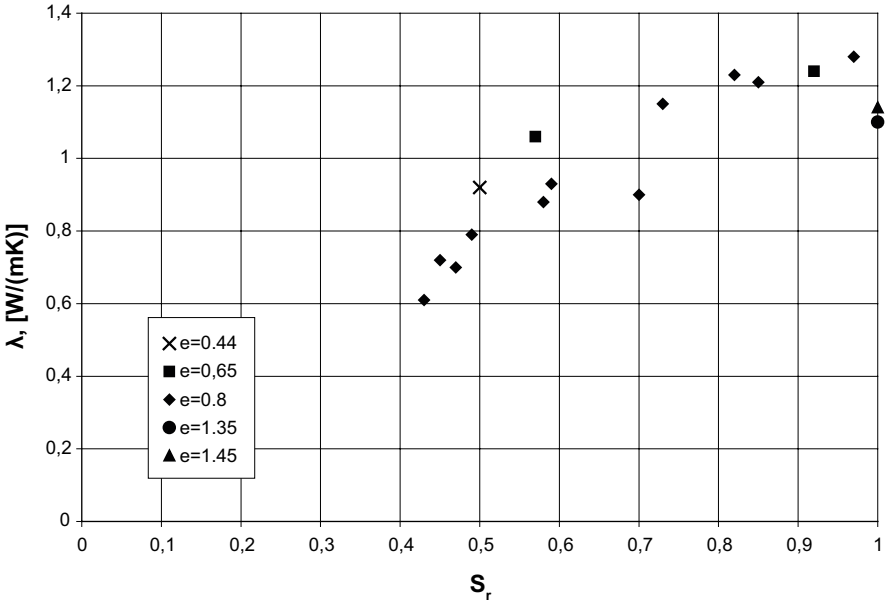

Figure A2-8. *Variation of thermal conductivity with degree of saturation.*

Appendix 3

Determination of the retention curve

A3.1 Introduction

The laboratory experiment was used as an evaluation test for different models in the Task Force Benchmark 1.1.1. The material used was MX-80, a sodium bentonite which has been investigated by many authors. Two different tests were made with different initial conditions; Cell 1 and Cell 2. In the following the input data from the specifications (Section 2.2) and the retention curves (*RH* vs. *w*) from others are used for calculation of the confined retention curves (S_r vs. suction) which could be used in the evaluation modelling.

The confined retention curve was calculated from data representing 20 °C. An attempt was made to take influence of temperature into account. Values from the literature were used to predict the confined retention curve for 80 °C. However, it is not obvious how this should be done.

In the following the term specific retention curve is used for the relation between *RH* and *w* when the initial water content diverge from 0 % in contrast to the basic retention curve which is used when the material is initially dry. If the material is confined and exposed to external pressure the term confined retention curve is used for the relation between S_r and suction.

A3.2 Input data

Given input data for the modelling of the laboratory tests is shown in Table A3-1. The last row in Table A3-1 represents measured *RH* at the beginning of phase 1, i.e. after mounting.

Table A3-1. Given input data and measured initial RH.

Material: MX-80	Cell 1	Cell 2
RH conditioning (%)	60	90
w (%)	13.7	17.9
ρ_d (Mg/m^3)	1.791	1.735
RH measured (%)	59–61	75

With the particle density equal to 2.78 Mg/m^3 (e.g. Börgesson et al. 1988) the void ratio and the degree of saturation were calculated to the values presented in Table A3-2.

Table A3-2. Calculated variables from Table A3-1 and ρ_s = 2.78 Mg/m^3.

Material: MX-80	Cell 1	Cell 2
e	0.55	0.6
$S_{r,ini}$ (%)	69.0	82.6

A3.3 Specific retention curves

General

In Figure A3-1 the test results from Dueck (2004) are marked with small symbols. Lines are drawn between the measured data. In this figure also the initial conditions from Table A3-1 are shown, two large circular points.

From Figure A3-1 conclusions about a probable moisture history can be drawn. With regard to cell 1, w_I = 13.7 %, the material first dried in a climate corresponding to *RH* = 33 % and then absorbed moisture in a climate corresponding to *RH* = 60 %. *RH* about 60 % was also measured at the beginning of phase 1, after installation of Cell 1. The material used for Cell 2 was conditioned

at RH = 90 % according to input data but interpreted with data from Dueck (2004) the material must have dried from this condition to reach the water content w_2 = 17.9 %. After installation the measured RH was about 75 % which coincide with the value valid for w_2 in Figure A3-1.

A continuous formulation of the retention curve in the range of RH > 40 % valid for absorption was formulated according to Equation A3-1. The constants a = 6.6 and b = 0.17 were taken from curve fitting with measured data according to Dueck (2004), see Figure A3-2. This equation was used for both Cell 1 and Cell 2 for absorption.

$$w = (a - \ln[-(10^{-6} \cdot \rho_w * R * T / \omega_w) * \ln(RH/100)])/b \quad \text{(A3-1)}$$

where

w =water content (%)

T =temperature (K)

R =universal gas constant (8.31432 J/(mol K))

ρ_w =density of water (kg/m^3)

ω_v =molecular mass of water vapour (0,018 kg/mol)

$RH = 100 \cdot (p/p_s)$

p =partial pressure of pore-water vapour (kPa)

p_s = saturation pressure of water vapour over a flat surface of pure water at the temperature T (kPa)

Desorption of the material in Cell 1 was supposed to follow the curve with w_{ini} = 9.4 % in Figure A3-1 and Figure A3-2 while desorption of the material in Cell 2 was supposed to follow the curve with w_{ini} = 17.5 %.

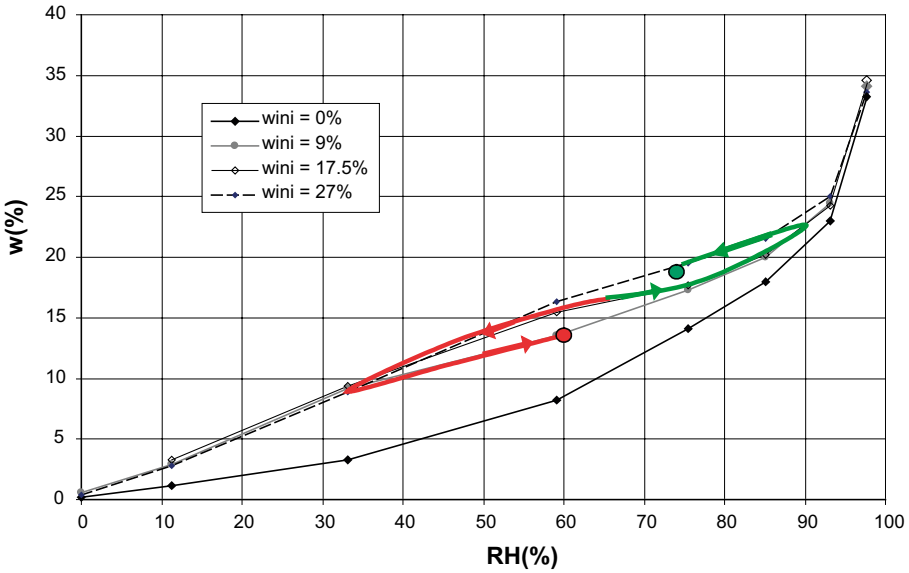

Figure A3-1. *Specific retention curves. Assumed moisture history for Cell 1 and Cell 2 are shown.*

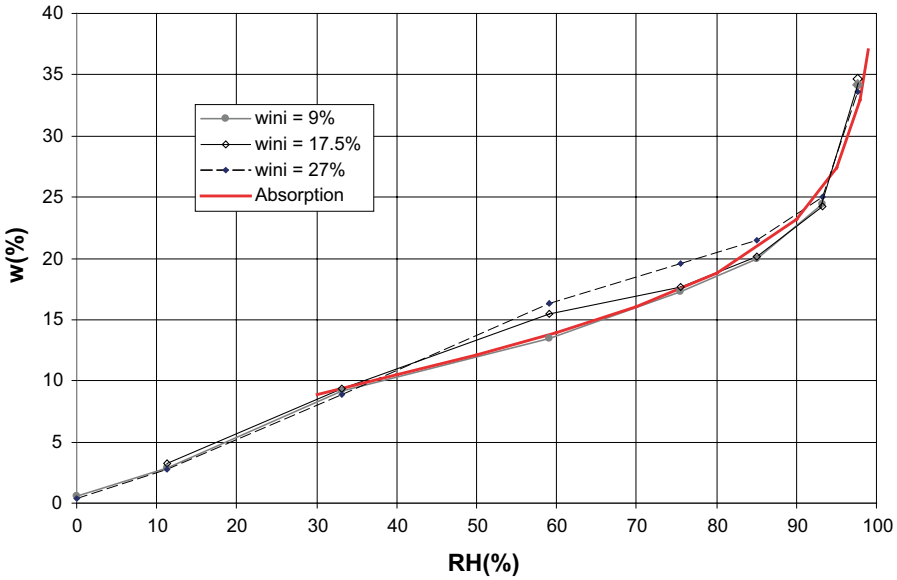

Figure A3-2. *Specific retention curves. Results from Dueck (2004) and equation A3-1 with a = 6.6 and b = 0.17.*

A3.4 Influence of high temperature

The influence of temperature on the retention properties of MX-80 was investigated by for example Villar et al. (2005b) and Tang and Cui (2005). This is illustrated in Figure A3-3. The investigation made by Villar et al. (2005b) was mainly done by measuring *RH* inside samples placed at different temperatures. The samples consisted of compacted powder mixed with different amounts of deionised water. The *RH* sensors (capacitive sensors) were installed in drilled holes inside the samples. Some of the squares are interpolated between measurements. Tang and Cui investigated the moisture uptake of free swelling compacted samples placed over different saturated salt solutions and at different temperatures.

The change in RH with increased temperature was determined from the data presented in Figure A3-3. The suction change rate was given by Tang & Cui as $\Delta\log(\text{suction})/\Delta T = -0.003$ log(MPa)/°C which represented a mean value of suction in the range of 20 to 178 MPa (i.e. 27 % < RH < 86 % at 20 °C). From the measured data given by Villar et al. (2005b) the suction change rate was calculated to values between −0,002 and −0,004 log(MPa)/°C at temperatures between 30 and 80 °C and at water contents 16 and 19 %. At lower water content −0,001 log(MPa)/ °C was calculated.

In the following a correction for an increase in temperature from 20 °C to 80 °C was done by adding $\Delta\log(\text{suction})/\Delta T = -0{,}003$ log(MPa)/ °C to all values, also outside the range where it was determined. In Figure A3-4 values from Equation A3-1 and temperature corrected values are shown representing 20 and 80 °C, respectively.

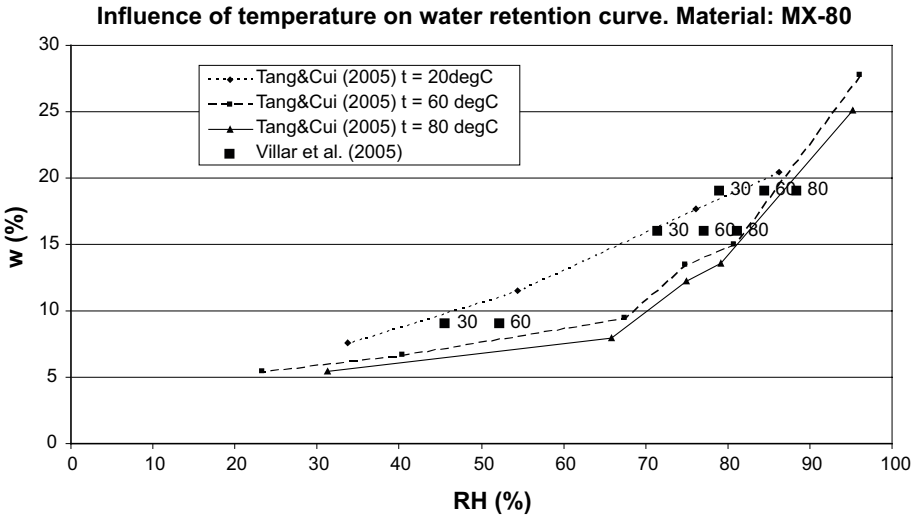

Figure A3-3. *Influence of temperature on the retention curve of MX-80. After Villar et al. (2005b) and Tang and Cui (2005). The numbers after the filled squares show the temperature of those tests.*

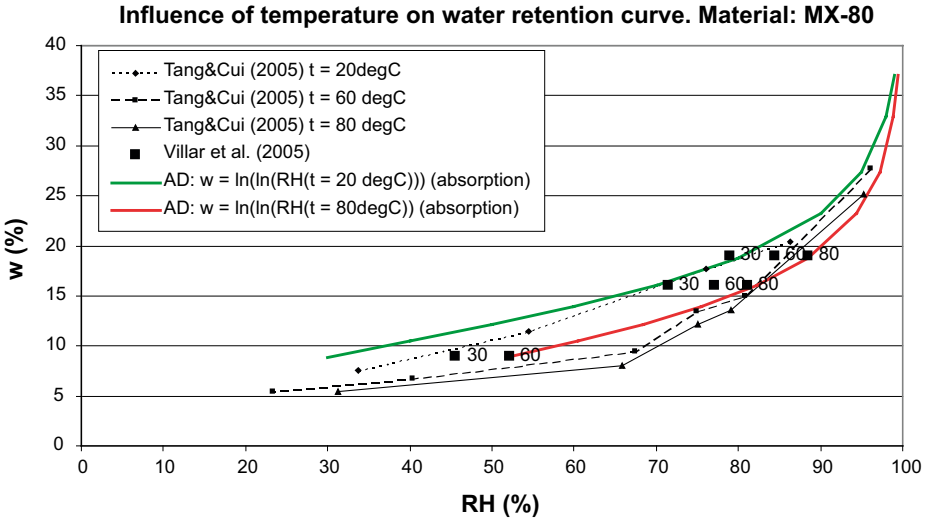

Figure A3-4. *Temperature corrections applied to equation A3-1 with measurements by Villar et al. (2005b) and Tang and Cui (2005), see Figure A3-3.*

A3.5 Confined retention curve

Influence of total pressure

The confined retention curve is presented as the relation between the degree of saturation S_r (%) and suction s (kPa). Suction is determined from relative humidity RH according to Equation A3-2 (e.g. Fredlund and Rahardjo 1993).

$$s = -\frac{R \cdot T \cdot \rho_w}{\omega_v} \ln\left(\frac{RH}{100}\right) \qquad \text{(A3-2)}$$

where

s =suction (kPa)

T =temperature (*K)*

R =universal gas constant (8.31432 J/(mol K))

ρ_w =density of water (kg/m^3)

ω_v =molecular mass of water vapour (18 kg/kmol)

$RH = 100 \cdot (p/p_s)$

p =partial pressure of pore-water vapour (kPa)

p_s =saturation pressure of water vapour over a flat surface of pure water at the temperature T (kPa)

The confined retention curve valid for constant volume conditions can be calculated according to a model presented by Dueck (2004) where the equations below are further described and where more references are given. Data input to the model are the void ratio e, the initial degree of saturation $S_{r,ini}$ and a retention curve. The parameters required for the model can be calculated from those input data. The water content at saturation w_s can be calculated from the void ratio according to Equation A3-3. *RHret* corresponding to w_s can be determined from the retention curve, here represented by the confined retention curve described by Equation A3-1. Finally the swelling pressure at saturation can be calculated according to Equation A3-4. The equation has previously been used by others, e.g. Kahr et al. (1990).

$$w_s = 100 \cdot \frac{e \cdot \rho_w}{\rho_s} \qquad \text{(A3-3)}$$

$$P_{ret}(e) = -\frac{R \cdot T \cdot \rho_w}{\omega_v} \cdot \ln\left(\frac{RH_{ret}(w_s)}{100}\right) \qquad \text{(A3-4)}$$

where

P_{ret} =swelling pressure at saturation (kPa)

e =void ratio

RH_{ret} =relative humidity according to the specific or basic retention curve (%)

w_s =water content at saturation (%)

ρ_s =particle density (kg/m^3)

To determine the confined retention curve the actual RH_{act} was increased in steps from 0 to 100 %. At each RH_{act} iterations were made to find the correct w corresponding to the confined retention curve, i.e. with the swelling pressure taken into account. The iterations were made according to steps 1 to7 below. An equation similar to Equation A3-5 was used for saturated conditions by e.g. Karnland et al. (2005).

1. A swelling pressure P_{assume} was assumed.
2. RH_{ret} was determined from Equation A3-5 where the other parameters were known.
3. The water content w corresponding to RH_{ret} was determined from Equation A3-1.
4. The degree of saturation S_r was determined from the void ratio e and the water content w.
5. From Equation A3-6 the swelling pressure P was calculated.
6. The calculated pressure P and the assumed pressure P_{assume} were compared and the difference between them was minimized by assuming a new pressure P_{assume} and going back to point 2.
7. Suction representing RH_{act} was calculated from Equation A3-2. The water content w and the calculated suction represent one point on the confined retention curve.

$$P(RH_{act}, w) = -\frac{R \cdot \boldsymbol{T} \cdot \rho_{\boldsymbol{w}}}{\omega_v} \cdot \ln\left(\frac{RH_{ret}(w)}{RH_{act}}\right) \qquad \text{(A3-5)}$$

where

P =swelling pressure (kPa)

RH_{ret} =relative humidity according to the specific or basic retention curve (%)

w =water content (%)

RH_{act} =actual relative humidity (%)

$$P(S_r, e) = \frac{S_r - S_{r,ini}}{1 - S_{r,ini}} \cdot P_{ret}(e) \qquad \text{(A3-6)}$$

where

P =swelling pressure (kPa)

P_{ret} =swelling pressure at saturation from Equation A3-4

S_r =degree of saturation

$S_{r,ini}$ =initial degree of saturation

The equations above are valid for absorption. For desaturation it was assumed that no swelling pressure was present and thus for each RH_{act} the corresponding water content could be calculated directly from Equation A3-1. The point on the confined retention curve is then calculated according to step 7 above.

The confined retention curves are shown in Figure A3-5 for two different void ratios but the same specific retention curve (represented by Equation A3-1). The confined retention curves for absorption is valid for $e = 1$ ($\rho_d = 1.4$ t/m^3) and $e = 0.4$ ($\rho_d = 2$ t/m^3).

Influence of high temperature

The confined retention curve at higher temperatures than 20°C was estimated from data presented by Villar et al. (2005b) and Tang and Cui (2005), see above. This was done by moving the specific retention curve and evaluating the water content from the moved retention curve. The steps 2a to 2c below were done between step 2 and 3 mentioned above.

2a. Suction s corresponding to RH_{ret} was calculated according to Equation A3-2.

2b. A correction of −0,003 log(MPa)/°C was added to the logarithm of the calculated suction s.

2c. A new RH_{ret} was calculated from the corrected suction with Equation A3-2.

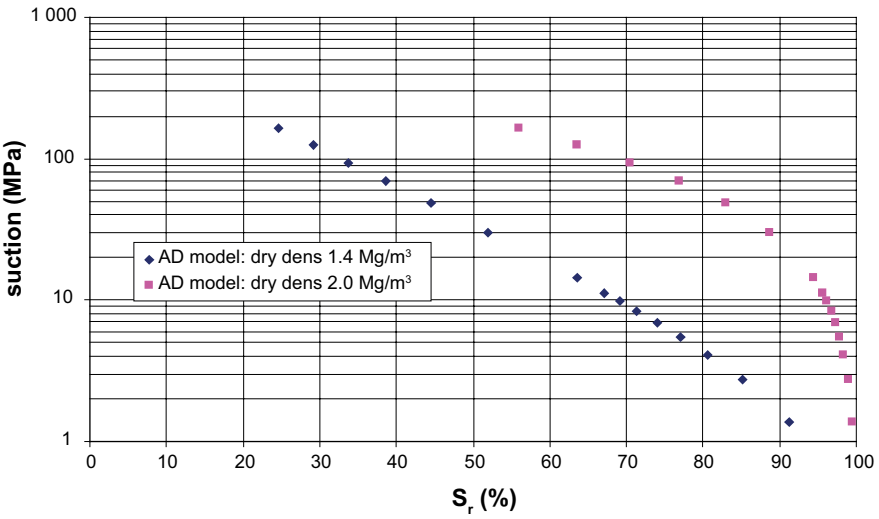

Figure A3-5. *Confined retention curves e = 1 (rd = 1.4 t/m³) and e = 0.4 (rd = 2 t/m³).*

Comments

The model presented by Dueck (2004) is mainly based on measurements of swelling pressure during absorption and constant volume conditions. The retention curves (S_r vs. suction) are calculated for this condition. The calculated curves only represent the two void ratios predicted for Cell 1 and Cell 2, respectively.

The correction for high temperature was based on measurements presented in the literature. An average correction was calculated and the correction was then used over the whole range of suction, also outside the range of the tests of which the correction was based on. Thus for the calculated retention curves valid for 80 °C one correction (unit log(MPa)/°C) was applied in the suction range of 0 to 200 MPa.

Resulting confined retention curves for Benchmark 1.1.1

The following includes Figures and Tables with results from the determination of a confined retention curve for the modelling of the benchmark 1.1.1.

Below data points according to Figure A3-8 and Figure A3-11 are presented. The abbreviations SRT and CRT mean specific retention curve and confined retention curve, respectively. RH = 0 % is represented by 1 GPa in suction.

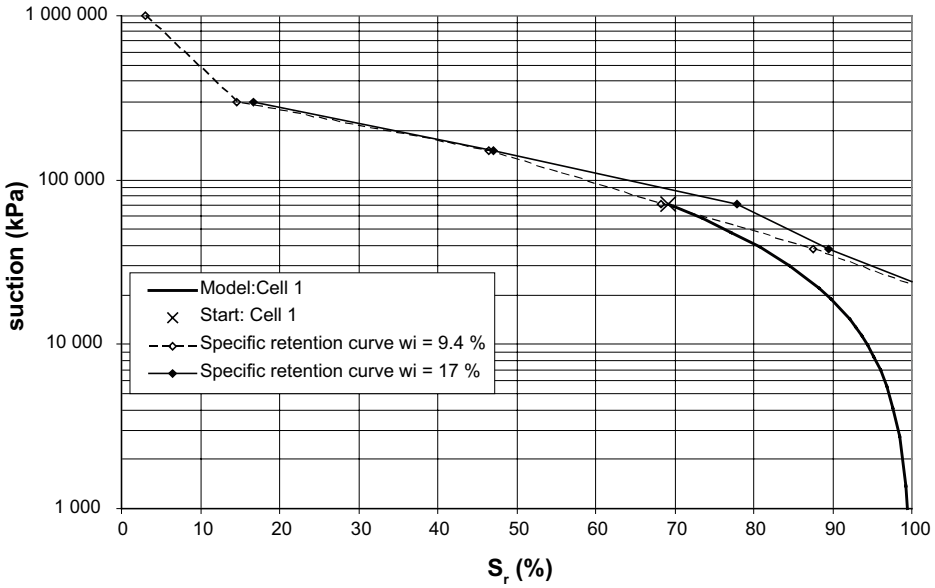

Figure A3-6. *Retention curves valid for Cell 1 (e =0.55).*

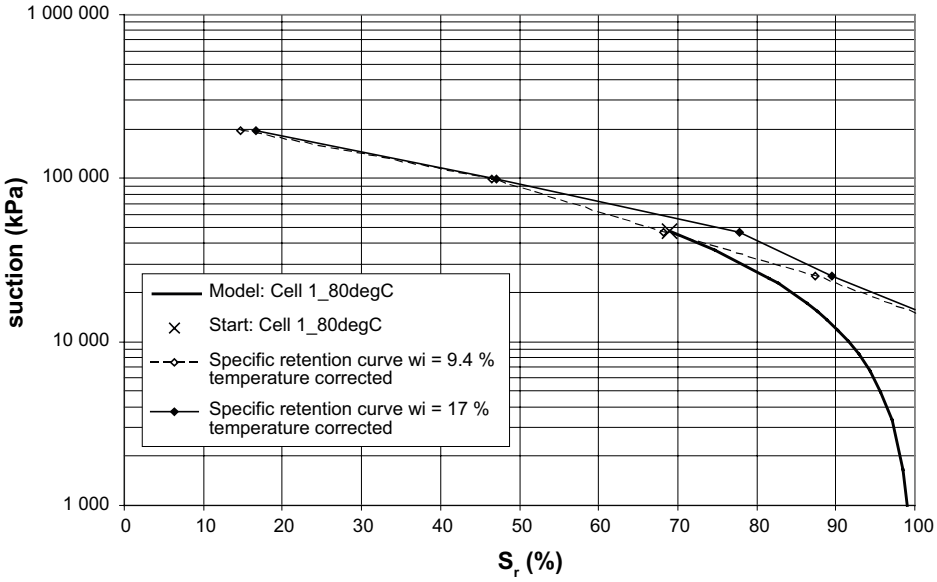

Figure A3-7. *Temperature corrected retention curves for Cell 1 (e = 0.55).*

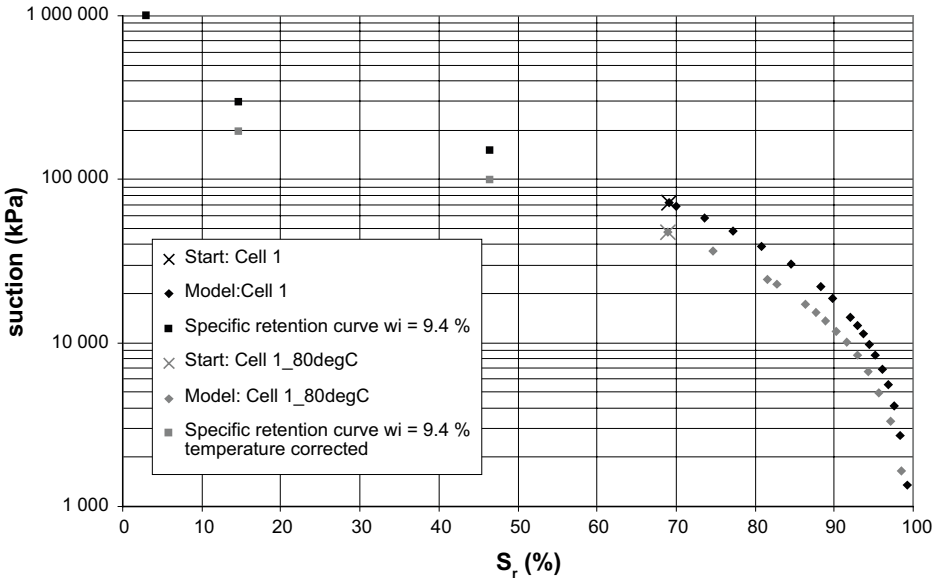

Figure A3-8. *Applied confined retention curve valid for Cell 1 (e = 0.55).*

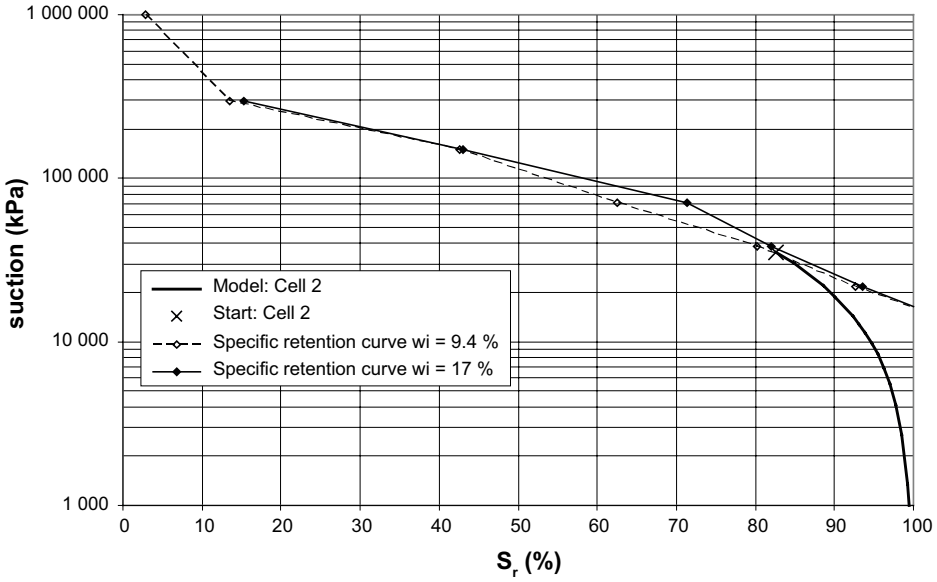

Figure A3-9. *Retention curves valid for Cell 2 (e = 0.6).*

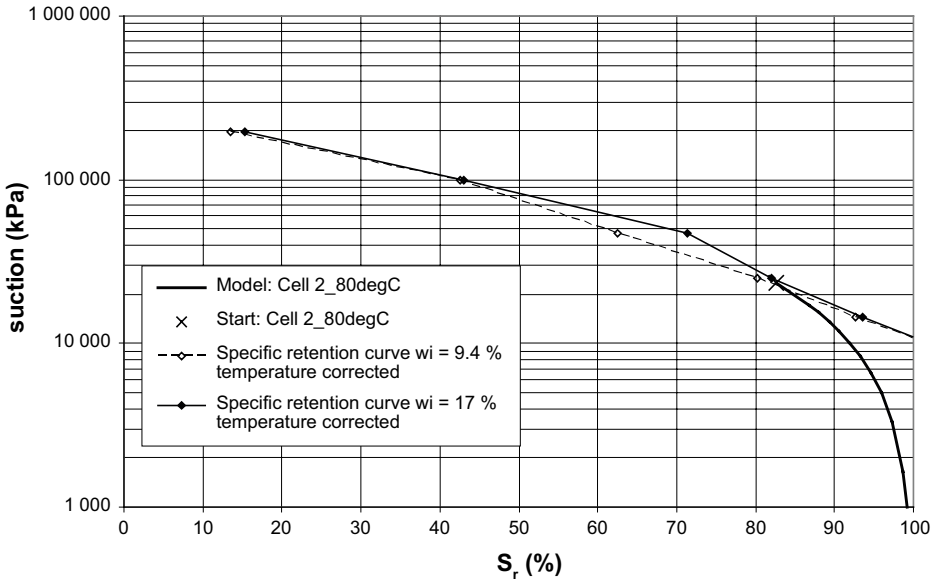

Figure A3-10. *Temperature corrected retention curves for Cell 2 (e = 0.6).*

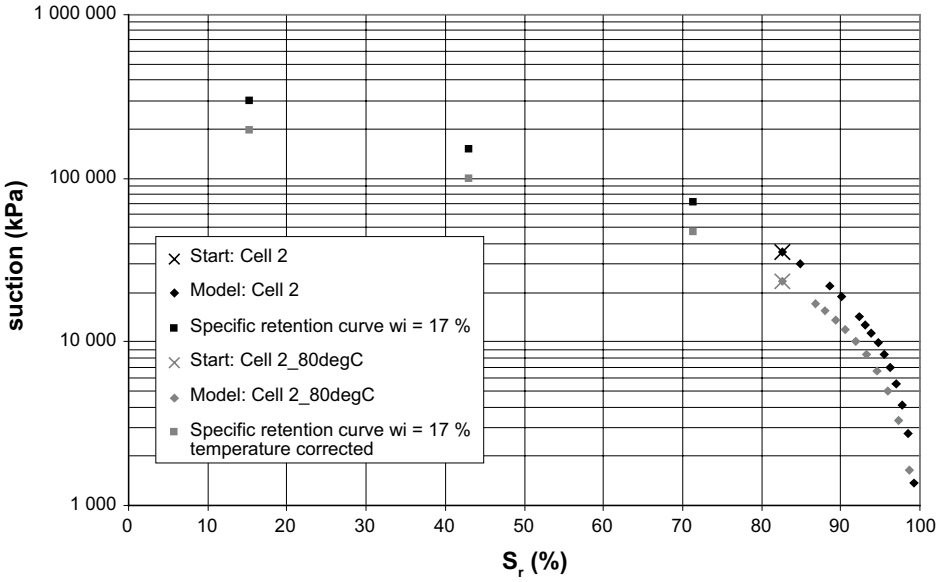

Figure A3-11. *Applied confined retention curve valid for Cell 2 (e = 0.6).*

Table A3-3. Used data points Cell 1 and 20 °C.

Start	w % 13,7	Sr % 69	s kPa 71 869
	e 0,55	T °C 20	
	Sr %	**Suction kPa**	
SRT	3,0	1 000 000	*
	14,7	295 148	
	46,5	149 666	
CRT	69,1	71 869	
	70,0	69 134	
	73,6	58 302	
	77,2	48 272	
	80,8	38 935	
	84,5	30 200	
	88,3	21 995	
	89,8	18 848	
	92,1	14 259	
	92,9	12 764	
	93,7	11 285	
	94,5	9 822	
	95,2	8 374	
	96,0	6 942	
	96,8	5 525	
	97,6	4 122	
	98,4	2 734	
	99,2	1 360	
	99,6	678	
	100,0	135	
	100,0	0	
	100,0	0	

SRT with w_{ini} = 9.4 %.

Table A3-4. Used data points Cell 2 and 20 °C.

Start	w % 17,9	Sr % 82,7	s kPa 35373
	e 0,6	T °C 20	
	Sr %	**Suction kPa**	
SRT	15,3	295148	
	43,1	149666	
	71,4	71194	
CRT	82,7	35373	
	84,9	30200	
	88,6	21995	
	90,1	18848	
	92,4	14259	
	93,2	12764	
	93,9	11285	
	94,7	9822	
	95,4	8374	
	96,2	6942	
	97,0	5525	
	97,7	4122	
	98,5	2734	
	99,3	1360	
	99,6	678	
	99,9	135	
	100,0	0	

SRT with w_{ini} = 17 %.

Table A3-5. Used data points Cell 1 and 80 °C.

Start	w % 13,7	Sr % 69	s kPa 47779
	e 0,55	T °C 80	
	Sr %	**Suction kPa**	
SRT	14,7	195002	
	46,5	98883	
CRT	69,0	47779	
	74,7	36384	
	81,5	24592	
	82,7	22707	
	86,4	17179	
	87,7	15378	
	89,0	13596	
	90,3	11833	
	91,6	10089	
	93,0	8364	
	94,3	6656	
	95,7	4966	
	97,1	3294	
	98,6	1639	
	99,3	817	
	99,9	163	
	100,0	0	

SRT with w_{ini} = 9.4 %.

Table A3-6. Used data points Cell 2 and 80 °C.

Start	w % 17,9	Sr % 82,6	s kPa 23459
	e 0,6	T °C 80	
	Sr %	**Suction kPa**	
SRT	15,3	195002	
	43,1	98883	
	71,4	47038	
CRT	82,6	23459	
	86,8	17179	
	88,0	15378	
	89,3	13596	
	90,6	11833	
	91,9	10089	
	93,2	8364	
	94,5	6656	
	95,9	4966	
	97,3	3294	
	98,6	1639	
	99,3	817	
	99,9	163	
	100,0	0	

SRT with w_{ini} = 17 %.

Appendix 4

Properties of FEBEX bentonite

In this Appendix, selected information on THM properties of FEBEX bentonite as reported in Villar et al. (2005a) is highlighted. More detailed information can be found in the references of this report.

A4.1 General properties

The liquid limit of the bentonite is 102 ± 4, the specific gravity 2.70 ± 0.04, and 67 ± 3 percent of particles are smaller than 2 μm. The hygroscopic water content in equilibrium with the laboratory atmosphere (relative humidity 50 ± 10 %, temperature 21 ± 3 °C, total suction about 100 MPa) is 13.7 ± 1.3 percent. Table A4-1 shows the average content values of the exchangeable cations along with the cation exchange capacity (CEC), as determined by different methods and laboratories.

Table A4-1. Average values of exchangeable cations and cation exchange capacity (CEC) as determined by different methods (meq/100g).

	CSIC-Zaidín[1]	CIEMAT[1]	CIEMAT[2]
Ca^{2+}	43 ± 5	42 ± 3	35 ± 2
Mg^{2+}	32 ± 3	32 ± 2	31 ± 3
Na^{+}	24 ± 4	25 ± 2	27 ± 0
K^{+}	2.1 ± 0.2	2.5 ± 0.3	2.6 ± 0.4
Sum of exchangeable cations	**101 ± 4**		**96 ± 0**
CEC[3]		102 ± 4	

[1] Determined by displacement by 1M NH_4AcO at pH 7 after washing of soluble salts (ENRESA 2000), the values are recalculated to give a sum of cations equal to CEC;
[2] Determined by displacement by 0.5M $CsNO_3$ at pH 7 (Fernández 2003);
[3] Determined by NaAcO/NH_4AcO pH=8.2 (ENRESA 2000).

A4.2 Retention curve

The retention curve of the bentonite was determined in samples compacted to different dry densities under different temperatures (Lloret et al. 2004, Villar and Lloret 2004). The volume of the samples remained constant during the determinations, since they were confined in constant volume cells. To impose the different relatives humidities (*i.e.* suctions) the cells were placed in desiccators with sulphuric acid solutions of various concentrations. Some data from these laboratory determinations are shown in Figure A4-1.

Following an approach similar to that presented by Sánchez (2004) to fit the data from these laboratory determinations, the following empirical equation can be obtained:

$$w = (a + b\,n)\left[1 + \left(\frac{s}{P_0\, e^{-\eta(n-n_0)}\, e^{-\alpha(T-T_0)}}\right)^{\frac{1}{1-\lambda}}\right]^{-\lambda} \qquad \text{(A4-1)}$$

where w is the water content in percentage, n the porosity, s the suction in MPa, and T the temperature in °C. The values of parameters a, b, P_0, η, n_0, α, T_0 and λ are indicated in Table A4-2. The differences between measured values and the estimated values using Equation A4-1 are smaller than 2 percent in terms of water content.

Table A4-2. Values of parameters in Equation A4-1.

a	b	P_0 (MPa)	λ	η	n_0	α (1/°C)	T_0 (°C)
10.96	41.89	12.68	0.211	7.97	0.4	0.00647	20

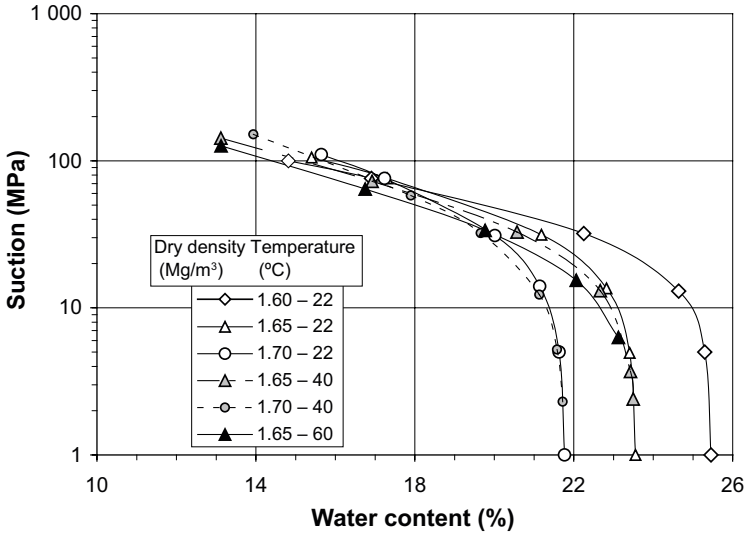

Figure A4-1. *Water retention curves at different temperatures and for different bentonite densities (Lloret et al. 2004).*

In unconfined conditions, the relationship between suction (s, MPa) and water content (w, %) changes, taking into account the initial dry density of the bentonite (ρ_{d0}, g/cm^3), it may be fitted to the following equation:

$$w = (45.1\ \rho_{d0} - 39.2) - (18.8\rho_{d0} - 20.34)\log s \qquad \text{(A4-2)}$$

A4.3 Hydraulic properties

The saturated permeability to deionised water (k_w, m/s) of samples of untreated FEBEX bentonite compacted at different dry densities is exponentially related to dry density (ρ_d, g/cm^3). A distinction may be made between two different empirical fittings depending on the density interval (Villar 2002):

for dry densities of less than 1.47 g/cm^3:

$$\log k_w = -6.00\ \rho_d - 4.09 \qquad (r^2 = 0.97,\ 8 \text{ points}) \qquad \text{(A4-3)}$$

for dry densities in excess of 1.47 g/cm^3:

$$\log k_w = -2.96\ \rho_d - 8.57 \qquad (r^2 = 0.70,\ 26 \text{ points}) \qquad \text{(A4-4)}$$

The determinations were done at room temperature. The variation in the experimental values with respect to these fittings is smaller for low densities than it is for higher values, with an average – in absolute values – of 30 percent.

Some isothermal infiltration tests and heat flow tests at constant overall water content were performed during FEBEX I project and they were backanalysed using CODE_BRIGHT (Pintado et al. 2002). It is possible to fit the experimental data using a cubic law for the relative permeability ($k_r = S_r^3$) and a value of 0.8 for the vapour tortuosity factor (τ).

A4.4 Thermal properties

The thermal conductivity (λ, W/m·K) of the compacted bentonite at laboratory temperature is related to the degree of saturation (S_r) through the following expression:

$$\lambda = \frac{A_1 - A_2}{1 + e^{\frac{S_r - x_0}{dx}}} + A_2 \qquad \text{(A4-5)}$$

where A_1 represents the value of λ for S_r=0, A_2 the value of λ for S_r=1, x_0 the degree of saturation for which thermal conductivity is the average of the two extreme values and dx is a parameter. This

equation was chosen because it accurately represents the behaviour of thermal conductivity versus water content (degree of saturation), which are directly related but not in a linear fashion (Villar 2002). The fitting obtained, with an r^2 of 0.923, gives the following values for each parameter:

$A_1 = 0.57 \pm 0.02$

$A_2 = 1.28 \pm 0.03$

$x_0 = 0.65 \pm 0.01$

$dx = 0.100 \pm 0.016$

Alternatively, an approximate representation of the variation of thermal conductivity with degree of saturation (Figure A4-2) can be obtained using the expression

$$\lambda = \lambda_{sat}^{\ S_r}\ \lambda_{dry}^{\ (1-S_r)} \qquad \text{(A4-6)}$$

with the values of λ_{sat} = 1.15 W/mK and λ_{dry} = 0.47 W/mK (ENRESA 2000).

A4.5 Swelling pressure

The swelling pressure (P_s, MPa) of FEBEX samples compacted with their hygroscopic water content and flooded with deionised water up to saturation at room temperature can be related to dry density (ρ_d, g/cm^3) through the following equation (Villar 2002):

$$\ln P_s = 6.77\ \rho_d - 9.07 \qquad (r^2 = 0.88,\ 52 \text{ measurements}) \qquad \text{(A4-7)}$$

In this case, the difference between experimental values and this fitting is, on average, 25 percent. This dispersion, which is wider for higher dry densities, is due both to the natural variability of bentonite and to the measurement method used, which does not allow high degrees of accuracy.

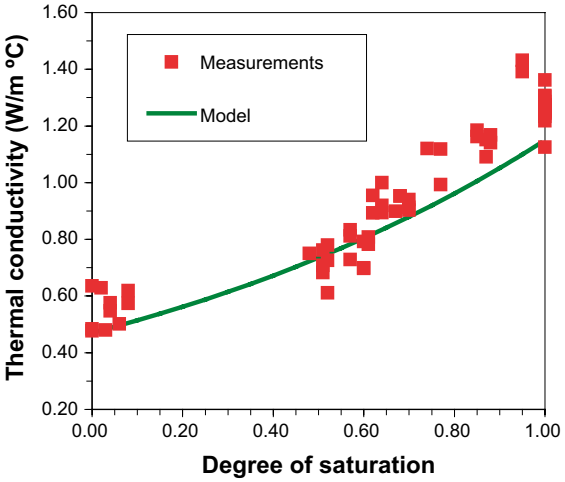

Figure A4-2. *Thermal conductivity results and equation (A4-6).*